INO/2006/01
Project Report
Volume I

INDIA-BASED NEUTRINO OBSERVATORY

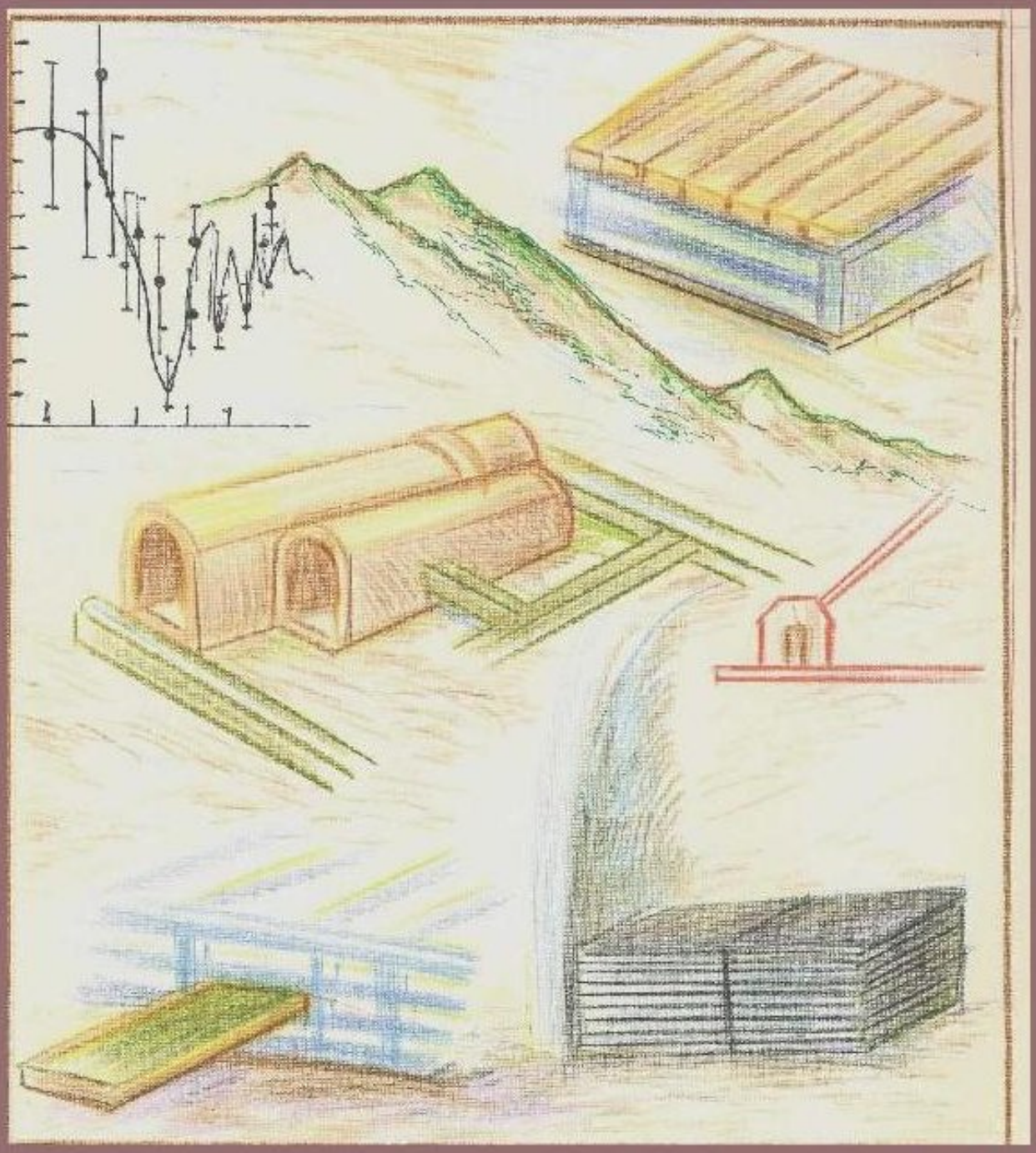

I N O

The INO Collaboration[1]

- **Aligarh Muslim University, Aligarh:**

  M. Sajjad Athar, Rashid Hasan, S. K. Singh

- **Banaras Hindu University, Varanasi:**

  B. K. Singh, C. P. Singh, V. Singh

- **Bhabha Atomic Research Centre (BARC), Mumbai:**

  V. Arumugam, Anita Behere, M. S. Bhatia, V. B. Chandratre, R. K. Choudhury, V. M. Datar, M. P. Diwakar, M. G. Ghodgaonkar, A. K. Mohanty, A. W. Matkar, P. K. Mukhopadhyay, S. C. Ojha[2], L. M. Pant, K. Srinivas

- **Calcutta University (CU), Kolkata:**

  Amitava Raychaudhuri

- **Delhi University (DU), Delhi:**

  Brajesh Choudhary, Debajyoti Choudhury, Sukanta Dutta, Ashok Goyal, Kirti Ranjan

- **Harish Chandra Research Institute (HRI), Allahabad:**

  Sanjib K. Agarwalla, Sandhya Choubey, Anindya Datta, Raj Gandhi, Pomita Ghoshal, Srubabati Goswami, Poonam Mehta, Sukanta Panda, S. Rakshit, Amitava Raychaudhuri

- **University of Hawaii (UHW), Hawaii:**

  Sandip Pakvasa

- **Himachal Pradesh University (HPU), Shimla:**

  S. D. Sharma

- **Indian Institute of Technology, Bombay (IITB), Mumbai:**

  Basanta Nandi, S. Uma Sankar, Raghav Varma

- **Indira Gandhi Center for Atomic Research, Kalpakkam:**

  J. Jayapandian, C. S. Sundar

- **The Institute of Mathematical Sciences (IMSc), Chennai:**

  D. Indumathi, H. S. Mani, M. V. N. Murthy, G. Rajasekaran, Nita Sinha, D. V. Ramakrishna [3]

- **Institute of Physics (IOP), Bhubaneswar:**

  Pankaj Agrawal, D. P. Mahapatra, S. C. Phatak

- **North Bengal University (NBU), Siliguri:**

  A. Bhadra, B. Ghosh, A. Mukherjee, S. K. Sarkar

[1] This is an open collaboration and experimentalists are especially encouraged to join.
[2] since retired
[3] Replacing Abdul Salam who was a member until March 5, 2005

- **Panjab University (PU), Chandigarh:**

  Vipin Bhatnagar, M. M. Gupta, J. B. Singh

- **Physical Research Laboratory (PRL), Ahmedabad:**

  A. S. Joshipura, Subhendra Mohanty, S. D. Rindani

- **Saha Institute of Nuclear Physics (SINP), Kolkata:**

  Sudeb Bhattacharya, Suvendu Bose, Sukalyan Chattopadhyay, Ambar Ghosal, Asimananda Goswami, Kamales Kar, Debasish Majumdar, Palash B. Pal, Satyajit Saha, Abhijit Samanta, Abhijit Sanyal, Sandip Sarkar, Swapan Sen, Manoj Sharan

- **Sikkim Manipal Institute of Technology, Sikkim:**

  G. C. Mishra

- **Tata Institute of Fundamental Research (TIFR), Mumbai:**

  B. S. Acharya, Sudeshna Banerjee, Sarika Bhide, Amol Dighe, S. R. Dugad, P. Ghosh, K. S. Gothe, S. K. Gupta, S. D. Kalmani, N. Krishnan, Naba K. Mondal, P. Nagaraj, B. K. Nagesh, Biswajit Paul, Shobha K. Rao, A. K. Ray, L. V. Reddy, B. Satyanarayana, S. Upadhya, Piyush Verma

- **Variable Energy Cyclotron Centre (VECC), Kolkata:**

  R. K. Bhandari, Subhasish Chattopadhyay, Premomay Ghosh, B. Mohanty, G. S. N. Murthy, Tapan Nayak, S. K. Pal, P. R. Sarma, R. N. Singaraju, Y. P. Viyogi

Scientific Steering Committee

C. V. K. Baba, *Nuclear Science Centre, New Delhi*
Ramanath Cowsik, *Indian Institute of Astrophysics, Bangalore*
H. S. Mani, *The Institute of Mathematical Sciences, Chennai*
V. S. Narasimham, *Tata Institute of Fundamental Research, Mumbai*
G. Rajasekaran, *The Institute of Mathematical Sciences, Chennai*
Amit Roy, *Nuclear Science Centre, New Delhi*
Probir Roy, *Tata Institute of Fundamental Research, Mumbai*
Bikash Sinha, *Saha Institute of Nuclear Physics, Variable Energy Cyclotron Centre, Kolkata*

INO Spokesperson

Naba K Mondal,
Tata Institute of Fundamental Research,
Homi Bhabha Road, Mumbai 400 005, India
E-mail: nkm@tifr.res.in

Each one of us adds a
little to our understanding
of nature and from all the
facts assembled arises
a certain grandeur.
Aristotle

PREFACE

Very important developments have occurred recently in neutrino physics and neutrino astronomy. Oscillations of neutrinos and the inferred discovery that neutrinos have mass are likely to have far-reaching consequences. This discovery has come from the study of neutrinos from the Sun and those produced by cosmic rays.

The pioneering solar neutrino experiments of Davis and collaborators in the USA, the gigantic Super-Kamiokande detector and the KamLAND detector in Japan, the heavy-water detector at the Sudbury Neutrino Observatory in Canada, and a few other laboratories, together, have contributed in a very fundamental way to our knowledge of neutrino properties and interactions. In particular, the Canadian experiment has given direct experimental proof of the 80 year-old hypothesis that the Sun and the stars are powered by thermonuclear fusion reactions.

Impelled by these discoveries and their implications for the future of particle physics, plans have been made—world-wide—for new neutrino detectors, neutrino factories and long base-line neutrino experiments.

Indian scientists were pioneers in neutrino experiments. In fact neutrinos produced by cosmic ray interactions in the Earth's atmosphere were first detected in the deep mines of the Kolar Gold Fields (KGF) in India in 1965.

It is planned to revive underground neutrino experiments in India. A multi-institutional Neutrino Collaboration has been formed with the objective of creating an India-based Neutrino Observatory (INO). This Report is based on the feasibility study conducted by the collaboration. The report discusses specific physics goals both for the near term and the future. More information may be found on the INO web-site: http://www.imsc.res.in/∼ino.

This is an open collaboration and it is hoped that many more physicists from within and outside the country will join in this effort. The success of this project crucially depends upon international participation and support.

Note added: This report is an updated and revised version of the Interim Report Vol I, submitted to the Department of Atomic Energy (DAE), Department of Science and Technology (DST) and University Grants Commission (UGC), of the Government of India, on May 1, 2005. Major additions have been made to the Physics, Detector and Simulation chapters with some minor changes elsewhere.

Contents

1 Project Summary **1**
1.1 Organisation of the Report . . . 3
1.2 Summary of current status of INO . . . 5
1.3 A vision for INO . . . 5

2 Introduction **7**
2.1 Current Status of neutrino physics experiments . . . 8
2.2 Open questions and future goals . . . 10

3 Neutrino Physics with Magnetised Iron Calorimeter **15**
3.1 Three flavour neutrino oscillation . . . 16
3.2 Parameter values gleaned from experiments . . . 16
3.3 Atmospheric Neutrinos . . . 19
3.3.1 Precision measurement of $|\delta_{32}|$ and θ_{23} . . . 21
3.3.2 Matter effects in μ^- and μ^+ events . . . 24
3.3.3 Determination of mass hierarchy . . . 27
3.3.4 Deviation from maximality of θ_{23}: octant determination . . . 34
3.3.5 Discrimination between $\nu_\mu \to \nu_\tau$ and $\nu_\mu \to \nu_s$ . . . 40
3.3.6 Probing CPT Violation . . . 40
3.3.7 Constraining long-range leptonic forces . . . 43
3.4 Neutrino Factories . . . 46
3.4.1 Determination of θ_{13} . . . 48
3.4.2 Sign of δ_{32} . . . 50
3.4.3 Probing CP violation in the leptonic sector . . . 50
3.5 Large matter effects in $\nu_\mu \to \nu_\tau$ oscillations . . . 52

4 Other Physics issues with Magnetised Iron Calorimeter **59**
4.1 Probing cosmic rays through muons underground . . . 59
4.1.1 The cascade event rate for muons with energies 1–1000 TeV . . . 61
4.1.2 Muon Fluxes . . . 64
4.1.3 Results and Discussion . . . 65
4.2 Kolar events . . . 66

5 The Magnetised Iron Calorimeter **69**
5.1 Choice of the detector . . . 69
5.2 The ICAL Detector . . . 70
5.2.1 Basic parameters . . . 70
5.2.2 RPCs as active detector elements . . . 71
5.2.3 Detector arrangement and readout schemes . . . 73
5.2.4 Readout Electronics . . . 74

5.2.5 Voltage Comparator ASIC . . . 75
5.2.6 Gas System . . . 75
5.2.7 Structural stability of ICAL detector . . . 76
5.3 Current status of detector R & D . . . 76
5.3.1 Gas mixing units . . . 76
5.3.2 RPC operation and characterisation . . . 79
5.3.3 Long term stability tests of INO RPCs . . . 84
5.3.4 Tracking of cosmic ray muons using small size RPCs . . . 84
5.3.5 ICAL Prototype . . . 88
5.4 The Magnet . . . 89
5.4.1 Design criteria . . . 90
5.4.2 A toroidal design for the ICAL magnet . . . 91
5.4.3 A small magnet for detector prototype tests . . . 93
5.4.4 Final Design . . . 98

6 ICAL Simulations 101
6.1 The detector geometry . . . 101
6.1.1 Digitisation of tracks . . . 102
6.2 The neutrino source . . . 103
6.2.1 The atmospheric neutrino flux . . . 103
6.2.2 Events generation . . . 104
6.2.3 Muon energy distribution . . . 104
6.2.4 Muon zenith angle distribution . . . 104
6.3 Event tracking and reconstruction . . . 107
6.3.1 Reconstruction of test events . . . 107
6.3.2 Muon energy reconstruction . . . 107
6.3.3 Muon direction reconstruction . . . 110
6.3.4 Muon charge identification . . . 111
6.3.5 Hadron energy calibration . . . 112
6.4 Atmospheric neutrino analysis with GEANT . . . 113
6.4.1 Data Analysis . . . 114
6.4.2 L and E resolutions . . . 114
6.4.3 The oscillation parameters . . . 116
6.4.4 Precision Plots . . . 117
6.5 Cosmic ray muons . . . 118
6.5.1 The surface muon flux . . . 119
6.5.2 Cosmic rays underground . . . 120
6.5.3 The slant depth X . . . 120
6.5.4 The aperture . . . 121
6.5.5 Results . . . 121
6.5.6 Pattern of hits in the ICAL detector . . . 123
6.6 Very high energy muons . . . 124
6.7 Open issues . . . 126

7 A tale of two sites 129
7.1 Site requirements . . . 129
7.2 Summary of the sites . . . 130
7.3 Comparison of PUSHEP and Rammam . . . 132
7.4 Tunnel and Cavern Complex . . . 134
7.4.1 Surface laboratory and Portal . . . 134

7.4.2 Design of access tunnel 134
7.4.3 Cavern complex 136
7.4.4 Basic Services 136

8 Cost and Time Schedules **141**
8.1 Cost factors: INO Laboratory 141
8.2 Cost factors: ICAL detector 143
8.3 Time Scale 144

9 Laboratory Management **145**

10 Ideas for Human Resource Development **149**

11 Education and Outreach **153**

12 INO as a Facility for the Future **157**
12.1 Low Energy Neutrinos 157
12.2 Neutrino Astronomy 160
12.3 A low energy accelerator for nuclear astrophysics 160
12.4 Others 161

13 Acknowledgements **163**

A Neutrino Experiments in India **165**

B Introduction to Neutrino Oscillations **171**

C Structural Stability of the ICAL Detector **181**

D ICAL as an End Detector for a Beta Beam Experiment **185**

E Double Beta Decay Experiment at INO **189**

F Neutrino Detectors of the Future: A Comparison **193**

G Possible Site for INO at Rohtang **199**

H Memorandum of Understanding (MoU) **203**

Bibliography **211**

Chapter 1

Project Summary

Over the past decade, data from several neutrino detectors around the world, in particular, that from the Super-Kamiokande (Super-K) and KamLAND detectors in Japan, and the Sudbury Neutrino Observatory (SNO) in Canada have shown that neutrinos have mass and *oscillate*. This provides the first unambiguous evidence for physics beyond the Standard Model of particle physics.

The existence of non-zero neutrino masses has profound implications on fields as varied as nuclear physics, geophysics, astrophysics and cosmology apart from being of fundamental interest to particle physics. The discovery of neutrino mass and oscillation is but a first step and there are several questions which may require several experiments spanning many decades to be resolved: we still do not know the scale of neutrino mass, we only partially know the extent of their mixing, we are not even sure if the neutrino is its own antiparticle or not, to name a few. The experimental field of neutrino physics is now moving into a phase where decisive and high precision experiments are needed.

It is in this context that an initiative began to take shape a few years ago leading to the idea of the India-based Neutrino Observatory (INO). Historically the Indian initiatives in cosmic ray and neutrino physics go back to several decades. As a result of extensive studies of the muon flux at several depths in the Kolar Gold Fields (KGF) underground laboratory, it was realised that the muon flux was low enough to permit measurements on atmospheric neutrinos. The first ever such neutrino interaction was observed as early as in 1965 [1]. This laboratory later looked for nucleon decay and placed upper limits on the half-life for the proton decay [2].

Another interesting finding is the observation of the so-called Kolar events, which have not been explained to date. These suggested a decaying heavy particle with an amazingly long lifetime of a few nanosececonds. Most of these experiments were done using calorimeters weighing up to 300 tons in iron and with visual detection. The Kolar experiments were indeed the harbingers of present day atmospheric neutrino experiments. Unfortunately the mines were closed in 1990 and the Kolar experiments were discontinued. In view of the importance of the neutrino physics and the past experience, it was widely felt that neutrino physics experiments should be revived in India.

The possibility of a neutrino observatory located in India was discussed as early as 1989 during several meetings held that year. Since then this question has come up, off and on, in many discussions. The issue was raised again in the first meeting of the Neutrino physics and Cosmology working group during the Workshop on High Energy Physics Phenomenology (WHEPP-6) held at Chennai in January 2000 [3] and it was decided then to collate concrete ideas for a neutrino detector.

Further discussions took place in August 2000 during a meeting on Neutrino Physics at the Saha Institute of Nuclear Physics, Kolkata, when a small group of neutrino physics

enthusiasts started discussing the possibilities. The Neutrino 2001 meeting was held in the Institute of Mathematical Sciences, Chennai during February 2001 with the explicit objective of bringing the experimentalists and theorists in this field together. The INO collaboration was formed during this meeting. The first formal meeting of the collaboration was held in the Tata Institute of Fundamental Research, Mumbai, during September 6 and 7th, 2001 at which various subgroups were formed for studying the detector options and electronics, physics goals and simulations, and site survey.

In 2002, a document [4] was presented to the Department of Atomic Energy (DAE), Government of India, which laid out an ambitious goal of establishing an *India-based Neutrino Observatory* outlining the physics goals, possible choices for the detector and their physics reach. Since then many new and fast paced developments have taken place in neutrino physics. The award of the Nobel Prize in Physics (2002) to the pioneers in neutrino physics is a measure of the importance of this field.

As a result of the support we have received from various research institutes, universities, the scientific community and the funding agency, the Department of Atomic Energy, a Neutrino Collaboration Group (NCG) was established to study the possibility of building an India-based Neutrino Observatory (INO). The collaboration was assigned the task of doing the feasibility studies for which funds were made available by the DAE. A memorandum of understanding (MoU) (see appendix H for details) was signed by the directors of the participating institutes on August 30th 2002 to enable a smooth functioning of the NCG during the feasibility period.

The NCG has the goal of creating an underground neutrino laboratory with the long term goal of conducting decisive experiments in neutrino physics as also other experiments which require such a unique underground facility.

Considering the physics possibilities and given the past experience at Kolar, it was decided, after a prolonged discussion, to start with a modern Iron CALorimeter (ICAL) detector with Resistive Plate Chambers (RPCs) as the active detector elements. The detector, to be described in the Chapter 5, will be housed in low-background surroundings at a suitable place. There is world-wide interest in this type of detector and a quick implementation of such a project can achieve many physics goals such as:

- Unambiguous and more precise determination of *oscillation parameters* using atmospheric neutrinos.
- Study of *matter effects* through electric charge identification, that may lead to the determination of the unknown sign of one of the mass differences.
- Study of *charge-conjugation and parity (CP) violation* in the leptonic sector as well as possible *charge-conjugation, parity, time-reversal (CPT) violation* studies.
- Study of *Kolar events*, possible identification of *very-high energy* neutrinos and *multi-muon* events.

Although INO will start its activity with atmospheric neutrinos, it is envisaged that it will ultimately have other neutrino experiments as well under its umbrella. Indeed, several possibilities are open for future directions:

- High-precision determination of the oscillation parameters when ICAL is (perhaps upgraded and) used in the future as a far-end detector for a *long base-line neutrino oscillation* experiment.

- *Neutrino-less double beta decay*, to determine whether neutrinos are Dirac or Majorana particles,
- *Solar*, *supernova* and *geo-neutrino* studies.
- *Tomography of the Earth* using natural and laboratory neutrino sources.

The geographical location for such a laboratory is particularly interesting, as all existing neutrino detectors are scattered around the world at latitudes larger than 35° N or S. There is none close to the equator as yet. In principle it is possible to push such a detector down to very low latitudes in South India. Such a location permits neutrino astronomy searches covering the whole celestial sky and study of solar neutrinos passing through the Earth's core.

Two possible locations for INO were identified; PUSHEP in Nilagiri district, and Rammam in Darjeeling district. The former has been chosen as the *preferred site* by the site selection committee of INO.

The interim report of INO was submitted to the Department of Atomic Energy (DAE), Department of Science and Technology (DST) and University Grants Commission (UGC), of the Government of India, at a meeting in Tata Institute of Fundamental Research, on May 1, 2005. A report on INO was presented at a meeting of the Scientific Advisory Committee to the Prime Minister on August 28, 2005 at Indore.

1.1 Organisation of the Report

The next few chapters will outline details of the work done to achieve the physics goals set for ICAL in the short term and INO in the long term. We also include, where possible, a short status report of the project at the current stage:

- *Chapter 2* provides a brief history of neutrinos, discovery of neutrino mass and neutrino mixing and the current status of neutrino physics. We also give a list of on-going and planned large scale neutrino experiments.
- *Chapter 3* contains a discussion of physics issues relevant to the ICAL detector, both with respect to atmospheric neutrinos and long-baseline physics. Especially in the latter case, discussions include site-dependent results; results for the two possible locations of INO are presented.
- *Chapter 4* contains a discussion of how detectors like ICAL can also be utilised to study multi-TeV cosmic ray muons through the so called pair meter technique. Such studies in the TeV PeV regions can throw light on possible extensions of the standard model in the high energy region.
- *Chapter 5* is devoted to the design and development of the ICAL Detector. A report on the working of RPC detector elements is given, along with discussions of detector electronics and magnet design. Engineering aspects related to the design of the support structure for stability are also discussed.
- *Chapter 6* includes the results of numerical simulations of the iron calorimeter with atmospheric neutrinos. The main focus is on characteristic signals from atmospheric neutrinos and how best ICAL can pin down the parameters which are not yet determined or known only imprecisely. We also discuss the physics issues involved in the long base-line neutrino experiments.

- *Chapter 7* contains a summary of the geology and related issues of two possible sites for locating INO, namely Singara in the Nilagiris and Rammam in the Darjeeling Himalayas.

  The details of Site Surveys are given in *Volume II* of the INO Interim Report. This volume has restricted access since it includes survey maps for which government restrictions apply.

- *Chapter 8* includes the budgetary estimates for creating INO and a time scale over which INO will be fully realised keeping in mind the physics goals of ICAL. If necessary the time scale may be advanced using modern techniques of construction. Given the world-wide interest and the number of experiments planned and proposed in this field, and the need for obtaining results from ICAL that are competitive with those from other experiments, it is critical to construct the ICAL detector in a time-bound and phased manner.

- *Chapter 9* outlines a possible management structure of INO which is radically different from that of any other experimental program in the country.

- *Chapter 10* discusses strategies for human resource development. A project of the magnitude that is envisaged needs to draw on considerable human resources. Strategies for tapping the resources already available, as well as training more manpower for INO, are vital. Furthermore, international collaboration, both now and for the future long base-line efforts, is not only a desirable feature but an essential one. This is one of the most important aspects and the realisation of the goals of INO depends on achieving the targets set up based on these strategies.

- *Chapter 11* discusses the possible impact of the project on industry, especially the development of detector technology, as also the impact on scientific outreach and education.

- *Chapter 12* gives a perspective view of INO as a basic facility for a healthy and balanced development of both high energy and nuclear physics. The surface labs of INO may become focal centres for detector R & D for different types of particle and nuclear physics studies. We also discuss the possible development of a much bigger underground science laboratory where it would be possible to do experiments related to geology, biology and material sciences.

- *Appendix A* contains a historical documentation of neutrino experiments in India. *Appendix B* contains details of neutrino oscillations with emphasis on the underlying physics involved. *Appendix C* contains a brief report on the structural stability of the ICAL detector. The possibility of using the ICAL detector as a far detector for a beta-beam experiment is discussed in *Appendix D*. The possibility of locating a double-beta-decay(DBD) experiment in the INO laboratory is discussed in *Appendix E*. *Appendix F* contains a list of neutrino detectors of the future, their physics goals and the proposed time scale for achieving such goals. A proposal for locating INO at Rohtang Tunnel is discussed in *Appendix G*. This particular site has many attractive features which makes it a possible contender for locating a deep underground laboratory but a little far in the future. *Appendix H* contains the original Memorandum of Understanding (MoU) which kick-started this feasibility study.

1.2 Summary of current status of INO

The INO group, which has at present about 100 members from sixteen institutions and universities, is now engaged in the following activities.

1. **Detector R & D work:** The glass RPC detector has been shown to operate with the desired efficiency and the required spatial and time resolution. However, the observed lifespan is smaller than expected and efforts are on to remedy this situation. Larger modules and the related data acquisition systems are being tested. These will be needed for the prototype 1 m^3 calorimeter (12 layers of 1 m $\times$ 1 m plates).

2. **Site survey:** Two sites have been identified as most suitable after detailed surveys. A site selection committee has gone through the available data on both these sites and recommended that the site situated in Nilagiri mountains of South India near PUSHEP as the preferred site for locating INO. Further studies to assess stress conditions for the access tunnel, laboratory cavern design and construction will be initiated soon.

3. **Numerical simulations:** Simulations for both atmospheric neutrinos and long base line neutrinos are reasonably well understood and under control. The detector simulation, track recognition and event reconstruction programs are getting ready or at testing stage.

4. **Documentation:** This involves preparing reports on the status of INO. These **Interim Reports**, of which the current one is the latest, clearly show the progress of INO activity [5].

5. **Collaboration Meetings:** This includes organising meetings of subgroups engaged in the activities listed above, and also collaboration meetings. The INO members also meet frequently at all possible venues of conferences in order to review the progress made by individuals and sub-groups. Several members of INO collaboration have already presented INO related work at both national and international meetings.

6. **International Collaborations:** This is being pursued under the Indo-Italian and Indo-US scientific exchange programmes for detector design and development. Some preliminary contacts have been made for Indo-Japanese collaboration as well.

7. **Human Resource Development:** Lectures on neutrinos and INO have been given to students in Colleges and Universities to attract them to INO, as a part of our attempt towards HRD for INO. The first INO training school for about 15 young members of INO was conducted in April-May 2005.

1.3 A vision for INO

INO has been conceived on a scale that no other basic sciences project in India has attempted. The MoU signed by seven institutions, that brought the Neutrino Collaboration Group into existence, is already the first of its kind. It is a testimony to the enthusiasm and collaborative spirit shown by the scientific community in India.

A magnetised tracking iron calorimeter is under design and proto-typing. In the first phase of its operation this detector will be used for atmospheric neutrino physics. The aim is to make precision measurements of the parameters related to neutrino oscillations. An exciting possibility is to determine the ordering of the neutrino mass levels. This is one of

the fundamental open questions in neutrino physics and no other detector either existing or planned except perhaps NOνA may be able to provide an answer in the next 10 years. Because of its ability to distinguish the positive and negative muons, this detector can settle this question.

This detector can be used as the far-detector of a long-base-line (6000 to 11000 km) neutrino experiment using the neutrino beam from a neutrino factory in Japan, Europe or USA. While this is envisaged as the second phase of the INO activity, it is clearly a long-term goal since neutrino factories are yet to become a reality.

Two sites for an underground neutrino laboratory, where the iron calorimeter detector can be located, were identified. A site selection committee has already prioritised them. Many other experiments such as neutrino-less double beta decay, detection of geo-neutrinos and tomography of the Earth are also possible at such a site.

Over the years, INO is expected to develop into a full-fledged underground science laboratory hosting experiments that can exploit its special low background environment and infrastructure, including other disciplines such as geology and biology.

Chapter 2

Introduction

Neutrino physics has come to occupy the centre stage of high energy physics, after the discovery of non-vanishing neutrino mass by observations of atmospheric neutrinos at the Super-Kamiokande underground laboratory in Japan [6, 7, 8] as well as from observations of solar neutrinos at Super-Kamiokande and the Sudbury Neutrino Observatory in Canada [9, 10, 11, 12, 13, 14].

Neutrino physics is one of the fastest evolving fields in physics today. Neutrinos, introduced by Pauli in 1930, were first proposed to explain the continuous electron energy distribution in nuclear beta decay. Their name is due to Enrico Fermi who, in 1934, made them the basis for a theory of weak interactions. Very early on, it was clear that these particles would be difficult to observe because of their very small interaction cross sections with matter. But in a series of experiments [15] Reines and Cowan conclusively proved their existence through the inverse beta decay weak interaction process where an *electron-type* anti-neutrino $\overline{\nu}_e$ is captured by a proton p giving rise to a positron e^+ and a neutron n: $\bar{\nu}_e + p \rightarrow e^+ + n$.

Apart from electron-type neutrinos which are produced in nuclear beta decay, the separate identity of *muon-type* neutrinos ν_μ was proved in 1962. The discovery of the τ lepton a decade later implied the existence of a third *tau-type* neutrino, ν_τ. It was only in the year 2001 that its existence was directly observed. A result of fundamental importance to neutrino physics is the precise measurement of the decay width of the Z-boson which is saturated by (and hence indicates the existence of only) three active light neutrino flavours.

The sources of naturally occurring neutrinos are both terrestrial and extraterrestrial. They are also produced in the laboratory. Each of these sources provides information, sometimes overlapping, that is extremely important in understanding the intrinsic properties of the neutrinos and their sources. The energy spectrum of naturally produced neutrinos starts from fractions of electron-volts and spans an impressive range: Fig. 2.1 shows the spectra of neutrinos [16] from different sources. Some of the spectra shown are based on observation while others, especially at high energies, are based on model calculations. While no single detector can fathom such a large range in energy, the very fact that neutrinos are produced over such a wide energy range poses challenging problems in their detection and understanding.

Neutrino (and other particle) interactions are described by the "Standard Model" (SM) of particle physics. In this model, neutrinos are massless and come in three distinct *types* or *flavours*, ν_e, ν_μ, ν_τ. These interact only via weak interactions and hence are difficult to detect. In the SM there is no room for neutrino flavours to "oscillate" into each other, that is, to change from one type/flavour to another. If, however, neutrinos have mass, and, furthermore, the neutrino *flavour* states which participate in the weak interactions are mixtures of *mass* eigenstates with different masses, then quantum mechanical evolution of

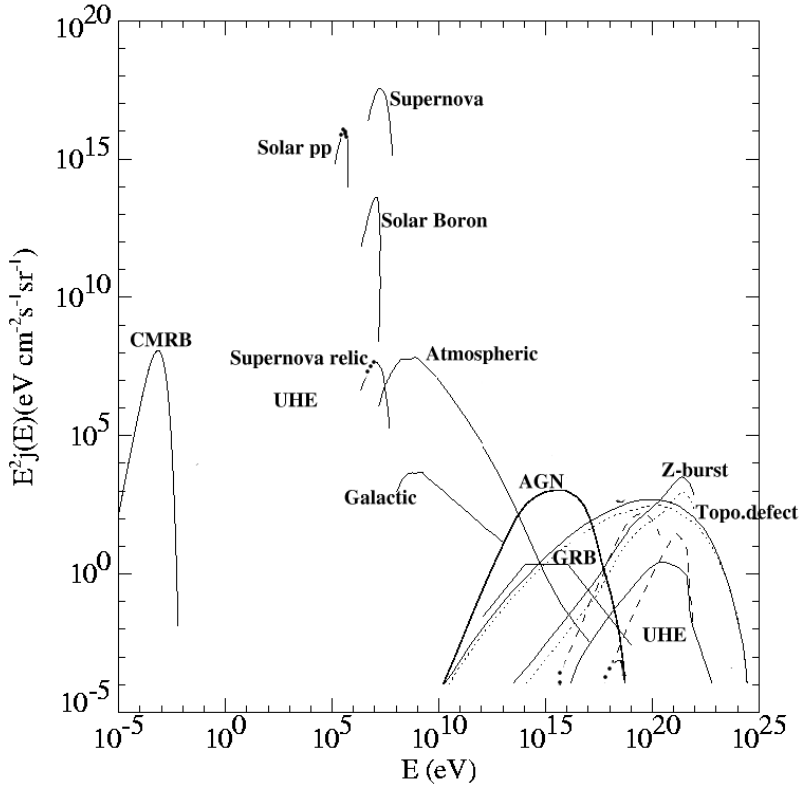

Figure 2.1: Neutrino spectrum from different sources as a function of energy

these flavour states leads to the phenomenon of neutrino oscillations [17]. The admixture of mass eigenstates in a given flavour state are parametrised by a set of mixing angles. A large mixing angle implies a large mixing between the eigenstates.

Experiments on solar [9, 10, 11, 12, 13, 14, 18, 19, 20, 21], atmospheric [6, 7, 8, 23, 22, 24, 25], reactor [26] and accelerator [27, 28] neutrinos clearly indicate that neutrinos do exhibit such flavour oscillations. Results from these experiments determine or constrain the extent of mixing as well as the differences between the squared masses (usually referred to as mass-squared difference). In particular, while the absolute masses themselves are not constrained by such observations, data indicate that at least two of the neutrinos must be massive, and with different masses. This is in fact the first evidence for physics beyond the Standard Model of particle physics. However, the estimated smallness of the neutrino mass (of the order of eV or much smaller) may have its origins near or beyond the scale of grand unified theories (GUTs), thus probing physics beyond the reach of present day accelerators.

2.1 Current Status of neutrino physics experiments

Experiments in the last several decades have provided many new and significant results. The main results may be summarised as follows:

- **Solar and Atmospheric neutrinos**: The observation of the deficit in electron neutrinos from the Sun, relative to the expectations from the Standard Solar Model [17], constitutes the Solar Neutrino problem. The combination of deficit in charged current interactions (involving only electron neutrinos) and the detection of all the predicted number of neutrinos in neutral current interactions (involving all neutrino flavours in full strength) indicates that the solution to this problem is through neutrino oscilla-

tions. The best fit solution to the solar neutrino plus the reactor neutrino data of the KamLAND experiment implies a mass squared difference $\delta_{\rm solar} \sim 8 \times 10^{-5}$ eV^2 and fairly large mixing [29]. The other problem involves the atmospheric ν_μ, whose deficit relative to the atmospheric ν_e is accounted for by a mass squared difference $\delta_{\rm atm} \sim 2 - 3 \times 10^{-3}$ eV^2 [30, 31]. The most recent result from MINOS[28] seems to favour a slightly larger best fit value, 3.05×10^{-3}, compared to earlier results while ruling out no-oscillation scenario at 5σ level. This is more than an order of magnitude larger than the mass-squared difference relevant to solar neutrino data, and yet another large mixing between states. These observations thus imply the existence of at least two non-zero masses for neutrino mass eigenstates.

- **Beta decay and double beta decay**: In contrast to neutrino oscillation-sensitive experiments, these yield direct mass limits. So far, there is only an upper limit of 2.2 eV on the dominant mass eigenstate for electron neutrinos involved in tritium beta decay. Several planned experiments such as KATRIN [32] will be capable of improving the limit to 0.3 eV. The limits from experiments involving muon and tau-type neutrinos are much higher and may not be relevant in the light of present information on neutrino oscillations.

  Neutrino-less double beta decay experiments address the issue of whether the neutrino is a Majorana or Dirac particle (whether or not it is its own antiparticle). If neutrinos are indeed Majorana particles, data from the experiments limit the effective mass parameter related to neutrino masses and mixing to less than 0.2 eV. Future neutrino-less double beta decay experiments such as GENIUS are capable of pushing the effective mass limit for Majorana neutrinos to 0.01 eV [33].

- **Cosmological data**: Cosmological experiments, including data from the recent WMAP experiment [34], apart from limiting the number of light neutrino flavour, set an upper limit on the sum of all the active neutrino masses. The most recent limit comes from the Sloan Digital Sky Survey (SDSS)[35], $\sum_i m_{\nu_i} < 0.5$ eV, but this limit is dependent on cosmological models.

- **Neutrinos from Supernova**: The observation of neutrinos from the Supernova SN1987a [36] has confirmed many qualitative features of the stellar collapse scenario. However, the number of observed events are statistically too small to draw conclusions on the properties of the neutrinos.

- **Other neutrino properties**: Stringent upper limits also exist for neutrino magnetic moments, decay rates , and other such properties. An upper limit on the magnetic moment of the neutrino is given by the MUNU experiment and the MAMONT experiment is expected to improve this limit further[37].

A schematic of the present status of masses and mixing is shown in Fig. 2.2 as obtained from a combined analysis of the experiments on solar, atmospheric, reactor and accelerator neutrinos. Note that we have chosen $m_3^2 - m_1^2 > 0$ in this figure. The present data does not distinguish between the two possible mass orderings: $m_3^2 > m_2^2 > m_1^2$ (direct), $m_2^2 > m_1^2 > m_3^2$ (inverted). Also, this figure does not include the unusual results obtained by the LSND experiment in Los Alamos laboratory [38], which are yet to be confirmed by an independent experiment. More details, including those from LSND and Karmen2, are given in Chapter 3.

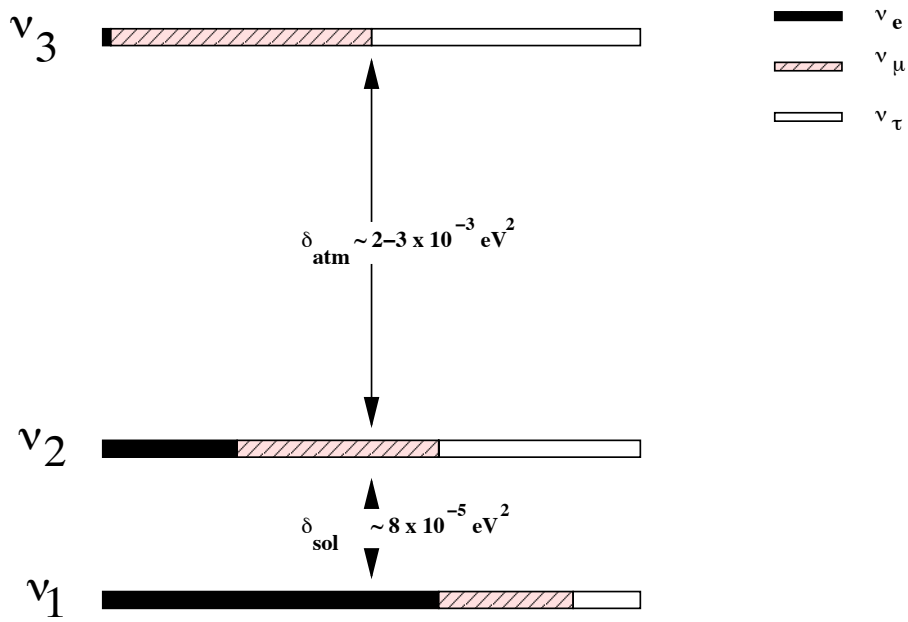

Figure 2.2: Schematic illustration of the status of masses and mixing of neutrino eigenstates. The flavour content is indicated by different shading; the ν_e contribution shown in the third mass eigenstate is an upper bound. The direct or normal mass hierarchy is assumed here; in the case of the inverted hierarchy, the ν_3 state would be the lightest. The mass squared differences as obtained from the data are also shown.

2.2 Open questions and future goals

In spite of these remarkable results, there are several outstanding issues of fundamental importance [39]:

1. A recent Super-Kamiokande [40] reanalysis of atmospheric muon neutrino data clearly shows a dip, indicating that the first oscillation minimum has been observed at the 3σ level; this implies that the oscillation hypothesis is the dominant mechanism. However, the oscillation pattern itself—periodic changes in the neutrino flux with minima and maxima—has not been seen explicitly. Such an observation will lead to the precision measurement of the oscillation parameters, which is now the focus of new experiments.

2. Analysis of solar and atmospheric neutrino data indicate that there are two large mixing angles. These imply that (1) the ν_μ and ν_τ states have large contributions from all three mass eigenstates while (2) the ν_e state is virtually saturated by the ν_1 and ν_2 mass eigenstates with large individual contributions; that is, the admixture of ν_e in ν_3 as parametrised by the 1–3 mixing angle, θ_{13}, is small, with $\sin^2\theta_{13} < 0.04$ or $\theta_{13} < 12^o$ (3σ) as indicated by the reactor neutrino data. However, it is not known whether this angle is different from zero. This has tremendous implications for observing Earth matter-dependent oscillation effects as well as CP violation in the leptonic sector. Indeed, if θ_{13} is exactly zero, neither of these effects will be seen.

3. Matter effects (on the propagation of neutrinos in the Sun) help to cleanly determine both the magnitude and sign of the mass squared difference occurring in the solar

neutrino problem. Since electron neutrinos are involved here, this translates to knowing the magnitude and sign of $\delta_{21} = m_2^2 - m_1^2$ due to the arguments given above: δ_{21} is positive.

The atmospheric neutrino data and indeed any reactor or accelerator (base-line) experiment is so far insensitive to the sign of the mass squared difference between the participating neutrinos. Hence the sign of the other mass-squared difference, $\delta_{31} = m_3^2 - m_1^2$, is not yet known. This can be determined through precision experiments sensitive to matter effects during propagation of the neutrinos through the earth. This has implications for building theoretical models that can accommodate the observed neutrino oscillation parameters.

4. Is there CP violation in the leptonic sector? It is known that these effects are small; however, this is a question of fundamental and deep significance which may be probed in future long-baseline neutrino experiments.

5. Do neutrinos decay? This is unlikely as a dominant scenario to explain the known data; currently both neutrino decay and decoherence effects are ruled out by more than 3σ by the reanalysis of super-K atmospheric neutrino data. However, they may still be allowed in combination with dominant neutrino oscillations. Data from future experiments can further constrain sub-dominant mechanisms such as neutrino decay or decoherence.

6. What is the absolute scale of neutrino mass? Direct mass measurements from beta decay place an upper limit of about 2.2 eV. Model dependent interpretation of the astrophysical results from WMAP and SDSS [41, 35] limits the sum of the neutrino masses to around 0.5 eV. Neutrino-less double beta decay, if observed, will also determine the mass scale.

7. Are the neutrinos Dirac or Majorana particles? There is a strong theoretical prejudice that neutrinos are Majorana particles, that is, they are their own antiparticles. Only charge-neutral fermions can be Majorana and hence neutrinos are the only candidates within the Standard Model. Hence there is great interest in establishing this by an unambiguous observation of neutrino-less double beta decay.

8. How many species of neutrinos exist? The number of active species with masses less than half the mass of the Z boson is limited to three by LEP experiments. Results from the LSND experiment suggests the existence of at least one more relatively light species, which has to be sterile (that is, cannot experience weak interactions), since there cannot be more than three light active species. Results from MiniBOONE are awaited to confirm or rule out the LSND results.

9. Does the neutrino have a non-zero magnetic moment? A non-zero magnetic moment is possible now that the neutrinos are known to be massive. The determination of its magnitude is therefore of fundamental importance. It may also have an impact on the solar neutrino problem. Several experiments have already placed upper limits on the magnetic moment of anti-neutrinos in the region $9 \times 10^{-11} \mu_B$ (given by MUNU experiment) and this limit needs to be improved further.

10. The energy spectrum and composition of primary cosmic rays (CR) entering the earth's atmosphere have historically provided and can provide crucially important information to both particle physics and astrophysics. The observed *knee and ankle* features of the CR spectrum are as yet not understood. Their resolution, as well as an understanding

of the sources and mechanism responsible for the highest energy CR, is likely to open new windows into our understanding of the highest energy acceleration and propagation processes in our Universe. The mechanism responsible for this may lead to production of very high energy neutrinos, and if this is the case, a study of high—PeV and higher—energy neutrinos may provide the vital clues to resolve this important question.

Many of these issues will be addressed at current and future planned experiments. Solar neutrino experiments are still going on at Kamioka, Sudbury, and Gran Sasso. Reactor neutrino experiments are going on at laboratories such as KamLAND and CHOOZ. More such experiments are being planned.

MONOLITH [42] was a detector designed as a 34 kton iron calorimeter for the study of atmospheric and accelerator neutrinos. However, the current status of the project is not known. The present proposal for an iron calorimeter detector, ICAL, at INO, which grew out of the experience with the KGF detector, is based on a similar design. The atmospheric neutrino studies are expected to be augmented by the neutrinos in GeV energy range produced and beamed from accelerators (or neutrino factories) at FNAL, KEK and CERN to detectors at existing sites such as Gran Sasso, Kamioka, etc. In order to take measurements at several distances from neutrino factories, many long base-line stations are also being planned. High precision neutrino oscillation measurements will use one or more of the following neutrino sources:

1. *a conventional proton beam* colliding with a target to produce pions and kaons which then decay to electron and muon neutrinos (and anti-neutrinos),

2. *reactor sources* with both near and far detectors to reduce systematic errors,

3. *super-beams*, which are essentially technologically upgraded high-flux versions of conventional beams,

4. *muon storage rings*, which exploit muon decay to produce intense and collimated neutrino beams. These are still in the R & D stage.

5. *beta beams*, which exploit the beta decay of nuclei to produce beams of ν_e and $\bar{\nu}_e$. Again these are still in R& D stage.

Some of the on-going and future detectors along with their important characteristics are mentioned in Table 2.1. A more complete list of experiments and their goals, including those on beta decay and neutrino-less double beta decay, is given in Appendix F.

Experiment	Country	Type of detector	Major Expt. type	Time schedule
Super-K	Japan	Water Cerenkov	Solar, Supernova, Atmospheric	1996–
K2K	Japan	Water Cerenkov	Long-baseline (from KEK)	1999–
Hyper-K	Japan	Water Cerenkov (1 Mton)	Atmospheric, Long-baseline	?
SNO	Canada	D_2O Cerenkov	Solar, Supernova	1999–
GNO	Italy	Gallium	Solar	1998–
ICARUS	Italy	Liquid Argon	Atmospheric, Proton Decay, Long-baseline	?
KamLAND	Japan	Scintillator	Reactor	2001–
Double-CHOOZ	France	Scintillator	Reactor	2007
MiniBooNE	USA	Scintillator	Short baseline (from Fermilab booster)	2003–
MINOS	USA	Mag. Iron Cal.	Long baseline (from Fermilab main injector)	2005–
OPERA	Italy	Lead/Emulsion	Long base-line (from CERN); tau appearance	Det. inst'll: 2003–
UNO	USA	Water Cerenkov (1 Mton)	Atmospheric, Long-baseline	?
ICAL/INO	India	Mag. Iron Cal.	Atmospheric, Long-baseline?	?

Table 2.1: On-going and planned large scale neutrino experiments [43]. If approved shortly, ICAL at the proposed INO laboratory is expected to be operational by 2010–11.

Chapter 3

Neutrino Physics with Magnetised Iron Calorimeter

We will focus on neutrino physics issues that can be addressed by an iron calorimeter detector, ICAL, to be described in detail in Chapter 5. The ICAL detector is contemplated as both a detector for atmospheric neutrinos and as a future end detector for a neutrino factory beam; in both cases, the primary detection mechanism is via detection of muons produced in charged current (CC) neutrino interactions. The detector will have layers of iron interleaved with the active detector elements which are resistive plate chambers (RPC) and an approximately uniform magnetic field of 1–1.4 T, that allows for charge discrimination of muons. Physics issues which are not directly related to neutrino oscillation physics are discussed in chapter 4.

There has been a paradigm shift in the nature of the goals to be pursued in neutrino physics. From a search for an understanding of the particle physics and/or the astrophysics that drives the solar [13, 18, 19, 21, 44, 45, 46] and atmospheric neutrino deficits [6, 7, 24, 27, 47], the focus has shifted to one where *increasingly precise measurements of neutrino mass and mixing matrix parameters* are sought [26, 40]. Experiments planned over the next fifteen to twenty years reflect this change in focus.

These are primarily measurements of neutrino oscillation parameters. Specifically, the aims are

- To observe the oscillation pattern over at least one full period, in order to make a precise measurement of the oscillation parameters.
- To obtain unambiguous evidence for matter effects and determine the sign of the mass-squared difference δ_{32} involved in atmospheric neutrino oscillations.
- To determine whether the mixing angle θ_{23} is maximal, if not explore how well its octant can be determined.
- To improve the existing upper limit on the mixing angle θ_{13} and to ascertain if its value is different from zero or not.
- To determine whether the leptonic CP phase δ is non-zero, and if so, obtain some measure of its magnitude, provided $\theta_{13} \neq 0$.
- To determine whether sterile neutrinos exist.
- Last but not the least, to look for any non-standard effects beyond neutrino oscillations.

Many of the above challenges can be addressed in a set-up such as ICAL at INO, including the major open problem—*the sign of* δ_{32}—even with atmospheric neutrinos as source. Below we briefly describe the prospects of the ICAL detector, first for atmospheric neutrinos and subsequently using it as an end detector of a high energy high intensity neutrino beam from a distant source.

In order to understand the notation and concepts used in the text we give a brief introduction to three-flavour-oscillation physics. For more details see Appendix B.

3.1 Three flavour neutrino oscillation

The neutrino flavour states $|\nu_\alpha\rangle$, $\alpha = e, \mu, \tau$, are linear superpositions of the neutrino mass eigenstates $|\nu_i\rangle$, $i = 1, 2, 3$, with masses m_i :

$$|\nu_\alpha\rangle = \sum_i U_{\alpha i}|\nu_i\rangle. \tag{3.1}$$

Here U is the 3×3 unitary mixing matrix. A physically motivated form of the mixing matrix is [48, 49]

$$U = \begin{pmatrix} c_{12}c_{13} & s_{12}c_{13} & s_{13}e^{-i\delta} \\ -c_{23}s_{12} - s_{23}s_{13}c_{12}e^{i\delta} & c_{23}c_{12} - s_{23}s_{13}s_{12}e^{i\delta} & s_{23}c_{13} \\ s_{23}s_{12} - c_{23}s_{13}c_{12}e^{i\delta} & -s_{23}c_{12} - c_{23}s_{13}s_{12}e^{i\delta} & c_{23}c_{13} \end{pmatrix}.$$

where $c_{ij} = \cos\theta_{ij}$, $s_{ij} = \sin\theta_{ij}$, and δ denotes the CP violating (Dirac) phase. More details are given in the Appendix B. The 3×3 neutrino mass matrix M_ν^2 in the basis of the charged leptons e, μ and τ is diagonalised by U:

$$U^\dagger M_\nu^2 U = \mathrm{diag}(m_1^2, m_2^2, m_3^2). \tag{3.2}$$

The probability of an initial neutrino ν_α of flavour α and energy E being detected as a neutrino ν_β of the same energy but with flavour β after travelling a distance L in vacuum is

$$P_{\alpha\beta} = \delta_{\alpha\beta} - 4\sum_{i>j} \mathrm{Re}[U_{\alpha i}U^*_{\beta i}U^*_{\alpha j}U_{\beta j}]\sin^2\left(\frac{\pi L}{\lambda_{ij}}\right) + 2\sum_{i>j} \mathrm{Im}[U_{\alpha i}U^*_{\beta i}U^*_{\alpha j}U_{\beta j}]\sin\left(2\frac{\pi L}{\lambda_{ij}}\right),$$

where $\lambda_{ij} = 2.47$ km$(E/\mathrm{GeV})(\mathrm{eV}^2/\delta_{ij})$ when L is also expressed in km, and $\delta_{ij} = {m_i}^2 - {m_j}^2$. The above expression is given for vacuum. In matter, the probabilities are drastically modified as discussed in Appendix B.

Before we specialise to the effects of matter on atmospheric neutrinos and long-baseline neutrinos of interest at ICAL, we list the known central values or bounds on the oscillation parameters obtained from earlier experiments. These values allow us to focus on narrow regions in parameter space and discuss how an ICAL-type experiment can further improve the results for some of these parameters, or yield new results on currently unknown parameters.

3.2 Parameter values gleaned from experiments

The reactor data indicate that there is very little admixture of the ν_3 mass eigenstate in the flavour state ν_e. In the chosen parametrisation of the mixing matrix, U, this means that θ_{13} is small and the solar neutrino problem can be well-approximated as a 2-flavour (or

2-generation) problem involving only ν_1 and ν_2. Hence the only parameters that appear in the analysis of these (and also the KamLAND reactor) experiments are δ_{21} and θ_{12}. For the same reason, there is only one dominant mass-scale and one mixing angle appearing in the atmospheric neutrino experiments, viz., δ_{32} and θ_{23}. Their values are given below. Notice that the central values as well as the limits are continuously shifting slightly, depending on availability of more data, or mode of analysis (combined global fit or not). The numbers indicated are therefore to be taken as guidelines and may not be the latest or currently favoured values.

Allowed region from Solar + KamLAND results : Assuming CPT invariance, the 3σ allowed range of parameters and the spread (in parenthesis) of δ_{21} and $\sin^2\theta_{12}$ from solar and recent 766.3 day KamLAND data [29] are given by

$$\begin{aligned} 7.2\times 10^{-5} < \delta_{21} &\equiv \delta_{\rm sol} < 9.5\times 10^{-5}\ {\rm eV}^2\ ; \\ 0.21 < \sin^2\theta_{12} &\equiv \sin^2\theta_{\rm sol} < 0.37\ . \end{aligned}$$

A combined analysis gives the best-fit points to be [53] $\delta_{21} = 7.9\times 10^{-5}$ eV^2 and $\sin^2\theta_{12} = 0.31$ with allowed ranges as shown in Table 3.1. Note that δ_{21} has to be positive for MSW [50] mechanism to work for solar neutrinos.

Atmospheric + accelerator experiments : The allowed range at 3σ of parameters from atmospheric and K2K data [51] is

$$\begin{aligned} 1.4\times 10^{-3} < |\delta_{32}|/{\rm eV}^2 &\equiv \delta_{\rm atm} < 3.3\times 10^{-3}\ {\rm eV}^2\ ; \\ 0.34 \le \sin^2\theta_{23} &\equiv \sin^2\theta_{\rm atm} \le 0.68\ . \end{aligned}$$

The best-fit values are $|\delta_{32}| = 2.2\times 10^{-3}$ eV^2 with $\sin^2\theta_{23} = 0.5$. Whereas δ_{21} is determined to be positive, the sign of δ_{32} is *not* known.

CHOOZ reactor + Atmospheric + Solar + KamLAND experiments : The combined analysis of solar data and the KamLAND and CHOOZ reactor data gives an upper bound [29] on this parameter,

$$\sin^2\theta_{13} \le 0.046 \quad (3\sigma)\ .$$

This bound, which requires a three-flavour analysis, is sensitive to the value of $|\delta_{32}|$ [52]. The result of the CHOOZ experiment, which requires the U_{e3} element to be small, plays a key role here. Due to the small value of θ_{13}, the 2-flavour bounds are stable.

In Table 3.1 we summarise the results of the global three-neutrino analysis. The same results are shown in graphical format in Fig. 3.1. More detailed results for atmospheric neutrinos are presented, along with the new results from the MINOS collaboration in Fig. 3.2. We use these best-fit values to focus attention on new directions and results with an ICAL detector using atmospheric and long baseline neutrinos as sources.

If the results of the LSND experiment receive independent confirmation then the third different mass squared difference, denoted as δM^2 in the bottom-right panel of Fig. 3.1, will make it imperative to consider mixing amongst four neutrinos. Since the Z_0-boson width shows that there can be only three active neutrinos (ν_e, ν_μ and ν_τ), the fourth state would have to be a sterile neutrino without a charged lepton partner and immune to the weak interactions. Indeed, much work has already been done in this direction [54].

We first discuss the physics of atmospheric neutrinos at ICAL.

Parameter	best-fit	3σ
$\delta_{21}[10^{-5}\ \mathrm{eV}^2]$	7.9	7.1 – 8.9
$\delta_{32}[10^{-3}\ \mathrm{eV}^2]$	2.2	1.4 – 3.3
$\sin^2\theta_{12}$	0.31	0.24 – 0.40
$\sin^2\theta_{23}$	0.50	0.34 – 0.68
$\sin^2\theta_{13}$	-	≤ 0.046

Table 3.1: Best-fit values and 3σ intervals for three flavour neutrino oscillation parameters from global data including solar, atmospheric, reactor (KamLAND and CHOOZ) and accelerator (K2K) experiments [53].

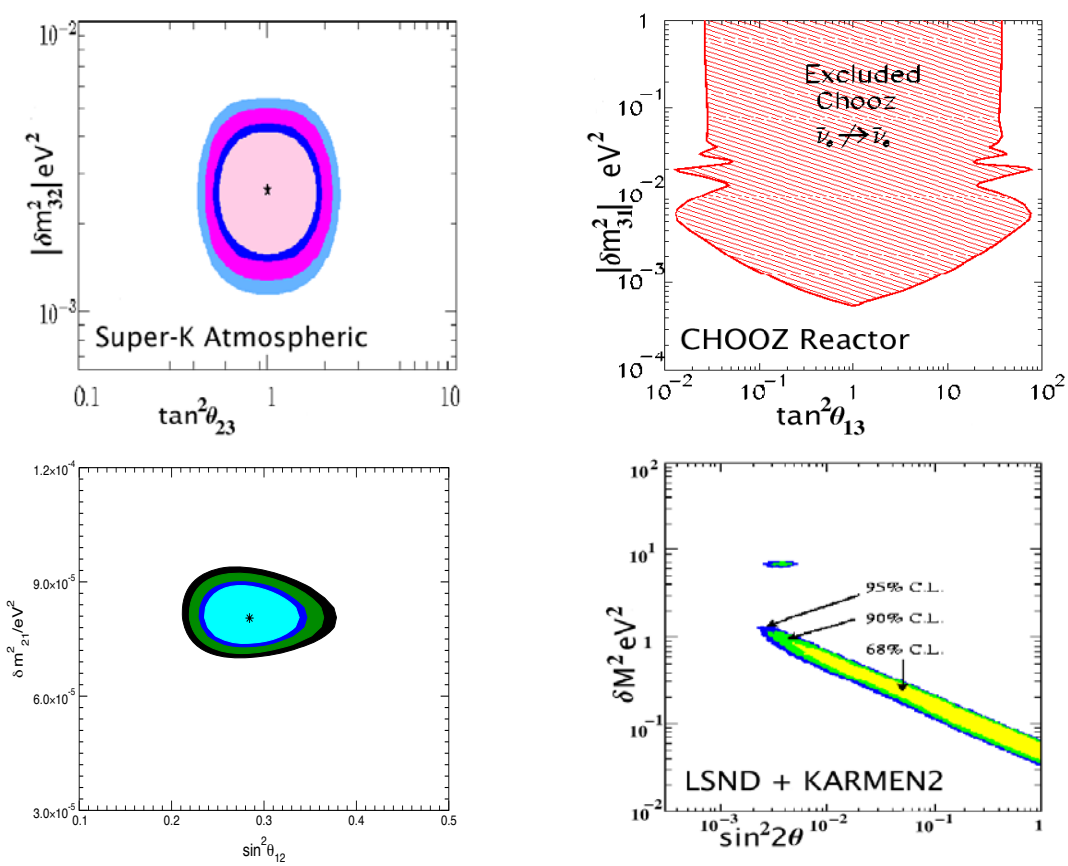

Figure 3.1: The allowed neutrino parameter space allowed from solar, atmospheric, reactor and accelerator experiments [29, 30].

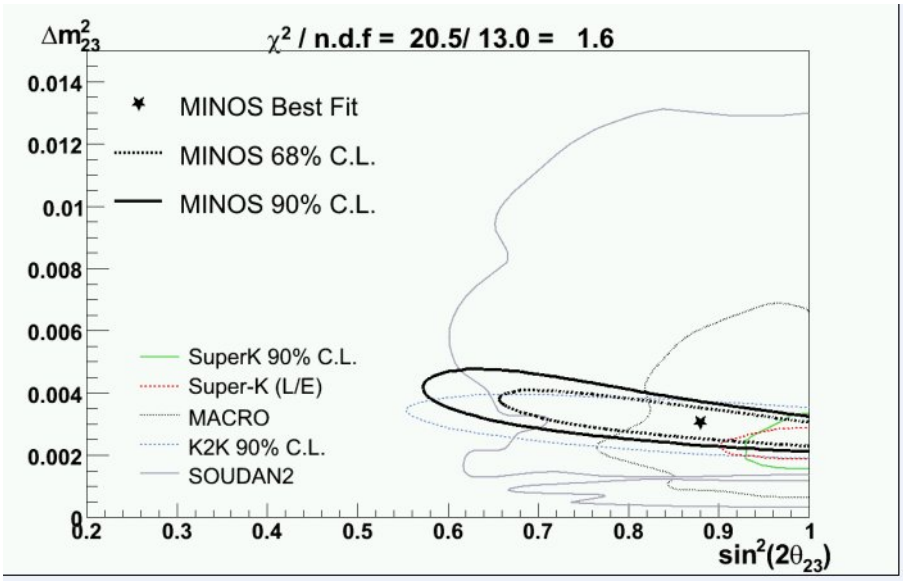

Figure 3.2: The current neutrino parameter space relevant to atmospheric neutrino oscillations. Figure from Ref. [28].

3.3 Atmospheric Neutrinos

The atmospheric neutrino physics program possible with a magnetised iron tracking calorimeter is substantial. It is possible to observe a clear signal of oscillation by observing one full oscillation period so that the *precision of the parameters,* δ_{32} *and* θ_{23}, can be improved to 10%. A broad range in both path length L (see Fig. 3.3) and energy, E, and indeed in their ratio, L/E, possible with atmospheric neutrinos, offers the opportunity to probe a large range of δ_{32}. Among the physics capabilities, in addition, are the *sensitivity to matter effects*

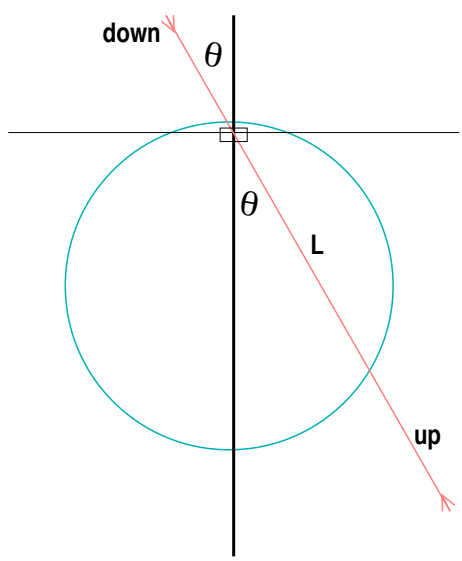

Figure 3.3: Schematic showing the up-coming and down-going neutrino directions and the path length L associated with the zenith angle θ.

and sign of δ_{32}. We can also use atmospheric neutrinos to *probe CPT invariance* which is one of the fundamental paradigms of quantum field theories, of which the Standard Model is one.

Atmospheric neutrinos are produced by cosmic ray interactions in the atmosphere, from decays of pions and muons produced in these interactions:

$$\pi \to \mu\,\nu_\mu \;; \qquad \mu \to e\,\overline{\nu}_e\,\nu_\mu \;.$$

Roughly twice as many muon-type neutrinos (and anti-neutrinos) are produced as electron-type ones. The flux peaks at zenith angles $\theta_z \sim \pm 90^\circ$, i.e., near the horizon, due to the larger length of atmosphere available in this direction. While the low energy ($E < 1$ GeV) neutrinos have a complicated (θ_z, ϕ) dependence due to various causes including the Earth's magnetic field, they are roughly ϕ-independent at higher energies.

The atmospheric neutrino flux peaks just below a GeV (see Fig. 2.1) and falls thereafter faster than $1/E^2$. While capturing the low energy flux enhances the event-rate, such events do not contribute significantly to the interesting region where the oscillation has a minimum or a maximum; hence a trade-off between the requirement of higher energy (to enable better detection) and better event rates (to enhance statistics) is required. Typically we assume that ICAL has sensitivity to neutrinos with energy greater than 1 GeV.

While the electron-neutrino flux appeared to be as expected, the Super-K collaboration [6, 7, 8] observed that the muon-neutrino events were depleted compared to expectations, with the depletion increasing up to 50% in the case of completely up-going neutrinos. The Super-K data does not distinguish the charge of the electrons or muons and so is unable to distinguish neutrino and anti-neutrino events; hence it is not sensitive to matter effects which are different in the two cases.

The number of muon events N_μ has been calculated using,

$$N_\mu = N_n \times M_Y \int \mathrm{d}E \int \mathrm{d}\cos\theta_z \left[\frac{\mathrm{d}^2\Phi_\mu}{\mathrm{d}E\mathrm{d}\cos\theta_z} P_{\mu\mu}(E,L) + \frac{\mathrm{d}^2\Phi_e}{\mathrm{d}E\mathrm{d}\cos\theta_z} P_{e\mu}(E,L) \right] \sigma_\mu(E) \;, \tag{3.3}$$

We define the various terms below.

E is the neutrino energy, θ_z is the zenith angle and the path-length traversed, L, is related to the zenith angle θ_z as

$$L = \sqrt{(R+L_0)^2 - (R\sin\theta_z)^2} - R\cos\theta_z \;, \tag{3.4}$$

where $\theta_z = 0$ corresponds to neutrinos reaching the detector vertically downwards after traversing a distance L_0 which is the average height above the surface of the earth at which the atmospheric neutrinos are produced. We take this to be about 15 km, as is the convention. Here R is the radius of the earth.

N_n is the number of nucleons per kton of target material and we define *exposure* M_Y in kton-years to be the product of the target mass and exposure time.

$P_{\mu\mu}$ is the muon neutrino survival probability, $P_{e\mu}$ is the probability of conversion of a ν_e to ν_μ.

Φ_i, $i = e, \mu$ are the electron and muon atmospheric neutrino fluxes; we have used the Bartol atmospheric flux [55] (unless otherwise mentioned). Finally, σ is the charged current (CC) cross section. For neutrino energies below 1.8 GeV the quasi-elastic ν-nucleon cross-section has been used, while above this energy we have put in the deep inelastic scattering (DIS) value of the cross-section. We have used CTEQ4LQ [56] parametrisations for the parton distribution functions to estimate the DIS cross-section.

For anti-neutrinos, we have a similar equation

$$N_{\bar\mu} = N_n \times M_Y \int \mathrm{d}E \int \mathrm{d}\cos\theta_z \left[\frac{\mathrm{d}^2\Phi_{\bar\mu}}{\mathrm{d}E\mathrm{d}\cos\theta_z} P_{\bar\mu\bar\mu}(E,L) + \frac{\mathrm{d}^2\Phi_{\bar e}}{\mathrm{d}E\mathrm{d}\cos\theta_z} P_{\bar e\bar\mu}(E,L) \right] \sigma_{\bar\mu}(E) \;. \tag{3.5}$$

3.3.1 Precision measurement of $|\delta_{32}|$ and θ_{23}

Apart from their charge discrimination capability, iron calorimeters have a large range in sensitivity to L/E variations compared to water Cerenkov detectors and can substantiate the evidence of neutrino mass and oscillation already observed by Super-K, via the observation of dips and peaks in the event rate versus L/E. In the following, we present the sensitivity to the oscillation parameters for such a detector setup.

The replacement of the zenith angle, $\theta_z \leftrightarrow (\pi - \theta_z)$, effectively changes the sign of the second term in Eq. 3.4, thus taking, for instance, a down-going neutrino to an up-coming one. We define the reference path length L for down-going neutrinos to be that of the associated up-going neutrino with zenith angle $(180 - \theta_z)$ so that the range of L/E remains the same for up-going and down-going neutrinos [57].

A useful measure of oscillations is the ratio of up-coming to down-going neutrinos with nadir/zenith angles interchanged. The fluxes of atmospheric neutrinos from directions θ_z and $(\pi - \theta_z)$ are expected to be similar in the absence of oscillations, especially for larger energies, $E >$ few GeV. This deviates from unity in the presence of oscillations, when the up-going neutrino rates are expected to be modified.

The ratio of events in the up-down directions for a given $x = L/E$, therefore, reflects the asymmetry of the up-down fluxes, due to oscillations, and hence is a direct measure of the oscillation probability. We define

$$\mathcal{R}(x) = \frac{U}{D}(x) = \frac{\text{No. of events from up-coming muon neutrinos}(x)}{\text{No. of events from down-going muon neutrinos}(\tilde{x})} \ .$$

Note that the event rates are a function of L/E alone only in the case of vacuum oscillations. In the presence of matter the rates become separately a function of E, L. For the sake of simplicity, we consider here the case $\theta_{13} = 0$, which corresponds to taking the 2-flavour limit.

In Fig. 3.4, the number of up- and down-going muons (of either sign) in $x = L/E$ bins ($\tilde{x}$ for down-going neutrinos) are presented as solid and broken histograms respectively for two values of δ_{32}, for an exposure of 250 kton-years.

The two histograms are similar in the absence of oscillations. When oscillations are included, the rate for the down-going neutrinos is virtually the same while that for up-coming neutrinos is greatly modified. The dips in L/E bins visible in Fig. 3.4 for the up-going case are the effect of oscillations; the first dip is especially clear.

Fig. 3.5, shows, for the same values of δ_{32}, the ratio $\mathcal{R}$ of up to down going muons in the detector. Note that such a ratio eliminates [57] the large systematic errors in the normalisation of the atmospheric neutrino flux, which may be as large as 30%. Since the down-going neutrino event rate is hardly affected by oscillations, we expect $\mathcal{R}$ to be a measure of the ν_μ survival probability, $P_{\mu\mu}$, smeared, however, by the finite detector resolution. For example, in the case of 2-flavour oscillations, the survival probability is,

$$P_{\mu\mu}(x) = \left[1 - \frac{\sin^2 2\theta_{23}}{2}\left[1 - \cos(2.54\,\delta_{32}x)\right]\right] \ . \tag{3.6}$$

The position of the dip in the observable $\mathcal{R}$ is thus a measure of δ_{32} while the *value* of this observable at the minimum is a measure of θ_{23}. It is clear that the dip and subsequent rise in this quantity should yield firm evidence of oscillations within a few years of data-taking. It is evident that poor resolutions decrease the sensitivity to θ_{23}.

The observation of the L/E dip can allow us to measure the atmospheric mass-squared difference with a high precision. The precision is a function of the relative error in the parameters and is defined as

$$\mathcal{P}(p) = \frac{(p_{\max} - p_{\min})}{p_0} \ , \tag{3.7}$$

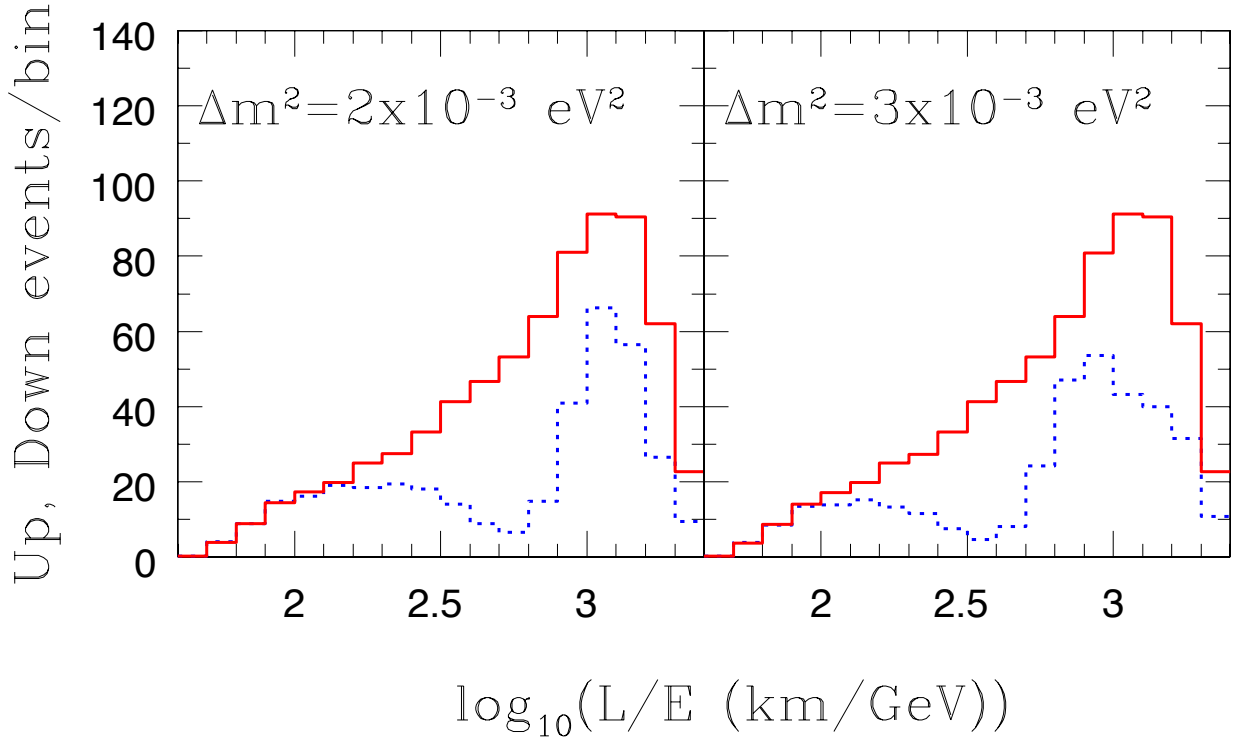

Figure 3.4: The number of up- (broken histogram) and down-going (solid histogram) muons (of either sign) in L/E bins are presented for two values of $|\delta_{32}| = 0.002,\ 0.003$ eV^2 and $\sin^2\theta_{23} = 0.5$ for an exposure of 250 kton-years at ICAL.

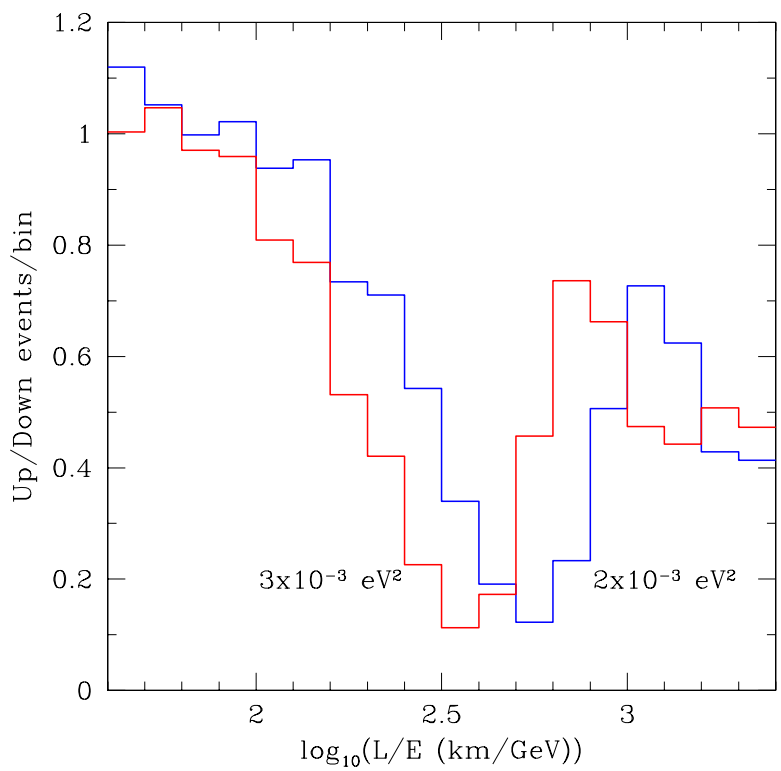

Figure 3.5: The ratio of up to down muon events shown in Fig. 3.4. It is seen that the position of the dip is sensitive to the magnitude of δ_{32} while the value of the ratio at the dip is sensitive to $\sin^2 2\theta_{23}$.

where $p_{\max}$ and $p_{\min}$ are the maximum and minimum allowed values of the parameter p, at a given confidence level, and p_0 is the best-fit value. The precision on δ_{32} and $\sin^2\theta_{23}$ is currently set by the Super-K and K2K data and is shown at 3σ level in Table 3.2.

Experiment	$\lvert\delta_{31}\rvert$	$\sin^2\theta_{23}$
current	88%	79%
MINOS+CNGS	26%	78%
T2K (Super-K, 0.75 MW, 5years)	12%	46%
NOνA (30 kton, 0.6 MW, 5 years)	25%	86%
ICAL (50 kton, atm. nu, 5 years)	20%	60%

Table 3.2: Precision for $|\delta_{31}|$ and $\sin^2\theta_{23}$ at 3σ for the true values $\delta_{31} = 2\times10^{-3}$ eV^2, $\sin^2\theta_{23} = 0.5$ for 5 years exposure. Table reproduced from [39] with information added on ICAL/INO. Note that the table refers to the older NOνA proposal; the revised March 2005 "totally active" NOνA detector is expected to be competitive with T2K.

The achievable precision from future running or proposed experiments is also listed, along with the precision from ICAL. All numbers correspond to 5 years exposure of the detector [39]. It is seen that ICAL will be marginally better than the MINOS experiment. Of course, in all cases, the precision will improve with exposure. Moreover, this precision is strongly sensitive to the central values of these parameters. This dependence is shown in Fig. 3.6 at the 2σ level. Again, it is seen that the advantages of ICAL will be fully exploited if δ_{32} is at the lower end of the allowed range.

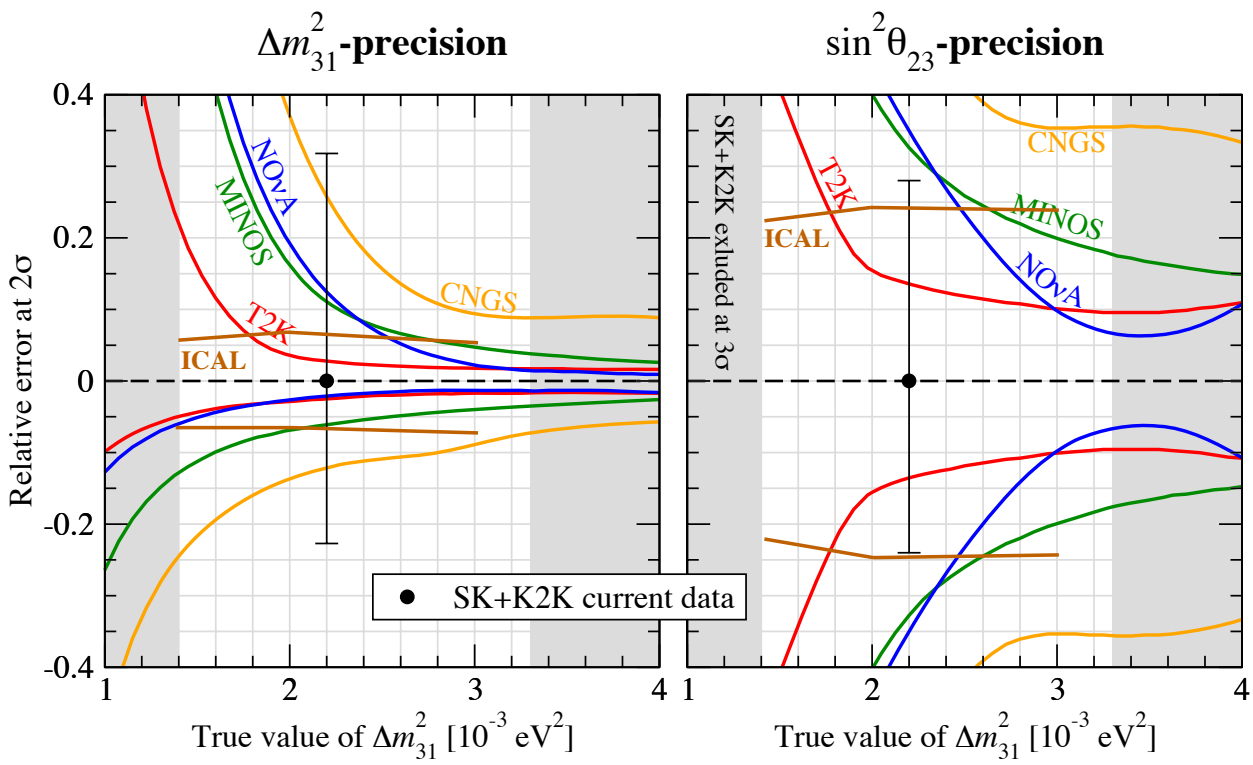

Figure 3.6: The relative error on δ_{32} and $\sin^2\theta_{23}$ as a function of the input value of δ_{32} at the 2σ level. The figure is adapted from Ref [39]. As in Table 3.2, the curve for NOνA corresponds to the older proposal. The precision with the revised March 2005 "totally active" NOνA is expected to be comparable to that from T2K. The errors for a 5 year exposure at ICAL have been overlaid.

Note that, when extended to the full 3-flavour case, the precision is also sensitive to the value of θ_{13}. In particular, at $\theta_{13} \neq 0$, the precision in δ_{32} becomes worse and that for a non-maximal θ_{23} becomes better by about 5–7%. Clearly, the ultimate extraction of the oscillation parameters will require a complex and detailed procedure.

3.3.2 Matter effects in μ^- and μ^+ events

Neutrinos and anti-neutrinos interact differently with matter. A magnetised ICAL detector, with its ability to distinguish neutrino- and anti-neutrino-initiated processes by detecting the charge of the produced muons, may be in a position to observe matter dependent effects. Such effects are sensitive [58, 59, 60, 63, 64] to the *sign of* δ_{32} and the magnitude of θ_{13}, both of which are as yet unknown.

In the absence of matter effects, we have $P_{\mu\mu} = P_{\bar{\mu}\bar{\mu}}$ and $P_{e\mu} = P_{\bar{e}\bar{\mu}}$ in the approximation where $\delta_{21} \simeq \delta_{sol}$ is neglected. In the multi-GeV range, the fluxes of neutrinos and anti-neutrinos are nearly equal. Hence in Eqs. 3.3 and 3.5 the quantities in the square brackets are nearly equal. So the ratio $R_\mu = N_\mu/N_{\bar{\mu}}$ is essentially equal to $\sigma_\mu/\sigma_{\bar{\mu}} > 2$. We call this ratio R_0.

However, matter effects induce changes in all probabilities and depending on the sign of δ_{32}, the ratio R_μ can be greater or less than R_0. We study the changes in R_μ due to matter effects for likely values of neutrino parameters. The relevant probabilities are $P_{e\mu}$ and $P_{\mu\mu}$. We discuss them in turn below.

First we study $P_{e\mu}$. In vacuum,

$$P_{e\mu} = \sin^2\theta_{23}\sin^2 2\theta_{13}\sin^2\left(1.27\frac{\delta_{32}L}{E}\right), \tag{3.8}$$

with $P_{\bar{e}\bar{\mu}} = P_{e\mu}$. Including matter effects modifies the above probability to

$$P^m_{e\mu} = \sin^2\theta_{23}\sin^2 2\theta^m_{13}\sin^2\left(1.27\frac{\delta^m_{31}L}{E}\right), \tag{3.9}$$

where

$$\delta^m_{31} = \sqrt{(\delta_{32}\cos 2\theta_{13} - A)^2 + (\delta_{32}\sin 2\theta_{13})^2} \tag{3.10}$$

$$\sin 2\theta^m_{13} = \sin 2\theta_{13}\frac{\delta_{32}}{\delta^m_{31}}. \tag{3.11}$$

In the above equations $A = 0.76 \times 10^{-4}\rho(gm/cc)E(GeV)$ is the Wolfenstein term, characterising the matter effects. Resonance occurs when $A = \delta_{32}\cos 2\theta_{13}$. If δ_{32} is positive, then we have $\delta^m_{31} < \delta_{32}$ and $P^m_{e\mu} > P_{e\mu}$ in the neighbourhood of the resonance. For anti-neutrinos $A \to -A$ and we have $P^m_{\bar{e}\bar{\mu}} < P_{\bar{e}\bar{\mu}}$; furthermore there is no resonance in this case. For negative δ_{32} the situation is reversed. Matter effects also affect muon and anti-muon survival probabilities in such a way that unitarity is preserved.

We wish to study the energy and trajectory length ranges where the matter effects are very large. The condition for resonance and the width of the resonance are given by

$$A = \delta_{32}\cos 2\theta_{13} \tag{3.12}$$

$$\delta A = \delta_{32}\sin 2\theta_{13} \tag{3.13}$$

For illustrative purposes, we choose $\sin^2 2\theta_{13} \simeq 0.1$. For $\delta_{32} = 0.002$ eV^2, the resonance condition gives

$$\rho E \simeq 25 \pm 8, \tag{3.14}$$

where ρ is measured in g/cm^3 and E in GeV. In the mantle, the average density of matter is about 4.5 g/cm^3. Hence the resonance occurs for an energy of about 5.5 GeV. At this resonant energy, $\sin^2 2\theta_{13}^m = 1.0$. For the energy range $3 - 7.5$ GeV, we have $\theta_{13}^m > \pi/4$ and $\sin^2 2\theta_{13}^m > 0.5$. Naively, one would expect $P_{e\mu}^m$ to be maximum at $E = E_{res}$ since $\sin 2\theta_{13}^m = 1$. But this is not true in general because at the resonance energy, δ_{31}^m attains its minimum value $\delta_{32} \sin 2\theta_{13}$. Hence, only for very long path lengths will it be possible to have significant $\nu_e \to \nu_\mu$ oscillation probability.

We note that $P_{e\mu}^m$ remains small for path lengths, $L \leq 1000$ km. We need

$$0.5 \leq \sin^2 \left(1.27 \frac{\delta_{31}^m L}{E} \right) \leq 1 \tag{3.15}$$

$$\pi/4 \leq 1.27 \frac{\delta_{32} \sin 2\theta_{13} L}{E} \leq \pi/2 \tag{3.16}$$

From the above equation, we find that for path lengths in the range 6,000–12,000 km, the path dependent phase term has a value greater than 0.5.

$P_{e\mu}^m$ is maximum when both $\sin 2\theta_{13}^m = 1$ and $\sin^2 (1.27\delta_{31}^m L/E) = 1 = \sin^2[(2p+1)\pi/2]$ are satisfied. This occurs when $E_{res} = E_{peak}^{mat}$. This gives the condition [65]:

$$\rho L_{e\mu}^{max} \simeq \frac{(2p+1)\pi 5.18 \times 10^3}{\tan 2\theta_{13}} \text{ km gm/cc} . \tag{3.17}$$

Here, p takes integer values. This condition is independent of δ_{32} but depends sensitively on θ_{13}. Using the product $\rho_{av} L$ vs L for the earth (calculated using the PREM profile), where ρ_{av} is the average density for a given length L , we identify the particular values of $\rho_{av} L$ which satisfy Eq. 3.17 with p=0 for three different values of $\sin^2 2\theta_{13}$.

These occur at $L \simeq 11200$ km, 10200 km, and 7600 km for $\sin^2 2\theta_{13} = 0.05, 0.1$ and 0.2 respectively. This identifies both the values of L at which $P_{\mu e}^m$ is large and also demonstrates its sensitivity to θ_{13}. At and around the resonant energies and these baselines (depending on the value of θ_{13}) $P_{\mu e}^m$ significantly impacts not only $P_{\mu\mu}$, but also $P_{\mu\tau}$, as we discuss below. Note that p=0 is the only possible value of p, given earth densities and baselines[1].

Probability $P_{e\mu}$ is a product of three terms. First of these terms $\sin^2 \theta_{23} \simeq 0.5$ from the fit to atmospheric neutrino data. Without matter effects, the second term $\sin^2 2\theta_{13} = 0.1$. The path length dependent third term will average out to half for very long path lengths. Hence we expect the average value of $P_{e\mu}$ to be about 0.025. Including the matter effects boosts this number by an order of magnitude. In the energy range of resonance width $(3-7.5)$ GeV the second term is always greater than 0.5 and for the range of path lengths $(6,000-12,000)$ km we have chosen, the third term is again always greater than 0.5. Conservatively we can expect the average value of the product of the second and third terms to be about $0.5(\simeq 0.75 \times 0.75)$. Thus including the matter effects, for positive δ_{32}, boosts $\nu_e \to \nu_\mu$ oscillation by a factor of about 10. In the case of anti-neutrinos, the $\bar{\nu}_e \to \bar{\nu}_\mu$ oscillations are suppressed by a factor of about 4. This occurs because $\delta_{31}^m \simeq 2\delta_{32}$ near resonance. Hence the second term in $P_{\bar{e}\bar{\mu}}^m$ is smaller by a factor of 4 and the third term has an average value of 0.5.

We now turn to muon neutrino survival probability which has a more complicated matter dependence. In the limit $\delta_{21} = 0$, we can choose vacuum eigenstates such that m_1 is essentially ν_e and m_2 has no ν_e component. Because of this reason, m_2 state is unaffected by inclusion of matter term. However, m_1 value rises with the Wolfenstein term and the $m_1 - m_2$ degeneracy of the vacuum is broken. The matter dependent mass-squared eigenvalues are given by

[1]The approximation of "average constant density" is not a good one for core passage but is included here since it delineates the range of $\sin^2 2\theta_{13}$ where core passage is a requisite for maximal matter effects.

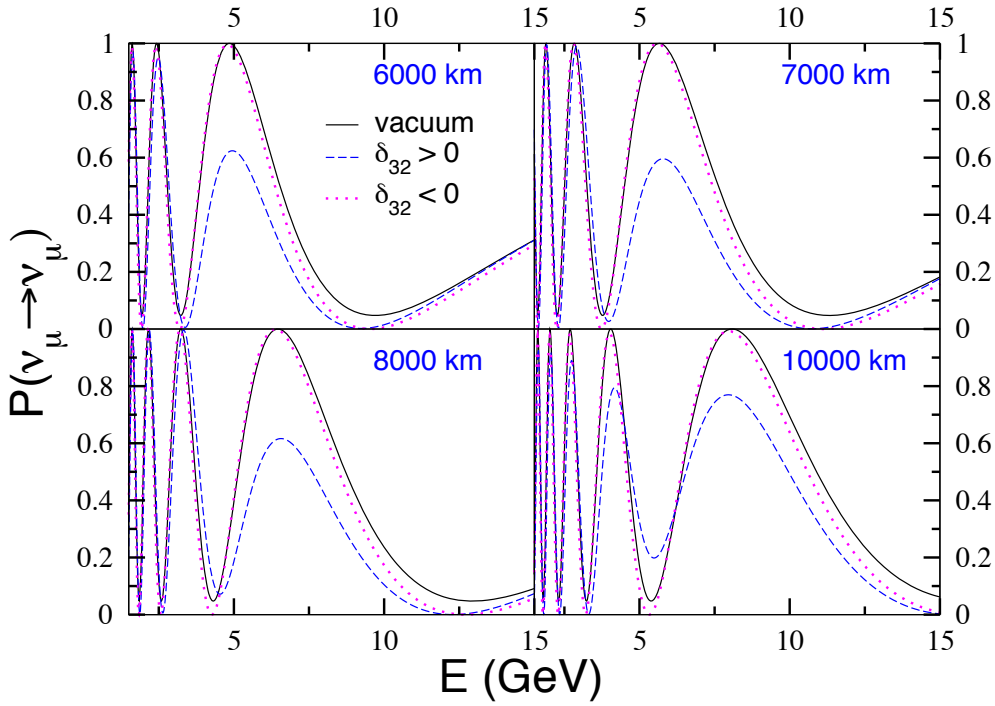

Figure 3.7: The muon survival probability in vacuum and in matter for both signs of δ_{32} plotted against the neutrino energy for different values of baseline lengths, L (in km). The oscillation parameters used in all the plots are : $\delta_{32} = 2 \times 10^{-3} eV^2$ and $\sin^2 2\theta_{23} = 1$.

$$
\begin{aligned}
m_1^2(mat) &= \frac{\delta_{32} + A - \delta_{31}^m}{2} \\
m_2^2(mat) &= 0 \\
m_3^2(mat) &= \frac{\delta_{32} + A + \delta_{31}^m}{2}
\end{aligned} \tag{3.18}
$$

In vacuum, we have

$$
\begin{aligned}
P_{\mu\mu} &= 1 - \sin^2 2\theta_{23} \cos^2 \theta_{13} \sin^2 \left(1.27 \frac{\delta_{32} L}{E}\right) \\
&\quad - \sin^4 \theta_{23} \sin^2 2\theta_{13} \sin^2 \left(1.27 \frac{\delta_{32} L}{E}\right).
\end{aligned} \tag{3.19}
$$

Including matter terms leads to

$$
\begin{aligned}
P_{\mu\mu}^m &= 1 - \sin^2 2\theta_{23} \cos^2 \theta_{13}^m \sin^2 \left(1.27 \frac{(\delta_{32} + A + \delta_{31}^m) L}{2E}\right) \\
&\quad - \sin^4 \theta_{23} \sin^2 2\theta_{13}^m \sin^2 \left(1.27 \frac{\delta_{31}^m L}{E}\right) \\
&\quad - \sin^2 2\theta_{23} \sin^2 \theta_{13}^m \sin^2 \left(1.27 \frac{(\delta_{32} + A - \delta_{31}^m) L}{2E}\right).
\end{aligned} \tag{3.20}
$$

In the above equation, the first two terms have their counterparts in the vacuum oscillation probability also. The third term is completely new and it arises because the matter term splits the degeneracy between m_1 and m_2.

Consider the difference

$$
\begin{aligned}
P_{\mu\mu} - P^m_{\mu\mu} &= 0.5(P^m_{e\mu} - P_{e\mu}) + \cos^2\theta^m_{13}\sin^2\left(1.27\frac{(\delta_{32}+A+\delta^m_{31})L}{2E}\right) \\
&\quad + \sin^2\theta^m_{13}\sin^2\left(1.27\frac{(\delta_{32}+A-\delta^m_{31})L}{2E}\right) \\
&\quad - \cos^2\theta_{13}\sin^2\left(1.27\frac{\delta_{32}L}{E}\right), \qquad (3.21)
\end{aligned}
$$

where we have set $\theta_{23} = \pi/4$. We search for energy and path length ranges where this difference is large. We expect the energy range to be range of resonance, from the first term. This is nearly true. The fourth term, which has a negative sign, is zero when the phase $(1.27\delta_{32}L/E) \simeq n\pi$. Hence the above difference is likely to be large for those energies which are in the resonance energy range and for which the phase condition is satisfied.

We see from Fig. 3.7 that the maximum suppression of muon neutrino survival probability due to matter effects occurs when the values of L and E are such that $(1.27\delta_{32}L/E) \simeq \pi$ and in all the cases the energy range of significant suppression has a large overlap with the resonance energy range. From Fig. 3.7, we note that observable matter effect occur for the energy range 5–10 GeV and L range 6,000–9,700 km.

3.3.3 Determination of mass hierarchy

We discuss below the possibility of determining the mass ordering or hierarchy of neutrino masses. The question of hierarchy specifically refers to the sign of the mass-squared difference δ_{32} involved in atmospheric neutrino oscillations which is not known unlike the δ_{21} whose sign is known to be positive from solar neutrino oscillations.

Mass hierarchy from event rates

Using the probabilities of Fig. 3.7, we have calculated the expected events for μ^- and μ^+ event rates in a magnetised iron calorimeter and an exposure of 1000 kton-years. The event rates are calculated for the energy range $5 - 10$ GeV and L range 6000–9700 km. The distribution of the event rates, both in the case of vacuum and matter oscillations are shown in Fig. 3.8 as function of L and in Fig. 3.9 as function of (L/E). We also show that the L/E distribution of muon events essentially follows the variation of probability as a function of L/E (shown in Fig. 3.9).

In both cases we notice that for the L range of $6000 - 9700$ km, the matter dependent μ^- rate is noticeably smaller than vacuum rate, whereas the rates are identical for μ^+. This conclusion holds for δ_{32} positive. For negative δ_{32}, vacuum and matter rates of μ^- coincide and matter rates of μ^+ show a deficit with respect to vacuum rates. The total number of μ^+ events, in the case of vacuum oscillations is 105 and it changes to 103 on inclusion of matter effects. The total number of μ^- events, in the case of vacuum oscillations is 261 and this reduces to 204 on inclusion of matter effects. Thus we have a 4σ signal [63, 64] for matter effects for neutrino parameters $\delta_{32} = 0.002$ eV^2 and $\sin^2 2\theta_{13} = 0.1$. We estimate that the matter effect will lead to about 2.5σ signal for the same δ_{32} and $\sin^2 2\theta_{13} = 0.05$. A systematic study of sensitivity of magnetised iron detectors to matter effects as function of θ_{13} and δ_{32} is underway.

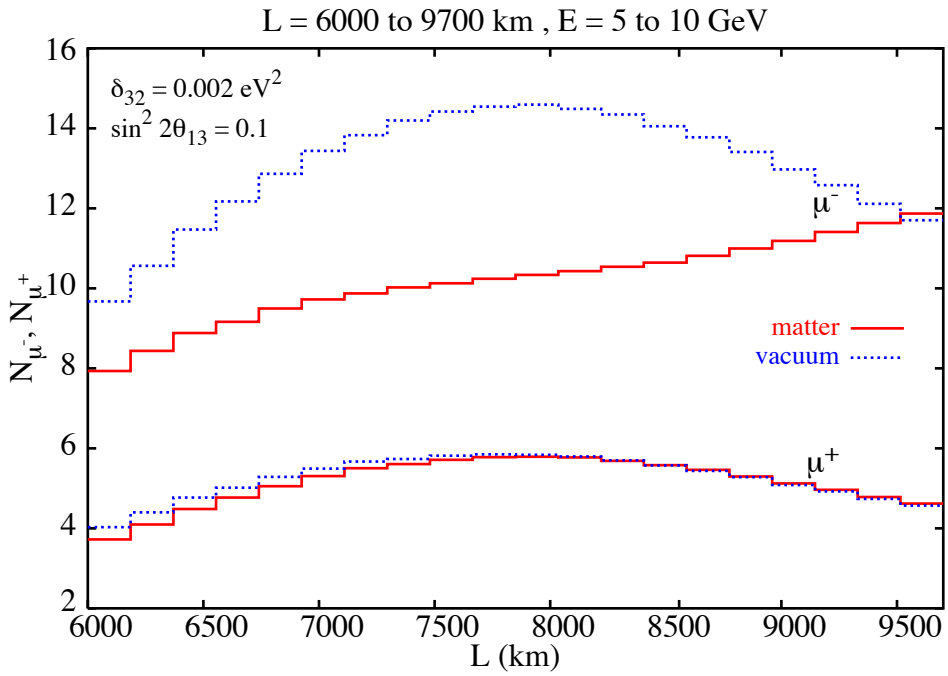

Figure 3.8: The total event rate for muons and anti-muons in matter and in vacuum plotted against L for the restricted choice of L and E range.

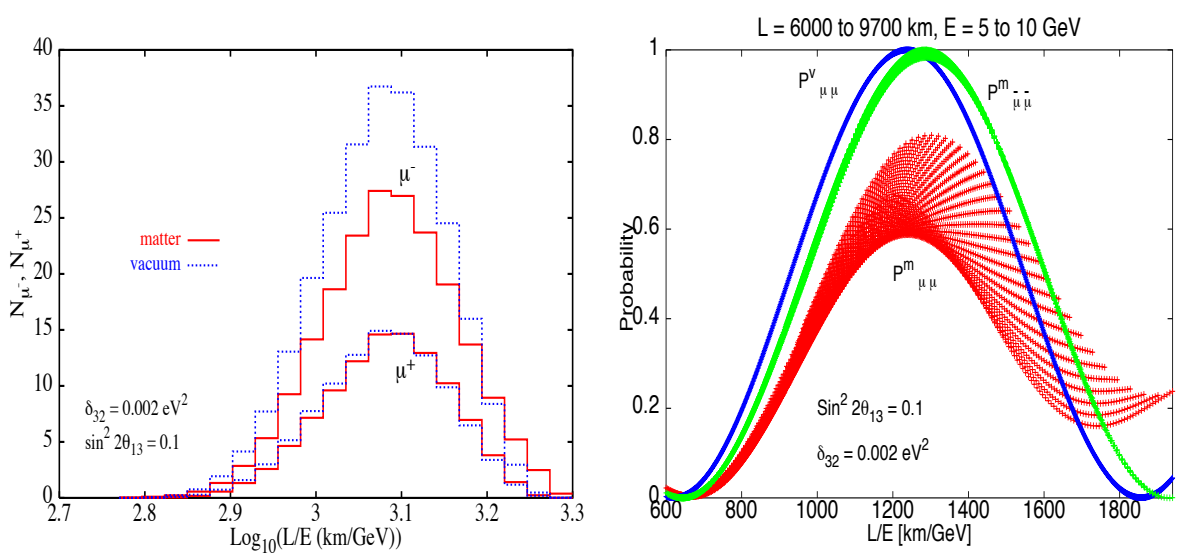

Figure 3.9: Left: The total event rate for muons and anti-muons in matter and in vacuum plotted against $\log_{10}(L/E)$ for the restricted choice of L and E range. Right: The muon survival probability $P^m_{\mu\mu}$ and the anti-muon survival probability $P^m_{\bar{\mu}\bar{\mu}}$ in matter and in vacuum $P_{\mu\mu}$ plotted against $\log_{10}(L/E)$ for positive sign of δ_{32}.

Mass hierarchy from the matter-induced asymmetry

As is clear from Figs. 3.8 and 3.9, the earth matter effects are not the same for neutrinos and anti-neutrinos. The neutrino and anti-neutrino up/down event ratios are different from each other as well as different with direct ($\delta_{32} > 0$) and inverted ($\delta_{32} < 0$) mass ordering (due to matter effects); the distinction (and hence measurement possibilities) between the two orderings can be amplified by defining the asymmetry (for details of calculations, see Ref.[60]),

$$\mathcal{A}_N(x) = \frac{U}{D}(x) - \frac{\overline{U}}{\overline{D}}(x) \ , \tag{3.22}$$

where x denotes the appropriate choice of variable to study the asymmetry (we choose this to be L/E) and $U(\overline{U})$ denotes the up-going events for neutrinos (anti-neutrinos) and $D(\overline{D})$ denotes the down-going events for neutrinos(anti-neutrinos) respectively. The asymmetry, calculated numerically, and integrated over $E_{\rm min} > 4$ GeV is plotted as a function of L/E in Fig. 3.10 for $|\delta_{32}| = 1, 2, 3 \times 10^{-3}$ eV^2. The thick (blue) curves in the figure correspond to the direct or normal mass ordering (labelled D) and the thin (red) curves to the inverted mass ordering (labelled I). The curves in each envelope correspond to $\theta_{13} = 5, 7, 9, 11$ degrees ($\sin^2 2\theta_{13}$ from 0.03–0.14) with the asymmetry increasing symmetrically with θ_{13} about the $\mathcal{A}_N = 0$ line for direct and inverse orderings. It is seen that the direct and inverted asymmetries are exactly out of phase. The maximum divergence between the direct and inverted orderings is smaller in the first envelope than in the second; these correspond to the first dip and rise in the up/down events ratio.

Asymmetries with finite detector resolution : Inclusion of finite detector resolution reduces the sensitivity, especially beyond the first oscillation minimum and maximum. A straightforward way to include such effects is to smear the observed L and E and observe the impact of this. To this end, we define Gaussian resolution functions for both L and E:

$$\begin{aligned} R_1(E', E) &\equiv \frac{1}{\sqrt{2\pi}\sigma_1} \exp\left[\frac{-(E-E')^2}{2\sigma_1^2}\right] \ ; \\ R_2(L', L) &\equiv \frac{1}{\sqrt{2\pi}\sigma_2} \exp\left[\frac{-(L-L')^2}{2\sigma_2^2}\right] \ . \end{aligned} \tag{3.23}$$

Hence, the event rate now includes the probability that a neutrino of any possible L' and E' is detected in the detector with path-length L and energy E. We have

$$N_{\rm bin}^{\alpha,R}(x) = \int_{\rm bin} {\rm d}x \int_{E_{\rm min}} \frac{{\rm d}E}{E} \int_0^\infty {\rm d}E' R_1(E', E) \int_0^\infty {\rm d}L' R_2(L', L) \frac{{\rm d}^2 N^\alpha}{{\rm d}\ln E' {\rm d}x'} \ , \tag{3.24}$$

where[2] $x' = L'/E'$. Furthermore, the differential event rate is given by

$$\frac{{\rm d}^2 N^\alpha}{{\rm d}\ln E' {\rm d}x'} = K_y \sum_\beta P_{\beta\alpha}(E', x') \ \Phi_\beta(E', x') \ \sigma_\alpha(E') \ , \tag{3.25}$$

where σ_α is the total interaction cross-section for the α type neutrino to interact with the detector material. Here $P_{\beta\alpha}$ is the conversion probability of a neutrino of flavour β to a flavour α.The flux-dependent term $\Phi_\alpha(E, x)$ is obtained from the doubly-differential neutrino

[2]The combination of Gaussian resolution functions for L and E integrates to a Lorentzian in their ratio provided the integration over *all* variables is unrestricted. We need to specify individual resolution functions here because of the cut on E.

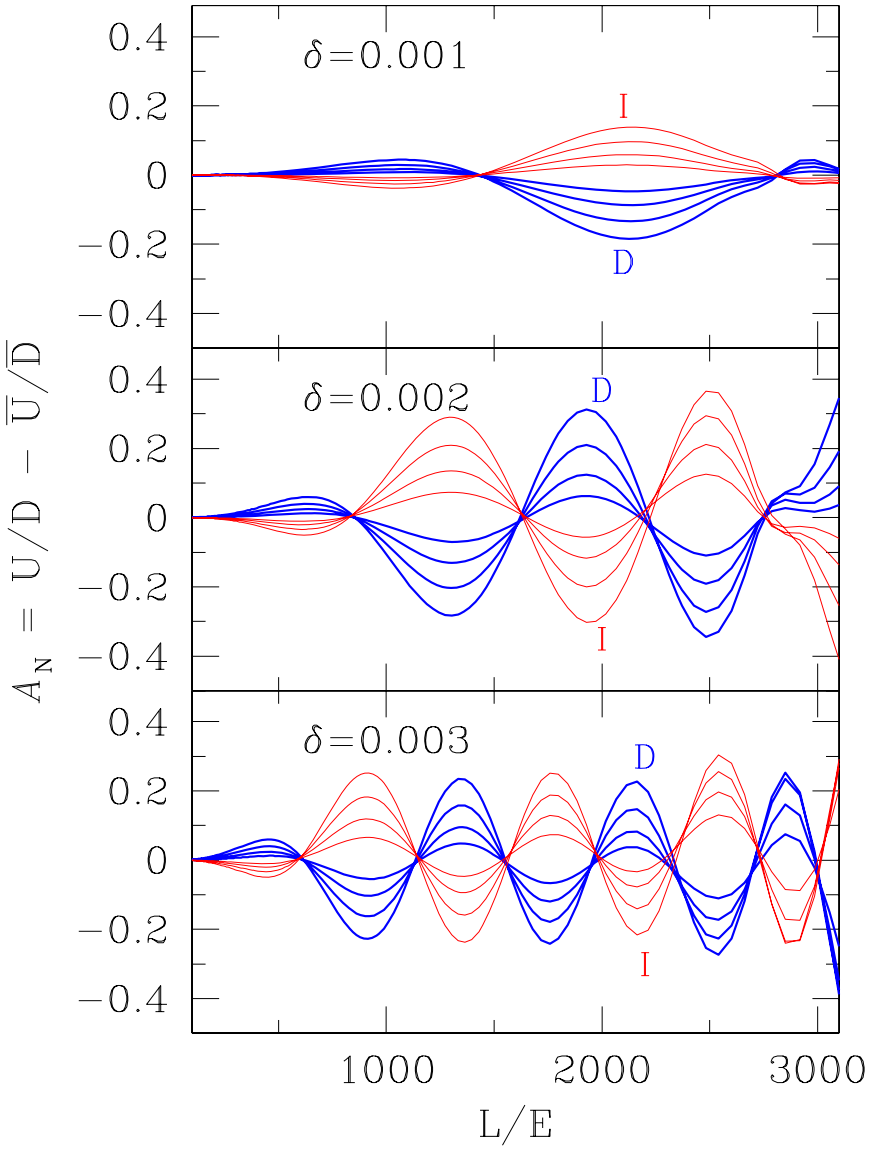

Figure 3.10: The difference asymmetry (difference of up/down ratios of muon neutrinos and anti-neutrinos) as a function of L/E for $E > 4$ GeV. The three panels correspond to $\delta \equiv |\delta_{32}| = 1, 2, 3 \times 10^{-3}$ eV^2. The thick (blue) curves correspond to the direct $\delta_{32} > 0$ and the thin (red) curves correspond to the inverse $\delta_{32} < 0$ ordering. The innermost curve in each envelope corresponds to $\theta_{13} = 5°$ and the outermost corresponds to $\theta_{13} = 11°$ with $7°$ and $9°$ in between. For other parameters the best fit values given in the text are chosen.

(or anti-neutrino) flux of flavour α, $\mathrm{d}^2\phi_\alpha(E', z)/\mathrm{d}\ln E'\mathrm{d}z$, which is a function of the energy E and zenith (actually nadir) angle $z = \cos\theta$, by multiplying with a suitable Jacobean factor. The factor K_y is the detector dependent factor measured in units of kton-years. The detector is assumed to be mainly made up of magnetised iron with active detector elements.

We evaluate the event rates and the up/down asymmetries with $\sigma_1 = 0.15E'$ and $\sigma_2 = 0.15L'$. These are realistic widths obtained by a GEANT analysis of atmospheric neutrino events by both the MONOLITH and the ICAL/INO collaborations; this gives a typical FWHM for their ratio (L/E) to be about $\sim 0.4L/E$.

The resulting asymmetry, that is, the difference of the neutrino and anti-neutrino events ratios, $\mathcal{A}_N$, is plotted in Fig. 3.11. Again, the panels on the right correspond to the rates calculation including resolution, while those on the left correspond to rates without including resolution effects. There is virtually no difference for small L/E. In general, however, the amplitude of the asymmetry decreases although it is still largest in the second envelope (corresponding to the third bin in the earlier discussions).

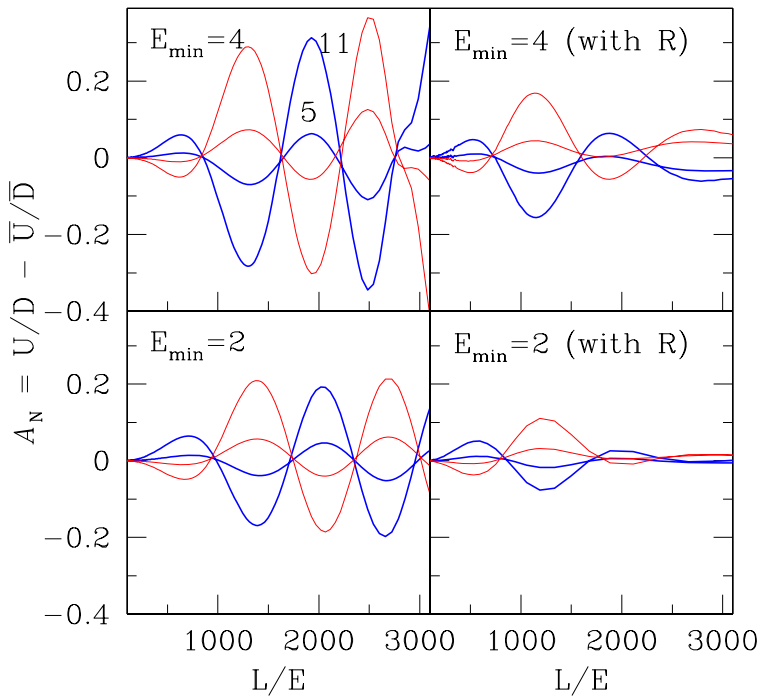

Figure 3.11: A comparison of the difference asymmetry as in Fig. 3.10 with (right) and without (left) inclusion of resolution functions for $\delta \equiv |\delta_{32}| = 2 \times 10^{-3}$ eV^2 and $\theta_{13} = 5, 11°$. The thick (blue) curves correspond to the direct and the thin (red) curves to the inverted hierarchy. Two cases, $E > 4$ and $E > 2$ GeV, are shown. It is clear that the higher energy cut better emphasises the asymmetry and hence the matter effects; however, the event rates are roughly halved in this case, for the same exposure times.

It is seen that the asymmetry is larger with a cut of $E_{\rm min} = 4$ GeV than with a cut of $E_{\rm min} = 2$ GeV while the *number of events* is smaller by roughly half in the case of the larger energy cut. In particular, by lowering the cut to $E_{\rm min} = 2$ GeV, not only does the sample size effectively double, the contribution from various processes changes to the proportion $1 : 1.5 : 1$ from $2.5 : 2 : 1$ for DIS, RS and QE processes.

Thus there are two conflicting requirements: to enhance the size of the asymmetry, we need a larger value of $E_{\rm min}$, but to improve statistics, we need a larger sample size. The final choice of $E_{\rm min}$ should optimise these two requirements.

We note in passing that, for $E_{\rm min} = 4$ GeV, there is a fairly large asymmetry for large L/E as well; the statistical significance in this bin is however small. In both cases, the

asymmetry in the penultimate envelope is almost vanishingly small; the oscillation length in this case is also very small.

In short, it appears that a finite resolution function causes smearing of the data across bins in such a way that the magnitude of the asymmetry becomes significantly smaller, and even vanishes beyond the third envelope/bin. We can improve the result by summing the asymmetries over several envelopes. We define

$$\mathcal{A}_n^H = \sum_{i=1}^{n} (-1)^i \mathcal{A}_N^{H,i} \ , \tag{3.26}$$

where H corresponds to a given hierarchy, direct, or inverted, $H = D, I$. Typically, $\mathcal{A}_N^D \sim -\mathcal{A}_N^I$ in a bin, and therefore the sum in Eq. 3.26 is roughly equal and opposite for the two hierarchies. Furthermore, the statistics are not very different with either hierarchy. The significance of the result is thus estimated by comparing the difference

$$\Delta\mathcal{A}_n = \mathcal{A}_n^D - \mathcal{A}_n^I \tag{3.27}$$

with the error σ corresponding to a given exposure. In fact, the ratio $\Delta\mathcal{A}_n/\sigma$ indicates the probability of the observed asymmetry being assigned to the correct hierarchy.

The error σ arises primarily from statistics. This is because the asymmetry is defined as a difference of two ratios. Systematic errors (due to uncertainties both in fluxes and cross-sections) in the ratio are therefore very small and can be ignored; this was pointed out very early on by the MONOLITH collaboration [42].

We list the values of $\Delta\mathcal{A}_n$ and the corresponding statistical error σ_n (we have chosen the larger of the errors for the direct and inverted hierarchy) in Tables 3.3, 3.4 for different resolutions in E and L of 15% and 10%, respectively. In each table, results for both $n = 2$ and $n = 3$ (that is, a sum over two or three envelopes), corresponding to $|\delta_{32}| = 2.0 \times 10^{-3}$ eV^2 and $\theta_{13} = 7, 9, 11, 13^\circ$ are shown for different exposures of 480, 800 and 1120 kton-years respectively. The resulting confidence level of the measurement is also indicated in the tables.

It is clear that the asymmetry and hence $\Delta\mathcal{A}_n$ increases with θ_{13}, *independent* of exposure. The effect of increasing the exposure is to improve the errors, without changing the central values of the asymmetry. This can be seen by comparing results for the same θ_{13} in each table. Since the minimum exposure of 480 kton-years is already large, and statistical errors improve only as $\sqrt{N_{data}}$, it will be difficult to greatly enhance the significance of the result by going to larger and larger exposures.

The effect of improving the resolution function (obtained by comparing the same row in the tables 3.3 and 3.4 is two-fold. For a given exposure, improving the resolution function (by which we mean the improving the Gaussian widths of the resolutions in E and L as defined in Eq. 3.24 above) *increases the central value of the asymmetry* in each case. It also results in marginally improved errors for $n = 3$, that is, when summing over all the three significant bins in the L/E distribution, which further enhances the significance of the result. For example, the improvement upon increasing the exposure from 480 to 1120 kton-years at 15% resolution is similar to that obtained by improving the resolution, *at 480 kton-years*, from 15% to 10%.

Note also that the significance of the results for $\Delta\mathcal{A}_2$ is higher than for $\Delta\mathcal{A}_3$ for larger resolutions of 15%; this may imply that best results are obtained from single-bin information when the resolutions are poorer.

While resolutions with widths of 10% may not be hard to achieve, it is not clear whether it is possible to reach below that. One way is to exclude the DIS events (perhaps by cutting out events with large hadronic activity). The resulting data set is smaller by about 45%;

Exposure (kton-year)	$\Delta\mathcal{A}_2$ (CL %)		$\Delta\mathcal{A}_3$ (CL %)	
		$\theta_{13} = 7^\circ$		
480	0.166 ± 0.161	$(1.0\,\sigma,\ 68.3\%)$	0.167 ± 0.230	$(0.7\,\sigma,\ 51.6\%)$
800	0.166 ± 0.125	$(1.3\,\sigma,\ 80.6\%)$	0.167 ± 0.178	$(0.9\,\sigma,\ 63.2\%)$
1120	0.166 ± 0.105	$(1.6\,\sigma,\ 89.0\%)$	0.167 ± 0.151	$(1.1\,\sigma,\ 72.9\%)$
		$\theta_{13} = 9^\circ$		
480	0.257 ± 0.159	$(1.6\,\sigma,\ 89.0\%)$	0.280 ± 0.230	$(1.2\,\sigma,\ 77.0\%)$
800	0.257 ± 0.123	$(2.1\,\sigma,\ 96.4\%)$	0.280 ± 0.178	$(1.6\,\sigma,\ 89.0\%)$
1120	0.257 ± 0.104	$(2.5\,\sigma,\ 98.8\%)$	0.280 ± 0.150	$(1.9\,\sigma,\ 94.3\%)$
		$\theta_{13} = 11^\circ$		
480	0.357 ± 0.157	$(2.3\,\sigma,\ 97.9\%)$	0.415 ± 0.230	$(1.8\,\sigma,\ 92.8\%)$
800	0.357 ± 0.122	$(2.9\,\sigma,\ 99.6\%)$	0.415 ± 0.178	$(2.3\,\sigma,\ 97.9\%)$
1120	0.357 ± 0.103	$(3.5\,\sigma,\ 99.95\%)$	0.415 ± 0.150	$(2.8\,\sigma,\ 99.6\%)$
		$\theta_{13} = 13^\circ$		
480	0.459 ± 0.155	$(3.0\,\sigma,\ 99.7\%)$	0.560 ± 0.230	$(2.4\,\sigma,\ 99.4\%)$
800	0.459 ± 0.120	$(3.8\,\sigma,\ 99.98\%)$	0.560 ± 0.178	$(3.1\,\sigma,\ 99.8\%)$
1120	0.459 ± 0.102	$(4.5\,\sigma,\ 99.999\%)$	0.560 ± 0.151	$(3.7\,\sigma,\ 99.98\%)$

Table 3.3: Significance of the asymmetry for different exposures in kton-years for resolution widths $\sigma_{1,2}$ in E and L (see Eq. 3.24) of 15%. Asymmetries are shown for typical values of $\theta_{13} = 7, 9, 11, 13^\circ$; the CHOOZ bound limits this angle to $\theta_{13} \leq 14.9^\circ$.

Exposure (kton-year)	$\Delta\mathcal{A}_2$ (CL %)		$\Delta\mathcal{A}_3$ (CL %)	
		$\theta_{13} = 7^\circ$		
480	0.185 ± 0.167	$(1.1\,\sigma,\ 72.9\%)$	0.232 ± 0.220	$(1.1\,\sigma,\ 72.9\%)$
800	0.185 ± 0.130	$(1.4\,\sigma,\ 83.8\%)$	0.232 ± 0.170	$(1.4\,\sigma,\ 83.8\%)$
1120	0.185 ± 0.110	$(1.7\,\sigma,\ 91.1\%)$	0.232 ± 0.144	$(1.6\,\sigma,\ 89.0\%)$
		$\theta_{13} = 9^\circ$		
480	0.287 ± 0.165	$(1.7\,\sigma,\ 91.1\%)$	0.384 ± 0.220	$(1.8\,\sigma,\ 92.8\%)$
800	0.287 ± 0.128	$(2.2\,\sigma,\ 97.2\%)$	0.384 ± 0.170	$(2.3\,\sigma,\ 97.9\%)$
1120	0.287 ± 0.108	$(2.7\,\sigma,\ 99.3\%)$	0.384 ± 0.144	$(2.7\,\sigma,\ 99.3\%)$
		$\theta_{13} = 11^\circ$		
480	0.399 ± 0.163	$(2.4\,\sigma,\ 98.4\%)$	0.565 ± 0.221	$(2.6\,\sigma,\ 99.1\%)$
800	0.399 ± 0.126	$(3.2\,\sigma,\ 99.9\%)$	0.565 ± 0.171	$(3.3\,\sigma,\ 99.9\%)$
1120	0.399 ± 0.107	$(3.7\,\sigma,\ 99.98\%)$	0.565 ± 0.144	$(3.9\,\sigma,\ 99.99\%)$
		$\theta_{13} = 13^\circ$		
480	0.515 ± 0.161	$(3.2\,\sigma,\ 99.9\%)$	0.758 ± 0.223	$(3.4\,\sigma,\ 99.9\%)$
800	0.515 ± 0.125	$(4.1\,\sigma,\ 99.996\%)$	0.758 ± 0.173	$(4.4\,\sigma,\ 99.999\%)$
1120	0.515 ± 0.102	$(4.9\,\sigma,\ 99.9999\%)$	0.758 ± 0.146	$(5.2\,\sigma,\ 100\%)$

Table 3.4: Same as Table 3.3 for resolution widths $\sigma_{1,2}$ in E and L (see Eq. 3.24) of 10%.

however, it may be possible to resolve the energy and direction of the neutrino much better since there are only quasi-elastic and resonance events left in the sample. This needs to be studied in more detail.

Therefore it appears that, even for moderate to large exposures, it may be difficult to achieve effects larger than 2σ or so, unless of course Nature is kind and prefers large θ_{13}. For $\theta_{13} \geq 9^\circ$, a significance of 99.3% (nearly 3σ) or more is obtained with an exposure of 1120 kton-years and resolutions in both energy and angle of 10%. It is clear that a prior knowledge of θ_{13} from some other experiment would greatly facilitate the extraction of the mass hierarchy since the magnitude of the expected asymmetry would then be known.

In short, the major features of the analysis without including finite detector resolutions appear to hold, although with much reduced significance. While the asymmetry is partly washed out due to smearing in both L and E, its sensitivity to the mass ordering is very clear. Furthermore, it is a robust parameter and is only marginally sensitive to errors in flux or cross-section since it is a difference of ratios.

3.3.4 Deviation from maximality of θ_{23}: octant determination

We address the question of using matter effects to determine whether the mixing angle θ_{23} is indeed maximal (i.e., $\theta_{23} = \pi/4$), and, if not explore how well its octant can be determined. We present a summary of two independent and complementary analyses carried out in Ref.[61] and Ref.[62]. In the first instance, the analysis is done using the difference asymmetry given in Eq.3.22 where as the latter analysis uses the ratio of up and down event rates.

Deviation from maximality from rate asymmetry :

The key question is the measurability of $D = 1/2 - \sin^2\theta_{23}$ from atmospheric muon neutrino and anti-neutrino event rates in ICAL detector. Effects due to interactions of neutrinos with matter and sub-leading oscillations on account of the solar neutrino mass scale $\delta_{21} = m_2^2 - m_1^2$ cause departures from the simple $\sin^2 2\theta_{23}$ dependence of 2-flavour vacuum oscillations in the survival probability $P_{\mu\mu}$ ($P_{\bar{\mu}\bar{\mu}}$) for a ν_μ ($\bar{\nu}_\mu$). Both these effects as well as vacuum oscillation terms play a role in the measurement of $|D|$. However, matter effects are found to be crucial in resolving the octant ambiguity $\sin^2\theta_{23} \leftrightarrow 1 - \sin^2\theta_{23}$, through a determination of the sign of D.

The numerical code used in [61] exactly solves the three generation neutrino equations of motion in earth matter with the PREM density profile. Normal neutrino mass ordering is assumed, but the analysis for the inverted case may also be done. Some of the oscillation parameters are chosen at benchmark values, $\delta_{31} = 2 \times 10^{-3}$ eV^2, $\delta_{21} = 8 \times 10^{-5}$ eV^2, $\sin^2\theta_{12} = 0.28$, $\sin^2 2\theta_{13} = 0.1$, $\delta = 0$. Using the atmospheric neutrino flux of Honda *et al.* and the DIS cross sections of the CTEQ collaboration, 14000 (7000) events were simulated for ν_μ ($\bar{\nu}_\mu$) events for 1000 kton-year of exposure for ICAL assuming a 50% trigger efficiency.

The data is binned *both* in energy E and the cosine of the zenith angle $c_\xi = \cos\theta$. The difference between the ν_μ and $\bar{\nu}_\mu$ up-down asymmetry ratios $U_N/D_N - U_A/D_A$ is shown in Fig.3.12 with solid (dashed) pink and black lines corresponding to $\sin^2\theta_{23} = 0.36$ and 0.5 respectively in matter (vacuum). The largest usable effects are in the topmost right panel (the lower most right panel having problems due to earth-core uncertainties) with the 5-7 GeV energy bin corresponding to a maximum SPMAX in $P_{\mu\mu}$.

The sign of D resolves the octant ambiguity $\theta_{23} \leftrightarrow \pi/2 - \theta_{23}$. We have done a χ^2 analysis using the pull approach, as detailed in Ref.[61]. Fig.3.13 shows the regions of $\sin^2\theta_{13}$ for which the octant ambiguity can be resolved at 3σ (yellow), 2σ (green) and 1σ (magenta) levels.

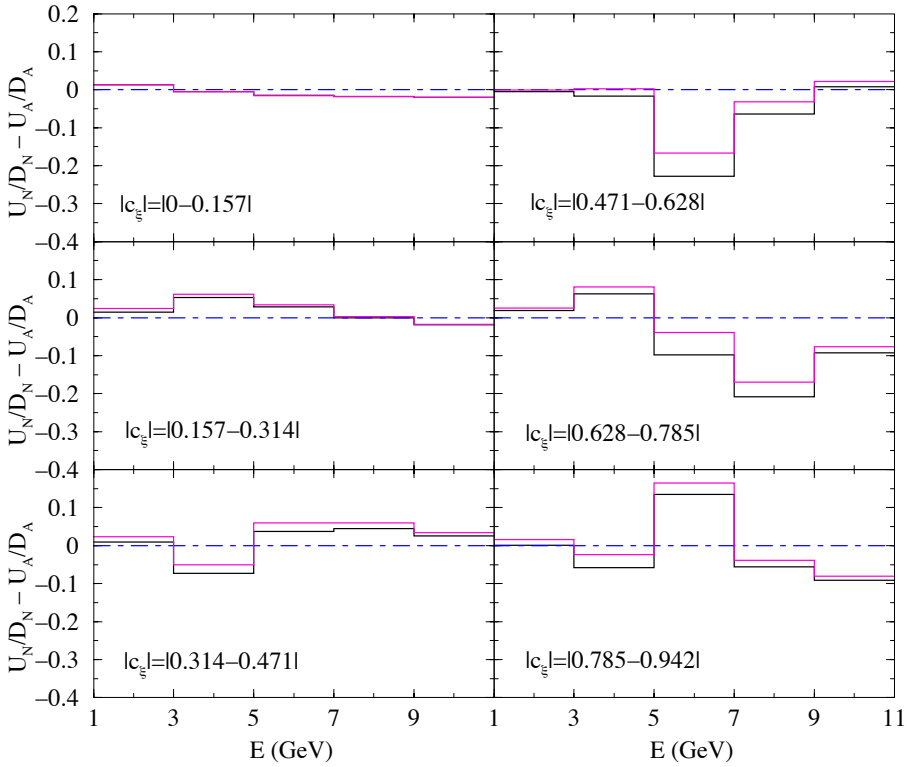

Figure 3.12: The difference $U_N/D_N - U_A/D_A$ for various bins of E and $|c_\xi|$.

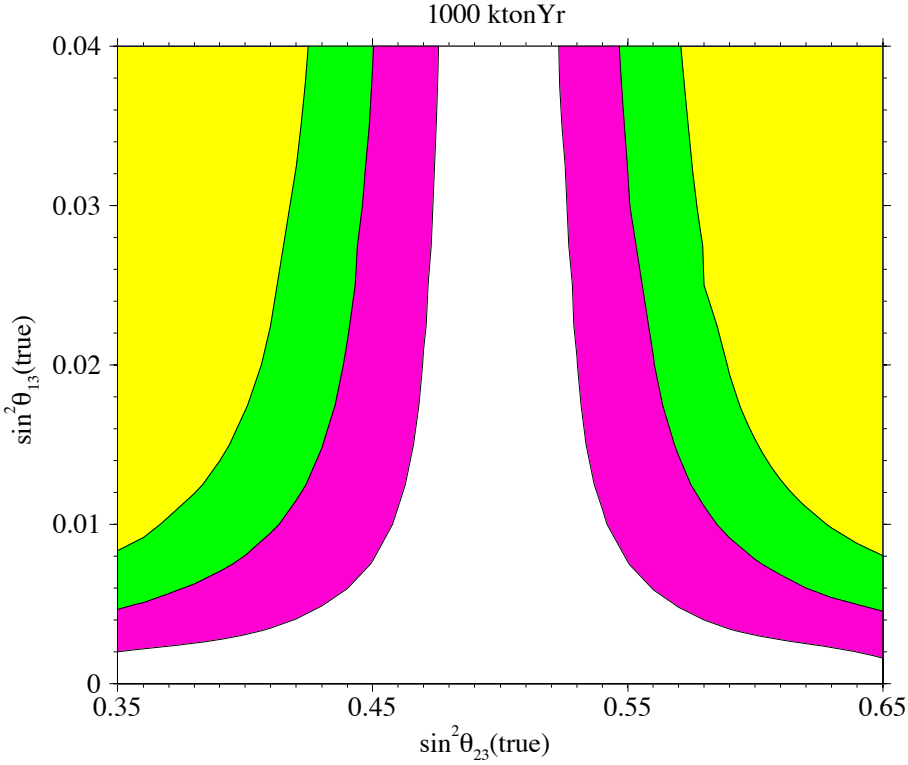

Figure 3.13: Sensitivity to octant ambiguity resolution in terms of θ_{13}

An analysis of the capability of ICAL for a resolution of the octant ambiguity from a 500 kton-year of exposure with an 80% trigger efficiency has also been done. It is found that if $\theta_{13} > 8^\circ$ and $|45^\circ - \theta_{23}| > 4^\circ$, ICAL will be able to resolve the θ_{23} octant ambiguity with such an exposure at the 90% c.l.

Deviation from maximality from event ratios :

We focus on the precision to which the magnitude of δ_{32} and the octant of θ_{23} can be determined from the event rate ratios themselves[62]. It is convenient to introduce the scale Δm^2[31] instead of δ_{32}:

$$\Delta m^2 \equiv \delta_{32} + \delta_{21}/2 \;=\; m_3^2 - \frac{1}{2}(m_1^2 + m_2^2),$$

so that a normal or inverted hierarchy is simply indicated by a sign (and not magnitude) change in this parameter. Current data from the Super-Kamiokande collaboration restrict these to the ranges $1.8 \leq |\Delta m^2| \times 10^3$ eV$^2 \leq 2.9$ and $36.5 \leq \theta_{23} \leq 54.5^\circ$.

The analysis depends on $\sin^2\theta_{13}$, which is expected to be shortly measured with good precision (to within a few percent) by the Double-CHOOZ experiment [206]. While we have studied both cases, i.e., when θ_{13} is known and hence kept fixed in the analysis, as well as the case when it is allowed to vary freely only the first case is summarised here. We restrict ourselves to the normal hierarchy, with Δm^2 positive, so that matter effects (and hence sensitivity to the octant of θ_{23}), are enhanced in the neutrino channel. We integrate event rates over an energy range of $E = 5$–10 GeV to maximise statistics while retaining sensitivity to matter effects. The details of the calculations and results may be found in Ref.[62].

In Fig. 3.14 we show the variation of the up/down events ratio for different Δm^2 values as a function of $\log_{10} L/E$ for two values of $\theta_{23} = 40^\circ, 50^\circ$, in two octants. Here θ_{13} is fixed to 9°. Two features are immediately noticeable: (1) the position of the minima and maxima in L/E are not altered by changing θ_{23}; furthermore, the events ratio at the first minimum is not very sensitive to θ_{23}, and (2) the effect of changing θ_{23} from a value in the first octant to a corresponding one in the second octant is to systematically *decrease the event rates in all bins* for all Δm^2 values.

Furthermore, although not shown in the figure due to constraints of clarity, the curve for maximal $\theta_{23} = 45^\circ$ lies between the two curves for $\theta_{23} = 40, 50^\circ$ in all L/E bins beyond the first minimum. Note that the number of events for maximal $theta_{23}$ may lie below or above those corresponding to $theta_{23}$ in the second octant, depending on the energy and zenith angle. . By a judicious choice of the energy and L/E interval, this effect has been converted to a systematic difference for all bins to the right of the first minimum; moreover, it is in these bins that the sensitivity to θ_{23} is significant, so that this dependence is robust and easy to observe.

We now ask how sensitive these results are to the finite resolution (in determining neutrino energy and direction, and hence its L/E) of the detector.

Event rates with finite detector resolution

Inclusion of finite detector resolution reduces the sensitivity, especially beyond the first oscillation minimum and maximum in L/E. The detector resolutions for energy and path-length are given in Eq.3.24.

We re-evaluate the event rates and the up/down ratios using this equation, with $\sigma_E = 0.15E'$ and $\sigma_L = 0.15L'$. These are realistic widths obtained by a GEANT analysis of atmospheric neutrino events by both the MONOLITH and the ICAL/INO collaborations. Such a

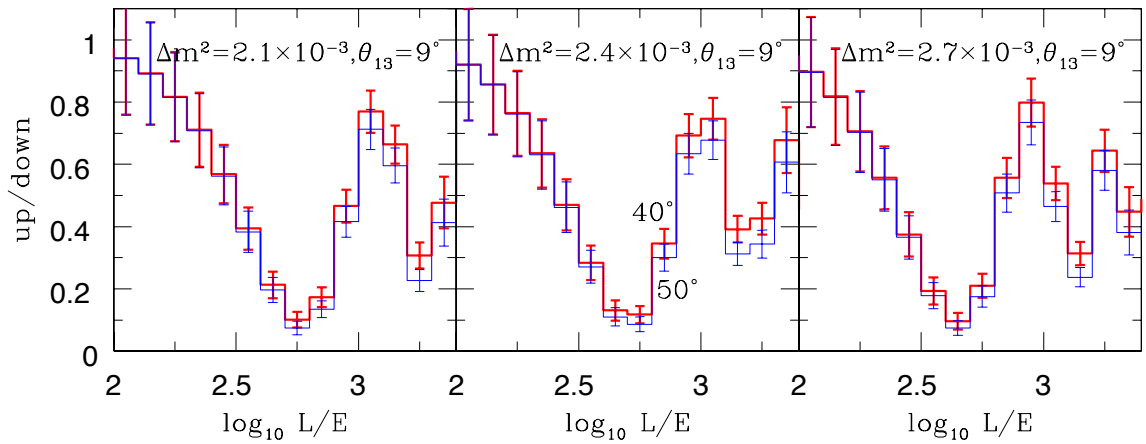

Figure 3.14: Variation of the ratio of the rates for up-coming and down-going neutrinos, integrated from $E = 5$–10 GeV, in bins of $\log_{10} L\,(\mathrm{km})/E\,(\mathrm{GeV}) = 0.1$. The variation with Δm^2 is shown in the three panels, where results for a Δm^2 over the currently allowed 1σ range, via., $\Delta m^2 = (2.1, 2.4, 2.7) \times 10^{-3}$ eV^2 are shown. The two histograms in each panel correspond to $\theta_{23} = 40°$ (upper) and $50°$ (lower). The value of θ_{13} is kept fixed at $9°$. Statistical error bars corresponding to an exposure of 1000 kton-years are also shown.

smearing has the effect of accounting for errors in correctly identifying the L/E bin for a given event, and so accounting for bin-to-bin correlations.

In Fig. 3.15 we show the variation of the up/down events ratio for different Δm^2 values as a function of $\log_{10} L/E$ for $\theta_{23} = 40°, 50°$ when the resolution function is included. Here θ_{13} is fixed to $9°$. A comparison with the similar Fig. 3.14, where no resolution functions have been included, shows immediately that the effect of changing the octant of θ_{23} remains roughly the same as before (about 1σ maximum deviation in each bin) while the oscillation pattern itself gets smeared away due to finite resolution functions so that the minima and maxima of the oscillations are not as clearly visible, especially beyond the first minimum.

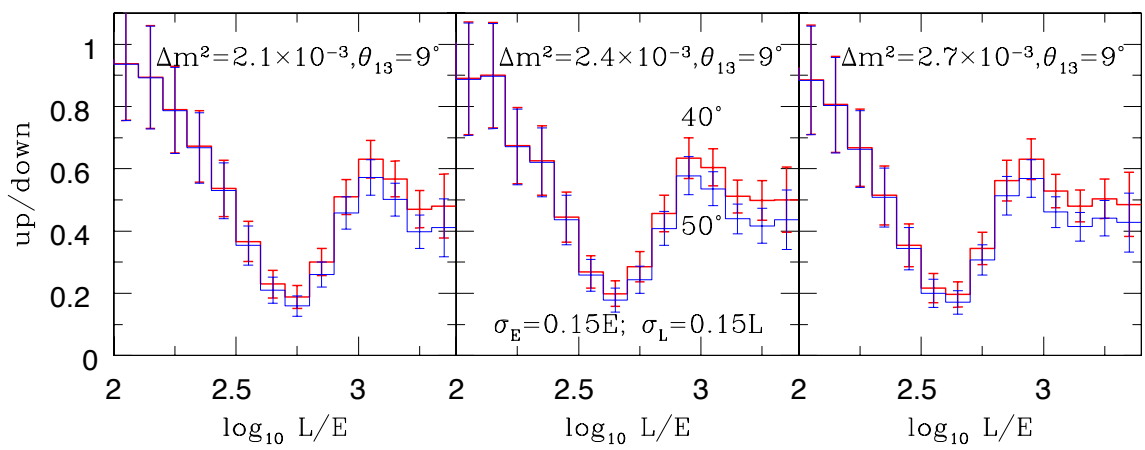

Figure 3.15: As in Fig. 3.14, for $\theta_{13} = 9°$, including finite detector resolutions. Above: smearing in E and θ by Gaussian resolutions with widths $\sigma_E/E = 0.15$ and $\sigma_\theta = 5°$, and Below: smearing in E and L by Gaussian resolutions with widths $\sigma_E/E = \sigma_L/L = 0.15$.

We now go on to study the effect of finite detector resolutions on the extraction of oscillation parameters. We generate contours of allowed parameter space for an input data of up/down neutrino and anti-neutrino event rates in fixed L/E bins for a set of input values for $(\theta_{13}, \Delta m^2, \theta_{23})$ and focus, as before, on the octant resolution. The other parameters,

δ_{21} and θ_{21} have been fixed at their best-fit values, and we have used $\delta = 0$. We find that atmospheric neutrino (and anti-neutrino) data accumulated over 1000 kton-years is sufficient to distinguish a non-maximal solution from a maximal solution as well as the octant of θ_{23} for $\theta_{13} \geq 8^\circ$ and $\theta_{23} \leq 39^\circ$ or $\theta_{23} \geq 51^\circ$. The inclusion of finite detector resolution severely degrades the errors on the parameters. For instance, the error on Δm^2 is twice as large as that with an ideal detector. This is shown for two values of θ_{13}, $\theta_{13} = 7^\circ, 8^\circ$, for $\theta_{23} = 39^\circ$ ($\sin^2\theta_{23} = 0.4$) and $\Delta m^2 = 2.4 \times 10^{-3}$ eV^2 in Figs. 3.16 and 3.17 respectively.

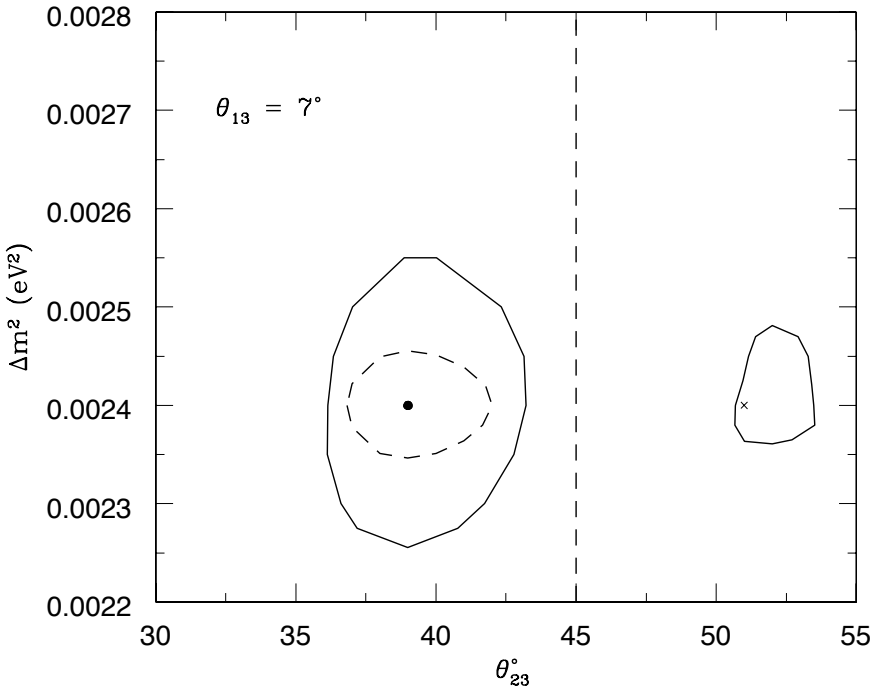

Figure 3.16: Allowed parameter space from neutrino and anti-neutrino up/down event rates for an exposure of 1000 kton-years and input parameter values $(\theta_{23}, \theta_{13}) = (39^\circ, 7^\circ)$ for fixed $\Delta m^2 = 2.4 \times 10^{-3}$ eV^2. The 99% CL contours are shown for an ideal detector (dashed lines) and for a detector with finite Gaussian resolutions of widths 15% in E and L. An island of allowed parameter space near the "wrong octant" solution, $\theta_{23} = \pi/2 - \theta_{23}^{\rm input} = 51^\circ$, marked with a a cross, is seen.

While maximality in θ_{23} can be excluded and the octant distinguished at 95% CL, only deviation from maximality can be established at 99% CL for the smaller $\theta_{13} = 7^\circ$ due to the island around the "wrong octant" solution.

From Figs. 3.16 and 3.17 it is seen that a larger θ_{13} is instrumental in suppressing the "wrong octant" solutions but does not shrink the allowed parameter space around the correct θ_{23} value. In fact, the allowed parameter space around $\theta_{23} = 39^\circ$ is virtually the same in both figures. With larger $\theta_{13} = 9^\circ$, it is possible to obtain octant discrimination for larger $\theta_{23} = 40^\circ$, but the issue of maximality can only be settled at little less than 99% CL in this case. Of course, if deviation from maximality cannot be established, the octant determination appears to have no meaning. What we mean here is that the allowed parameter space lies mostly in the first octant. The octant mirror of the best-fit point is ruled out, but not the maximal value. We will refer to such solutions as discriminating the octant but not deviations from maximality. It turns out that both octant and maximality discrimination can be established at 95% CL for values of θ_{23} 15% away from the maximal value.

We wish to point out that resolution functions worsen the precision with which the magnitude of Δm^2 and θ_{23} can be determined but do not substantially alter the sensitivity

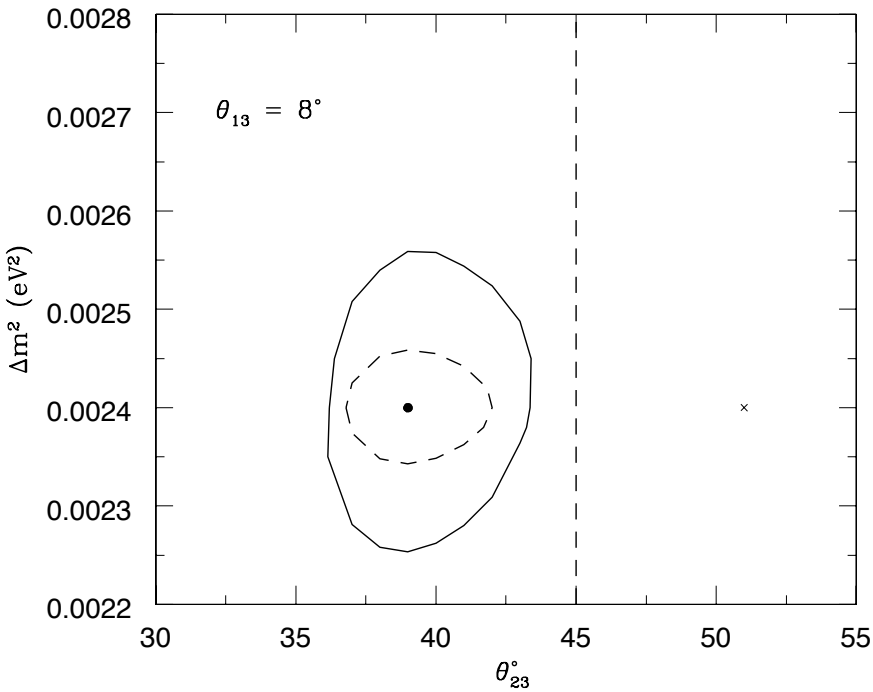

Figure 3.17: As in Fig. 3.16 for $\theta_{13} = 8°$. There is no allowed parameter space near the "wrong octant" solution, $\theta_{23} = \pi/2 - \theta_{23}^{\rm input} = 51°$, marked with a cross in the figure.

to the octant of θ_{23}. That is, $\theta_{13} = 7°$ ($\sin^2\theta_{13} = 0.015$) remains the limit at which matter effects are substantial enough to determine the octant of the (23) mixing angle (as also the mass ordering of the (23) mass eigenstates, as discussed in Ref. [60]), even on including finite resolution functions, while the actual value of the (23) angle which simultaneously allows maximality and octant discrimination at 99% CL level moves marginally from $\theta_{23} = 40°$ in the absence of finite resolution effects, to $\theta_{23} = 39°$ ($\sin^2\theta_{23} \approx 0.4$) at the lower limit of θ_{13}.

We note that the situation is not as clean when the true value of θ_{23} lies in the second octant. The muon survival probability in this case is not as well separated from that for maximal θ_{23}, unlike when θ_{23} is in the first octant. Hence, while results for octant discrimination will be symmetric with the case when θ_{23} is in the first octant, the issue of maximality may not be so easily settled. For example, with other parameters as before, and using $\theta_{23} = 51°$, which is the octant mirror of $\theta_{23} = 39°$, the "data" discriminate between the right and wrong octant at 99% CL, but cannot discriminate the true value of θ_{23} from maximality. By going farther away from maximality, for example, at $\theta_{23} = 52.5°$, we once again have maximality discrimination.

To summarise therefore

- If θ_{13} is known precisely in the near future, as is likely from Double-CHOOZ, then in the energy range $E = 5$–10 GeV, where matter effects are largest, the data from ICAL/INO will be able to study deviations of θ_{23} from maximality as well as determine the octant of this angle, provided $\theta_{13} \geq 8°$.

- It must be emphasised that the octant discrimination is more easily done than establishing deviation from maximality for larger θ_{13} and the reverse is true for smaller θ_{13} when islands of allowed parameter space begin to appear near the "wrong octant" solution. Also, values of θ_{23} in the first octant are more easily distinguished from maximality than those in the second octant.

- In particular, deviations from maximality and octant discrimination to 99% CL can be obtained if $\sin^2\theta_{23} \leq 0.4$ and $\sin^2\theta_{13} \geq 0.015$ using standard Gaussian resolution functions with widths $\delta L/L = \delta E/E = 15\%$ to smear the events. Similarly, we must have $\sin^2\theta_{23} \geq 0.63$ for corresponding results in the second octant.

- In an earlier analysis [60], we have also shown that the same processes are also eminently suited to determine the (23) mass ordering. Both these determinations need large exposures of roughly 1000 kton-years as well as, crucially, the charge discrimination.

- The issue of determining the (23) mass ordering and hence establishing the neutrino mass hierarchy is best done using the difference asymmetry which is the *difference* of the up/down events ratios with neutrinos and anti neutrinos. For the octant discrimination the relevant observable is in fact the *sum* of these two ratios.

- The same experiment can therefore study both these questions, while requiring large exposures, 1000 kton-years, in both cases. Hence, studies of neutrino oscillations with atmospheric neutrinos, while being difficult, are probably the only source of precision measurements, at least until very large megaton detectors and/or neutrino factories become a reality.

It is important to point out that the determination of the hierarchy is likely to be relatively easier than the octant determination.

3.3.5 Discrimination between $\nu_\mu \to \nu_\tau$ and $\nu_\mu \to \nu_s$

The ICAL detector may also provide a new way of distinguishing whether the muon neutrino deficit observed by previous experiments is due to oscillations of muon neutrinos to tau neutrinos or to sterile ones. If the dominant oscillation is $\nu_\mu \to \nu_\tau$, as was established at 99% C.L. by Super-K data in 2000 [6, 7, 8], then there will be CC production of τ leptons in the detector, originating from the ν_τ produced due to these oscillations. At these energies, the τ lepton decays very rapidly, and roughly 80% of the time this decay does *not* produce a muon.

The visible hadronic activity generated in these events has the appearance (if specific cuts for τ detection are not incorporated) of a neutral-current (NC) event due to the lack of a visible lepton charged track. Thus this oscillation scenario significantly alters the up/down ratio of the "muon-less" events when compared to the $\nu_\mu \to \nu_s$ possibility. In fact, the asymmetry in the ratio $(U - D)/(U + D)$ assumes positive values in one case ($\nu_\mu \to \nu_\tau$) and negative values in the other ($\nu_\mu \to \nu_s$), since the upward rate is enhanced significantly by CC τ events (which appear as "fake" NC events) in the former case, but depleted if the oscillation is to sterile neutrinos since they will have neither CC nor NC interactions [42].

Fig. 3.18 quantifies this, where we show the ratio of the asymmetry in the rates for two different values of δ_{32}, for both possible modes of oscillation. Note also the relative difference visible for both these values, showing that this provides an independent handle on the value of this parameter, in addition to the sensitivity discussed in the CC mode above; However, the ability of the current detector to distinguish between upward versus downward going events, in the absence of a muon, needs more detailed simulation which is currently underway.

3.3.6 Probing CPT Violation

Atmospheric neutrinos, in conjunction with a large mass magnetised iron calorimeter can allow us to detect both the presence of CPT violation (CPTV) and putting bounds on them

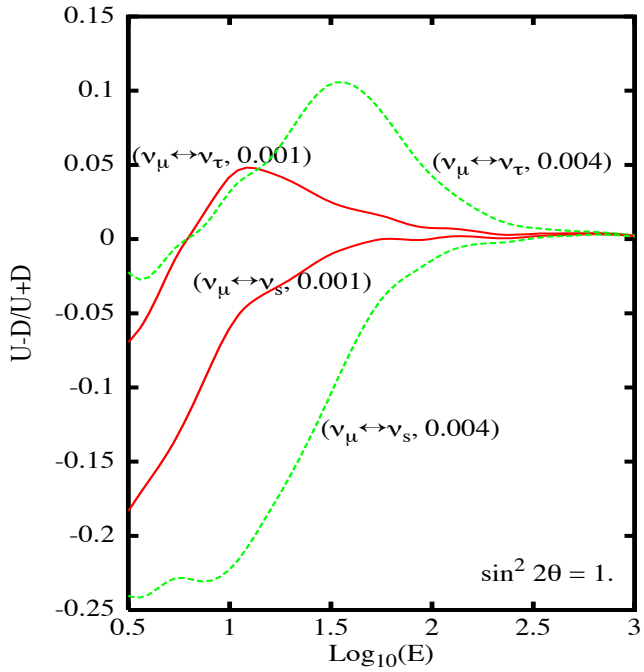

Figure 3.18: Ratio of asymmetry plotted against E (GeV) for different values of δ_{32}, for both possible modes of oscillation, $\nu_\mu \to \nu_\tau$ and $\nu_\mu \to \nu_s$.

which compare very favourably with those possible from a future neutrino factory [66].

The CPT theorem is one of the few robust predictions of relativistic local quantum field theory in flat space time which respects locality, unitarity and Lorentz symmetry. We consider the effective C- and CPT-odd interaction terms $\bar{\nu}_L^\alpha b^\mu_{\alpha\beta}\gamma_\mu \nu_L^\beta$, where α and β are flavour indices. In presence of this CPTV term, the neutrino energy acquires an additional term which comes from the matrix $b^0_{\alpha\beta}$. For anti-neutrinos, this term has the opposite sign. The expression for survival probability for the case of CPTV 2-flavour oscillations is

$$\mathrm{P}_{\mu\mu}(\mathrm{L}) = 1 - \sin^2 2\theta \, \sin^2\left[\left(\frac{\delta_{32}}{4\mathrm{E}} + \frac{\delta \mathrm{b}}{2}\right)\mathrm{L}\right], \tag{3.28}$$

where δ_{32} and δb are the differences between the eigenvalues of the matrices m^2 and b, respectively. Note that δb has units of energy (GeV). We assume equal masses for neutrinos and anti-neutrinos. For simplicity we have assumed that the two mixing angles that diagonalize the matrices m^2 and b are equal (i.e. $\theta_m = \theta_b = \theta$). In addition, the additional phase that arises due to the two different unitary matrices needed to diagonalize the δ_{32} and δb matrices[3] is set to zero. The difference between $P_{\mu\mu}$ and $P_{\bar{\mu}\bar{\mu}}$ is given by

$$\Delta \mathrm{P}^{\mathrm{CPT}}_{\mu\mu} \;=\; -\sin^2 2\theta \, \sin\left(\frac{\delta_{32}\mathrm{L}}{2\mathrm{E}}\right) \sin(\delta \mathrm{b}\mathrm{L}) \tag{3.29}$$

Observable CPTV in 2 flavour case is a consequence of interference of the CPT-even and CPT-odd terms. We focus on the survival probabilities for ν_μ and $\bar{\nu}_\mu$.

An important consequence of the modified dispersion relation in presence of CPTV is that the characteristic L/E behaviour of neutrino oscillations is lost. Hence depending on which term is larger for a given set of parameters and the energy, the mixing angle and

[3]Only one of the two phases can be absorbed by a redefinition of neutrino states.

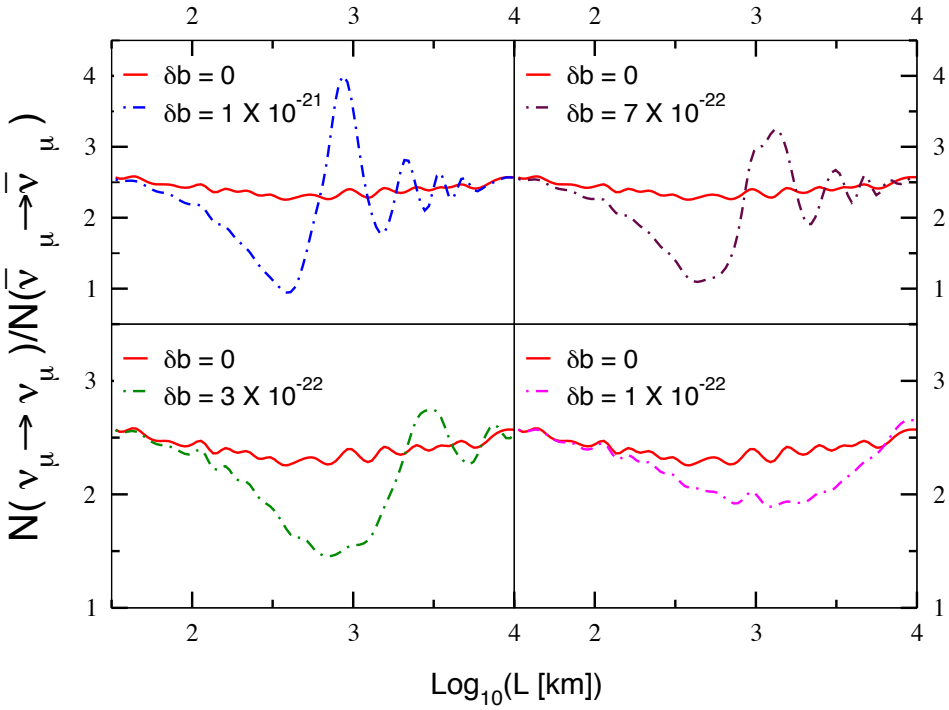

Figure 3.19: The ratio of total (up+down) muon to anti-muon events plotted against $\log_{10}(L)$ for different values of δb (in GeV). The oscillation parameters used in all the plots $\delta_{32} = 2 \times 10^{-3} eV^2$ and $\sin^2 2\theta_{23} = 1$.

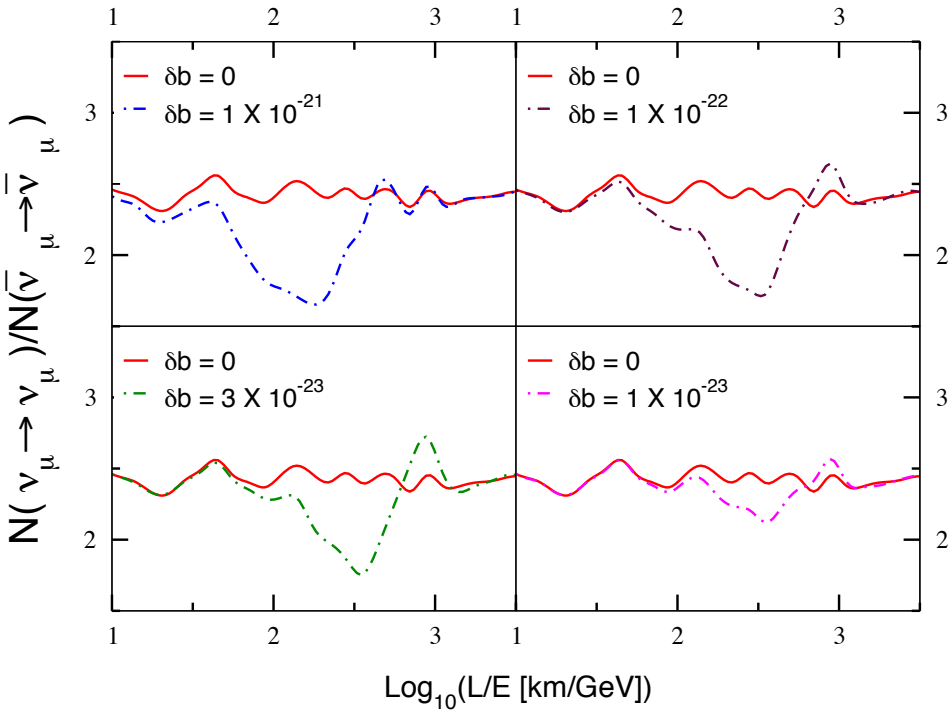

Figure 3.20: The ratio of total (up+down) muon to anti-muon events plotted against $\log_{10}(L/E)$ for different values of δb (in GeV).

oscillation length can vary dramatically with E. Thus precision oscillation measurements can set unprecedented bounds on such effects. Also, in order to see any observable effect of CPTV, one must have both CPT-even and CPT-odd terms to be non-zero.

In Fig. 3.19, we plot the ratio of muon to anti-muon events vs L using Bartol atmospheric neutrino flux. We show that (by studying the variation with L), it is possible to detect the *presence* and also obtain a *measure of the magnitude* of δb by studying their minima and zeros for $\delta b \geq 3 \times 10^{-22}$ GeV. For somewhat lower values of δb (but $\geq 3 \times 10^{-23}$ GeV), the plots vs L/E (see Fig. 3.20) indicate only the *presence* of CPTV without the same discriminating capability. The bounds that we have obtained compare very favourably with those obtained from neutrino factory [67]. We note that the value of δb compares with $\delta_{32}/2E \approx 10^{-21}$ GeV.

Our calculations indicate that *an exposure of 400 kton-years would be sufficient for statistically significant signals to emerge.* Errors for diagnostic ratios like up$(\nu_\mu + \bar{\nu}_\mu)$/down$(\nu_\mu + \bar{\nu}_\mu)$, would be smaller, requiring shorter exposure to observe a signal.

3.3.7 Constraining long-range leptonic forces

Long range forces in the context of particle physics originated with the ideas of Yang and Lee [68] and Okun [69] who proposed that gauging the baryon number or lepton number would give rise to a composition dependent long range force which could be tested in the classic Eotvos type experiments [70]. A special class of long range forces which distinguish between leptonic flavours have far reaching implications for the neutrino oscillations [71, 72] which may be used as a probe of such forces.

The Standard Model Lagrangian is invariant under four global symmetries corresponding to the Baryon and three lepton numbers $L_\alpha(\alpha = e, \mu, \tau)$. Of these, only three combinations [73] of lepton numbers (i) $L_e - L_\mu$,(ii) $L_e - L_\mu$ or (iii) $L_\mu - L_\tau$, can be gauged in an anomaly free way without extending the matter content. The existence of neutrino oscillations imply that these symmetries have to be broken but the relevant gauge bosons can still be light if the corresponding couplings are very weak. It is possible in this case to obtain light gauge boson induced forces having terrestrial range (e.g. the Sun-Earth distance) without invoking extremely low mass scales [71]. The exchange of such boson would induce matter effects in terrestrial, solar and atmospheric neutrino oscillations.

For example, the electrons inside the Sun generate a potential V_{LR} at the earth surface given by

$$V_{LR} = \alpha \frac{N_e}{R_{es}} \approx (1.04 \times 10^{-11} eV) \left(\frac{\alpha}{10^{-50}}\right) , \tag{3.30}$$

where $\alpha \equiv \frac{g^2}{4\pi}$ corresponds to the gauge coupling of the $L_e - L_{\mu,\tau}$ symmetry , N_e is the number of electrons inside the Sun and R_{es} is the Earth-Sun distance $\approx 7.6 \times 10^{26} GeV^{-1}$. The present bound on the Z-dependent force with range $\lambda \sim 10^{13}$ cm is given [70] by $\alpha < 3.3 \times 10^{-50}$. Eq.3.30 then shows that the potential V_{LR} can introduce very significant matter-dependent effects in spite of very strong bound on α. One can define a parameter

$$\xi \equiv \frac{2E_\nu V_{LR}}{\Delta m^2} ,$$

which measures the effect of the long range force in any given neutrino oscillation experiment. Given the terrestrial bound on α, one sees that ξ is given by $\xi_{atm} \sim 8.3$ in atmospheric or typical long baseline experiments while it is given by $\xi_{solar} \sim 2.3$ in case of the solar or KamLAND type experiment. In either case, the long range force would change the conventional oscillation analysis. Relatively large value of α suppresses the oscillations of the atmospheric neutrinos. The observed oscillations then can be used to put a stronger

constraints on α which were analysed in [71]. One finds the improved 90% CL bound .

$$\alpha_{e\mu} \leq 5.5 \times 10^{-52} \quad ; \quad \alpha_{e\tau} \leq 6.4 \times 10^{-52} \ , \tag{3.31}$$

in case of the $L_e - L_{\mu,\tau}$ symmetries respectively.

The parameter ξ changes the vacuum mixing angle, (mass)^2 difference and consequently also the oscillation probabilities. Considering only the $\nu_\mu - \nu_\tau$ oscillations, the survival probability for the atmospheric muon neutrinos can be written as

$$P_{\mu\mu} = 1 - \sin^2 2\tilde{\theta}_{23} \ \sin^2 \frac{\tilde{\delta}_{32} L}{4E_\nu} \tag{3.32}$$

The neutrino flight path-length L in (3.32) is related to the cosine of the zenith angle as

$$L = ((R_e + h)^2 - R_e \sin^2 \theta_z)^{1/2} - R_e \cos \theta_z \tag{3.33}$$

where $R_e = 6374$ km is the mean radius of the earth and $h \simeq 15km$ is the average height in the atmosphere where the neutrinos are produced. The effective mixing angle $\tilde{\theta}_{23}$ and mass squared difference $\tilde{\delta}_{32}$ are given in terms of the corresponding vacuum quantities by the relations

$$\tilde{\delta}_{32} = \delta_{32}((\xi_{e\tau} - \cos 2\theta_{23})^2 + \sin^2 2\theta_{23})^{1/2} \tag{3.34}$$

and

$$\sin^2 2\tilde{\theta}_{23} = \frac{\sin^2 2\theta_{23}}{((\xi_{e\tau} - \cos 2\theta_{23})^2 + \sin^2 2\theta_{23})} \tag{3.35}$$

The $\bar{\nu}_\mu$ survival probability is obtained from the ν_μ survival probability by replacing $\xi \to -\xi$ in the expressions (3.34) and (3.35). We have restricted ourselves to the $L_e - L_\tau$ symmetry for definiteness.

It is clear from the above that the long range forces introduce a (solar) matter dependent term in the oscillations probability even when U_{e3} is zero unlike in the standard case which require participation of the electron neutrino and a non-zero U_{e3} for the matter to influence the atmospheric oscillations. In the following, we neglect the ordinary matter effect assuming a vanishingly small U_{e3}.

The bounds in Eq. 3.31 represent a significant improvement over the terrestrial bound. It is possible to improve them further using future long baseline experiments [74] and using more detailed information from the atmospheric neutrino oscillations. For a range in parameters, the effect of the long range potential is different for neutrinos and anti-neutrinos. The separate determination of neutrino and anti neutrino fluxes can thus help in further probing the long range forces. The iron calorimeter (ICAL) with capabilities of identifying muon charges can provide separate measurement of the neutrino and the anti neutrino fluxes. Such detectors are proposed by the MONOLITH [42], MINOS [76] and ICAL/INO [5, 75] collaboration. As we will see, such detectors provide additional information which can allow detection of the long range forces or improvement on the constraints on the corresponding couplings.

Several features of Eqs. 3.32 allow us to identify proper variable which can lead to significant difference in the neutrino and anti neutrino oscillations.

- It follows from Eq. 3.35 that the oscillations of neutrinos and anti neutrinos are suppressed identically if θ_{23} is maximal and $\xi \geq 1$. The difference in these oscillations can arise only for the non-maximal θ_{23}.

- The down going atmospheric neutrinos which travel average distance of around 15km do not oscillate significantly due to very small path length. The presence of ξ increases the oscillation length compared to the vacuum case (roughly by a factor of 40 for $E_\nu \sim 1$ GeV and α as given by Eq. 3.31) but it is also accompanied by the suppression in the effective mixing angle. The net result is that the down going neutrinos and anti neutrinos still do not oscillate and $P_{\mu\mu}$ in Eq. 3.32 is practically one both for neutrinos and anti neutrinos. Significant difference between them arise only for the upcoming neutrinos which travel long distances.

Based on the above observations, we identify the following asymmetry[4]:

$$A = \frac{r^\nu - r^{\bar\nu}}{r^\nu + r^{\bar\nu}} \ , \tag{3.36}$$

where

$$r^{\nu,\bar\nu} \equiv \frac{\int_0^1 d\cos\theta_Z dE_\nu P^{\nu,\bar\nu}_{\mu\mu}(E_\nu,\cos\theta_z)\sigma^{\nu,\bar\nu}(E_\nu)\phi^{\nu,\bar\nu}(E_\nu,\cos\theta_z)}{\int_{-1}^0 d\cos\theta_Z dE_\nu P^{\nu,\bar\nu}_{\mu\mu}(E_\nu,\cos\theta_z)\sigma^{\nu,\bar\nu}(E_\nu)\phi^{\nu,\bar\nu}(E_\nu,\cos\theta_z)} \ , \tag{3.37}$$

where $P^\nu_{\mu\mu}$ is the survival probability given in Eq. 3.32 and the corresponding probability for anti neutrino is obtained with the replacement $\xi \to -\xi$. $\sigma^{\nu,\bar\nu}$ are neutrino cross sections and $\phi^{\nu,\bar\nu}$ are fluxes of the atmospheric $\nu_\mu, \bar\nu_\mu$. We use the Fluka-3D flux given in [77]. We consider here only multi GeV neutrinos and carry out energy integral in the range 1-100 GeV. Neutrino cross section in this range are taken proportional to neutrino energy which is a fairly good assumption [78].

We show in Fig. 3.21 the absolute value of A (in %) as a function of the long range coupling constant α.

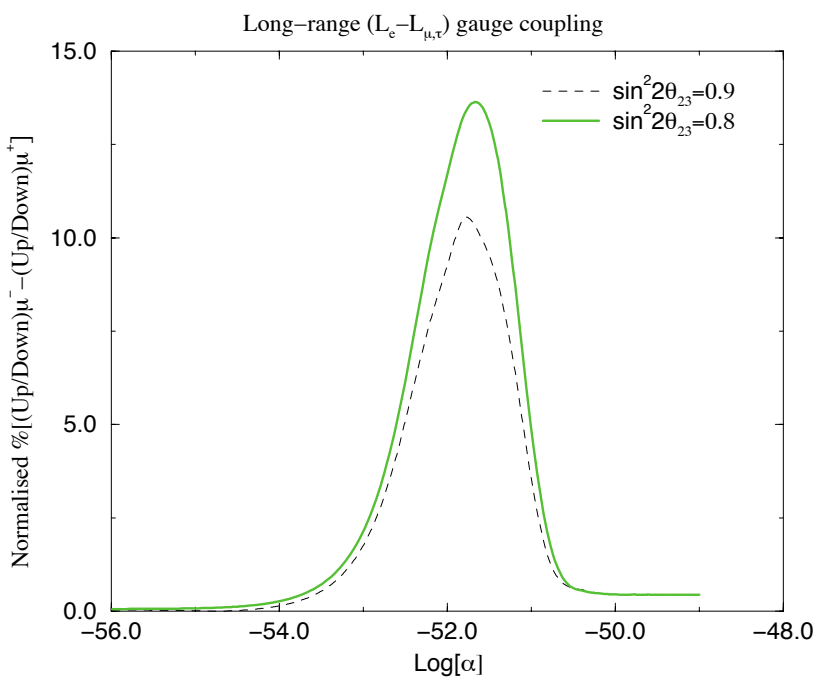

Figure 3.21: The neutrino-anti-neutrino asymmetry as a function of the $L_e - L_{\mu,\tau}$ coupling $\alpha \equiv g^2/4\pi$. The plots show the percentage asymmetry for different $\sin^2 2\theta_{23}$ and with $\delta_{32} = 3 \times 10^{-3}$ eV^2.

For definiteness, we have assumed $L_e - L_\tau$ symmetry and assumed normal mass ordering with $\delta_{32} = 3.0 \times 10^{-3}$ eV^2. A is very small for relatively large or small values of α. For

[4]A similar asymmetry has also been studied in the context of the ordinary matter effects in [60]

smaller α the long range force is negligible and neutrino and anti neutrinos oscillations are identical giving very small A. For relatively larger α, the $\cos 2\theta_{23}$ term in Eqs. 3.34, 3.35 is negligible and the long range force cannot distinguish between neutrino and anti neutrino resulting once again in very small A. The sizable effect of the long range forces on A occur for $\alpha \approx 10^{-51} - 10^{-53}$. In this range, A can be quite large, *e.g.*, even for an order of magnitude smaller α than the bound in Eq. 3.31, one can get very large asymmetry $A \geq 5\%$. Such a large value indicates that the ICAL detector has the potential to improve the bounds on α obtained without considering the charge separation. Observability of this relatively large asymmetry will depend on the details of the detectors and it would be worthwhile to do this analysis in the context of possible detectors at INO.

3.4 Neutrino Factories

The possibility of neutrino beams from muon storage rings has received a lot of attention in the recent literature [79]. Such facilities provide intense, controlled high luminosity neutrino beams that are almost pure $\nu_\mu + \bar{\nu_e}$ or $\nu_e + \bar{\nu_\mu}$ depending on the sign of the stored muon.

A neutrino beam from such a neutrino factory with a muon storage ring will contain equal amounts of e and μ flavours. For example, a μ^- beam will give equal amounts of ν_μ and $\overline{\nu_e}$ in the neutrino beam. Also, the fluxes of each flavour are precisely calculable [80]. The angular resolution of the beam is dominated by divergence due to decay kinematics. An angular precision of about 20 μr is feasible with a spatial resolution of about 500 microns, so that a beam size of about 1 km is achieved on the far side, at the detector. Also, a compact size (about 150 m circumference for a 20 GeV muon beam) implies that the whole instrument can be tilted with respect to the horizontal, an essential requirement for long baseline beams.

The main advantage of knowing the composition of beams from neutrino factories is that a primary signal for neutrino oscillation is *the detection of wrong-sign* muons. For example, if the original beam composition is ν_e and $\overline{\nu_\mu}$, then the CC interaction of the latter in the detector gives μ^+. However, the oscillation of ν_e as $\nu_e \to \nu_\mu$ results in a CC interaction with μ^- being produced. Hence, charge identification is a primary requirement of any far-end detector. Of course, a near-detector is essential for flux normalisation as well. The detector must be sensitive to electrons or muons or both.

ICAL at INO will be an admirable choice as a detector for a very long baseline experiment, with a source either in CERN, Geneva, or in KEK, Japan, or even in Fermilab, U.S.A. (see Table 3.5. Such a long baseline will therefore provide one of the largest possible L/E ratios where the neutrino will traverse a significant length inside the Earth's core. With its charge discrimination capability, a magnetised iron calorimeter offers unique capabilities to exploit the physics potential of such sources.

Fermilab to	JHF to	CERN to
Soudan (735)	Super-K (295)	Frejus (150)
Homestake (1290)	Beijing (1952)	Gran Sasso (730)
PUSHEP (11300)	**PUSHEP (6556)**	**PUSHEP (7145)**
Rammam (10480)	Rammam (4828)	Rammam (6871)

Table 3.5: Some possible baselines (in km) and source/detector combinations for neutrino factory experiments. Also included are the baselines to two possible sites for INO in Rammam and PUSHEP in India. PUSHEP, which has since been chosen as the preferred location, has close to magic baselines from JHF and especially CERN.

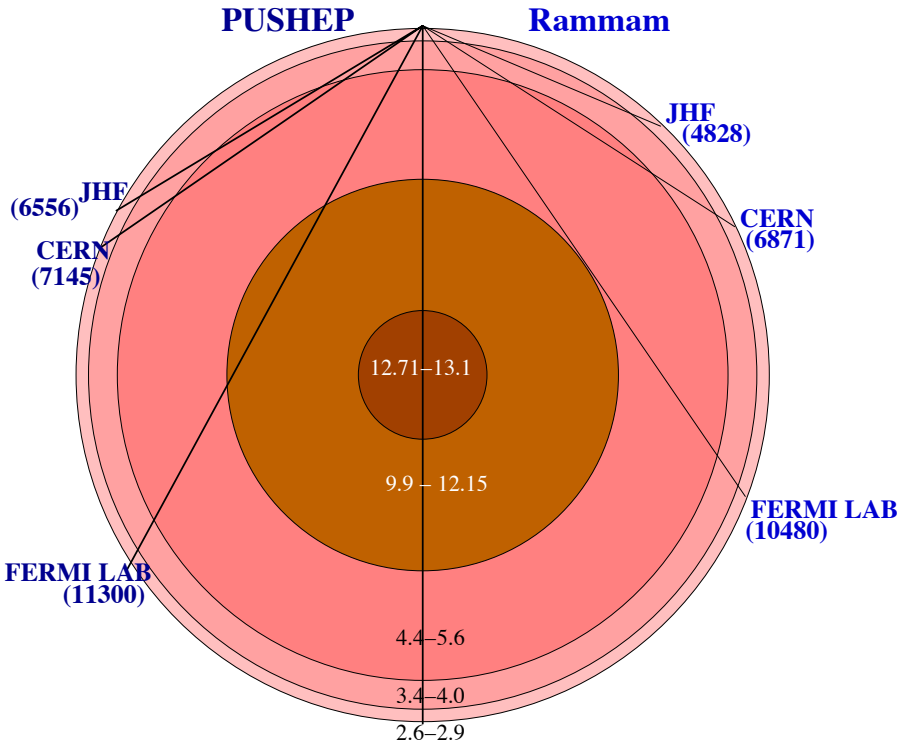

Figure 3.22: Base lengths (km) from the proposed neutrino factories to the two proposed INO sites in India: Left half shows the base lengths to the site at PUSHEP whereas the right-half shows the base lengths to the site at Rammam. The densities of the layers that the neutrinos pass through are also indicated.

As is well understood by now, the high purity, high intensity neutrino beams may provide the best and cleanest, if not the only way to achieve at least three goals mentioned above. While the determination of mass ordering seems to be rather straight forward, determination of θ_{13} and δ are sensitive to the baseline chosen. Many neutrino factory locations and corresponding end-detector sites are under consideration all around the world. In what follows, we explore the physics discovery potential of a ICAL at INO, when used as an end detector for a neutrino factory beam originating from the Japan Hadron Facility at Jaeri (JHF) and another from Fermilab, USA.

There are two possible locations in India. One is at PUSHEP in southern part of India. The other one is at Rammam in north-eastern part. PUSHEP has since been selected as the preferred site for INO. Typical baselines from the existing and proposed neutrino factories to the two possible sites for INO are shown in Fig. 3.22. There are two base lengths of around 7000 km—CERN (JHF) to PUSHEP and CERN to Rammam which are very close to the so called *magic baseline* of 7200 km since at this distance the CP-violating term is absent. This baseline therefore allows a clean determination of θ_{13}.

Kinematic cuts

We assume a muon energy resolution of within 5%, and for calculations where the muon detection threshold is fixed, we have assumed it to be 2 GeV.

It is also important here to discuss about the general backgrounds in such experiments. Backgrounds to wrong-sign muon signals arise from the following:

1. In the neutral current interactions, wrong sign muons are products of the decays of produced pions and kaons.

2. In the charged current interactions, if the primary muon is "lost" in the detector, then a wrong sign muon produced in charm, pion and kaon decays would constitute a background.

In long-baseline studies, such backgrounds can be significantly reduced by a transverse momentum, p_T^2 cut, and we employ a cut of 2 GeV^2. The backgrounds fall sharply as a function of energy, and are at the level of 10^{-2} at a muon threshold energy of 2 GeV, and fall to less than 10^{-4} at $E_\mu^{th} = 5$ GeV. We conservatively assume a background of 10^{-1} over the entire energy spectrum of the neutrinos. We do assume a 100% charge identification efficiency, and a perfect muon identification capability once the cuts and background are put in. This is based on the assumption that the segmentation of the detector is fine enough to almost always determine whether a charged muon track has penetrated the detector beyond the reach of the hadronic shower produced in the interaction.

In general, we note here that an NC event is identifiable by the absence of a charged muon track and the presence of large (hadronic) shower energy deposited in a small calorimeter area. The CC events are identified by the same hadronic characteristics accompanied by a long muon track which penetrates much beyond the shower. We assume for now that the detector segmentation cannot resolve CC electron/positron events, and as such they are indistinguishable from NC events.

In what follows we do not assume electron/positron detection capability. Although this may be an attractive addition to consider for future studies since it would enhance the overall physics program possible, albeit at higher cost due to the increase in sensitive elements necessary.

3.4.1 Determination of θ_{13}

The first set of calculations we have performed explore the reach for θ_{13}. We recall that the CHOOZ bound on this parameter is $sin^2 2\theta_{13} < 0.1$. Its importance lies in it being the driving parameter for $\nu_e \to \nu_\mu$ oscillations, and for CP violation searches. We stress that this is true with or without matter effects. The next generation of experiments will thus have its determination as one of the primary goals.

Figure 3.23 demonstrates the achievable values of $\sin\theta_{13}$ versus the muon detection threshold energy of the detector. The reach is determined as the value which is necessary to collect 10 signal events for a given kton-year exposure. We show the reach capabilities for an entry-level configuration ($E_\mu^{th} = 20$ GeV, 10^{19} decays per year). For the median exposure of 50 kton-years, at a muon detection threshold of 2 GeV, the reach corresponds to $\sin\theta_{13} = 0.038$ ($\sin^2 2\theta_{13} = 0.0057$) for Rammam and a slightly higher value of 0.04 for PUSHEP, as shown. The *reach* values improve to $\sin\theta_{13} = 0.026$ ($\sin^2 2\theta_{13} = 0.0027$) for Rammam if the energy of the beam is increased to 50 GeV, keeping other variables the same as before, with only a marginal improvement to $\sin^2\theta_{13} = 0.037$ for PUSHEP. In all of the above, the "passive" parameters $\delta_{32}, \delta_{21}, \sin^2 2\theta_{23}$ and $\sin^2 2\theta_{12}$ are held to their (best-fit) values specified above.

A second method of obtaining a *measure* of θ_{13} is via matter effects which show up once the baselines are long. In particular, the total wrong-sign muon rate varies measurably with θ_{13}, as demonstrated in Fig. 3.24 for the Fermilab–PUSHEP baseline. Here the number of such events are shown as a function of E_ν/δ_{32} for a neutrino factory with 10^{21} muon decays/year. Clearly, a measure of this important parameter, even if it is small, is possible

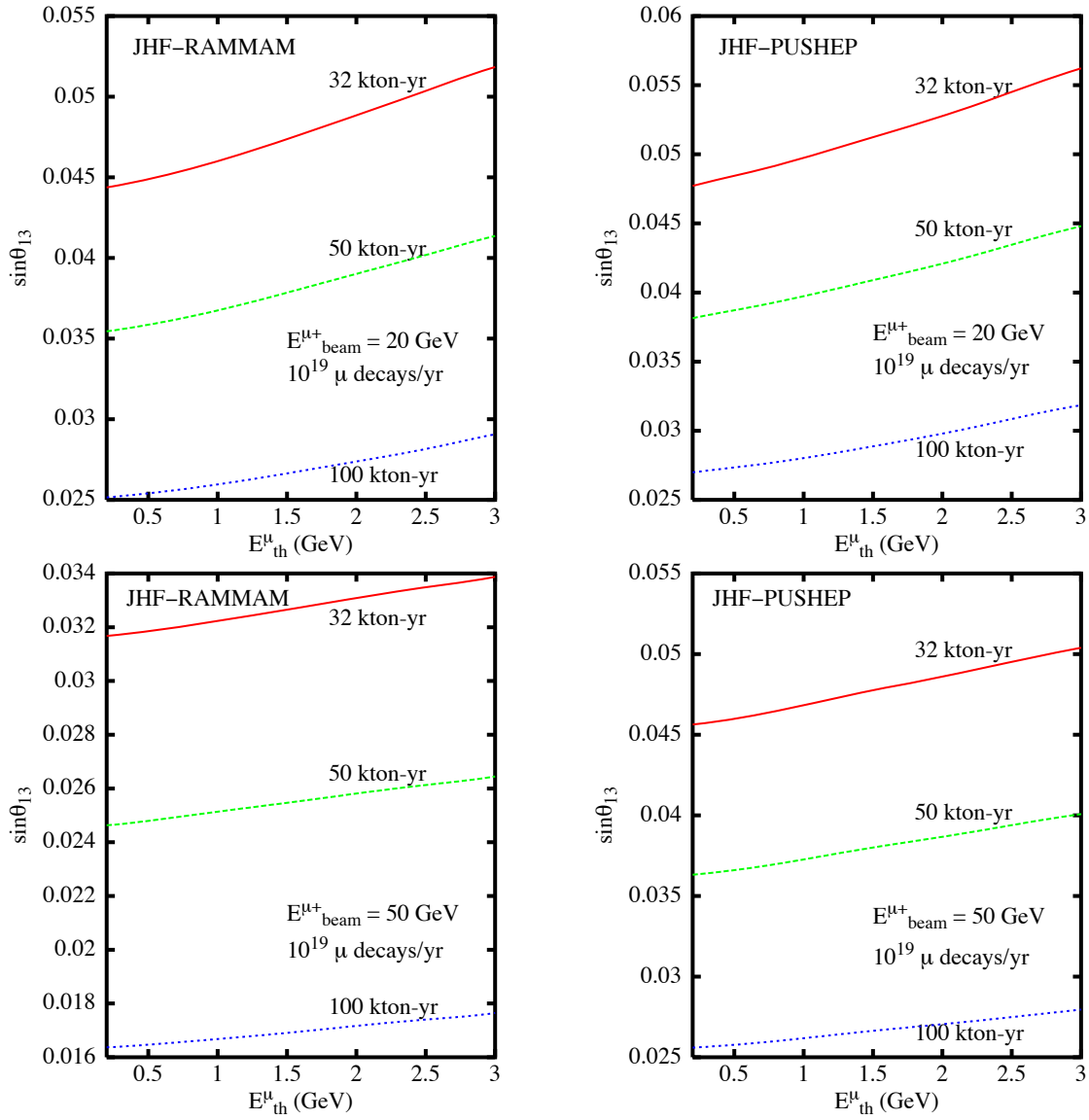

Figure 3.23: The $\sin\theta_{13}$ reach for detector exposures of 32 kton-year, 50 kton-year and 100 kton-year for an entry-level neutrino factory configuration with $E_\mu^{beam} = 20$ GeV for the JHF-Rammam and the JHF-PUSHEP baseline. The lower panels show the change in reach if the storage muon energy is increased to 50 GeV, keeping the number of decays per year the same, i.e, 10^{19}/year; there is substantial improvement in the reach in the case of the JHF-Rammam baseline.

via this method. Note that the event-rate peaks nicely for neutrinos in the 10-20 GeV range for the currently allowed and favoured range of values of δ_{32} from atmospheric neutrino data.

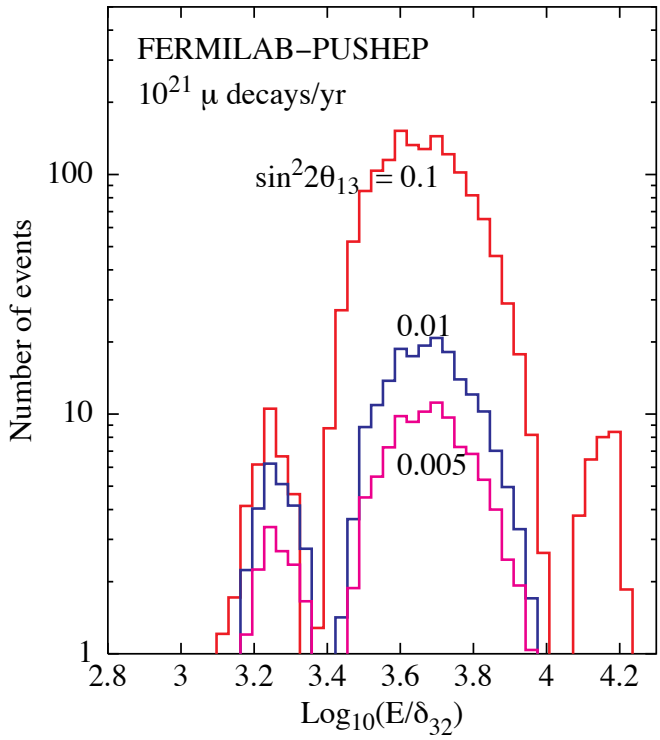

Figure 3.24: The number of wrong-sign muon events as a function of E_ν/δ_{32} (GeV/eV^2) for the Fermilab–PUSHEP baseline. The dip to the left of the distribution is due to a minimum of the oscillation probability.

3.4.2 Sign of δ_{32}

We next examine the capability to determine the sign of E_ν/δ_{32} that these baselines offer. This is sensitive once again to the wrong-sign muon rate generated by $\nu_e \to \nu_\mu$ oscillations. For small θ_{13}, and if the matter potential $A \sim E_\nu/\delta_{32} > 0$, then matter effects lead to an enhancement of $\nu_e \to \nu_\mu$ and a suppression of $\bar{\nu_e} \to \bar{\nu_\mu}$. The converse is true if the sign of $A \sim E_\nu/\delta_{32}$ is reversed.

Figure 3.25 shows the sign discrimination capability for an entry-level neutrino factory configuration with an exposure of 32 kton-years. For both the Rammam and PUSHEP baselines, the sign dependent difference in event rates is easily measurable in terms of wrong sign muon events. For comparison, we also show the difference in event-rates for a JHF–Beijing baseline (1952 km) where a far-end detector is under consideration. Figure 3.26 shows the improvement (or rather, the overkill) possible with an upgraded factory yielding 10^{21} decays per year with a beam energy of 50 GeV for an increased exposure of 50 kton-years.

3.4.3 Probing CP violation in the leptonic sector

We next examine the discovery potential for what many consider as the holy grail of physics in the lepton sector, i.e. the presence or absence of CP violation. In the standard three generation scenario, this is parametrised by a single phase δ in the lepton mixing matrix.

In principle, rates for particles and their CP conjugates will exhibit a difference stemming from terms proportional to $\sin\delta$ in the oscillation probability. Generally, these differences

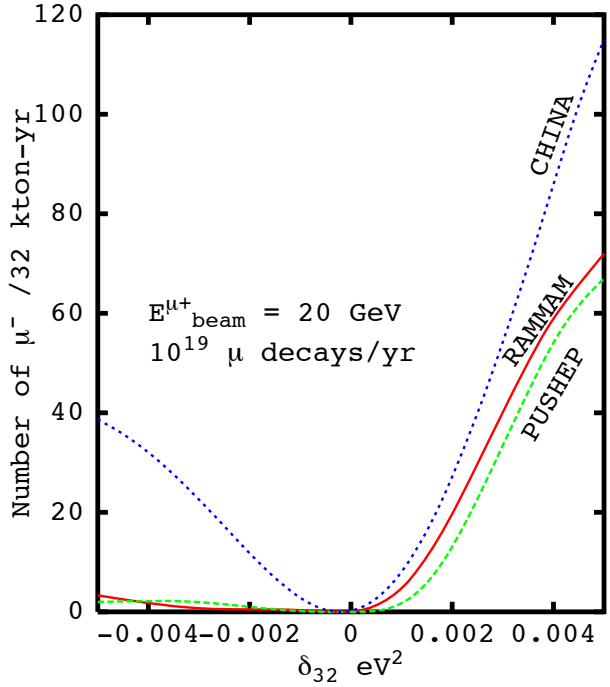

Figure 3.25: The number of wrong-sign muon events as a function of δ_{32} for the three baselines from JHF, demonstrating the sign discriminating capability which arises as a result of matter effects. Event rates are computed for an entry-level configuration with a 32 kton-year exposure, beam energy of 20 GeV and 10^{19} decays per year.

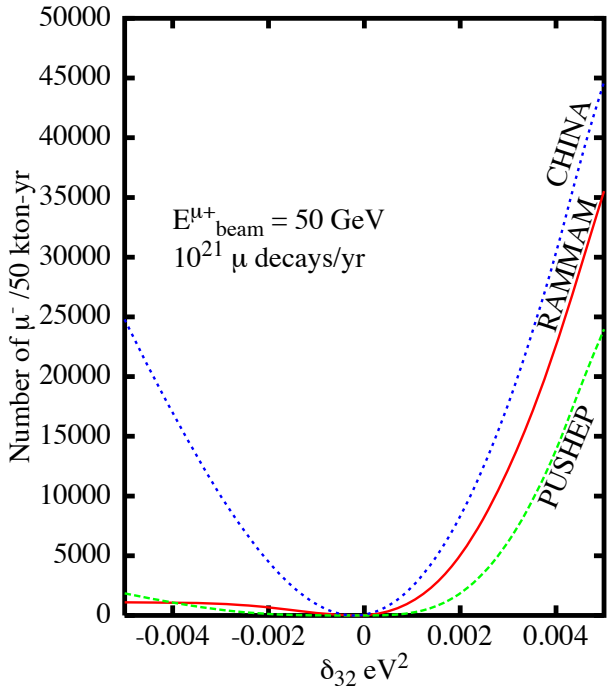

Figure 3.26: The same as Fig. 3.25, but for an upgraded neutrino factory configuration with a 50 kton-year exposure, 10^{21} decays per year and a beam energy of 50 GeV.

are small and difficult to disentangle from matter oscillation effects, which in long baseline situations dominate small differences due to non-vanishing of the CP phase. The sensitivity to the CP phase also depends on the actual values of $\sin^2 2\theta_{13}, \delta_{21}$, the energy and baseline, among other parameters, besides of course on the magnitude of $\sin\delta$.

One possible clean signature is the ratio of wrong sign muon events for equal exposures when the neutrino factory runs with muons and anti-muons stored in the ring in turn. Thus for stored muons with a negative charge, one expects $\bar{\nu_e} \to \bar{\nu_\mu}$ oscillations to produce CC induced muons with a positive charge in the detector, and vice-versa for a run with stored μ^+ in the ring.

In Fig. 3.27 we show (as a function of baseline length) the ratio of wrong-sign muon events for a run with negatively charged muons in the storage ring (and, hence, the resultant μ^+ events due to oscillations, denoted by $N(\mu^+)$) to that for a run with positively charged muons (yielding μ^- events via oscillations, denoted by $N(\mu^-)$). The calculations are performed for a factory with a beam energy of 20 or 50 GeV and a muon decay yield of 10^{21} decays per year. In the top left panel, a value of $\sin\theta_{13} = 0.1$ ($\sin^2 2\theta_{13} = 0.04$) has been assumed, along with a run of 1 year each of either sign of stored muon, and a detector mass of 32 kton. Note that the anti-neutrino cross-sections are about a factor of two smaller than the neutrino cross-sections. The dashed curves are for $\delta = \pm\pi/2$ and the data points show the values (along with statistical errors) for no CP violation ($\delta = 0$) for the Beijing, Rammam and PUSHEP baselines respectively.

The two sets of curves (upper and lower) correspond to opposite signs of δ_{32}, which reflect the effects of matter. We note that CP effects tend to cancel (i.e., are small) for this configuration at PUSHEP; hence the measurements there afford an opportunity to effectively isolate and measure the matter effects. Such measurements can be used in conjunction with measurements at a baseline where CP effects are relatively large and afford a cleaner discrimination between $\delta = 0$ and a non-zero value of this parameter. This is exemplified in the top right panel of Fig. 3.27 which uses a higher beam energy of 50 GeV and a slightly more massive detector of 50 ktons.

The Rammam baseline offers an opportunity to detect the presence of a δ which is different from zero, especially as exposure (in kton-year) and statistics improve. The bottom panels of Fig. 3.27 show the CP capabilities for the same two configurations but for a lower value of $\sin\theta_{13}$, namely 0.03. Note that both our chosen values of this parameter are well below the current CHOOZ bound. The conclusions for both Rammam and PUSHEP are similar to the ones above. The former provides us with an opportunity to measure the presence of a non-zero CP violation, while the latter provides us an opportunity to separate matter effects from the CP violation contributions in conjunction with another long-baseline experiment.

Finally in Fig. 3.28, we have presented the CP capabilities, for baseline lengths corresponding to PUSHEP to Fermilab and Rammam to Fermilab. The input parameters remain the same as the other set of plots. For comparison we have presented the same numbers for the baselines corresponding to JHF–Rammam and JHF–PUSHEP again.

3.5 Large matter effects in $\nu_\mu \to \nu_\tau$ oscillations

The $\nu_\mu \to \nu_\tau$ oscillation probability $P_{\mu\tau}$ can also undergo significant change (a reduction as high as $\sim 70\%$ or an increase of $\sim 15\%$) compared to its vacuum values over an observably broad band in energies and baselines due to matter effects. This can be directly observed in detectors that have tau detection capability. Such effects induce appreciable changes in the muon neutrino survival probability $P_{\mu\mu}$ in matter [81] discussed earlier.

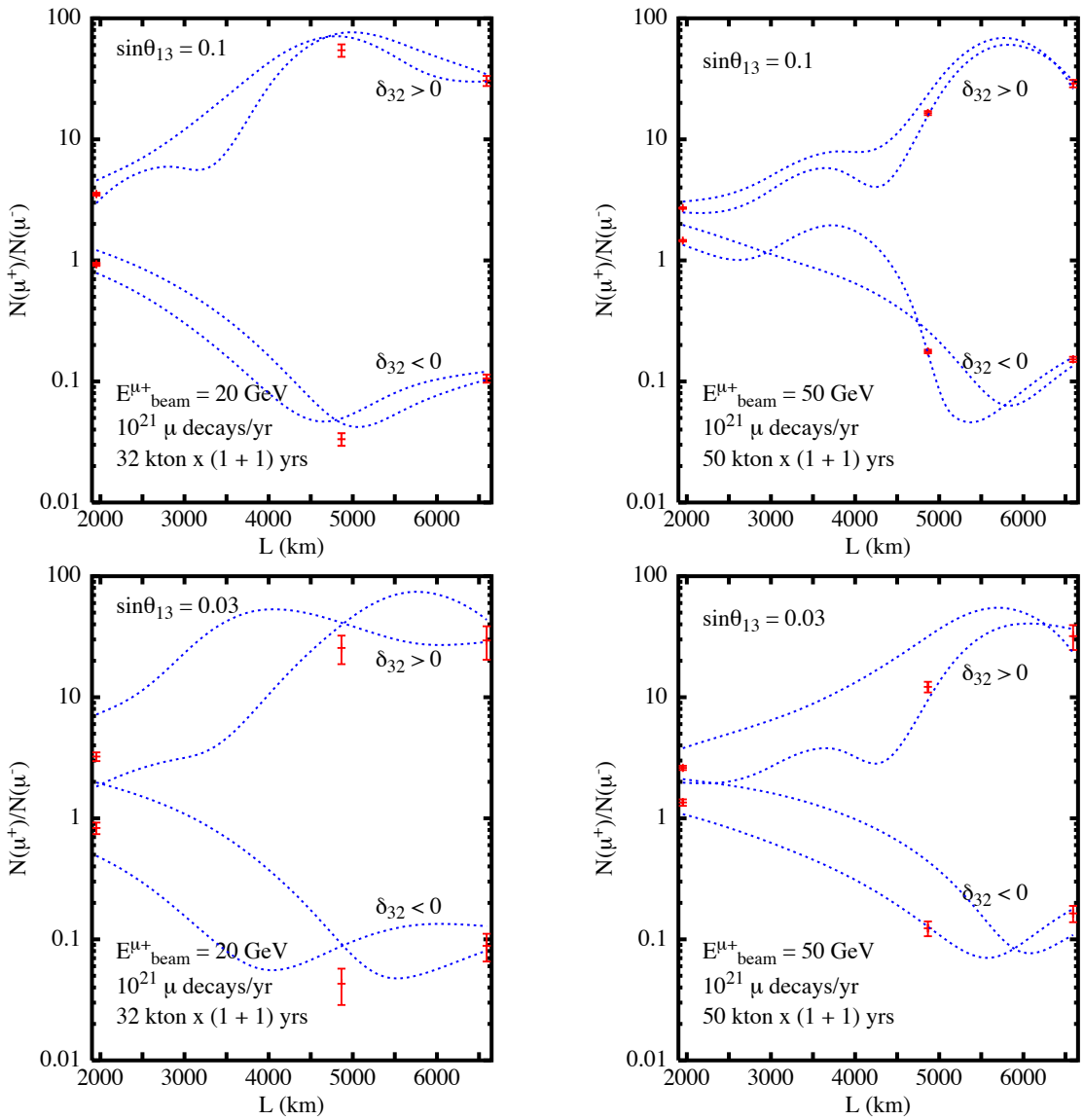

Figure 3.27: The ratio of wrong-sign muon events for equal-time runs of opposite sign muons and $\delta = \pm\pi/2$ (dashed curves) and $\delta = 0$ (data points, with statistical error bars) in the storage ring, versus base-length. All plots correspond to 10^{21} μ decays per year. The top row shows the results for $\sin\theta_{13} = 0.1$ ($\sin^2 2\theta_{13} = 0.04$) and 10^{21} decays per year, with beam energies of 20 GeV in one case and 50 GeV in the other. The bottom row shows the results when $\sin\theta_{13} = 0.03$ ($\sin^2 2\theta_{13} = 0.0036$). The positions of the data points reflect the base-lengths for detector locations at Beijing, Rammam and PUSHEP in order of increasing length.

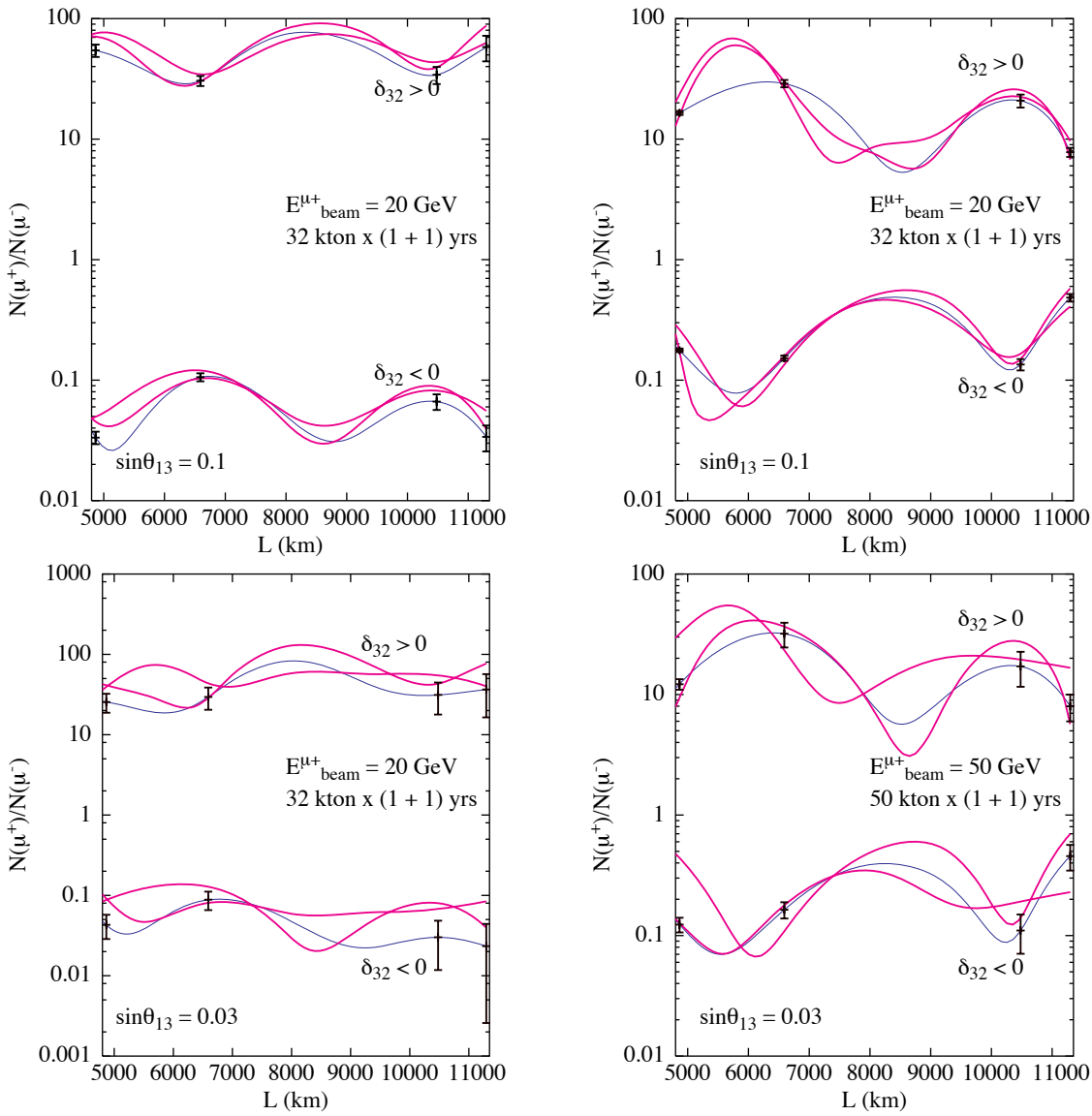

Figure 3.28: The same as Fig. 3.27, but for baselines corresponding to Fermilab–PUSHEP and Fermilab–Rammam along with the same ratios for JHF to the two proposed Indian sites. All other parameters are indicated in the plots. The data points with the sharp line through them are for $\delta = 0$. The other lines are for $\delta = \pm\pi/2$.

The muon survival rate is the primary observable in iron calorimeter detectors like MINOS [76] and the proposed MONOLITH [42] and INO [5] and a major constituent of the signal in Super-K [82], the planned BNL-Homestake [83] large water Cerenkov detector, and several detectors considered for future long baseline facilities. The τ appearance rate as a signal for matter effects can also be searched for in special τ detectors being thought of for neutrino factories [79]. We show that the energy ranges and baselines over which these effects occur are relevant for both atmospheric [84] and beam source neutrinos for the above experiments. Since all matter effects sensitively depend on the sign of δ_{32} and on θ_{13}, observation of the effects discussed here would provide information on these important unknowns.

Our discussion below uses the approximation of constant density and sets $\delta_{21} \equiv \delta_{sol} = 0$. Consequently the mixing angle θ_{12} and the CP phase δ drop out of the oscillation probabilities. This simplifies the analytical expressions and facilitates the qualitative discussion of matter effects. We consider matter effects in neutrino probabilities only but discuss both the cases $\delta_{32} = \pm|\delta_{32}|$. We find that for neutrinos dramatic matter effects occur only for $\delta_{32} > 0$.

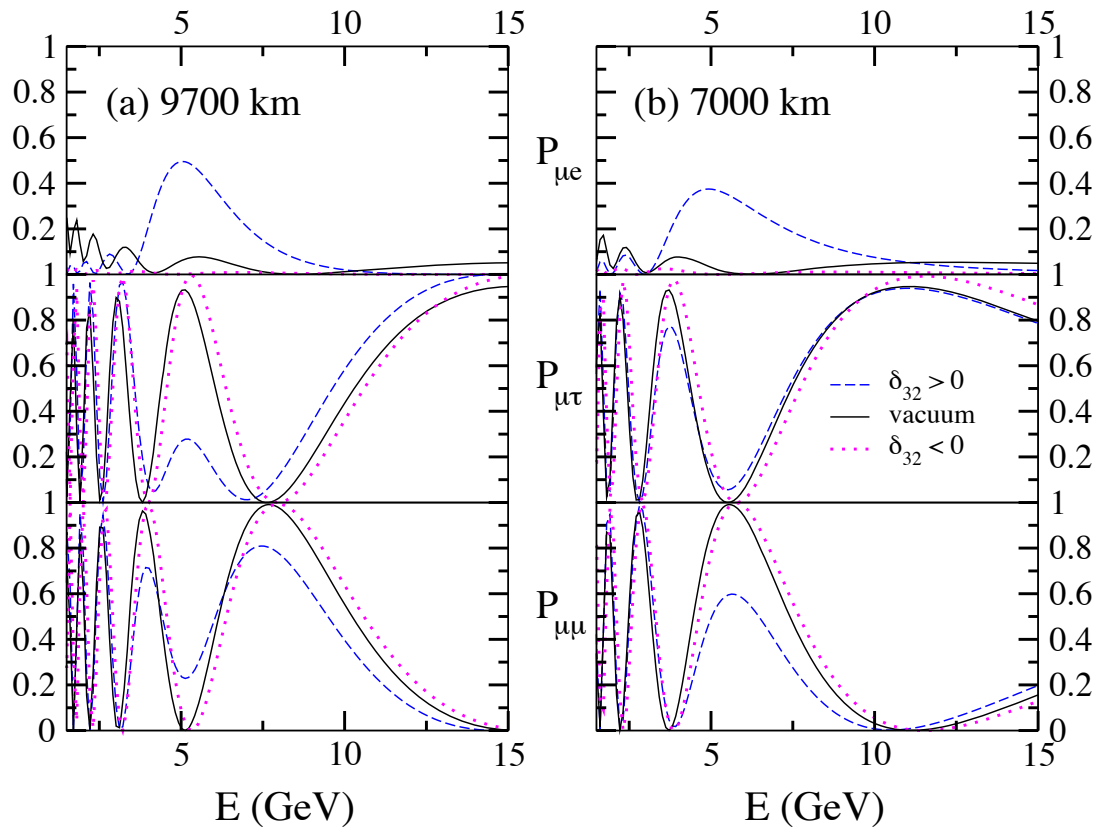

Figure 3.29: $P_{\mu e}$,$P_{\mu\tau}$ and $P_{\mu\mu}$ plotted versus neutrino energy,E (in GeV) in matter and in vacuum for both signs of δ_{31} for two different baseline lengths, (a) for L= 9700 km and (b) for L= 7000 km. These plots use $\delta_{32} = 0.002$ eV^2 and $\sin^2 2\theta_{13} = 0.1$.

In vacuum we have

$$\begin{aligned} P^{vac}_{\mu\tau} &= \sin^2 2\theta_{23} \cos^4 \theta_{13} \sin^2 (1.27\delta_{32} L/E), \\ &= \sin^2 2\theta_{23} \cos^2 \theta_{13} \sin^2 (1.27\delta_{32} L/E) - \cos^2 \theta_{23} P^{vac}_{\mu e} \end{aligned} \tag{3.38}$$

Including the matter effects changes this to

$$P^{m}_{\mu\tau} = \cos^2 \theta^m_{13} \sin^2 2\theta_{23} \sin^2 [1.27(\delta_{32} + A + \delta^m_{31}) L/2E]$$

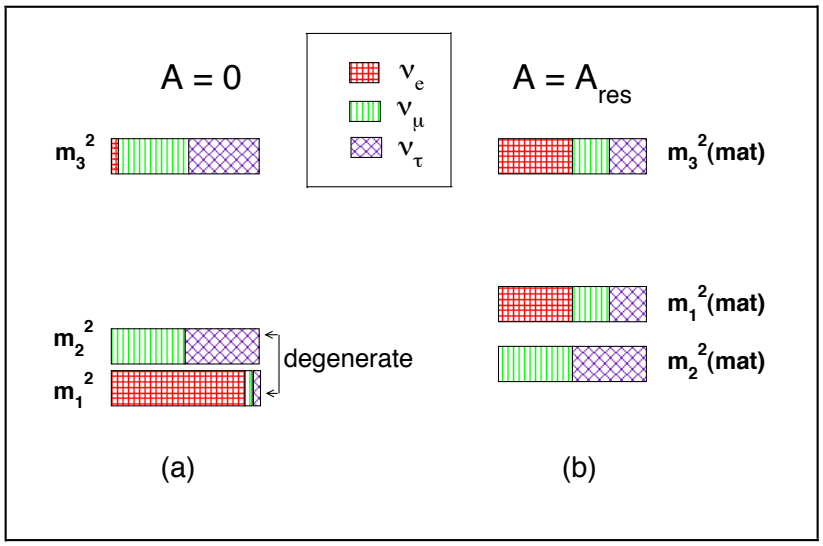

Figure 3.30: The flavour composition of mass eigenstates in vacuum ($A = 0$) and in matter at resonance ($A = A_{res}$). The vacuum parameters used are $sin^2 2\theta_{23} = 1.0$ and $sin^2 2\theta_{13} = 0.1$.

$$\begin{aligned} &+ \quad \sin^2\theta_{13}^m \sin^2 2\theta_{23} \sin^2\left[1.27(\delta_{32} + A - \delta_{31}^m)L/2E\right] \\ &- \quad \cos^2\theta_{23} P_{\mu e}^{mat} \end{aligned} \tag{3.39}$$

Compared to $P_{\mu e}^m$, the matter dependent mass eigenstates here have a more complicated dependence on the ν_μ and ν_τ flavour content. Labelling the vacuum mass eigenstates as ν_1, ν_2 and ν_3, in the approximation where $\delta_{21} = 0$, ν_1 is almost entirely ν_e and ν_2 has *no* ν_e component. This is depicted in figure 3.30. Inclusion of the matter term A leaves ν_2 untouched but gives a non-zero matter dependent mass to ν_1. As the energy increases, the ν_e component of ν_1^m decreases and the ν_μ, ν_τ components increase such that at resonance energy they are 50%. Similarly, increasing the energy increases the ν_e component of ν_3^m (and reduces ν_μ, ν_τ components) so that at resonance it becomes 50%. Thus in the resonance region, all three matter dependent mass-eigenstates ν_1^m, ν_2^m and ν_3^m contain significant ν_μ and ν_τ components. Hence, the matter dependent $\nu_\mu \to \nu_\tau$ oscillation probability will depend on all three matter modified mass-squared differences. We seek ranges of energy and path lengths for which there are large matter effects in $P_{\mu\tau}$, i.e for which $\Delta P_{\mu\tau} = P_{\mu\tau}^{mat} - P_{\mu\tau}^{vac}$ is large. We show that this occurs for two different sets of conditions, leading in one case to a *decrease* from a vacuum maximum and in another to an *increase* over a broad range of energies.

We identify the baseline and energy ranges where the matter effects in $\nu_\mu \to \nu_\tau$ oscillations will be maximal. The criterion for maximal matter effect, $E_{res} \simeq E_{peak}^{vac}$, leads to the following condition:

$$\rho L_{\mu\tau}^{max} \simeq (2p+1)\,\pi\, 5.18 \times 10^3\,(\cos 2\theta_{13}) \;\; \text{km gm/cc} \; . \tag{3.40}$$

Note that Eq. 3.40 has a much weaker dependence on θ_{13}. This enables one to go to a higher value of p without exceeding the baselines relevant for observing earth matter effects. From Eq. 3.40, for $p = 1$ and $\sin^2 2\theta_{13} = 0.1$ ($0.2, 0.05$), $E_{res} = E_{peak}^{vac}$ occurs at $L \sim 9700$ km (9300 km, 9900 km). For $p = 0$, Eq. 3.40 gives $L_{\mu\tau}^{max} \sim 4400$ km for $\sin^2 2\theta_{13} = 0.1$. However, $\Delta P_{\mu\tau}$ is roughly one-tenth of the $p = 1$ case. In general, for a given baseline, the choice of an optimal p is also dictated by the constraint that the vacuum peak near resonance have a width which makes the effect observationally viable.

In Fig. 3.29(a) we show all three matter and vacuum probabilities for 9700 km. In these plots δ_{32} is taken as 0.002 eV^2 which gives $E_{res} = E^{vac}_{peak} \sim 5$ GeV. The middle panel of Fig. 3.29(a) shows that near this energy $P^{mat}_{\mu\tau}$ (~ 0.33) is appreciably lower compared to $P^{vac}_{\mu\tau}$ (~ 1).

In Fig. 3.31 we show the θ_{13} sensitivity of $P^{mat}_{\mu\tau}$ at 9700 km. In particular, at $E_{res} \simeq E^{vac}_{peak}$ the strong dependence on θ_{13} can be seen. Unlike $P^{mat}_{\mu e}$, where the event-rate decreases as θ^2_{13} for small values of θ_{13}, the τ appearance rate at $E_{res} = E^{vac}_{peak}$ increases with decreasing θ_{13}. As $\sin^2 2\theta_{13}$ goes from 0.2 to 0, $P^{mat}_{\mu\tau}$ varies from a value ~ 0.05 to ~ 1. For very small values of $\sin^2 2\theta_{13}(< 0.05)$ it will be impossible to see a resonance enhancement in $P_{\mu e}$ because the distance for which this occurs exceeds the diameter of the earth. However, the observation of resonant suppression in $P_{\mu\tau}$ is possible, even for very small values of θ_{13}, if the criterion, $N_\tau(\theta_{13} = 0) - N_\tau(\theta_{13}) \geq 3(\sqrt{N_\tau(\theta_{13} = 0)} + \sqrt{N_\tau(\theta_{13})})$, is satisfied for the tau event rate.

It is also possible for $P^{mat}_{\mu\tau}$ to differ appreciably from $P^{vac}_{\mu\tau}$ away from resonance. This is evident in Fig. 3.29 (a) (central panel) in the energy range 7.5–15 GeV. This effect is an enhancement rather than a drop, *i.e.*, $\Delta P_{\mu\tau}$ is now positive. Specialised τ detectors operating in long baseline scenarios such as neutrino factories [79] should be able to observe effects like the ones discussed above. Also the large effects in $P^{mat}_{\mu\tau}$ discussed above can give rise to observably large effects in muon survival probabilities as is discussed below.

The deviation of $P^{mat}_{\mu\mu}$ from $P^{vac}_{\mu\mu}$ results from the combined effects in $P^{mat}_{\mu\tau}$ and $P^{mat}_{\mu e}$ *i.e.*, $\Delta P_{\mu\mu} = -\Delta P_{\mu\tau} - \Delta P_{\mu e}$. where, $\Delta P_{\mu e} = P^{mat}_{\mu e} - P^{vac}_{\mu e}$. For instance if, $\Delta P_{\mu\tau}$ is large and negative while $\Delta P_{\mu e}$ is positive, they do not contribute in consonance. However, the resulting change in $\mathrm{P}_{\mu\mu}$ is still large, given the magnitude of the change ($\approx 70\%$) in $\mathrm{P}_{\mu\tau}$. This is visible in the bottom panel of Fig. 3.29(a), in the energy range 4–6 GeV.

One also expects a significant drop in $P^{mat}_{\mu\mu}$ when either of $\Delta P_{\mu\tau}$ or $\Delta P_{\mu e}$ is large and the other one is small. The first of these cases ($\Delta P_{\mu\tau}$ large, $\Delta P_{\mu e}$ small) is shown in Fig. 3.29(a) in the energy range $\sim$ 6–15 GeV, with the enhancement in $P^{mat}_{\mu\tau}$ reflected in the decrease in $P^{mat}_{\mu\mu}$. The second case (small $\Delta P_{\mu\tau}$, large $\Delta P_{\mu e}$) occurs when a minimum in the vacuum value of $P_{\mu\tau}$ resides in the proximity of a resonance, and even the rapid changes in $\sin^2\theta^m_{13}$ and $\cos^2\theta^m_{13}$ in this region fail to modify this small value significantly. This condition can be expressed as $1.27\delta_{32}L/E = p\pi$. Note that this corresponds to a vacuum peak of $P_{\mu\mu}$. Substituting E as E_{res} gives the distance for maximum matter effect in $P_{\mu\mu}$ as

$$\rho L^{max}_{\mu\mu} \simeq p\,\pi\ \times 10^4\,(\cos 2\theta_{13})\ km\ gm/cc\ . \tag{3.41}$$

For $p = 1$ this turns out to be $L \sim 7000$ km. This effect is shown in the bottom panel of Fig. 3.29(b). The large (40% at its peak) drop in $\mathrm{P}_{\mu\mu}$ seen in this figure derives its strength from the resonant enhancement in $\mathrm{P}_{\mu e}$.

A sensitivity to θ_{13} around the peak similar to the one discussed above for $P^{mat}_{\mu\tau}$ also exists here which as θ_{13} becomes smaller leads to an increase in the muon survival rate in the energy range 6.5–15 GeV, while in energy range 4–7 GeV, muon survival probability decreases from a value of ~ 0.7 to ~ 0 as θ_{13} varies from 0.2 to 0 (Fig. 3.32).

The width of both these effects is significant, ranging from $4 - 10\ GeV$ in the first case (Fig. 3.29(b)) and $6 - 15\ GeV$ in the second. We have checked that they persist over a range of baselines *(6000 - 9700 km)*, making them observationally feasible.

Thus, large matter effects in neutrino oscillations are not necessarily confined to $\nu_\mu \to \nu_e$ or $\nu_e \to \nu_\tau$ conversions, but can be searched for in $\nu_\mu \to \nu_\tau$ oscillation and $\nu_\mu \to \nu_\mu$ survival probabilities. The effects discussed are strongly sensitive to the sign of δ_{31}, as is apparent in the figures above. Also, there is sensitivity to small θ_{13} at the energy and baseline ranges identified for $P^{mat}_{\mu\tau}$ and $P^{mat}_{\mu\mu}$.

Similarly, detectors capable of measuring muon survival rates, e.g. magnetised iron calorimeters can detect the effects visible in the bottom panels of Fig. 3.29(a) and (b) [59]

at neutrino factories. Typical baselines from existing and proposed neutrino factories to two the possible sites for INO include $L \sim 7000$ km (PUSHEP–CERN and Rammam–CERN). Also baselines $L \sim 10500$ km are possible for (PUSHEP–Fermilab and Rammam–Fermilab) and these are well within the range of baselines where these effects are large and observable [63].

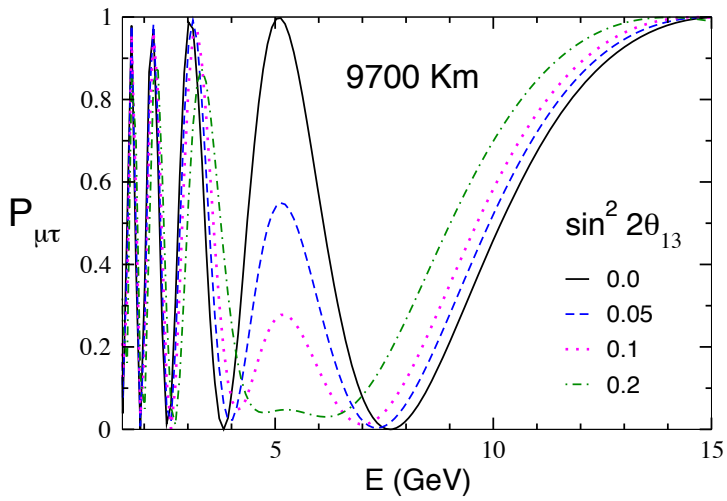

Figure 3.31: $P_{\mu\tau}$ as a function of the neutrino energy, E (GeV) for different values of θ_{13} and $\delta_{31} = 0.002$ eV^2.

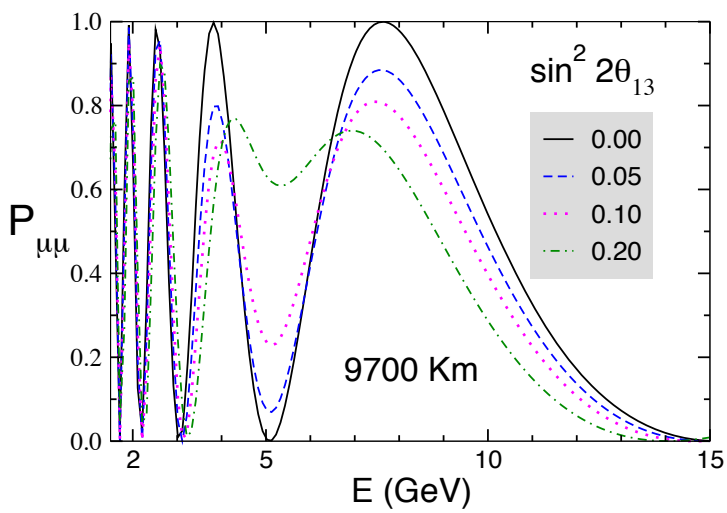

Figure 3.32: $P_{\mu\mu}$ plotted against the neutrino energy, E(in GeV) for different values of θ_{13}. Here $\delta_{31} = 0.002$ eV^2.

Chapter 4

Other Physics issues with Magnetised Iron Calorimeter

Solar neutrinos have confirmed the basic hypothesis of stellar energy generation, while handful of neutrinos from supernova SN1987A have shed insight into the mechanism responsible for supernova explosions. In a similar manner it may be possible to study the interiors of other astronomical objects like the Active Galactic Nuclei (AGN) through a study of (high energy) neutrinos from these objects. The phenomenon of Gamma Ray Bursts (GRB) suggests the possibility of the existences of such sources. Thus Neutrino Astronomy opens up a new window to the Universe and is likely to throw up new, unexpected phenomena. This has happened many times throughout history. Neutrino astronomy is an exciting new field with plenty of scope for surprises.

In what follows we discuss physics issues, other than neutrino oscillation physics, that can be studied with ICAL including the so-called Kolar events which have not been well understood yet.

4.1 Probing cosmic rays through muons underground

Cosmic ray studies, with the spectrum extending over ten decades in energy, have proved to be fertile terrain for furthering our knowledge of both astrophysics and particle physics (reviews may be found in [85, 86, 87, 88]).

Detectors like ICAL can also be utilised to study multi-TeV cosmic ray muons through the so called pair-meter technique. The motivation here is to study the knee in the cosmic ray primary spectrum. Cosmic rays are observed in wide range of energies. The differential cosmic ray (CR) spectrum shows a power-law behaviour, $\sim E^{\gamma}$ as a function of energy with index $\gamma = -2.7$ up to an energy of $\simeq 4$–7×10^{15} eV. This point is called the *knee* in the energy spectrum of CR, as can be seen from Fig. 4.1. Beyond the knee it exhibits a different power law with index -3.1 up to an energy of $\simeq 5 \times 10^{18}$ eV. This change in the behaviour of CR spectrum at the knee poses a puzzle which needs to be resolved. Such studies in the high energy (TeV–PeV) region can throw light on possible extensions of the Standard Model.

The physical reason for the existence of the knee in energy spectrum of cosmic rays is at present an unresolved problem of great significance to understanding the origin of galactic cosmic rays. It is generally believed that the reasons underlying this distinctive shift in the spectrum are astrophysical in nature, as opposed to those stemming from a change in hadronic interactions at these energies which, at present, are not within the reach of existing accelerators. This conclusion is based on the observed correspondence between independent measurements of the muon number spectrum, Cerenkov radiation and hadronic constituents

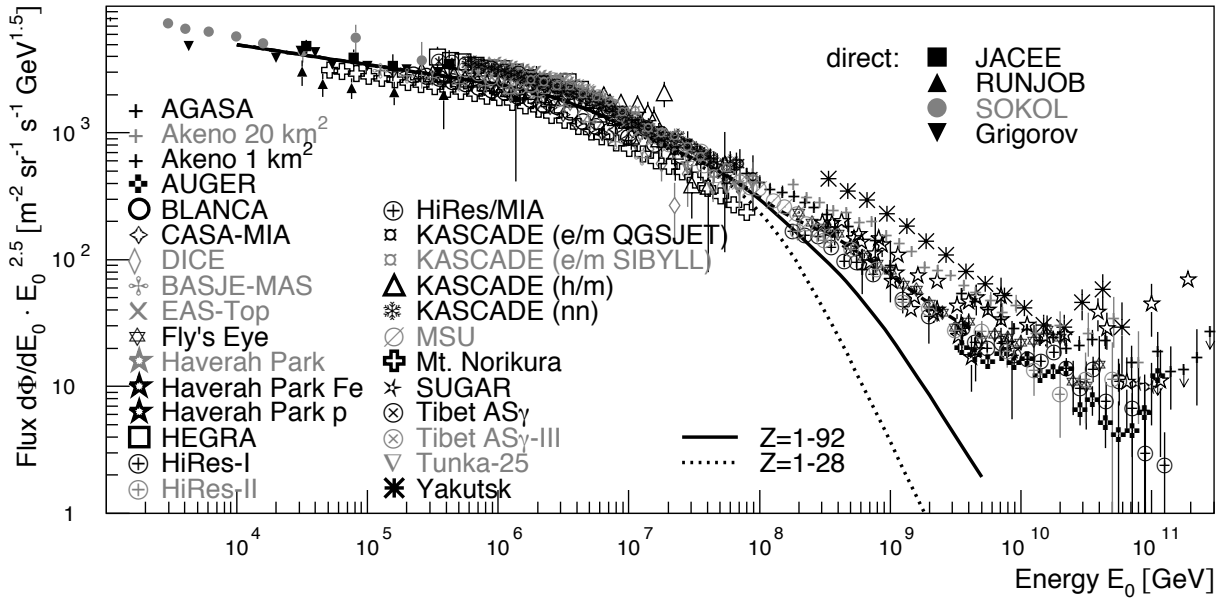

Figure 4.1: All-particle energy spectrum; results from various experiments. Figure reproduced from Ref. [89].

of air-showers [95, 96, 97, 98, 99]. While the reasons for the shift in the spectrum remain un-understood, these data exhibit an expected correlation which supports the absence of radically different physics interactions at these energies.

The case for the existence of new physics being responsible for the knee is not wholly without motivation since this region in E_p, (*i.e.*, the energy of the primary particle) corresponds to several TeV in centre of mass energies. In this energy regime, there are many conjectures for physics beyond the Standard Model. These could lead to energy being channelled into muons, neutrinos or other secondary particles in a manner that present cosmic ray experiments are insensitive to, causing the shift in the (measured) energy spectrum [100, 101, 102, 103]. We note here that beyond a few TeV or so, almost all present-day measurements of muons are sensitive to their number spectrum and not their energy. Measurements of the energy content of muons in the knee region (or beyond) would therefore be instrumental in either buttressing or refuting the conjecture of the onset of new interactions.

We discuss here the potential of the *pair meter* method [106, 107, 108] as applied to ICAL to add to our understanding of the origin of the knee, since individual muon energies will become measurable. Using this technique, it will be possible to augment the sparse existing data on cosmic ray muons in the important range where they have surface energies of $2-5000$ TeV. This when combined with balloon-based experiments (*e.g.* TRACER [109]) and upcoming hybrid air-shower experiments (*e.g.* KASCADE-Grande [110] and LOPES [111]) will enhance our understanding of the composition and origin of the primary cosmic ray spectrum around and beyond the knee. We mention here that this range in *surface muon energy* roughly corresponds to a range of $20-50000$ TeV in *primary cosmic ray energy*, which is crucial to an enhanced understanding of the origin of the knee.

An important motivation for such measurements is also provided by the fact that muons at the energies being considered here constitute the most important background to searches for ultra high energy (UHE) neutrinos [112, 113, 114, 115, 116, 117] from cosmological sources (*e.g.* active galactic nuclei, gamma-ray bursts etc.) in neutrino telescopes like AMANDA [118], ICECUBE [119] and NEMO[120]. At low (*i.e.* $\sim$ GeV) energies, the cosmic ray induced neutrino and muon fluxes receive their dominant contributions from the decays of π and K

mesons, whose interaction lengths significantly exceed their decay lengths[121, 122, 123, 124]. This is no longer true at $\sim$ TeV energies, and secondary interactions of these particles are expected to lead to the production of heavy short lived hadrons. In particular, our present lack of empirical knowledge of the flux of prompt muons from the production of charmed hadrons via secondary interactions in the atmosphere (and their subsequent decay via semi-leptonic modes) at energies above TeV renders this background to UHE neutrinos very uncertain; in spite of upper bounds on the flux of prompt muons from LVD [125] and AKENO [126].

Present phenomenological predictions for the diffuse fluxes of these prompt muons and neutrinos can differ by about two orders of magnitude [124, 127, 128, 129, 130, 131, 132] in a particular model. The sources of this large uncertainty lie, to a significant extent, in the choice of charm production models. We give a representative idea of the variation possible within a given charm production model in Fig. 4.4. Following Ref.[129], we show the prompt flux predictions with variations resulting from 2 different parton distribution functions and choices of the factorisation and renormalisation scales. Also shown is the prompt flux prediction from [124] and the conventional muon flux from π and K decays, which is relatively well understood.

In what follows, we first provide a discussion of the pair-meter technique and summarise the interactions and losses of muons in matter. We then calculate anticipated event rates for a 50 kton detector and demonstrate that even after accounting for energy losses in the surrounding rock, event rates can be appreciable in the $1 - 1000$ TeV range, corresponding to *surface* muon energies in the range of several TeV to several PeV.

4.1.1 The cascade event rate for muons with energies 1–1000 TeV

Due to the penetrating power of muons, their energy measurements require techniques which differ from those employed for photons, hadrons and electrons. Furthermore, muon energy measurement methods which work well in the GeV range are rendered impractical in the TeV range due to requirements of size imposed by the combination of high energies and a steeply falling spectrum. The pair meter provides a method of analysing the very high energy events with muons.

The pair meter method and the associated pair production cross section

The pair meter technique [106, 107, 108] skirts some of the disadvantages of traditional muon detectors by relying on a somewhat indirect method, *i.e.* the measurements of the energy and frequency of electron-positron pair cascades produced by the passage of a high energy muon in dense matter.

Differential cross section for pair production at small energy transfer $v = \frac{E_0}{E_\mu} < 10^{-3}$, where E_0 is the energy threshold, by the interaction of muons with nuclei can be approximated as

$$v\frac{d\sigma}{dv} \simeq \frac{14\alpha}{9\pi t_0} ln\left(\frac{\kappa m_e E_\mu}{E_0 m_\mu}\right) , \tag{4.1}$$

where $\alpha = 1/137$, $\kappa \simeq 1.8$ and t_0 is the radiation length (r.l) which is given by

$$t_0 = \left(\frac{4Z(Z+1)}{A_W}\ \alpha r_0^2 N_A\ ln(189Z^{-1/3})\right)^{-1} . \tag{4.2}$$

Here A_W is the atomic weight, r_0 is the classical electron radius and N_A the Avogadro number. For iron, this gives $t_0 = 13.75$ per cm^2.

The average number of interaction cascades M above a threshold E_0 for $v \leq 10^{-3}$ is given by

$$M(E_0, E_\mu) = T\sigma(E_0, E_\mu) \ , \tag{4.3}$$

where T is the thickness of the target in units of t_0 and $\sigma(E_0, E_\mu)$ is the integrated cross section,

$$\sigma(E_0, E_\mu) \simeq \frac{7\alpha}{9\pi t_0}\left(ln^2\left(\frac{\kappa m_e E_\mu}{E_0 m_\mu}\right) + C\right) \ , \tag{4.4}$$

where $C \simeq 1.4$.

The calculations which follow are performed for a 50 kton iron calorimeter. Our prototype is based on the suggested design for ICAL at INO. We note that a muon with energy $E_\mu = 100$ TeV generates approximately 40 cascades, each of energy greater than $E_0 = 10$ GeV and 10 cascades with energy in excess of 100 GeV. By counting the cascades for several choices of thresholds for a traversing muon, a reliable estimate of its energy may be obtained. Fig. 4.2 shows the average number of cascades above a threshold energy E_0 produced by a muon entering the detector with energy E_μ and $T = 1000$ radiation lengths. Three different choices of $E_0 = 1, 10, 100$ GeV are used.

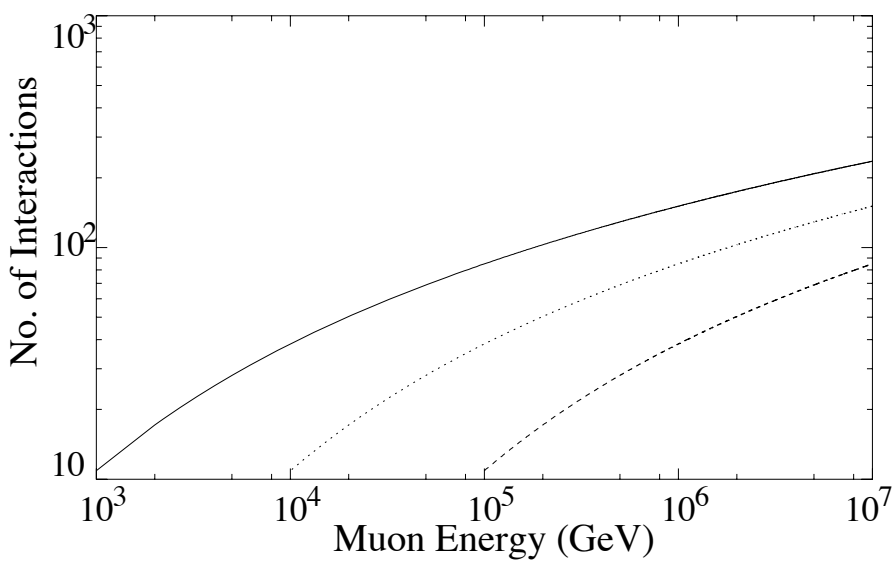

Figure 4.2: Average number of cascades above a threshold E_0 vs. muon energy. The three lines correspond to $E_0 = 1$ GeV(solid), $E_0 = 10$ GeV (dotted) and $E_0 = 100$ GeV(dashed), with $T = 1000$ radiation lengths.

It is also relevant to remark here that the relative energy measurement error, $\delta E_\mu/E_\mu$ in the pair meter is given by

$$\delta E_\mu/E_\mu = \sqrt{\frac{9\pi}{28\alpha T}} \simeq \sqrt{\frac{137}{T}} \ . \tag{4.5}$$

For $v = (10^{-3} - 10^{-2})$, which is the range we focus on for the most part, this allows a liberal tolerance for error in the measurements of individual cascade energies. We note also that the errors do not worsen with increasing muon energy, which is an important advantage of the pair-meter technique.

The surface muon energy determination for underground events

Muon energy measurements at energies higher than TeV in a high density pair meter like ICAL may shed light on the nature of the spectrum around and beyond the knee and the also on the nature and extent of the charm contribution to high energy fluxes which originate in cosmic rays. It is thus important to relate the inferred muon energy in an underground detector to its surface energy which would be the observed energy if the detector were placed on the surface of the earth. This requires a calculation of the energy loss as the muon traverses the rock between the earth's surface and the detector.

These losses originate from ionisation, bremsstrahlung, pair production and photo-nuclear interactions. They can be effectively parametrised [133, 134, 135] for $E_\mu \geq 1$ TeV, since the average loss increases predominantly linearly with energy as,

$$\frac{dE}{dX} = -\alpha - \beta E \ , \tag{4.6}$$

where α parametrises the contribution from ionisation of muons and β encapsulates the contribution from bremsstrahlung, pair production and photo-nuclear processes. Note that α and β carry a very weak (intrinsic) energy dependence. It is thus appropriate to assume that the average muon energy at depth X is

$$E_\mu(X) = \left(E_\mu^s + \frac{\alpha}{\beta}\right) e^{-\beta X} - \frac{\alpha}{\beta} \ , \tag{4.7}$$

where E_μ^s is the initial surface muon energy. This may be used to write down the minimum surface energy required of a muon to reach a depth X as,

$$E_{min}^s = \frac{\alpha}{\beta}\left(e^{\beta X} - 1\right) \ . \tag{4.8}$$

From Eq. 4.7, we get the relation between initial energy E_μ^s and degraded energy of muon E_μ after travelling a distance X as

$$E_\mu^s = \left(E_\mu + \frac{\alpha}{\beta}\right) e^{\beta X} - \frac{\alpha}{\beta} \ . \tag{4.9}$$

The differential muon flux at a depth X is given by,

$$\frac{dN}{dE_\mu} = \frac{dN}{dE_\mu^s} e^{\beta X} \ , \tag{4.10}$$

where $\frac{dN}{dE_\mu^s}$ is the initial muon flux with surface muon energy E_μ^s.

The α and β in the analytical expression can be obtained for standard rock. The depth relevant to the INO detector's proposed location is 3.5×10^5 gm/cm^2. (The depth in standard units is obtained by dividing by the rock density). The values are,

$$\beta = 4 \times 10^{-6} \text{ cm}^2/\text{g}, \ \frac{\alpha}{\beta} = 675 \text{ GeV}. \tag{4.11}$$

Figure 4.3 shows the degraded muon energies (*i.e.*, those measured for muons entering the detector after traversing the rock) vs their corresponding surface energies after losses are accounted for in the manner described above. We note that typically, $E_\mu^s \simeq (2\text{–}5) \times E_\mu$.

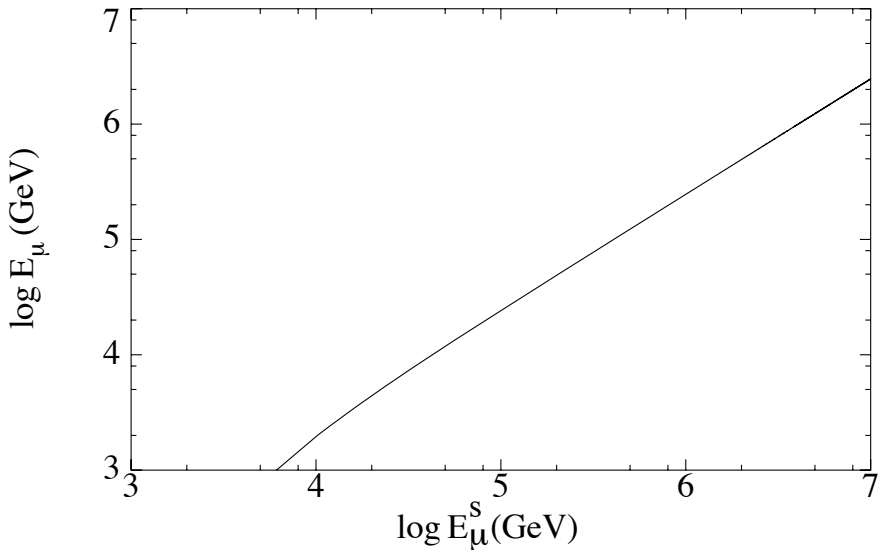

Figure 4.3: Degraded muon energy, E_μ vs. surface muon energy, E^s_μ after passing a depth of $3.5 \times 10^5 g/cm^2$, corresponding to the proposed INO location.

4.1.2 Muon Fluxes

For our representative calculations of muon event rates, we have used the relatively conservative predictions for charm induced fluxes given in [124, 129].

In Ref.[124], Thunman, Ingelman and Gondolo (TIG) have given the parametrisations for the conventional and prompt fluxes as

$$\frac{dN}{dE} = \frac{N_0 E^{-\gamma-1}}{1 + AE} \tag{4.12}$$

for $E < E_a$ and as

$$\frac{dN}{dE} = \frac{N_0^{'} E^{-\gamma^{'}-1}}{1 + AE} \tag{4.13}$$

for $E > E_a$. For the conventional muon flux $N_0 = 0.2$, $N_0^{'} = 0.2$, $\gamma = 1.74$, $\gamma^{'} = 2.1$, $E_a = 5.3 \times 10^5$, $A = 0.007$.

For the prompt muon flux $N_0 = 1.4 \times 10^{-5}$, $N_0^{'} = 4.3 \times 10^{-4}$, $\gamma = 1.77$, $\gamma^{'} = 2.01$, $E_a = 9.2 \times 10^5$, $A = 2.8 \times 10^{-8}$.

The second set of representative prompt muon fluxes we use are calculated in [129] (henceforth referred to as the PRS1,PRS2 and PRS3 fluxes). The differences in the three fluxes originate in different choices of parton distribution functions (PDF) and factorisation ($\tilde{M}$) and renormalisation scales ($\tilde{\mu}$) of the theory.

Flux model	PDF	Scales	a	b	c	d
PRS1	CTEQ3	$\tilde{M} = \tilde{\mu} = m_c$	5.37	0.0191	0.156	0.0153
PRS2	CTEQ3	$\tilde{M} = 2\tilde{\mu} = 2m_c$	5.79	0.345	0.105	0.0127
PRS3	D	$\tilde{M} = 2\tilde{\mu} = 2m_c$	5.91	0.290	0.143	0.0147

Table 4.1: PRS parameters for the prompt muon and anti-muon fluxes. m_c is the mass of the charm quark. The second column refers to the different parametrisations of the parton distribution.

These fluxes can be conveniently parametrised [129] as follows

$$\frac{dN}{dE} = 10^{-a+bx+cx^2-dx^3}, \tag{4.14}$$

where $x = Log_{10}(E/\text{GeV})$, with a, b, c and d as in Table.4.1.

In Fig. 4.4 (left panel) we show the conventional (TIG) and prompt (TIG and PRS) surface muon fluxes. We note that depending on the flux model, the prompt fluxes rise above the conventional flux for (surface) muon energies between 200 TeV and 1000 TeV. In terms of (degraded) muons entering the detector, we see from Fig. 4.3 and Fig. 4.4 (right panel) that this corresponds to measured muon energies of several tens of TeV and several hundreds of TeV. Thus, we note that underground muon measurements in this range will help reduce the present uncertainties in deducing the charm contributions to muon and neutrino fluxes. Our calculations below provide a quantitative estimate of the potential of these measurements to accomplish this.

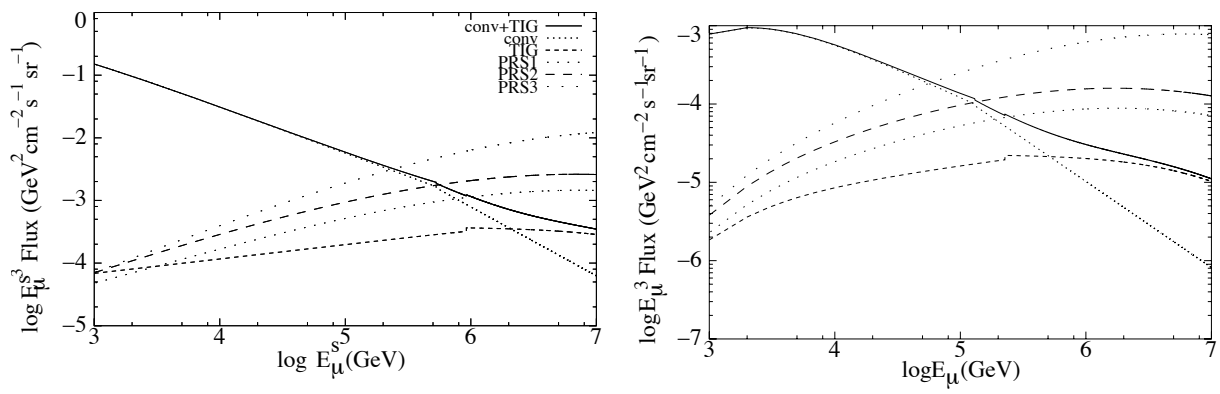

Figure 4.4: Left: ($E_\mu^{s3}\times$ Flux) vs. surface muon energy E_μ^s for total TIG flux (solid), conventional (dotted), TIG prompt (short dashed), and prompt fluxes corresponding to PRS1 (short spaced dots), PRS2 (large dashed) and PRS3 (large spaced dots). Right: ($E_\mu^3\times$ Flux) vs. energy of muon entering the underground detector E_μ, (for the flux models listed on the left) after passing through the rock distance of $3.5 \times 10^5 gm/cm^2$.

4.1.3 Results and Discussion

We are now in a position to calculate the expected cascade events for a 50 kton detector mass in the energy range of interest discussed above. It is thus pertinent to obtain a quantitative measure of this by estimating n_μ, the number of muons above a given threshold entering the detector per steradian for an exposure of t years,

$$n_\mu = \int_{E_{th}}^{\infty} dE_\mu \frac{dN}{dE_\mu} A \times t \ , \tag{4.15}$$

where A is the exposed area of a 50 kton iron detector. This is shown in Fig. 4.5 (left). We note that while the number of entering muons for the lowest energy *i.e.*, 1 TeV is very large, an observable number, *i.e.* 6 events, is obtained, after integrating over solid angle (considering that there is typically no "back-ground" for such events) over the 5 year period, even for $E_\mu = 1000$ TeV, for the most conservative flux choice (TIG). These energies delineate the muon energy range accessible. The number of entering muons for all choices of PRS fluxes will be substantially higher.

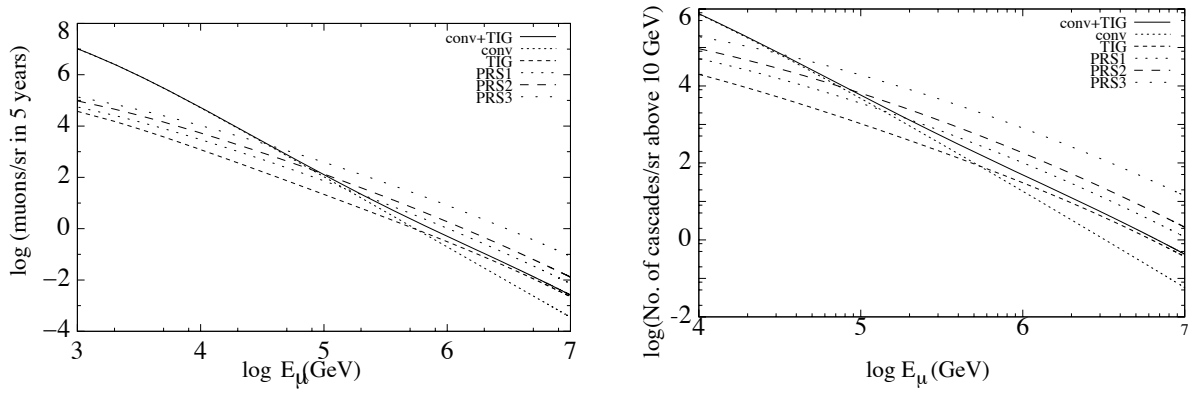

Figure 4.5: Left: Number of muons entering the 50 kton detector in 5 years per solid angle vs. muon energy. Energy losses in the surrounding rock are taken into account. Depth of the detector is assumed to be $3.5 \times 10^5 g/cm^2$. Right: Number of cascades above a threshold $E_0 = 10$ GeV per solid angle in 5 years of exposure time for a 50 kton iron detector, for various flux models described in the text. Here E_μ is the energy of the muon entering the detector, assuming it traversed a depth of rock corresponding to $3.5 \times 10^5 gm/cm^2$.

The number of expected cascade events per steradian $N_c(E_0)$ in time t is

$$N_c(E_0) = \int_{E_{th}}^{\infty} dE_\mu M(E_\mu, E_0) \frac{dN}{dE_\mu} A \times t \ , \tag{4.16}$$

where $M(E_\mu, E_0)$ is the cascade number. Fig. 4.5 (right) shows the number of cascades per steradian above $E_0 = 10$GeV in the 50 kton detector vs the muon energy for a time exposure of 5 years for both the TIG and PRS models.

We have used the TIG flux as a benchmark to establish the observability, since it leads to the most conservative event rate predictions. All other flux parametrisations lead to higher predictions. We note that even though TIG and PRS are not vastly different from each other in a qualitative sense since both are based on perturbative QCD inputs, their event rates in a large mass pair-meter differ significantly. Indeed, the variations amongst fluxes in the same family (PRS1, PRS2, PRS3) are also large.

Thus, the muon event rate can act as a discriminator between various prompt flux models and provide pointers to the physics input that should guide their development. Similarly, this rate provides a tool to better understand the present spectral uncertainties in the cosmic ray knee origin.

A detailed and comprehensive set of predictions for INO necessarily requires a much more elaborate calculation of the muon losses than what is presented here, since local topography plays an important role in determining the surface muon energy corresponding to a measured muon energy. Our aim in this section has been more to demonstrate observational feasibility rather than to make precise predictions. Thus the calculations here show that very high energy muon measurements are possible in a large iron calorimeter and can aid in illuminating two important outstanding questions, one in cosmic ray physics and the other in ultra high energy neutrino astronomy.

4.2 Kolar events

Earlier experiments at KGF had recorded unusual events indicating the possibility of a long-lived particle with a large production rate. This phenomenon is as yet not well understood.

The proposed detector ICAL at INO will be capable of observing many more such events leading to a better understanding and possibly clarifying the origin of these unusual events. We discuss these events briefly below:

In the neutrino experiments at 7000 hg/cm^2, as well as those conducted later at 3375 hg/cm^2 and the proton decay experiments in the KGF mines, it was noticed (Krishnaswamy *et al.* [136]) that some multi-track events (6 in total) had unusual features which could not be explained away by any known processes of muons or neutrinos. They are characterised by the following features:

1. The event consisted of two or more tracks, with at least one of them a muon or a pion as seen from their penetrating power without showering.

2. All tracks of the event seemed to originate from a vertex located either in air or thin detector materials - based on an extrapolation of projected angles of tracks.

3. The tracks had a large opening angle ($\sim 45°$) between them and

4. their rate was depth-independent and was a fraction of neutrino events.

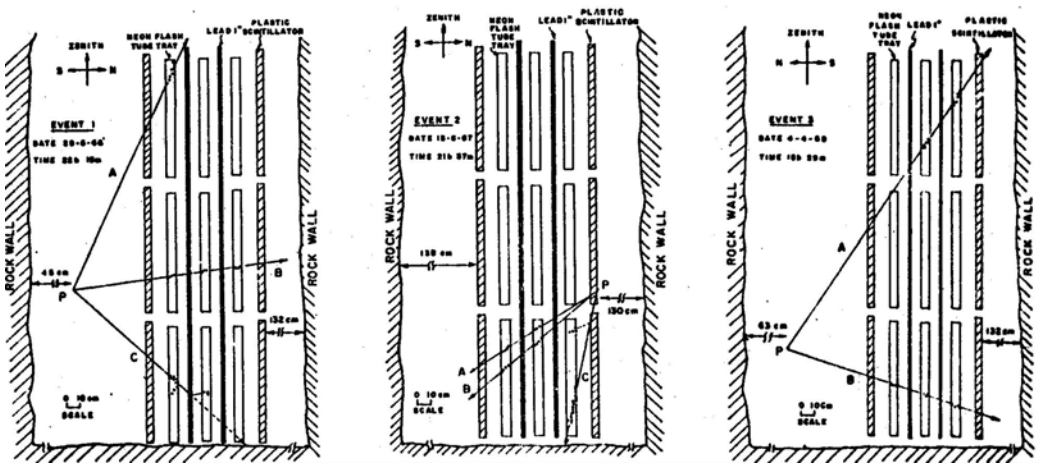

Figure 4.6: Multi-track (Kolar) events recorded in KGF neutrino-detectors.

A few examples of such events recorded in the neutrino detectors at 2.3 km depth are shown in Fig. 4.6. The first event had 3 tracks, out of which there is at least one penetrating track (μ/π) traversing lead absorber without showering; when extrapolated, they meet in air at a distance of ≈ 45 cm from the nearest rock wall. The second one had 3 penetrating tracks with a large opening angle. The third one has only 2 tracks, either due to μ or π at an opening angle of $\sim 63°$. In the proton decay experiments at KGF there were similar examples. One of them consisted of an upward going muon (> 1 GeV) at an angle of 62° , a down going shower at a median angle of 51° with visible energy of > 2 GeV and with the vertex close to the edge of the rock wall. It was suggested that most of these events could be due to new particles of mass of a few GeV with an unusually long life time of $\sim 10^{-9}$ secs. and produced at a rate of the same order of magnitude as that of the atmospheric neutrino interactions. Searches were made at the ν- experiments at CERN [137] and at Fermilab [138] but they lead to negative results with bounds on cross-sections (and masses) to produce neutral, long-lived particles in neutrino interactions.

A number of theoretical attempts were made [139, 140, 141] to understand the production processes and see if they could fit into the prevailing schemes of particles and their interactions. The Kolar events have so far remained an enigmatic puzzle and they need to be studied with specially designed detectors that can address their special characteristics.

Chapter 5

The Magnetised Iron Calorimeter

The goals of neutrino physics world wide in the next two decades have been discussed in Chapter 2. The major physics goals of the INO experiment as discussed in the previous chapter are

- to re-confirm the occurrence of oscillation in atmospheric muon neutrinos through the explicit observation of the first oscillation swing in ν_μ disappearance as a function of L/E,
- a significantly improved measurement of the oscillation parameters with respect to earlier measurements,
- search for potential matter effects in neutrino oscillations,
- determining the sign of δ_{23} using the matter effect,
- discrimination between $\nu_\mu \rightarrow \nu_\tau$ and the $\nu_\mu \rightarrow \nu_s$ oscillation,
- probing CPT violation in the neutrino sector using atmospheric neutrinos and
- constraining long range leptonic forces.

In this chapter we discuss the criteria for selecting a proper detector system for the INO experiment and the R&D and tests results of various components.

5.1 Choice of the detector

The basic criteria for selecting the detector for the INO experiment can be outlined as follows:

- A large target mass to achieve a statistically significant number of neutrino interactions in a reasonable time-frame (say 5 years) for the confirmation of atmospheric neutrino oscillation,
- Good energy and angular resolution so that L/E can be measured with an accuracy better than half of the modulation period,
- Identification of the electric charge of muons so as to distinguish between neutrino and anti-neutrino interactions. Charge determination is necessary to achieve most of the physics goals mentioned above.

To explicitly detect the oscillation pattern in the L/E spectrum of atmospheric muon neutrinos, the energy E and direction θ of the incoming neutrino have to be accurately measured in each event. The direction of the neutrino can be estimated in the simplest approach, from the direction of the muon produced from the ν_μ charged-current interaction. The energy of the neutrino can be estimated by measuring the energies of muon and the hadrons produced in each event. The energy and angular resolution of the detector should therefore be good enough so that L/E can be measured with an accuracy better than half of the modulation period.

In order to estimate the distance traversed by the neutrino, it is necessary to establish the flight direction (up vs. down) of the muon produced by the neutrino with high efficiency. Different techniques like increase of curvature in a magnetic field, multiple scattering along the track or the measurement of timing in successive detector layers can be used to achieve this. Of these the time-of-flight technique is the most effective and allows excellent up-down discrimination for a detector with a time resolution (σ) of 2 ns or better.

The following factors have also been considered while finalising the choice of detector type and technology. These are :

- technological capabilities available within the country,
- existence of other neutrino detectors around the world,
- modularity and the possibility of phasing, and
- compactness and ease of construction.

The Iron Calorimeter (ICAL) detector described in this chapter satisfies all of the design goals listed above. The ICAL is a large modular detector consisting of magnetised iron plates interleaved with layers of position sensitive detectors having a time resolution better than 2 ns and spatial resolution < 1 cm. Such a detector with a target mass of about 100 kton will be ideal to address the physics goals listed above. To begin with we propose a detector of about 50 kton, which may be enlarged to its final size of 100 kton in stages.

We now discuss the proposed detector in detail. The physics performance simulation for such a detector will be presented in Chapter 6.

5.2 The ICAL Detector

5.2.1 Basic parameters

The proposed detector will have a modular structure of total lateral size 48 m $\times$ 16 m and will consist of a stack of 140 horizontal layers of $\sim$ 6 cm thick magnetised iron plates interleaved with 2.5 cm gaps to house the active detector layers. The ICAL detector will be subdivided into three modules of size 16 m $\times$ 16 m. This modular structure will allow early operation with the completed modules while constructing others. The height of the detector will be 12 m. Considering the overall size of the apparatus and the large active detector area of $\sim$ 108,000 m^2, it is desirable that such a detector should be of low cost, modular in construction with elements of a size suitable for mass production on a time scale consistent with the requirement that the detector be internationally competitive.

It must also satisfy the spatial and time resolution criteria mentioned earlier. Considering all these factors the resistive plate chamber (RPC) seems to be the most appropriate choice as the active detector. While the RPC can be constructed using Bakelite or glass we have at present chosen glass mainly due to availability and cost. Fig. 5.1 shows the overall layout

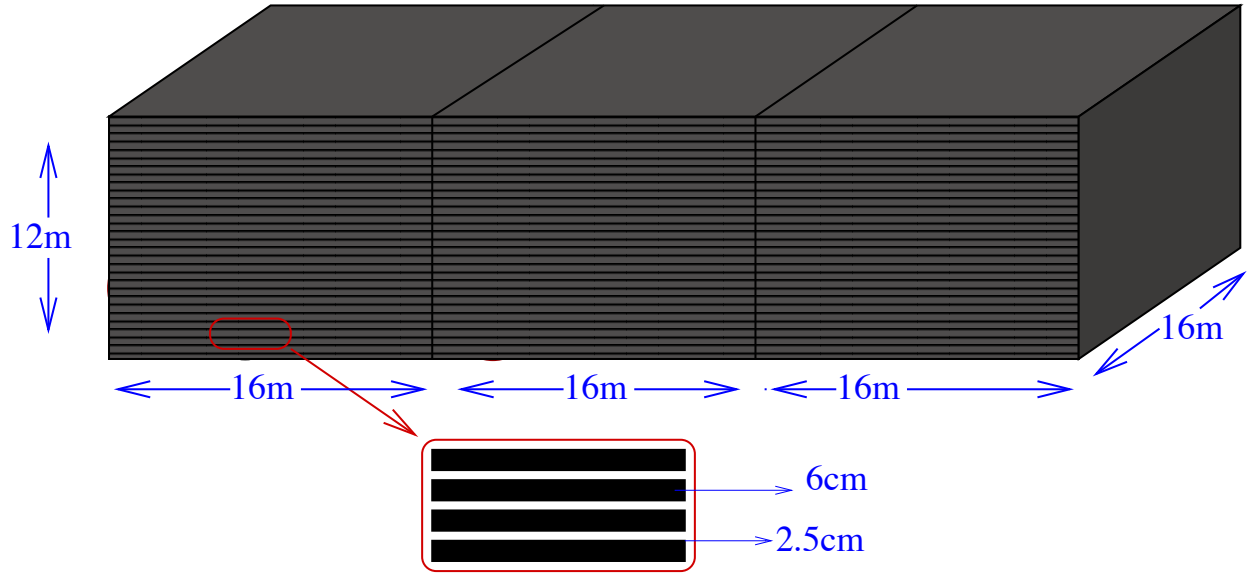

Figure 5.1: Schematic view of the 50 kton iron calorimeter detector consisting of 3 modules each having 140 layers of iron plates.

of the detector. Table 5.1 summarises the specifications of the ICAL detector and the RPC elements.

The iron structure for this detector will be self supporting with the layer above resting on the layer immediately below using iron spacers located every 2 m along the X-direction. The details are shown in Fig. 5.2. This will create 2 m wide roads along the Y-direction for the insertion of RPC trays. There will be a total of 8 roads per module in a layer. The iron plates will be magnetised with a field of about ∼1.3 Tesla. The total mass of the detector will be around 50 kton.

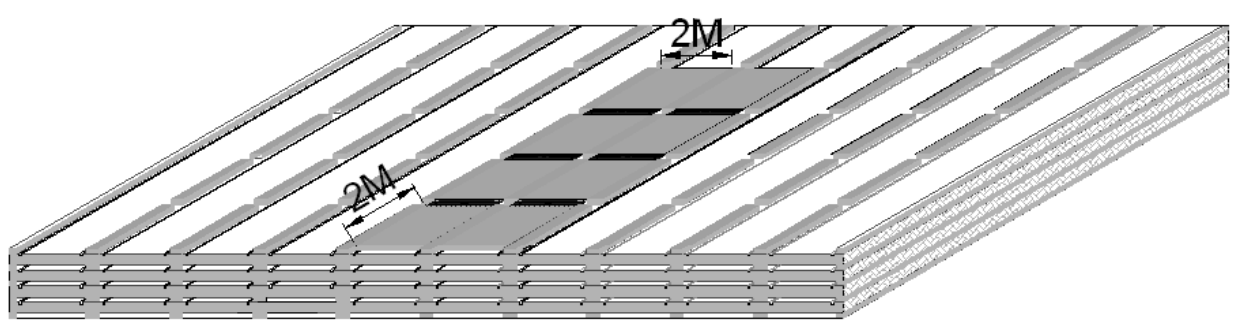

Figure 5.2: Structural detail of mounting active detector elements.

The whole detector, as described above, will be surrounded by an external layer of scintillation or gas proportional counters. This will act as a veto layer and will be used to identify muons entering the detector from outside as well as to identify partially confined events with the vertex inside the detector.

5.2.2 RPCs as active detector elements

The Resistive Plate Chamber (RPC) is a type of spark chamber with resistive electrodes. Since such a detector has very good timing ($\sigma \sim 1$ ns) and spatial resolution, it is well suited

ICAL	
No. of modules	3
Module dimension	16 m × 16 m × 12 m
Detector dimension	48 m × 16 m × 12 m
No. of layers	140
Iron plate thickness	∼ 6 cm
Gap for RPC trays	2.5 cm
Magnetic field	1.3 Tesla
RPC	
RPC unit dimension	2 m × 2 m
Readout strip width	3 cm
No. of RPC units/Road/Layer	8
No. of Roads/Layer/Module	8
No. of RPC units/Layer	192
Total no. of RPC units	∼ 27000
No. of electronic readout channels	3.6×10^6

Table 5.1: Specifications of the ICAL detector

for a fast tracking calorimeter. The first resistive spark chambers were developed by Fedotovich *et al.* [142], using semi-conductive glass and a gas gap of 100 μm. A planar chamber with gaps of 1.52 mm, simple in construction and having gas mixtures at atmospheric pressure was then developed [143] using Bakelite ($\rho \approx 10^{11}$ Ω cm) as resistive electrodes. This technique, although economical, had some difficulties in operation. To overcome some of these difficulties Anelli *et al.* [144] developed a new type of RPC based on low cost resistive glass plate electrodes.

The glass RPC is a gaseous detector composed of two parallel electrodes made of commercially available 2 mm thick float glass (Fig. 5.3). The bulk resistivity of glass is about 10^{12} Ω cm. The glass plates are separated by suitable spacers epoxied to both plates at regular intervals in such a way that they channel the gas flow through the chamber uniformly. Additional **T**-shaped spacers are epoxied at the edges of the glass plates to make the whole module gas tight. To distribute high voltage on the glass uniformly, the outer surfaces of the glass plates are coated with a thin layer of graphite paint. The expected surface resistivity of the graphite coated surface is 100-200 K$\Omega/\square$. An electric field of $\approx$ 4-5 kV/mm is applied between the two plates.

The RPCs may be operated either in the avalanche mode or streamer discharge mode. The avalanche mode corresponds to the generation of a Townsend avalanche following the release of primary charge due to the passage of an ionising radiation through the gas volume. In the streamer mode the avalanche is followed by a 'streamer' discharge. The RPCs working in the avalanche mode mostly use mixtures of tetrafluoroethane ($C_2H_2F_4$- also known as R134a) with 2-5% of isobutane (iso-C_4H_{10}). In the streamer mode, mixtures of argon with isobutane and tetrafluoroethane in widely varying proportions are used. Typical signal amplitudes in the avalanche and streamer modes are $\sim$ 5-10 mV and 100-200 mV (across a 50 Ω load), respectively.

Both glass and Bakelite based RPCs in either the streamer mode or avalanche mode are now being used extensively in high energy physics experiments for timing as well as position measurements. The Belle detector [151] at the KEK-B asymmetric B-factory uses glass based RPCs in the streamer mode to identify K_L's and muons. The Belle RPC system

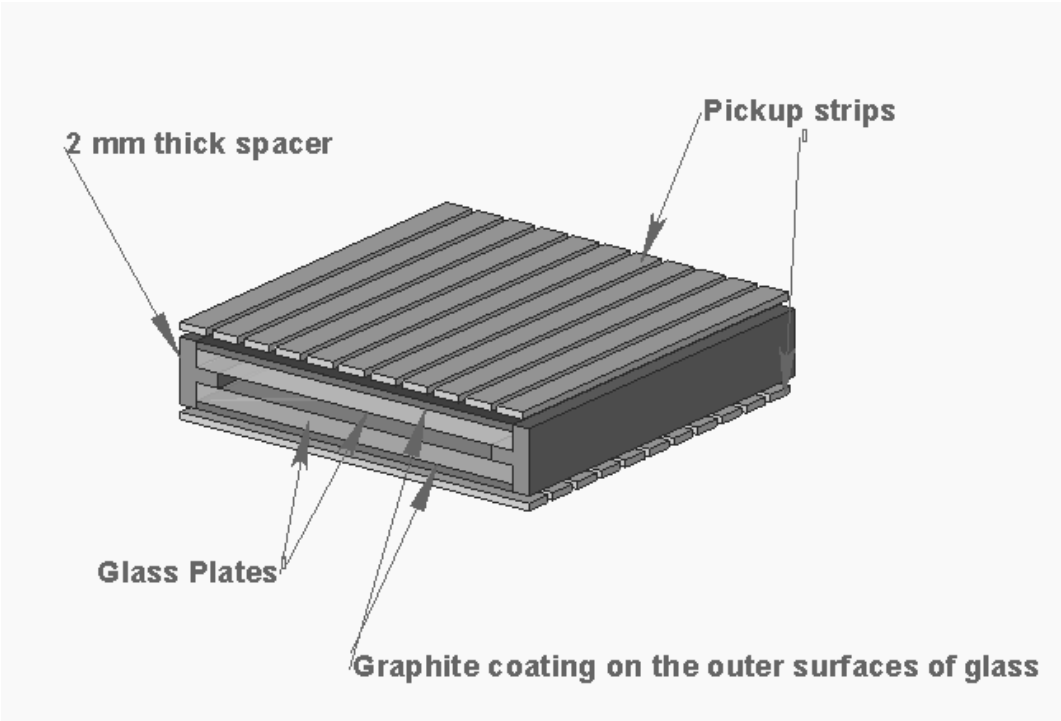

Figure 5.3: Sketch of a typical glass RPC unit.

consists of alternating layers of glass RPCs and 4.7 cm thick iron plates. There are 15 RPC layers and 14 iron plates in the octagonal barrel region and 14 iron layers and 14 RPC layers in each of the forward and backward endcap regions. The barrel RPCs are rectangular in shape and vary in size from 2.2×1.5 m^2 to 2.2×2.7 m^2. The RPCs used for the endcaps are trapezoidal in shape having length of 1.8 m and outer dimension of ≈ 1 m. This is the first experiment where glass RPCs in large numbers are operational for more than 5 years. There is extensive R & D work going on around the world for using glass RPCs for digital calorimetry in experiments at the proposed International Linear Collider [145].

Bakelite based RPCs in the avalanche mode will be used extensively for all the LHC experiments [146, 147, 148, 149] at CERN for muon detection and in the trigger.

5.2.3 Detector arrangement and readout schemes

The basic RPC detector element for ICAL will be 2 m in length and 2 m wide. Eight such elements will cover a road of 16 m $\times$ 2 m. A total of $\sim$ 27000 such elements will be needed to complete the detector.

The readout of the RPCs will be performed by external orthogonal pickup strips (X and Y strips). A localised streamer discharge due to the passage of charged particles will induce pulses on the appropriate strips. These will go to front end ASICs located near the strip ends which will have fast discriminators that will provide a fast timing signal. Presently we are proposing 3 cm wide strips. However this can be optimised through simulation studies which are currently ongoing. Thus in the current plan each road of RPCs will be read out by 64 strips along the X-direction (2 m) and 512 strips along the Y–direction (16 m).

Currently we are investigating several types of pickup boards. The first type is similar to one proposed by the MONOLITH Collaboration [150]. In this approach the strip planes will be realized by gluing a grooved copper foil on one side of a plastic honeycomb of 3.5 mm thickness. Another copper foil without any groove will be glued on other side of the honey-

comb and will be grounded. Another approach will be to use copper clad G10 sheets with readout strips grooved on one side and the other side acting as the ground plane.

In either of these techniques 8 readout boards along a road will be connected to each other. The X strips from individual boards will be connected to one another and will be read out at the edge of the detector. The Y-strips from individual boards will also be brought to the edge of the detector using impedance matched cables. All the front end ASICs will be located on boards near the edge of the detector.

5.2.4 Readout Electronics

The conceptual readout scheme is illustrated in Fig. 5.4. The incoming detector signals are passed through programmable threshold comparators for producing digital logic signals. These signals are used for recording Boolean hit information, for generating trigger primitives as well by time multiplexing blocks for generating timing signals. Signals from only one coordinate will be used for generating the trigger. Processing of only one coordinate signals for generating trigger primitives and using time multiplexing techniques for recording timing information will reduce the DAQ channel count and hence the cost. Similar techniques are already being used in other experiments such as the Belle experiment [151] in Japan and have been proposed by the Monolith Collaboration [42] in Italy.

The time multiplexing scheme combines hit information from a block of strip channels into a single data stream which can be passed on to multi-hit TDCs at the back end. In this scheme, the front-end processing will be achieved by a custom ASIC chip whereas the hit recording and time multiplexing is done by a commercial FPGA device.

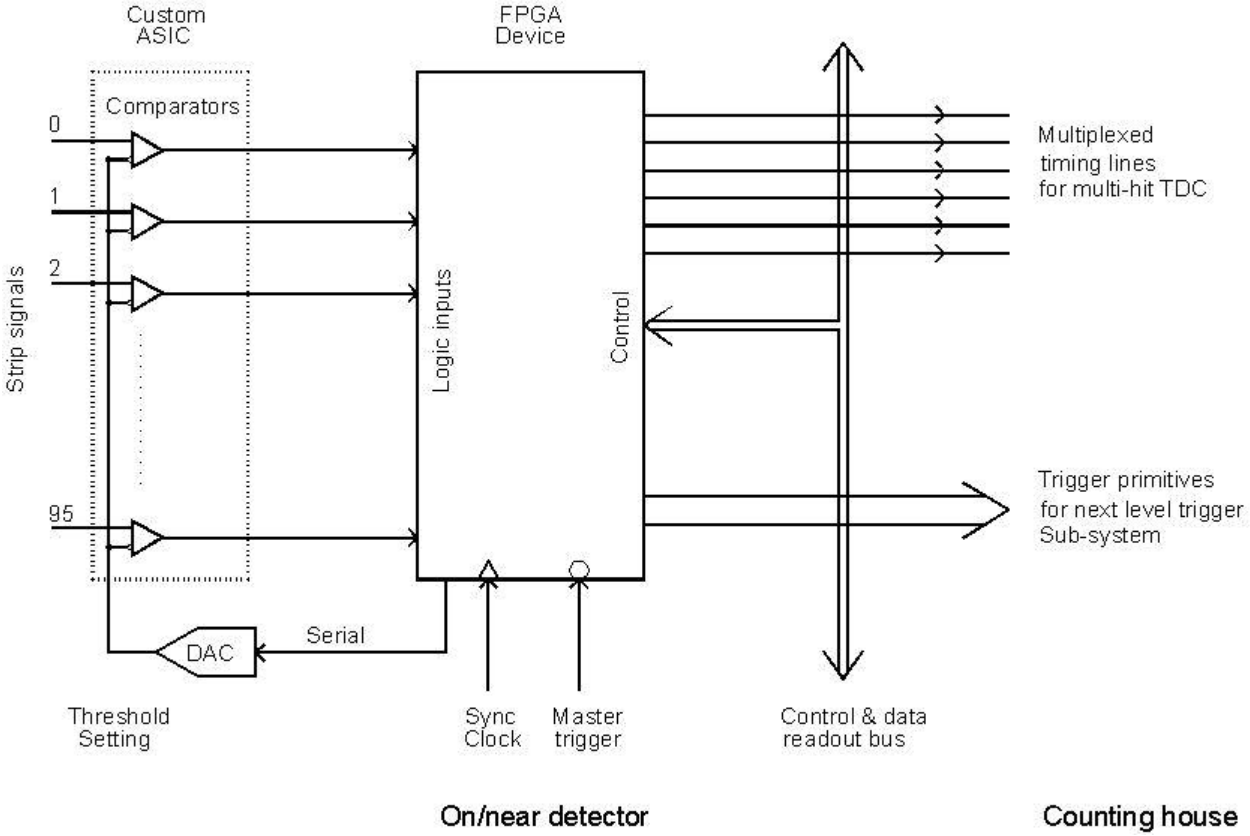

Figure 5.4: Proposed readout scheme for the ICAL detector.

The trigger generator is an independent sub-system which uses the same hit signals

Technology Power supply PSRR	SCL 1.2μm CMOS N-well $\pm$ 2.5 V 55 dB - 65 dB
Average power consumption (idle)	VDD = 0.85 mW/ch VSS = 0.85 mW/ch
Peak power consumption (C_L=5pf)	VDD = 100 mW/ch VSS = 140 mW/ch
Voltage gain Input offset voltage	100 dB 80 μV (typical)
Prop-delay (Low-High) (C_L=5pf, overdrive=40mV)	6.5 ns (typical)
Rise time (Low-High) Fall time (High-Low)	825 ps (typical) 625 ps (typical)
Max. operating frequency (sinusoidal with C_L=5pf)	150 MHz

Table 5.2: Simulated parameters of the voltage comparator ASIC

to look for required patterns of hits in the detector and initiate data recording if any of the interesting predefined hit patterns occur inside the detector. For instance, a trigger may be generated when certain hit patterns such as 2 or 3 hit layers out of 5 consecutive layers occur. This will ensure the trigger generation of nearly all the relevant atmospheric neutrino events. Programmability is the key requirement of this sub-system so that different physics motivated data recording plans may be supported during the course of experiment. A commercial FPGA device based design is best suited for this purpose.

We plan to use the VME standard for the DAQ system and hosts will be based on Linux PC boxes.

5.2.5 Voltage Comparator ASIC

A 16-channel ASIC for fast voltage comparators has been designed in CMOS technology at SINP by the group who has already developed the MANAS chip for the Muon Arm Project in ALICE. This takes as input the RPC negative pulse of amplitude 50-150 mV and a rise-time and fall-time of 1 ns and 20 ns, respectively. It consists of a preamplifier stage, a positive feedback stage (decision making circuit) and an output buffer. The simulated design parameters are given in Table 5.2. The front-end design for the ASIC is ready. Work is in progress to hand over the design to Semiconductor Complex Ltd., Chandigarh, for prototyping.

5.2.6 Gas System

The total volume of the active detector elements of ICAL will be $\sim$216 m^3. The gas distribution system for such a big detector will be a recycling system with approximately one volume change per day. The whole detector will be divided into several zones. Each zone will have a gas supply from a separate gas mixing system. The three gases (argon, isobutane and R-134a) will be sent to mass flow controllers for mixing in appropriate ratios. The gas distribution system will be designed to provide independent gas supply to each road (8 RPC modules). Mixed gas will be distributed to 24 $\times$ 140 roads through a series of manifolds.

Uniform distribution in each road will be maintained by flow resistors. Active control of the exhaust pressure and relief bubblers will be introduced to avoid an over pressure situation.

5.2.7 Structural stability of ICAL detector

The design capacity of the mechanical structure of the ICAL detector has been worked out in detail and is described in Appendix C. The study assumes a detector with 140 layers of 6 cm steel plates stacked vertically, with 48 m × 16 m plates in plane and spaced with a 2.5 cm gap in between.

The bending stress and deformation of steel plates and glass plates has been checked and found to be adequate when steel spacers separated by 2 m centre-to-centre are included for support, as shown in Fig. 5.5. The bearing width of the steel spacer and the concrete foundation has also been checked. The total load on the rock cavern due to the arrangement has been checked for the bearing capacity and is found to be adequate.

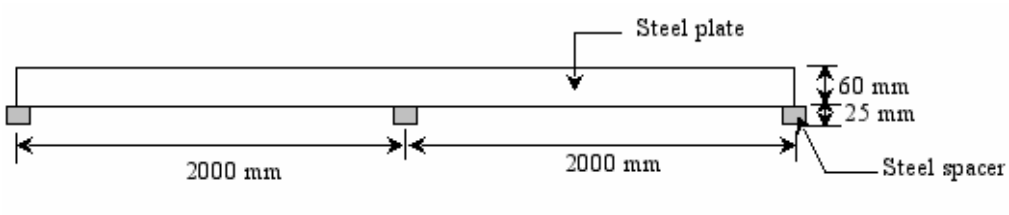

Figure 5.5: Schematic of steel structural supports for ICAL.

The possibility of orienting the plates at an angle depending on the physics requirement and its structural stability is also under consideration.

5.3 Current status of detector R & D

The development of RPCs has been undertaken at BARC, IIT-Mumbai, TIFR and SINP. We summarise the present status of the prototype fabrication and test results.

5.3.1 Gas mixing units

A gas mixture of argon, tetrafluoroethane (134A) and isobutane is required for the operation of RPCs. Sometimes a small quantity of SF_6 is also added. For the R&D stage, we have developed several 4-component gas mixing units at TIFR and at SINP.

The first gas mixing unit at TIFR, which can mix these individual gas components using rotameters and control the flow of the mixed gas through the detector chamber, was designed and developed two years back and is now being used extensively for carrying out long term tests of RPCs in the avalanche mode. A schematic of this unit is shown in Fig. 5.6. It has provision either to mix and flow the gas directly into the detector chambers or to store in a pre-mix gas cylinder for later use.

A new 16-channel gas mixing and distribution system using mass flow controllers (MFC) was designed and developed recently to be used for flowing gas to the proposed prototype detector with 12 RPCs. It mixes four input gases viz. argon, freon (134A), isobutane and SF_6 using the volumetric method. The mixed gas can be supplied simultaneously into 16 individually controlled output channels. The gas flow rate in each of output channels is kept the same using flow resistors. The return gas from the connected chambers is collected in

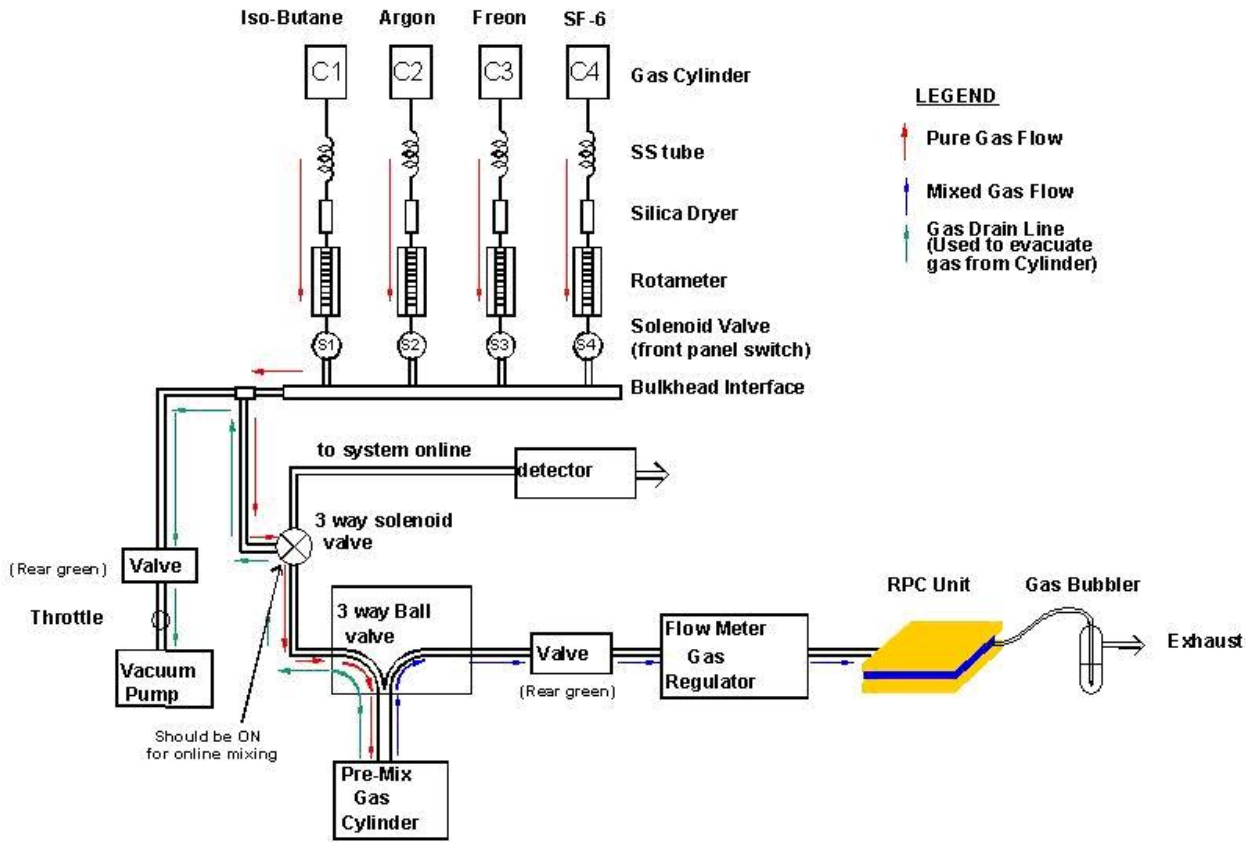

Figure 5.6: Schematic view of the first gas mixing unit and control system at TIFR.

a common manifold before it is finally vented out into the atmosphere. Gas flow at every stage of the system is achieved through the use of electrically or pneumatically operated switches or valves. The system is equipped with a host of sensors and monitoring devices and appropriate displays of various crucial operating and quality control parameters.

The main components and salient features of the system are:

1. Input gas purifier columns: Four (one for each input gas) in-situ rechargeable molecular sieve based columns, mounted on the input gas lines in order to absorb moister, oil traces and other contaminants from the input gases.

2. Gas mixing section: This crucial section is based on Tylan made FC-760 model Mass Flow Controllers (MFCs). The input section of these filters have 2 μm dust filters. Flow rates of individual gases, calibrated in Standard Cubic Centimetre per Minute (SCCM), are settable from, and displayed on, the front-panel. Small amounts of water vapour are added in the gas mixtures used for Bakelite RPCs. A provision has been made in this section for the same.

3. Moisture meter: A microprocessor based commercial (SHAW make) capacitive type sensor with a suitable display, in PPM as well as the dew point, is mounted on the mixed gas line to monitor the moisture content in the mixed gas.

4. Distribution unit: The mixed gas is distributed into 16 individually controlled gas outlets in parallel. This is achieved by using SS capillaries, 2 m long and 200 μm diameter, as flow resistors. A pressure sensor is mounted on this line to indicate the inside pressure of the system. A Parker made fine particle filter is mounted on this unit in order to purify the mixed gas further, before it enters the chambers.

5. Safety bubblers: These bubblers are mounted on individual output lines in order to take care of the back pressure exerted from, and to protect the RPCs from damage due to, over pressurising.

6. Isolation bubblers: These bubblers serve the dual purpose of preventing back diffusion of air into the RPCs as well as indicating the flow of gas through the chambers. The silicon oil levels in the safety and isolation bubblers are chosen taking into account the pressure gradient in the gas system.

7. Exhaust manifold: The return gas from all connected chambers is collected into this manifold, and a single output is provided to vent the used gas into the atmosphere. This manifold too has a pressure sensor to indicate the system pressure with reference to the ambient room pressure.

8. Remote control and monitoring: The required flow rates of individual gases in the system can be set and monitored through a PC interface. Other important system parameters such as pressures at various stages of the unit can also be monitored using this interface.

Figure 5.7: Front view of the 4-component gas mixing unit with 16 output channels.

Another gas mixing unit has also been developed at SINP. It uses mass flow controllers to mix and flow gas in the desired proportion. It can also be used in the pre-mixed mode where the gases are mixed in a definite proportion and stored in a chamber for later use. The gas proportions and flow rates can be changed through a user friendly control panel. The pressure and temperature of the output gas can be monitored. A schematic layout depicting the philosophy adopted to achieve the above goals is shown in Fig. 5.8.

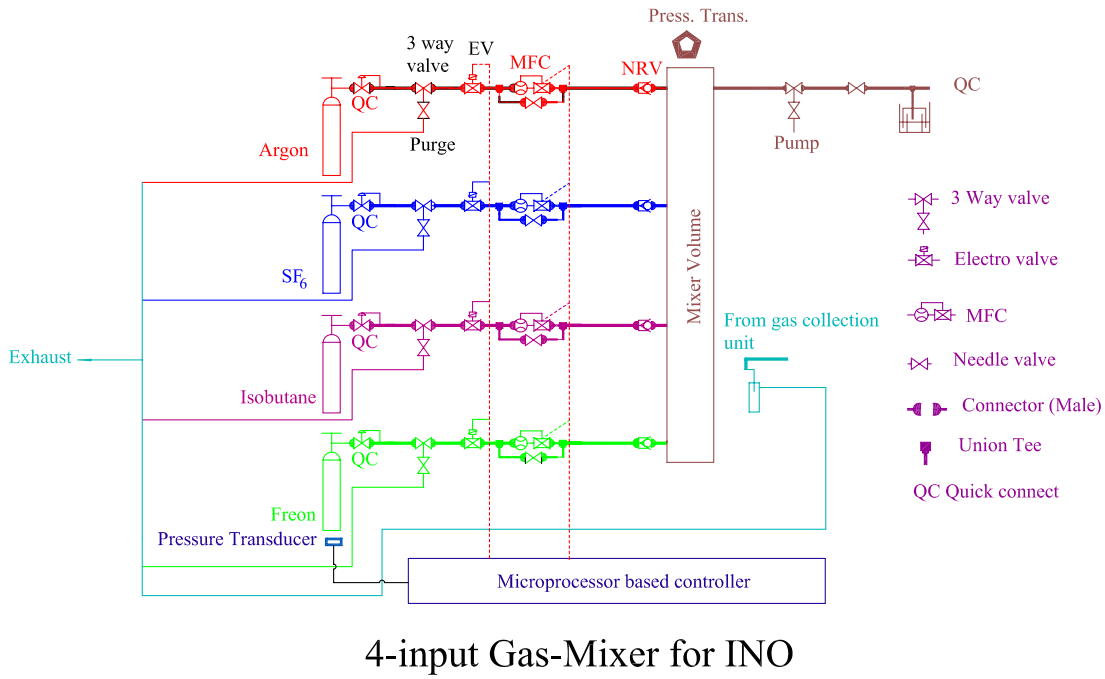

Figure 5.8: Schematic of gas mixing unit.

5.3.2 RPC operation and characterisation

A number of prototypes of the RPC have been fabricated and tested. These are described in the following.

Fabrication of prototypes

The main components of the RPC are : (a) glass plates (electrodes), (b) edge connectors and spacers (c) pick-up strips. The glass plates have to be coated with suitable conducting paint for high voltage distribution.

Several glass RPC prototypes of size 30 cm $\times$ 30 cm have been fabricated at TIFR and SINP using the construction principles outlined in Section 5.2.2. These prototypes have been made using 2 mm thick commercial float glass. The graphite coating was done using a spray technique to achieve uniformity. The method of spray-painting of graphite has been perfected to achieve a uniform coating on glass with a surface resistivity of $\sim$ 200 k$\Omega/\square$. Extruded noryl spacers of thickness 2 mm were used at 15 cm intervals between the glass plates. Edge connectors made of extruded noryl were used to seal the sides for gas tightness. The noryl components were obtained from Gran Sasso and Fermilab collaborators for the present phase of R&D. Indigenous production with suitable materials is under investigation.

Different types of pickup boards have been fabricated. The simplest ones were made of commercial double sided copper coated G10 boards (with 17 μm copper thickness, used in PCB industry) in the form of strips of a desired width. The other side of the board having continuous copper was used as ground plane. In another approach strip planes were realized using 12 mm thick extruded polystyrene insulation (used as insulation in buildings) with

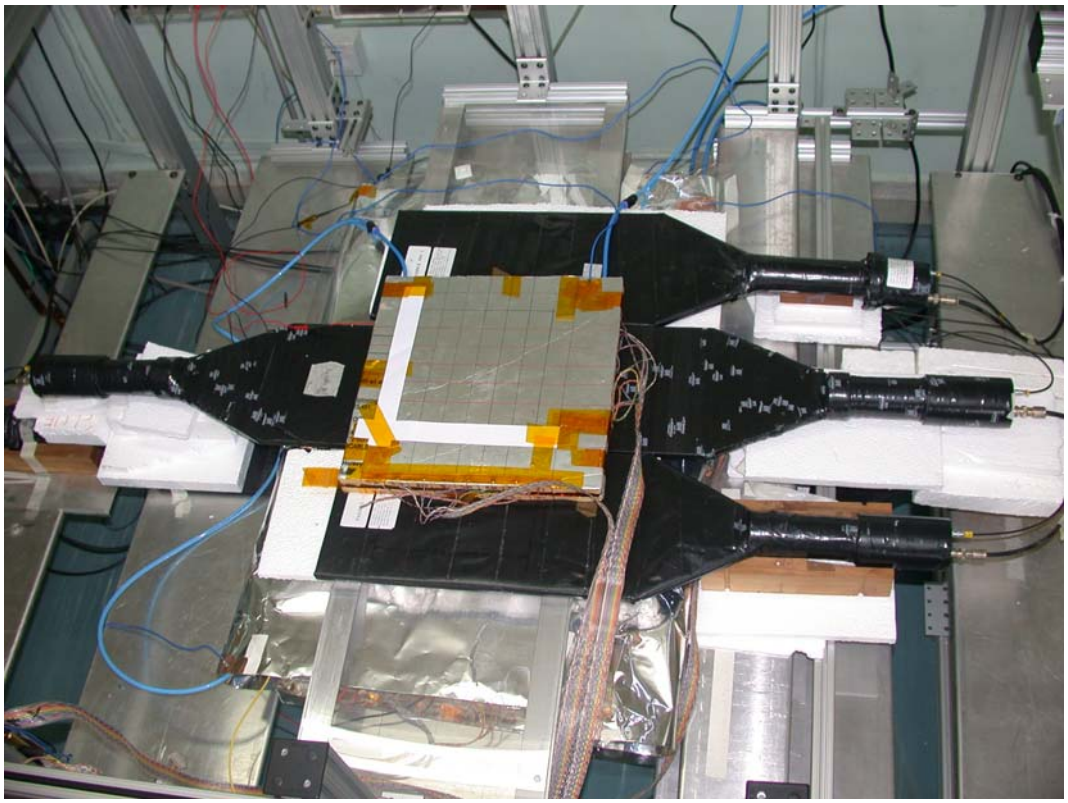

Figure 5.9: Photograph of the RPC test area at TIFR.

aluminium foil coverage on either side. Strips were machined on one side and the other side having a contiguous Al-foil was used as the ground plane.

Attempts have also been made to develop strip planes by gluing a grooved copper foil on one side of a plastic honeycomb of 3.5 mm thickness. Another copper foil without any groove was glued on the other side of the honeycomb and grounded. Furthermore, development of copper strip planes embedded between kapton foils of suitable thickness (so as to ensure electrical insulation) is also being investigated. The suitability of any of the above methods depends on various factors such as characteristic impedance of the strips, ease of fabrication in large quantities through local industry and cost.

Test setup and results

The prototypes have been tested for their performance (in the streamer mode) using a scintillator paddle based cosmic ray muon telescope. Fig. 5.9 shows the cosmic test setup at TIFR for testing RPCs. A schematic of this telescope arrangement along with the logic and timing sequence for the generation of the cosmic ray muon trigger is shown in Fig. 5.10.

The telescope consists of four cosmic ray muon trigger paddles (P1, P2, P5 and P6) and two veto paddles (P3 and P4). A paddle is made up of a scintillator tile, which is optically coupled to a photo multiplier tube (PMT) for converting the scintillation light into a fast electronic pulse. The geometry of the telescope using these paddles has been setup such that we define a window of about 14 cm $\times$ 2 cm (increased to 20 cm $\times$ 20 cm recently, enhancing the muon trigger rate by by a factor of $\sim$ 15 with a marginal worsening in time resolution) for the cosmic ray muons to pass through the telescope as well as through the RPC. The data from RPC pick-up strips is recorded whenever a cosmic ray muon generates a trigger signal through the following logic:

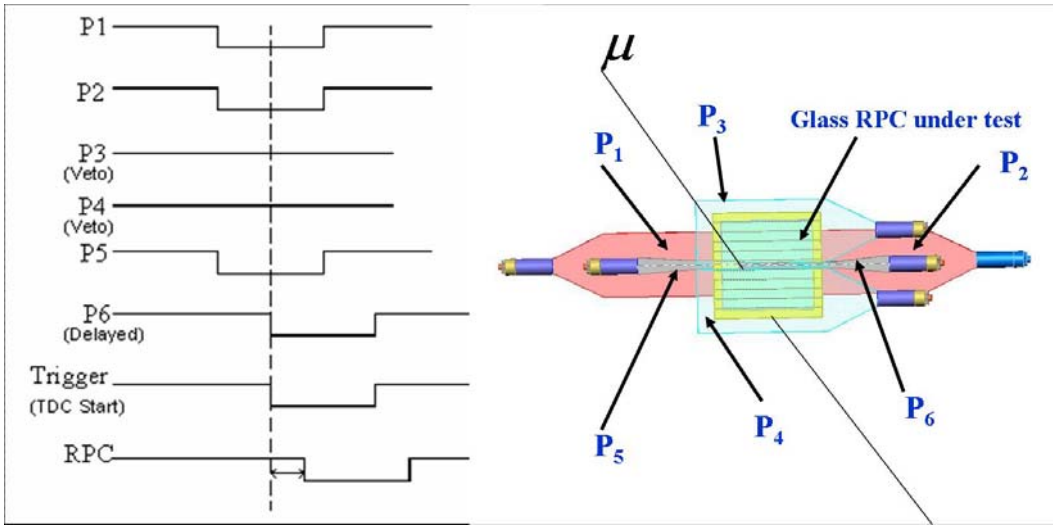

Figure 5.10: Schematic of cosmic ray telescope and muon trigger timing sequence.

$$\text{Muon trigger} = P_1.P_2.\bar{P}_3.\bar{P}_4.P_5.P_6$$

The efficiency of the glass RPC in the above setup is defined as the ratio of number of coincident muons recorded in the RPC to the number of muon triggers generated by the telescope.

Fig. 5.11 shows plots of the RPC efficiency as a function of high voltage applied between the glass electrodes for different gas mixtures. Plateau efficiencies of over 90% have been obtained for all the gas mixtures beyond 8.5 kV.

Fig. 5.12 shows the timing resolution σ as a function of applied voltage for one of the prototype RPC modules. As can be seen from the plot, the timing resolution improves with the increase of operating high voltage and reaches a value of about 1 ns in the plateau region.

Fig. 5.13 shows a typical mean pulse height (charge) of an RPC as function of its operating high voltage. The plot indicates a linear response while the standard deviation of the pulse height distribution is fairly constant.

The noise rate of an RPC is the individual counting rate of its signals above an operating threshold. These signals are produced by the cosmic ray charged particles of multiple energies as well as due to the dark current of the chamber. This rate per unit cross-section area of a particular RPC should be constant when integrated for a reasonably long period. The noise rate serves as a good measure to monitor long term stability of the chamber as well as its dark current. For instance, if the dark current of an RPC increases drastically, it will be indicated by a sharp increase in the noise rate. This will result in reduction of actual voltage across the electrodes and hence the chamber's gain as well as its efficiency. Fig. 5.14 shows a fairly linear dependence of the noise rate of the RPC on the applied high voltage. At the operating voltage of 8.5 kV, the noise hits are only $\sim$ 1/strip/s, which is well within the acceptable values.

The spatial resolution of the detector is mainly determined by the pitch of the pick-up strips. However, this is limited by the cross talk between the adjacent strips. Among many factors that contribute to the cross talk, electrical characteristics and thickness of the pickup strips as well as the driving scheme of the picked-up signals are the most important. The chambers that we had fabricated have shown a cross talk of about 6% between adjacent pick-up strips.

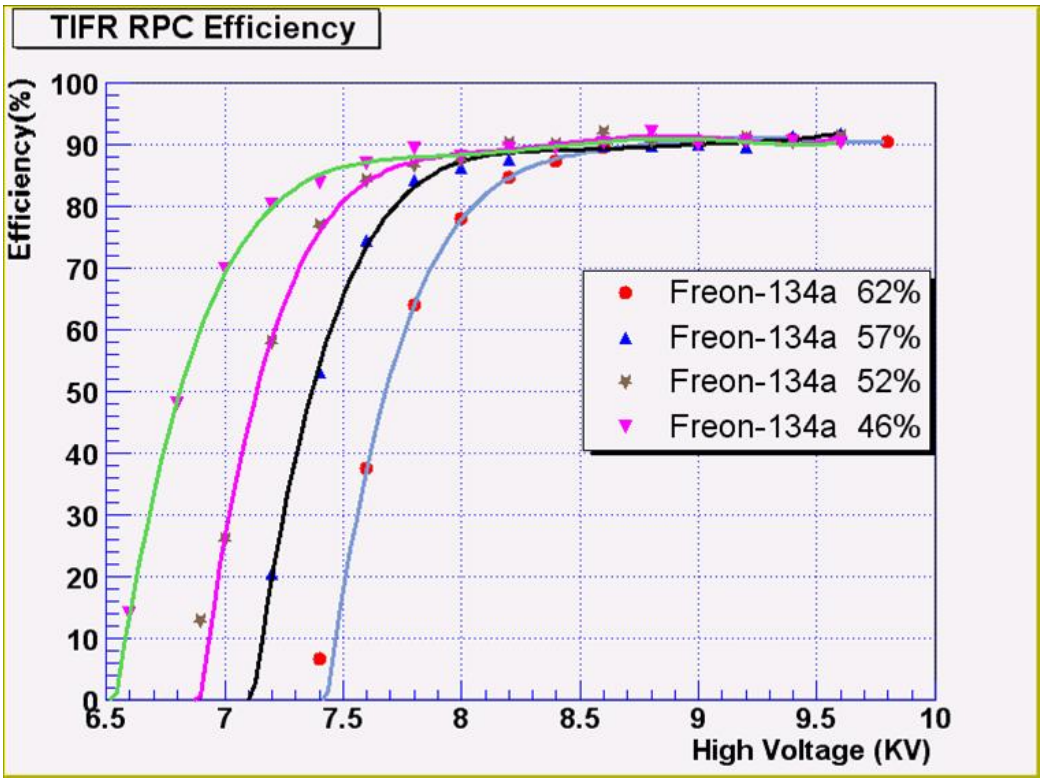

Figure 5.11: Efficiency plot of RPC as a function of applied voltage for various gas mixtures.

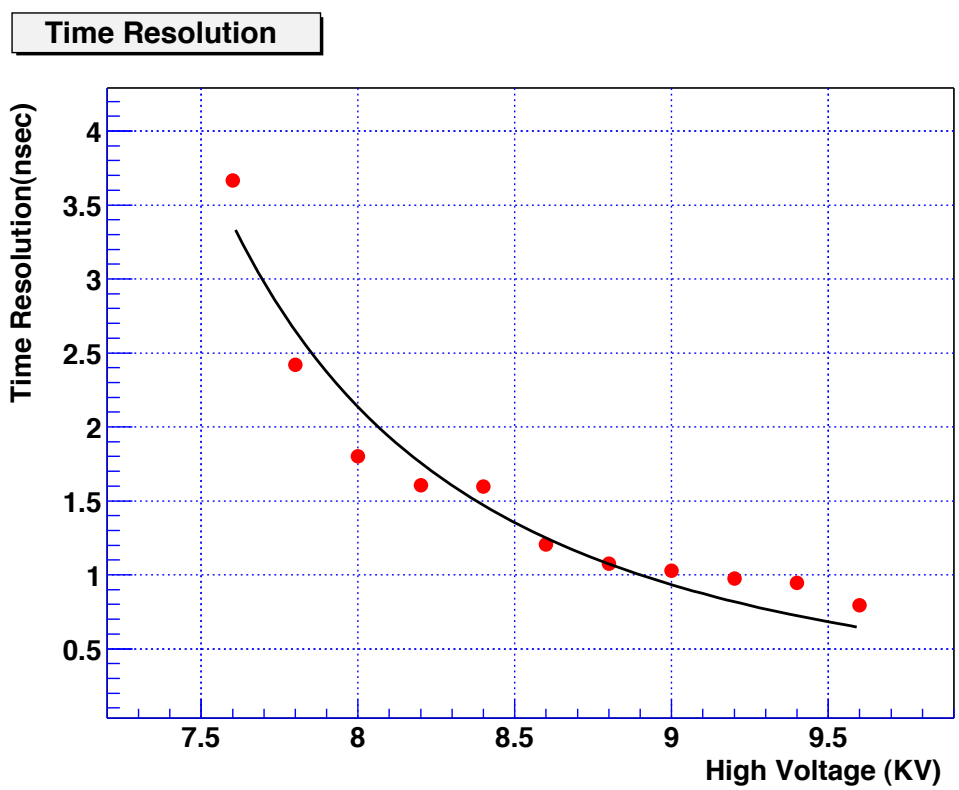

Figure 5.12: Typical timing resolution (σ) of an RPC as a function of applied voltage.

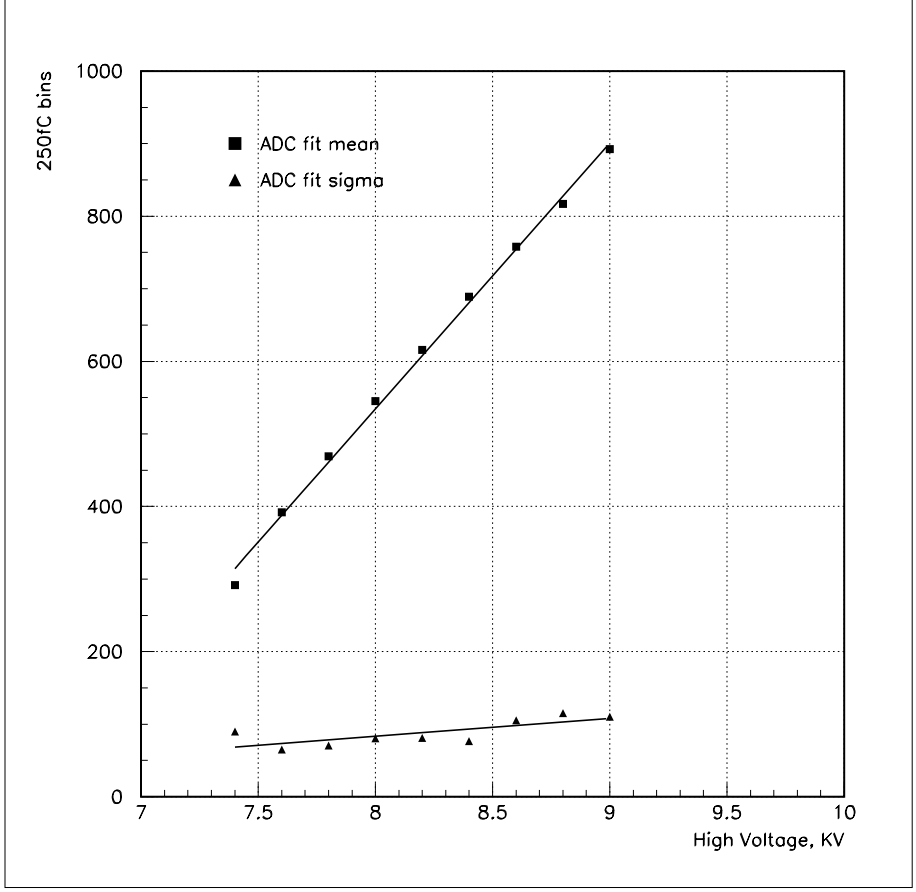

Figure 5.13: Typical mean charge (in arb. units) as a function of applied HV across an RPC.

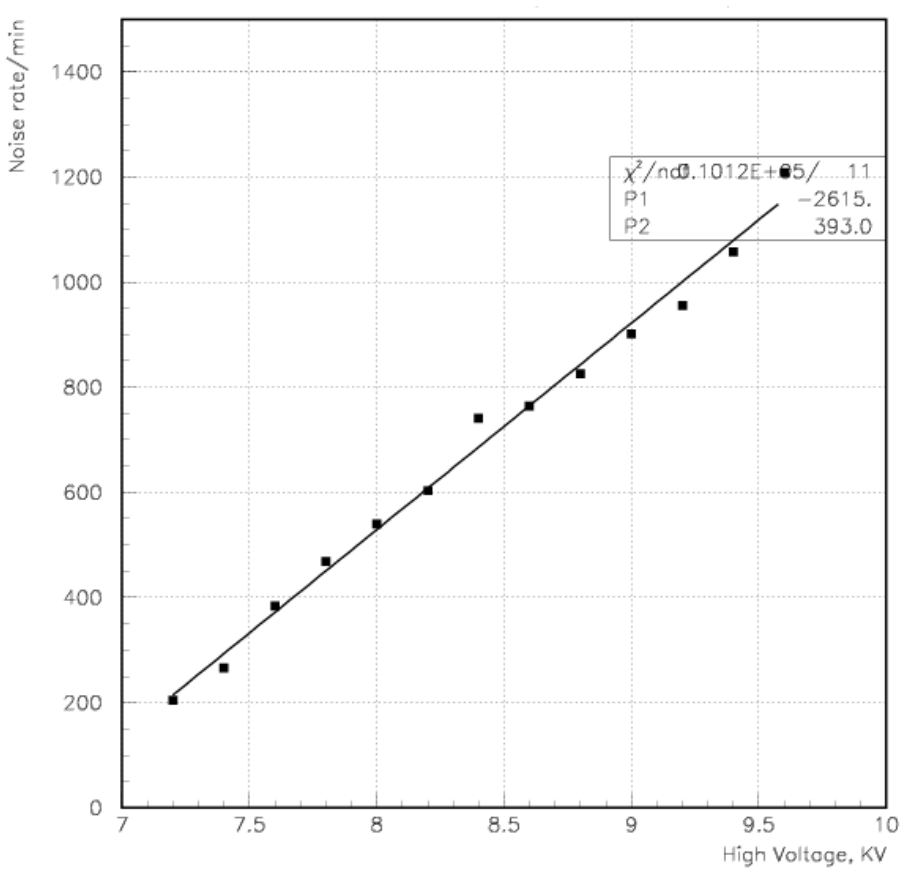

Figure 5.14: Typical noise rate plot of the RPC.

5.3.3 Long term stability tests of INO RPCs

Although glass RPCs operating in the streamer mode are known to be stable and have a long lifetime (more than 5 years) as evidenced by the successful operation of these chambers by the Belle Collaboration, those made by us earlier had a much shorter life time. While the problem of short lifetime of the glass RPCs produced by us is being investigated, we fabricated a few RPCs of dimension 40 cm $\times$ 30 cm using glass procured from Japan (from the same source as used in Belle RPCs). The same procedure for fabrication as well as testing as in the case of earlier RPCs was followed for these new chambers using Japanese glass. Two of these new chambers (called J2 and J3) are currently being operated in the avalanche mode, in which a gas mixture of freon (R134a) and isobutane in the proportion 95.5 : 4.5 by volume is used. The chambers are operated at a high voltage of 9.3 kV. Since the pickup signals in the avalanche mode are in the range of few millivolts, external amplification has been provided by preamplifiers of gain 10. The rest of the electronics and data acquisition chain is the same as that used earlier.

A comprehensive monitoring system for the periodic recording of the currents of these two RPCs as well as the ambient parameters such as temperature, pressure and relative humidity both inside and outside the laboratory has been designed and implemented. Using this data several correlations between the ambient parameters and the RPC operating characteristics could be established. The long term stability tests were started on these two chambers from September 2005. As can be seen from the plots in Fig. 5.15, the performance of these chambers, characterised by their efficiency, leakage currents and noise rates, have not changed over the last seven months. These tests indicate that the aging problem associated with the previous RPCs is related to the quality of glass plates used to fabricate those RPCs. While continuing with this long term stability test, we are also in the process of fabricating large size chambers using glass obtained from the same Japanese source.

5.3.4 Tracking of cosmic ray muons using small size RPCs

A separate laboratory has been setup for this test, in which the newly developed 16 channel gas mixing unit described earlier was installed. The RPCs for this setup were fabricated using the same materials and fabrication procedures and parameters as those described earlier. Float glass of thickness 2 mm and size 30 cm $\times$ 30 cm was used. RPCs using glass from different manufacturers were also used in the setup. This was done in order to make a comparison of the RPCs made using the glass sheets from different vendors and their deterioration with time.

A suitable rack to house 12 RPCs of the above size was fabricated. The rack allows easy access to any individual chamber in the stack. It also integrates a spring loaded mechanism to keep the signal pickup panels pressed uniformly against the chambers.

The cosmic ray muon telescope seen in Fig. 5.16 was set up using seven scintillator paddles. These include one narrow paddle of 2 cm width to define the telescope window such that it centres on an individual signal pickup strip as well as two more to veto muons which are passing outside the strip of interest. This allowed a measurement of the cross talk between adjacent strips.

A stack of 10 RPCs, as seen in Fig. 5.17 was mounted in the above mentioned rack such that the signal pickup strips of all the chambers were well aligned geometrically. The chambers were operated in the streamer mode, using a mixture of argon, isobutane and freon (30:8:62 by volume) from the new gas system described above. The operating high voltage for the tests was kept at 8.6 kV. The high voltage supply current was monitored online to diagnose any possible instability in the RPCs.

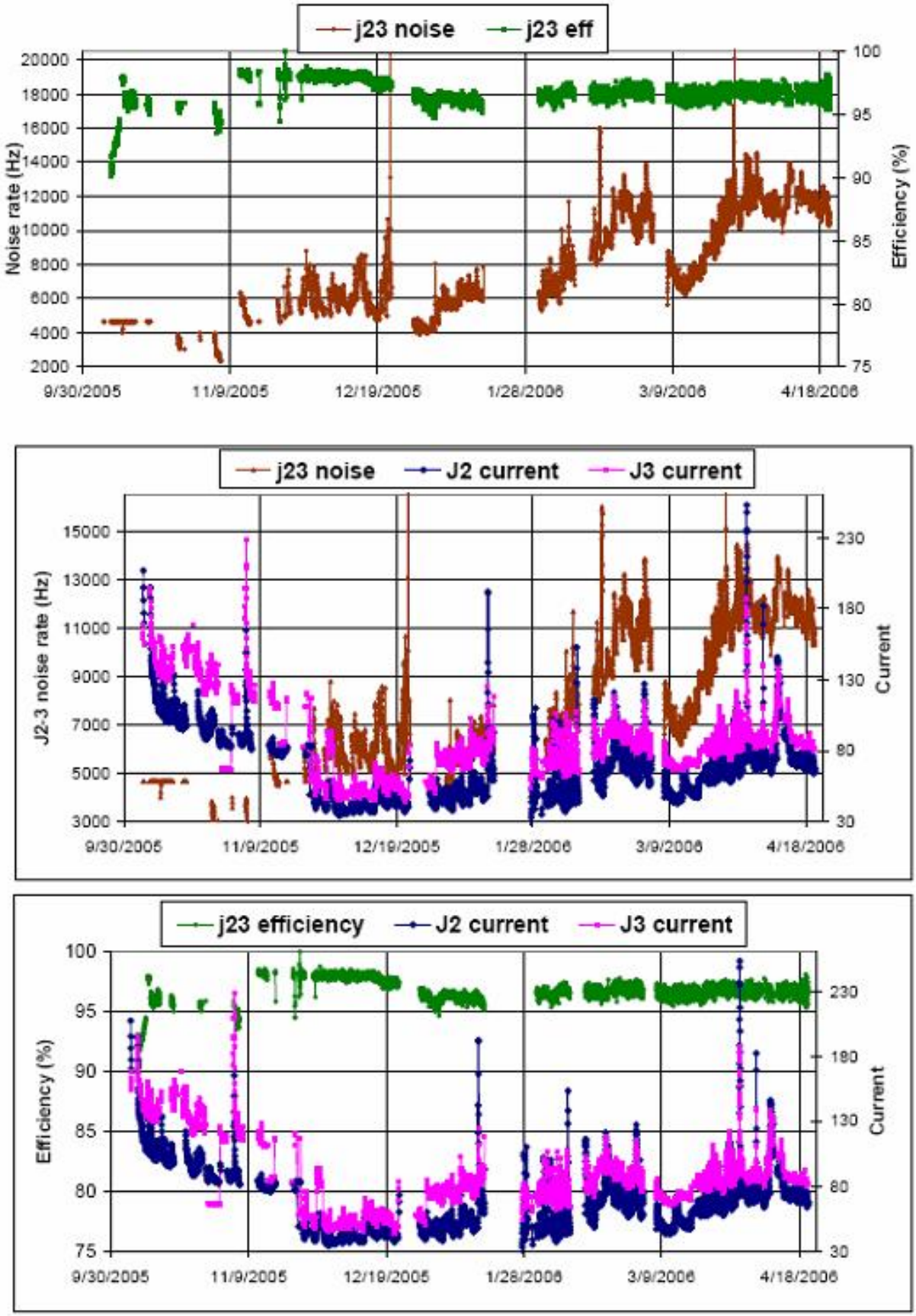

Figure 5.15: Long term stability monitoring plots of J2 and J3 RPCs.

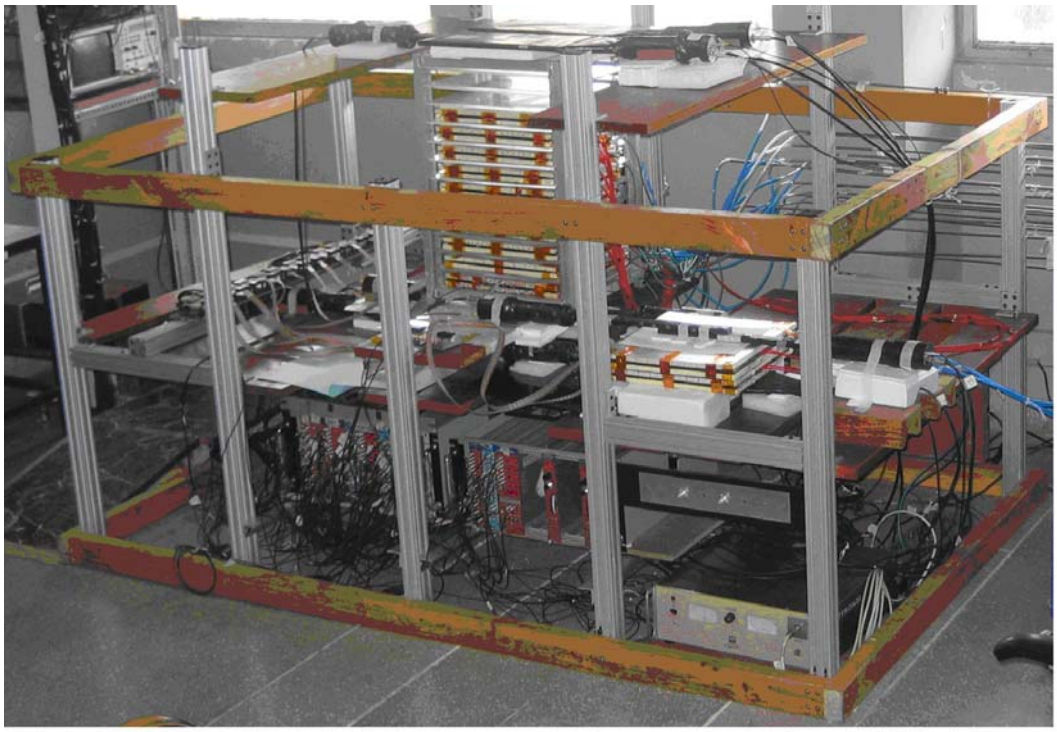

Figure 5.16: Muon tracking setup using RPC stack.

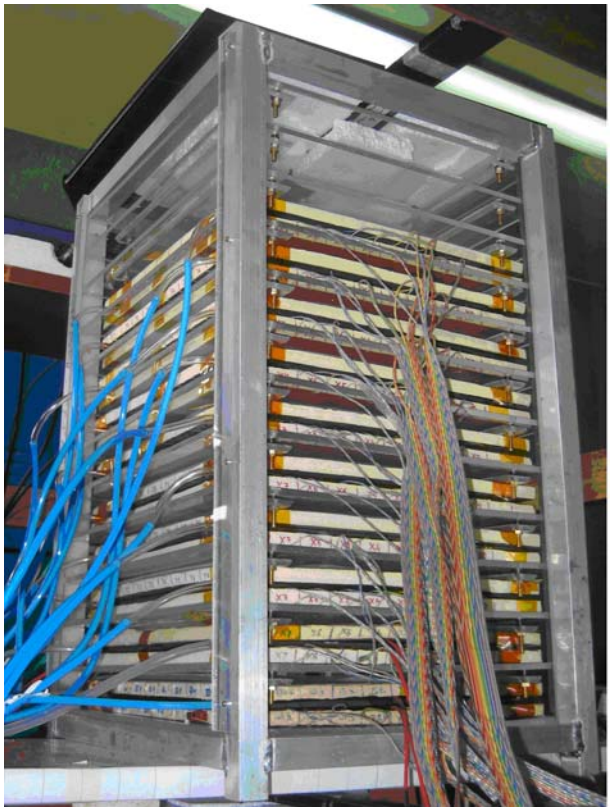

Figure 5.17: Close-up view of the stack of 10 RPCs mounted in a rack.

The signals from the pickup strips were transmitted through twisted pair cables onto patch panels, where the line impedances are transformed in order to match those of the NIM electronics. The RPC strip analog signals are fed to discriminator and latch modules. The cosmic ray telescope trigger signal is used as the strobe signal for the latch modules, which record binary information on the presence or absence of a signal on the RPC strip of interest for every trigger. The counting rates of the RPC strips of interest are measured with scalers using the corresponding logic signal. The logic signals from the strips are also used to record the timing information from the RPC, with respect to the cosmic muon trigger, using TDC modules. The strips of only one pickup panel are read out.

Fig. 5.18 shows some interesting cosmic ray muon induced tracks recorded using the above setup. Muons arriving at different angles could be captured simply by relocating the telescope window. This has demonstrated that indeed these prototype chambers are capable of effectively tracking cosmic ray muons.

The information recorded in these tests could also be used extract other parameters of interest, such as efficiency, noise rate and timing of individual RPCs and their long term stability. Parameters such as temperature, barometric pressure and relative humidity are also being monitored on-line in order to collate and correlate the dependence of chamber performance on these ambient parameters.

It was also established from these studies that the chambers made with Modi, Asahi and Saint Gobain float glasses suffered from the aging problem which was observed in the previous studies. However an RPC fabricated using the glass procured from Japan is surviving the long term stability tests up to the time of writing this report.

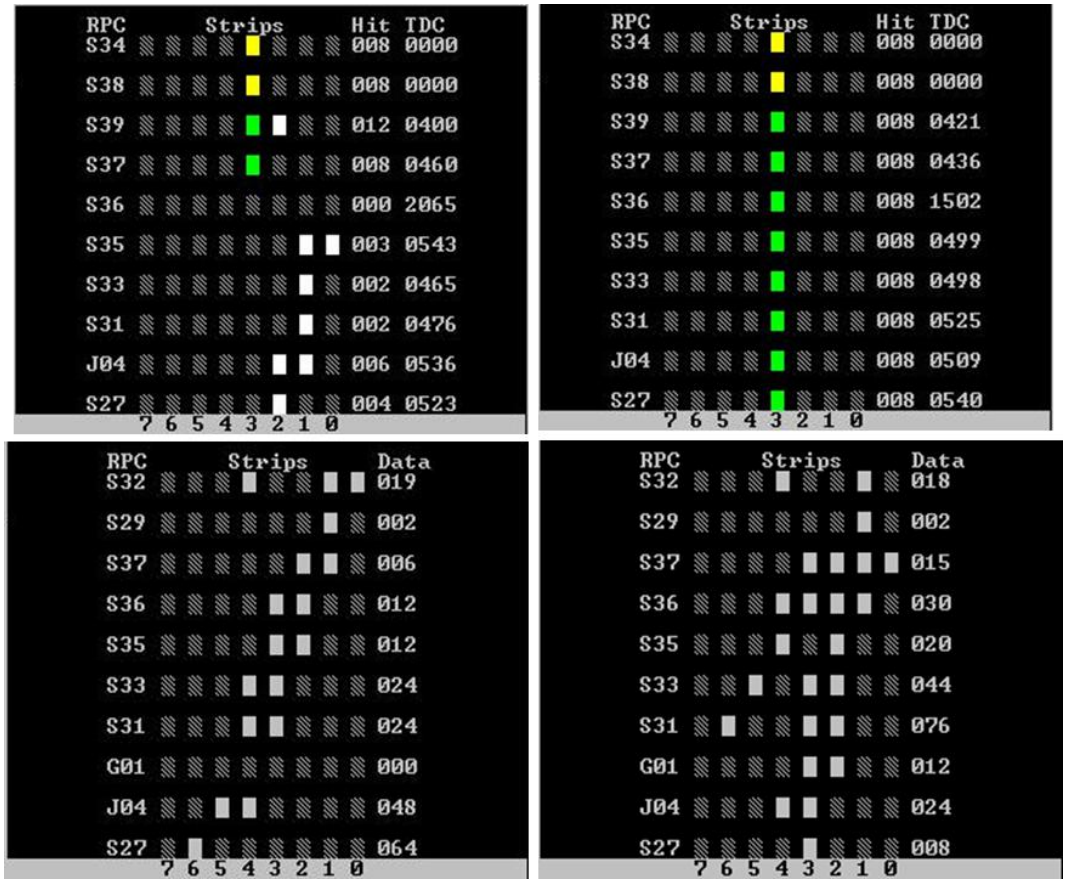

Figure 5.18: Some interesting tracks recorded in the detector.

5.3.5 ICAL Prototype

1 m^3 prototype

For the first stage of the ICAL prototype, it is planned to construct a set of 12 RPCs, having dimensions of 1 m $\times$ 1 m. These will be integrated within a magnetic volume for detailed tests on the position resolution of the detector and its momentum measurement capabilities. The detectors will be housed within 13-layers of steel plates, providing a magnetic volume of 1 m^3 for the prototype calorimeter. It is proposed to test this prototype using both the cosmic rays and beams of pions and muons from accelerators. This prototype detector will also be used to verify the results obtained from the physics and detector simulation studies that are currently underway as well as provide feedback to the simulation group.

Fig. 5.19 shows a picture of a 1 m^2 RPC fabricated at TIFR. This prototype has also been fabricated using commercial glass and noryl elements procured from collaborators. A uniform gap of 2 mm is maintained by using spacers at 15 cm intervals. Preliminary tests of this chamber are underway. The magnet for this prototype is described in Section 5.4.3

Figure 5.19: Photograph of 1 m^2 RPC module with its pickup strips to be used for the ICAL prototype.

Readout for ICAL prototype

The electronics, trigger and data acquisition systems will need to handle about 900 channels for the ICAL prototype. We plan to design and fabricate the front-end sub-systems for the trigger, event data readout and monitoring systems in-house and configure the back-end on the CAMAC data acquisition standard. This way we will use the hardware and expertise which exists within the collaboration allowing a quick deployment of the electronics and data acquisition system.

A schematic of the readout electronics for the prototype detector is shown in Fig. 5.20. There will be one front-end board per signal plane per layer of the detector. Detector signal conditioners, translators, Boolean latches, multiplexers for event data and monitoring and trigger system as well as timing measurement primitives are some of the major components that reside on the front-end board. Event data from either signal planes of a layer are mixed and routed to the back-end on high-speed serial links. The CAMAC back-end is driven by a Linux host and will house the master trigger generator, TDC, scaler, real-time clock and other front-end control modules.

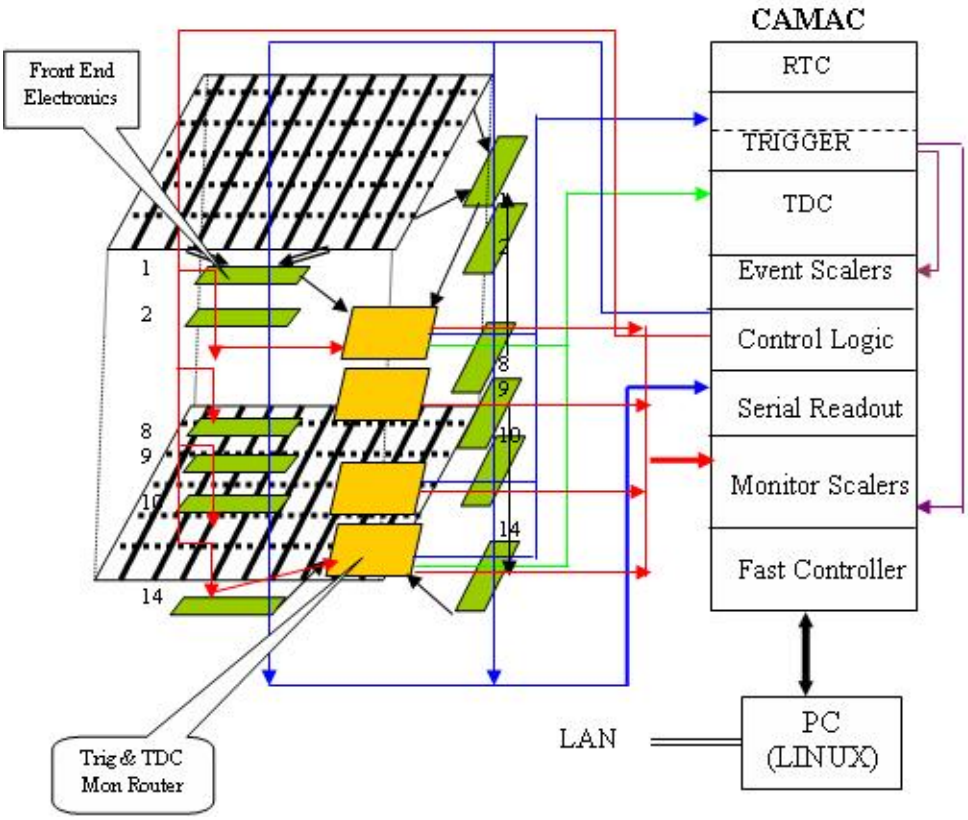

Figure 5.20: Schematic of the read-out electronics for the 1 m^3 prototype detector.

5.4 The Magnet

The ICAL detector has the twofold purpose of providing target nucleons for neutrino interactions and a medium in which secondary charged particles can be separated on the basis of their magnetic rigidity so that their momenta can be estimated. A stack of magnetised iron plates interlaced with position sensitive gas detectors make up the ICAL calorimeter. As discussed in Section 5.2, the total mass of magnetised iron required is 50 kton to start with, which may be finally enlarged to 100 kton. This makes it the single largest component in the calorimeter.

In this section we describe the design criteria of the ICAL magnet and a set of preliminary design results obtained using the 3D commercial code MagNet 6.0 [153]. A smaller prototype magnet has also been designed using this code. This magnet will be used with prototype RPC detectors for test and calibration purposes.

5.4.1 Design criteria

The magnetised iron calorimeter will consist of about 50 kton of low carbon steel. The carbon percentage should be 0.1% or less in order to have a good magnetic characteristics. ASE1010 or C10 steel will be suitable for this purpose. The detector will have a modular structure of lateral size 48 m $\times$ 16 m and a height of 12 m. It will consist of layers of horizontal iron plates interspersed with glass RPCs as active detector elements. The thickness of the steel plates will be $\sim$ 6 cm and the gap for inserting the glass RPC detectors will be 2.5 cm. The steel plates in the proposed detector system will be magnetised to a magnetic field of $\sim$ 1.3 T by using copper coils.

The design criteria for the ICAL magnet are basically the following :

- **Field uniformity**

  The performance of the detector will be the best when the magnetic field is uniform. An iron block can be uniformly magnetised by placing the coil surrounding the block. However, the electric power needed for magnetising a block of 50 kton will be prohibitive. Apart from that, the field will be present in a large air volume outside the magnet. In order to overcome these problems we adopt a gap-less (devoid of poles) toroidal design. In this design the magnetic field is predominantly inside the iron and field leakage outside is minimal. A similar design has been adopted by MINOS [154].

- **Modularity**

  A calorimeter with 50 to 100 kton of steel can only be realized if a modular structure is adopted from the beginning. The ICAL magnet will have a modular structure. Even in the basic design with 50 kton of steel, the detector and the magnet will be made in three modules. The modules can be added at any stage later, either singly or in pairs.

- **Optimum copper-to-steel ratio**

  The copper to steel ratio decides the cost and the electrical power consumption. If we take a larger ratio then the power consumption is low resulting in lower running cost but higher fixed cost. The opposite situation leads to higher running cost but lower fixed cost. Besides the cost the total permissible power dissipation may be limited by the cooling capability of the environment in the tunnel.

  The heat dissipation in the coil depends on the volume of copper used. A small amount of copper reduces the copper cost but dissipates a large amount of heat which one has to remove by using low conductivity water (LCW) flow through hollow copper conductors. This is the method in the near and far MINOS detectors [154]. Here, although the copper inventory cost is reduced, both the fixed cost (of the LCW plant and plumbing) as well as the running cost of the LCW plant go up significantly. If the temperature rise of a few degrees Celsius can be tolerated by the detector components, one can avoid the use of water flow by using a larger amount of copper so that the rise in temperature in the coil remains within the required limits. Such a design may be preferred from environmental considerations and also the fact that an uninterrupted period of usage of the order of 25 years is envisaged.

- **Access for maintenance**

  Modularity is of utmost importance from the point of view of accessibility to provide maintenance. The 100 kton magnet will have 6 modules whereas the total number of detector modules will be $\sim$50000. Hence quick replacement of faulty detectors will decide the overall availability factor of the ICAL detector. The modular design ensures

that the faulty elements can be easily replaced with the least effort. This amounts to minimising the distance that needs to be accessed to reach the faulty detector.

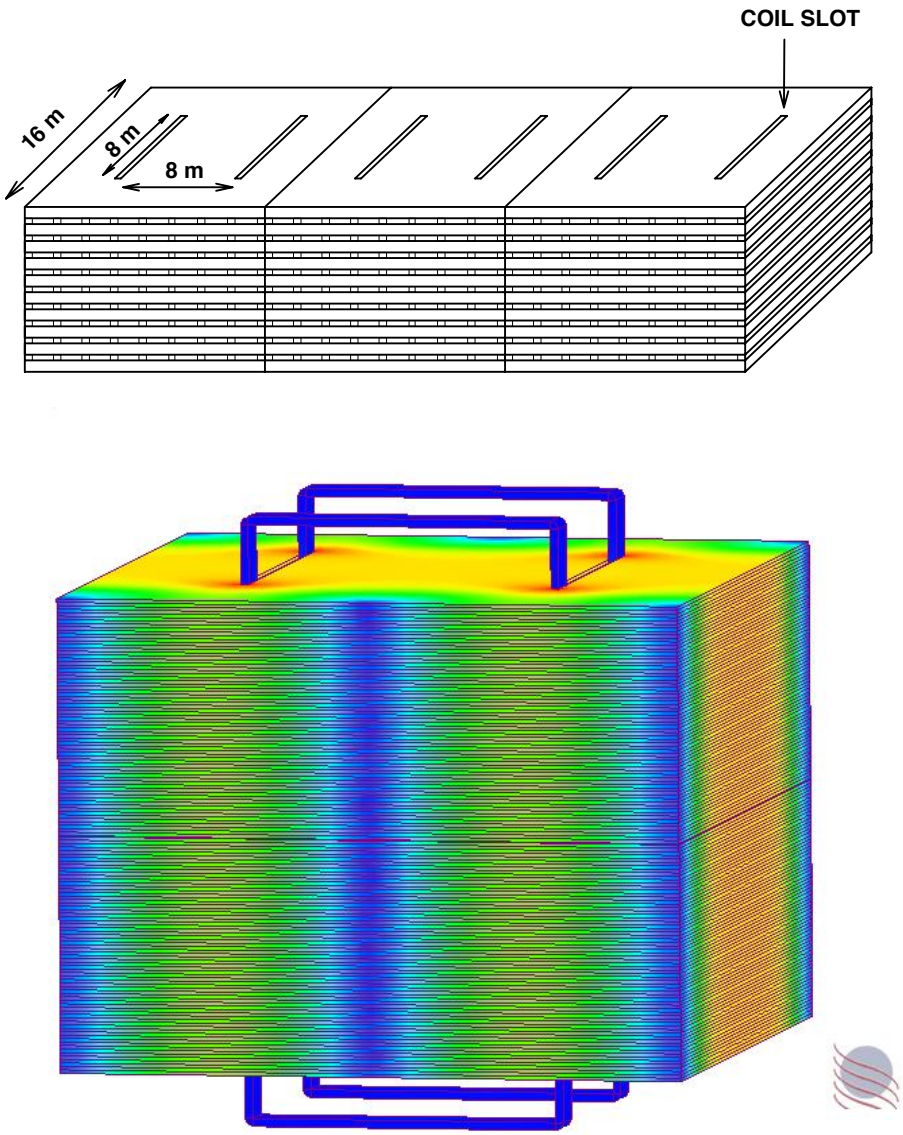

Figure 5.21: Top: ICAL magnet (three modules) showing the coil slots and the iron plate arrangement. Bottom: one module of the magnet with the coil inserted. Field uniformity can be judged by the colour pattern.

5.4.2 A toroidal design for the ICAL magnet

In the toroidal (gap-less) design, the copper coil goes through two rectangular slots in the stack of steel plates. Fig. 5.21 (top) shows the arrangement of the iron blocks with the coil slots in the ICAL magnet. Fig. 5.21 (bottom) shows the arrangement of the coil in the ICAL magnet and the field lines. The blue colour of the coils indicates negligible magnetic field inside the coils. The length, breadth and the positions of the slots are chosen to generate a uniform field in as large a volume of steel as possible. The design also facilitates insertion/removal of RPC trays from the sides (working perpendicular to the larger axis). The small cross-section of the copper conductor (1 cm $\times$ 1 cm) and the small width (20 cm) of the coil ensures negligible loss of active volume of the detector.

A coil with 40,000 amp-turns is needed for producing a field of 1.3 T in one module. The calculated magnetic field lines in a typical layer of the horizontal plates are plotted in Fig. 5.22. The arrows show the reversal of the field on the two sides of the coils. The variation of the field along the z-axis is shown in Fig. 5.23. Over the entire set of plates the variation is within 0.3%, the field varying by less than 0.15% over a height of ± 5 m from the centre. The variation of the field in y- and x- directions is shown in Fig. 5.23 and Fig 5.24 respectively. The field is quite uniform in the x-direction, varying by less than 0.25% but in the y-direction it starts falling beyond the length of the coil slot (± 4 m).

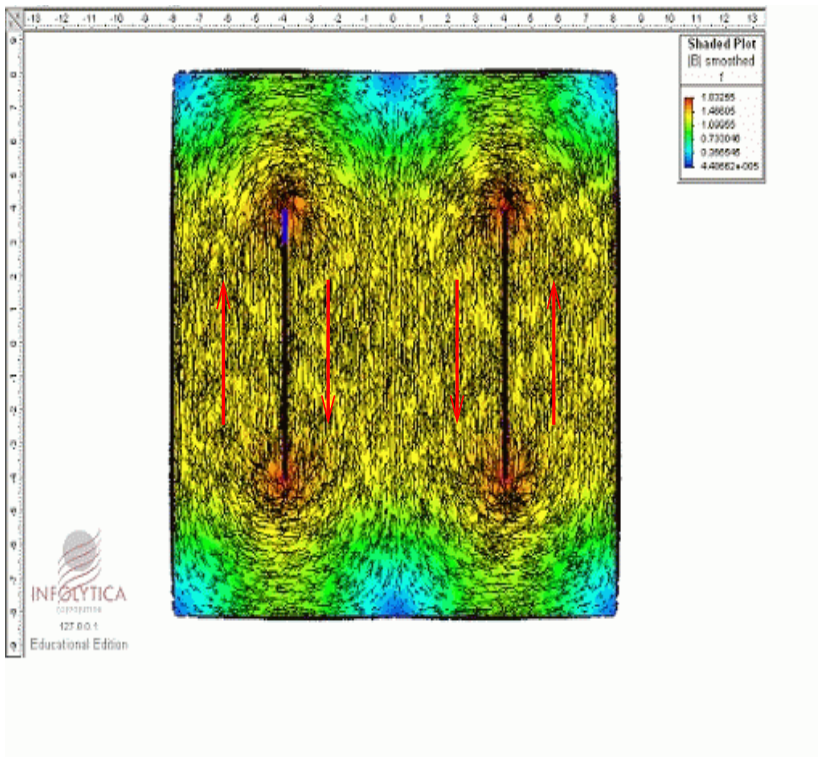

Figure 5.22: Field lines in a horizontal (x-y) plane of any of the iron plates, the arrows denote the field direction.

Table 5.3 gives the mechanical and electrical specifications of the magnet and the coil. We propose to use a solid copper conductor cooled by conduction through the iron plates and by radiation from the iron surface. Estimates of cooling due to conduction and radiation suggest that the rise in temperature is within a few degrees Celsius. Further cooling, if required, can be done by a forced air draft.

A model in the 1:100 scale of one ICAL module has been fabricated using only two layers of iron. Fig. 5.25 shows the schematic drawing and the photograph of the model. As the field inside iron cannot be directly measured, a slot has been cut dividing the magnet into two parts. The field has been measured inside the slot using a Hall probe.

Fig. 5.26 compares the measured field with the field calculated by using the POISSON code [152]. The measured field compares well with the calculated values.

In the actual magnet the field can not be measured by creating a slot. An estimate of the field can be obtained by using a wire loop (around the plates), which will pick up a signal when the magnet is being energised. The integrated signal will give a measure of the average field inside the loop.

Since a layer of iron will consist of many plates joined together, one should specify the allowable gaps in plate joints. We have studied the effect of having a gap between the plates.

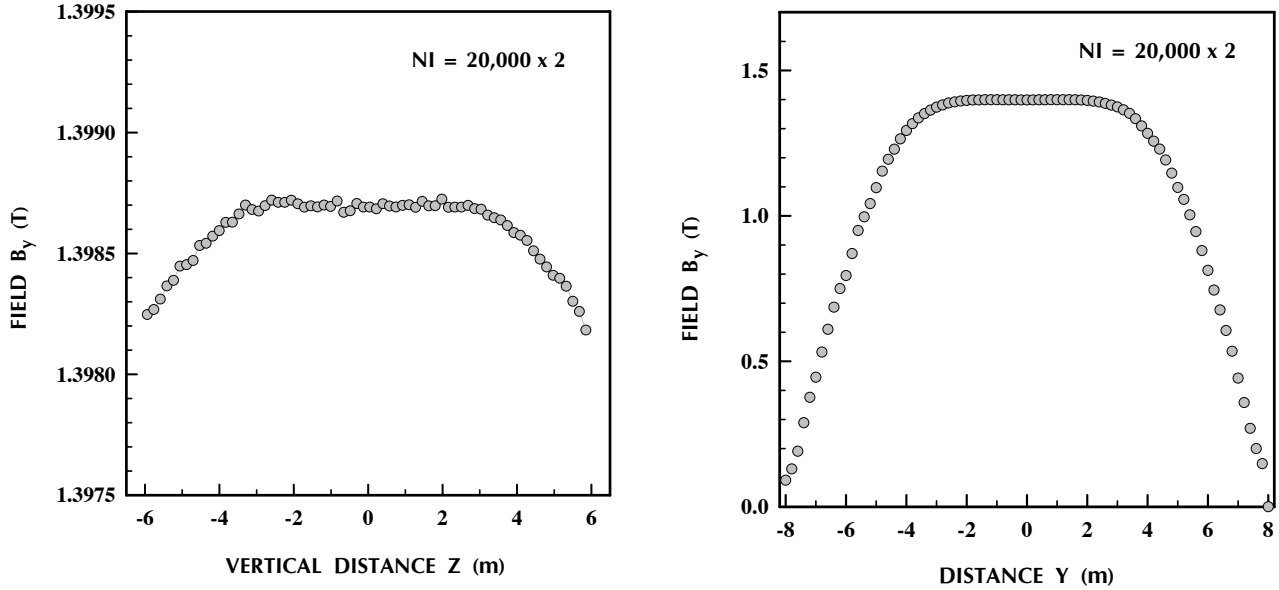

Figure 5.23: Left: Variation of field strength in z-direction, between horizontal plates. The value of NI is given in Amp.turn. Note the expanded scale. Right: Variation of field in a direction parallel to the coil slots.

Fig. 5.27 shows that for a gap of 1 mm the field changes by about 200 gauss. This suggests that one should minimise the gaps within the constraints of mechanical engineering and costs.

5.4.3 A small magnet for detector prototype tests

For the tests of 1 m^3 ICAL prototype described in Section 5.3.5 it is necessary to have a uniform magnetic field over the entire volume of the prototype detector which is also free from edge effects. In particular it is important that the field should not change direction within the given detector volume. It is also necessary that the design of the prototype magnet should be similar to that of a module of the full magnet so that not only the RPC detectors but also the design philosophy of the magnet is tested at the same time. The MagNet 6.0 3-D software has been used for the design of this magnet.

The prototype has been proposed to have the shape of a rectangular parallelepiped of dimensions 2.4 m $\times$ 2.2 m $\times$ 0.95 m. The thickness of the steel plates is 5 cm as these (Tata A grade magnetic steel which is similar to the low carbon C10 variety) are readily available. The gap between the plates is 2.5 cm, the same as that for the full magnet. The total weight is 26.6 ton. Several possibilities exist in the choice of the coils that carry current to energise the electromagnet. We have opted for two pairs of copper coils going through two rectangular slits in the magnet. This should provide a uniform magnetic field over the active volume of the RPC detector. Fig 5.28 shows the arrangement of the iron plates and the copper coils in the magnet. The magnet specifications are given in Table 5.4.

This design leaves both the sides in one direction open for pushing in and out the gas detectors. The total amount of copper is 218 kg. The power dissipation at 4000 $\times$ 2 Amp-turns, producing a field of 1.4 T, is about 1 kW. This dissipated power can be removed by air cooling. The stored magnetic energy is 10 kJ. The specification of the power supply depends on the size of the conductor to be used. For a conductor size of 0.5 cm $\times$ 0.5 cm, the current required is 40 A and the voltage is 25.6 V. So a 30 V, 50 A power supply will be needed for energising the magnet. Conductors of smaller dimension will reduce the supply

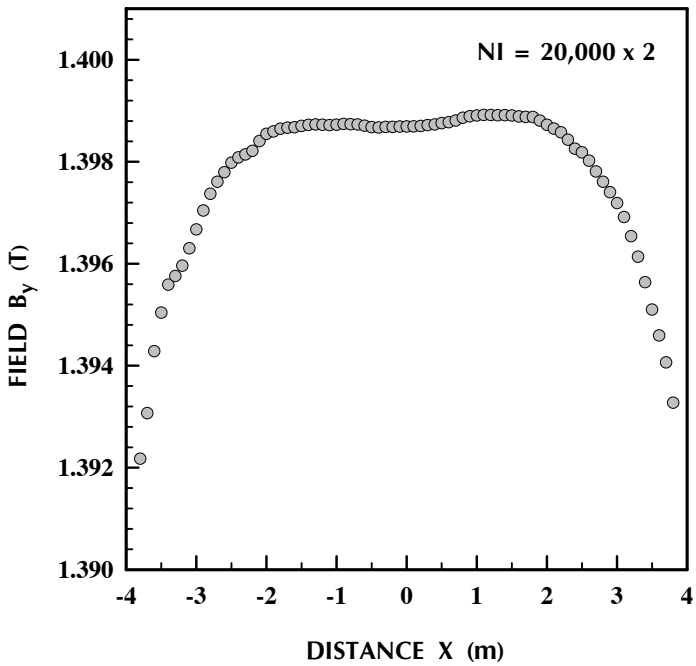

Figure 5.24: Field uniformity in between the two coil slots. The value of NI is given in Amp.turn.

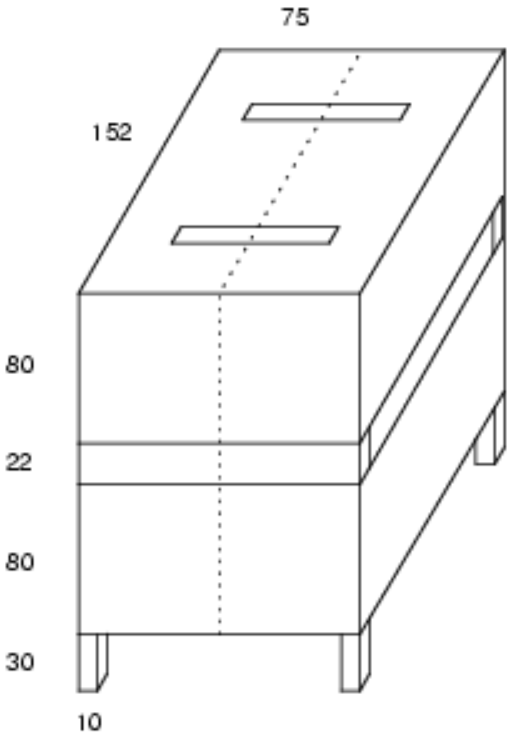

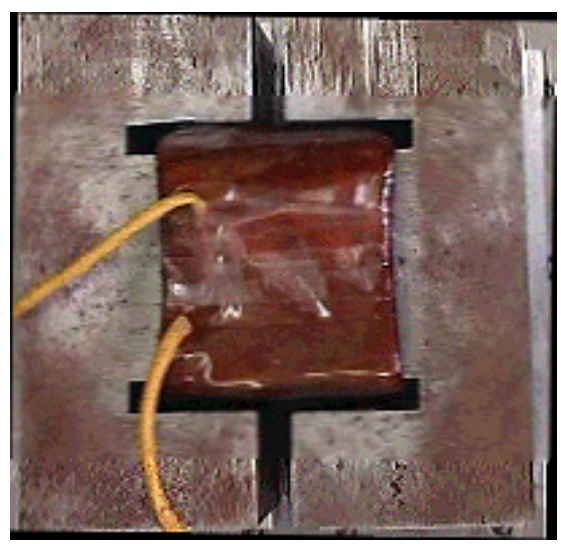

Figure 5.25: Left: Schematic drawing of the 1:100 scale model, Right: Photograph of the 1:100 model magnet with split iron pieces.

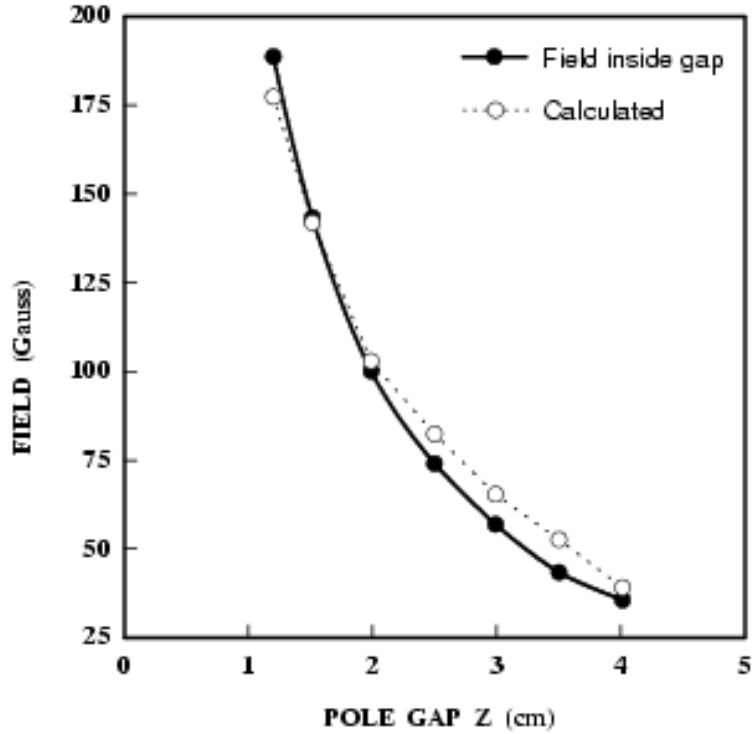

Figure 5.26: Calculated and measured field within the gap of the 1:100 prototypes.

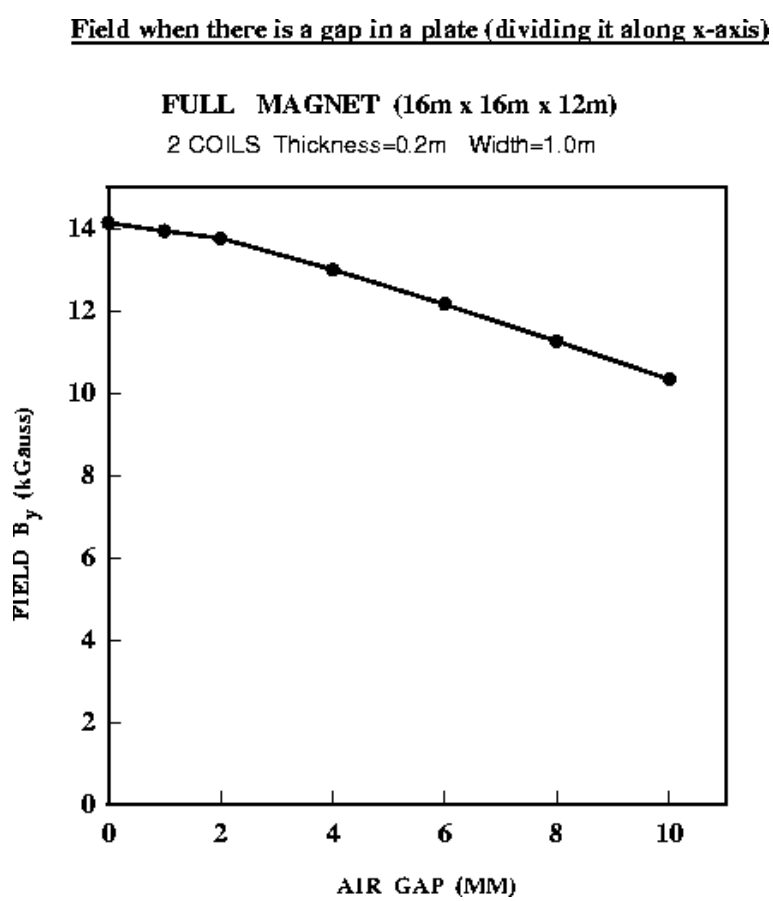

Figure 5.27: Field uniformity in between the two coil slots.

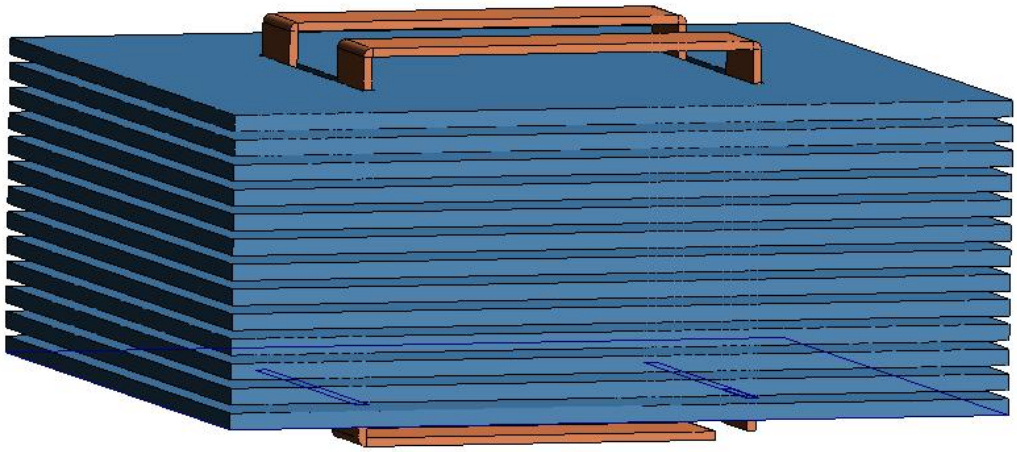

Figure 5.28: Overall view of the prototype magnet with the magnetised plates and the coil inserted. The z-axis is in the vertical direction.

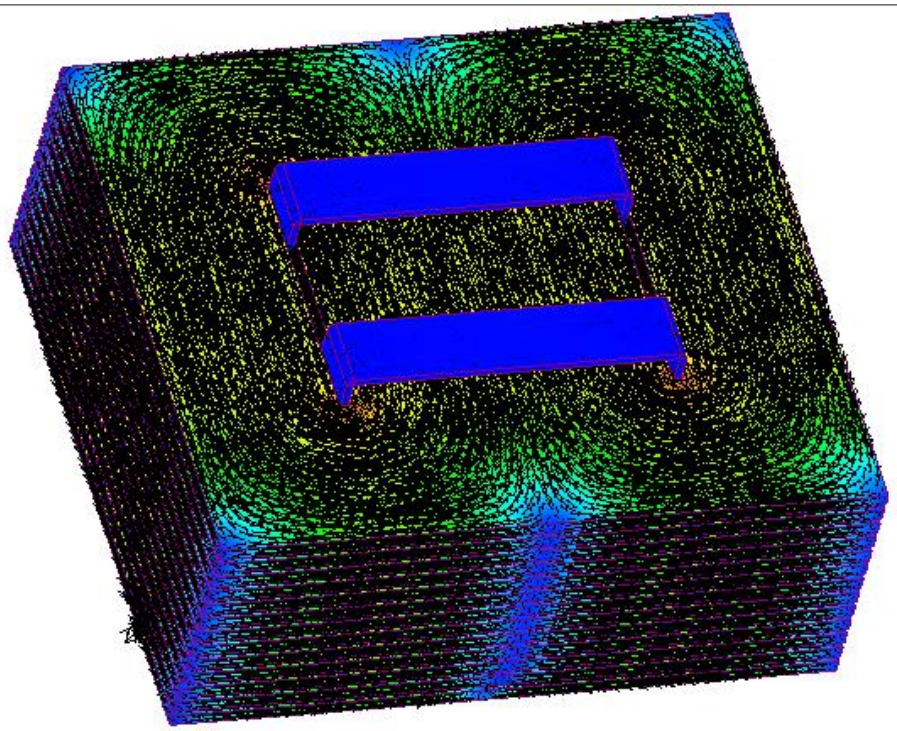

Figure 5.29: Field lines in the prototype magnet.

STEEL	
Length	16 m
Width	16 m
Height	11.9 m
Plate thickness	6.3 cm
No. of plates	135
Steel specification	ASE 1010 or C10
Carbon content	0.1%
Weight of steel	51,000 ton
COIL	
Coil dimension	20 cm $\times$ 100 cm
Coil height	15 m
Coil weight	82 ton
Amp-turns	40,000
No. of turns	20 $\times$ 100 $\times$ 2
Conductor size	1 cm $\times$ 1 cm
Current	10 A
Resistance	15.6 Ω
Voltage	156 Volt
Power dissipation	3.1 kW
Coil inductance	1710 Henry
Rise in temperature of coil	$\leq 4^0$C
Rise in temperature of iron surface	$\leq 2^0$C
Stored magnetic energy	5.3 MJ
Characteristic magnetisation time (L/R)	$\sim$ 110 s

Table 5.3: Specifications of the magnet steel and the coil for one module

current and hence the cost of the power supply.

A design based on the above considerations has been completed. Fig. 5.29 shows the field lines indicating the field direction. The colour scheme suggests the level of uniformity of the field. Fig. 5.30 shows the field component along the direction of the slots. The field uniformity is acceptable over a length of about 1 m. Fig. 5.30 shows that the field is very uniform in the middle of the detectors and has the same direction in a length of 1.2 m. The field, of course, has opposite directions on the two sides of the coil slots. Since this is outside the working area of the detector, this reversal of direction does not matter.

The design envisages the construction of the prototype magnet in two sections as shown in Fig. 5.31 and Fig. 5.31. This will enable easy assembly of the iron plates and insertion of the coils.

It is proposed to map the magnetic field strength after fabrication of the prototype to establish correspondence with the design value. This mapping of magnetic field will provide vital inputs in terms of practical inefficiencies and non-uniformities associated with the magnet construction. This input will be utilised while designing the full scale ICAL magnet.

The process for the fabrication of the magnet has started. The vendor has been selected. Tata A-grade steel from a dismantled 2 Tesla MHD magnet at BHEL, Tiruchirapalli, will be cut to size and used to make the C- and T-sections of the prototype magnet. The complete prototype magnet including the copper coils and power supply is expected to be tested and

STEEL	
Length	2.2 m
Width	2.4 m
Height	0.95 m
Plate thickness	5 cm
No. of plates	13
Steel specification	ASE 1010 or C10
Carbon content	0.1%
Weight of steel	26.6 ton
COIL	
Coil dimension	2.6 cm × 10 cm
Coil length	4.7 × 2 m
Coil weight	218 kg
Amp-turns	4000 × 2
No. of turns	5 × 20 × 2
Conductor size	0.5 cm × 0.5 cm
Current	40 A
Resistance	0.64 Ω
Voltage	25.6 V
Power dissipation	1.02 kW
Coil inductance	10 Henry
Stored magnetic energy	10 kJ
Characteristic magnetisation time (L/R)	∼16 s

Table 5.4: Physical parameters of the prototype magnet.

delivered by the end of August, 2006. A site at VECC, Kolkata, for locating the prototype magnet has been finalised and is under preparation to receive the prototype.

5.4.4 Final Design

Optimisation of the final magnet, relating to choice of plate thickness and size, their placement and desired field distribution within the active detector volume, will be carried out based on inputs from the detector simulation group. Apart from the toroidal design discussed in section 5.4.2 alternative designs based on Helmholtz-like pair of coils are also under investigation. Two conceptual arrangements of the coils are shown in Figs. 5.32 and 5.33. In one design the B-field is along the stacking direction of modules while in the other it is perpendicular to that direction. All the three designs are expected to generate fields with nearly equal efficiency. However uniformity of the magnetic field over the largest fraction of ICAL volume and minimum number of changes in the field orientation will be the criteria to be decided by simulation and event reconstruction.

While the final magnet is being designed using the MagNet 6.0 software, in addition to the 3D static design, we will also carry out transient and thermal analysis.

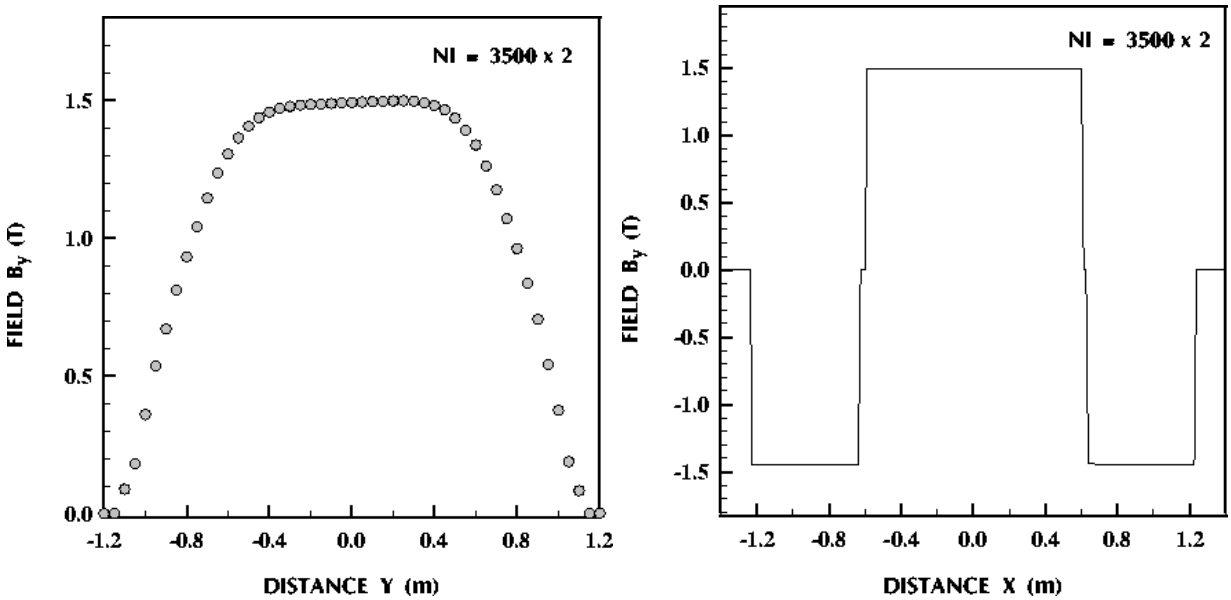

Figure 5.30: Left: Field in the prototype magnet in a direction parallel to the coil slots. Right: Field in the x-direction; the direction is reversed only outside the coils.

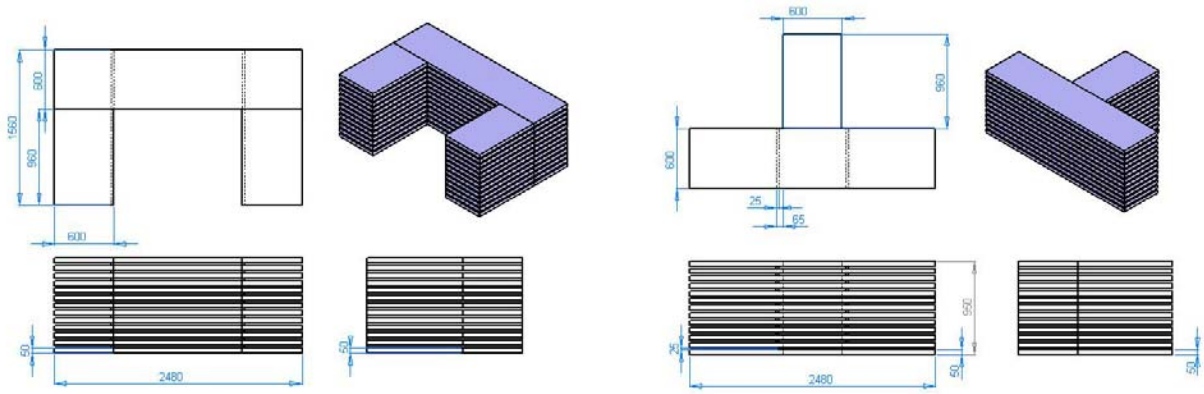

Figure 5.31: Arrangement of C-section (left) and T-section (right) of the prototype magnet.

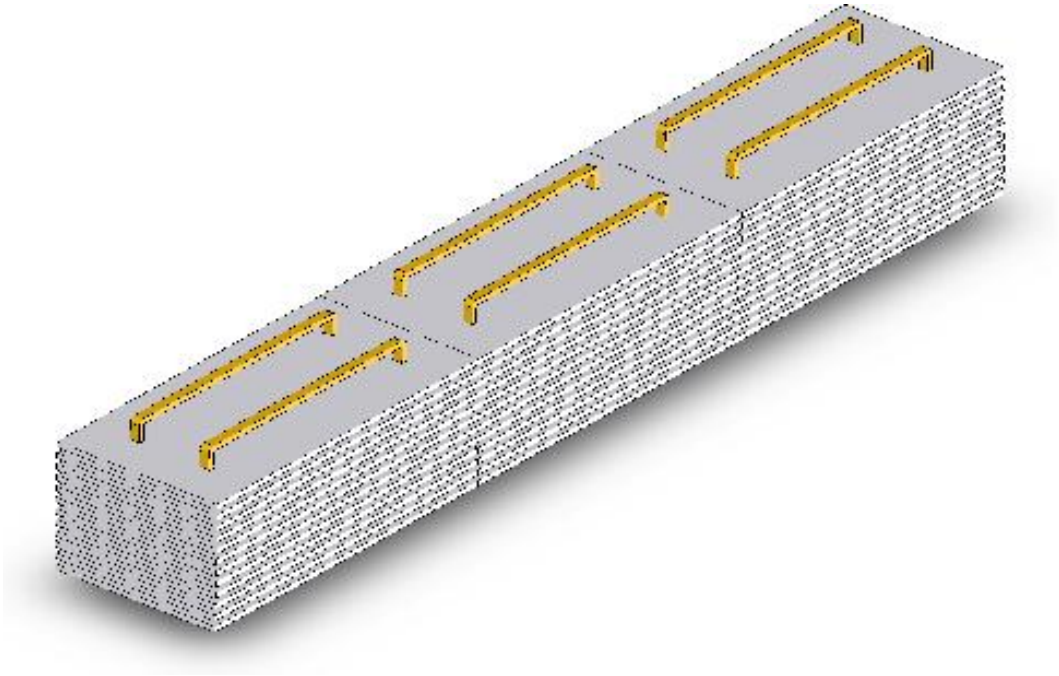

Figure 5.32: Layout of the coils (longitudinal) in Helmholtz-like pair design of the ICAL magnet.

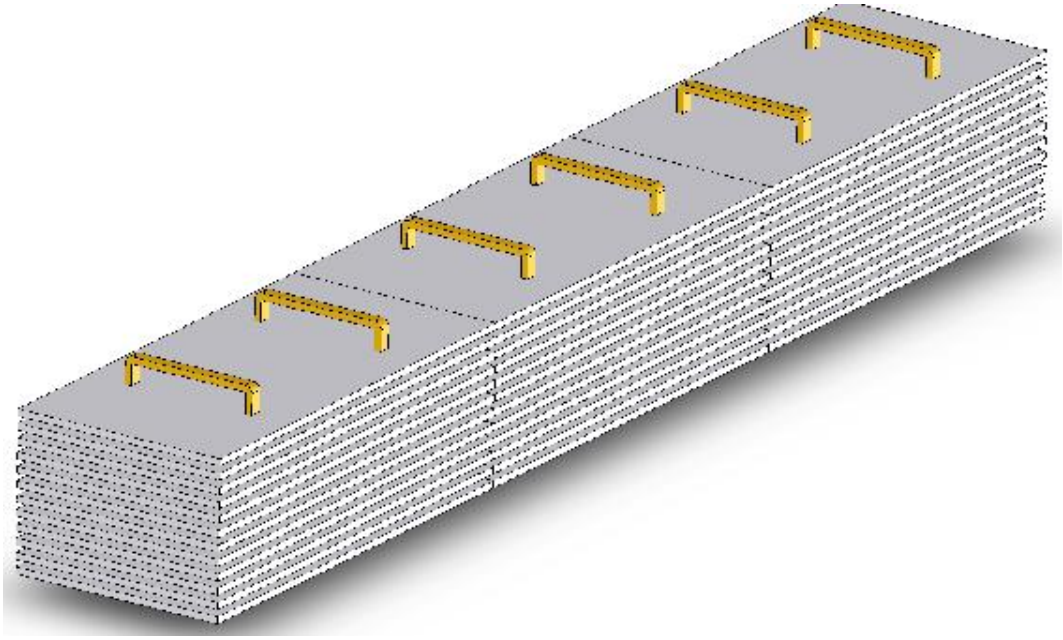

Figure 5.33: Layout of the coils (transverse) in Helmholtz-like pair design of the ICAL magnet.

Chapter 6

ICAL Simulations

The primary focus of ICAL at INO is a study of interactions involving atmospheric *muon neutrinos and anti-neutrinos*. This requires the construction of a detector that is sensitive to the energy, direction and sign of the electric charge of muons that are produced by charged-current (CC) interactions of the detector material with such neutrinos. Such a detector is described in Chapter 5. This detector (perhaps upgraded in terms of fiducial volume) will also be a suitable choice as a far-end detector of a long-base-line experiment. We briefly review the properties of such a detector.

6.1 The detector geometry

The CERN-library-provided *detector description and simulation tool*, GEANT [157], has been used both to define the detector geometry as well as simulate the detector response for the neutrino event, that is, propagate muons and hadrons, produced by neutrino interactions in the detector, through the simulated detector volume. The currently proposed detector is an iron calorimeter with magnetic field (ICAL). The detector design which has been implemented consists of 140 layers of 6 cm thick iron plates, with transverse dimensions of 48 m $\times$ 16 m, separated by a 2.5 cm air gap containing RPCs or glass spark chambers which are the active detector elements.

Some of the early simulations were also performed on a smaller detector with transverse dimensions of 32 m $\times$ 16 m. Note that this corresponds to two "modules" of a 16 m $\times$ 16 m set-up, while the larger detector geometry (also described in Chapter 5) refers to three such modules. Where simulations have been done with the "two module" geometry, the errors have been suitably scaled to that for three modules, for overall consistency, unless specifically stated otherwise.

The detector is simulated as layers of *unit cells* of the same transverse dimensions as ICAL, with a vertical dimension of 8.5 cm. A schematic of the unit cell is shown in Fig. 6.1. The sensitive part of the detector, the RPC, occupies 8.4 mm of the central part of the unit cell. It consists of a 2 mm layer of gas enclosed in 2 mm thick glass. The glass is overlaid by a 1 mm G10 sheet, with a 0.02 mm copper foil which form the pick-up strips for electrical contact.

The iron plate can be uniformly magnetised to 1 T in the x, y, or z- directions; a magnetic field map including the effects of non-uniform magnetic field is in place for the toroidal geometry of coils discussed in Chapter 5. Unless stated otherwise, results in this chapter are for a uniform magnetic field of 1 T in the y-direction. Detailed simulations of the magnetic field from different coil configurations are also being done, and have been described in Chapter 5.

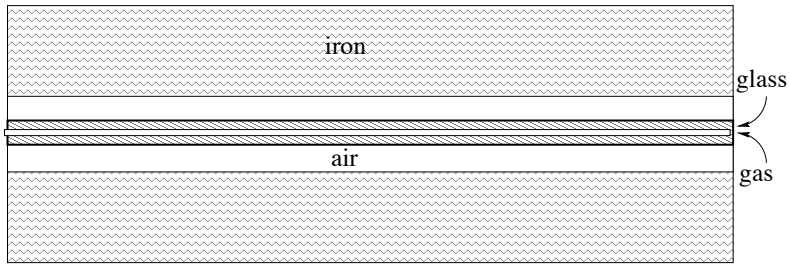

Figure 6.1: View of a unit cell of the simulated ICAL detector. The outermost layers are 3 cm of iron, with the sensitive detector (of gas, glass, G10 and copper from the centre out) symmetrically placed in a central 2.5 cm air gap. The detector is simulated as 140 unit cells, with top and bottom edge layers of 3 cm iron each.

Details such as spacers within the RPC, dead-spaces due to insertion of copper coils for magnetisation, alterations due to support structures required, etc., are yet to be included in the simulated detector geometry.

6.1.1 Digitisation of tracks

The principal issues to be studied are electric charge identification and tracking (direction) and energy resolution for muons. The energy of hadrons can be reconstructed as well, but rather coarsely.

Particles such as muons are *tracked* through the detector by determining the number of sensitive regions that the particle has passed through. The sensitive regions are the gas chambers in the RPCs, and the transverse size of the sensitive regions are assumed to be 2 cm each in the x and y directions. That is, the spatial resolution of the detector in the x and y directions is assumed to be 2 cm. The charged particle triggers the RPC by the energy it loses inside the medium and registers a *hit*. All secondaries that may be produced by passage of the primary particle through the detector medium are tracked as well. While there are very few secondaries generated by minimum-ionising particles such as muons, hadrons generate secondaries copiously due to their strong interactions with the medium. Many of these secondary showers are absorbed by the iron layer, and some of the remaining produce hits inside the detector.

For purposes of digitisation, the unit cell is composed of 16 modules of transverse dimension 2 m $\times$ 16 m. Each module consists of 8 chambers of transverse size 2 m $\times$ 2 m each. The chambers have 5 trays of size 0.4 m $\times$ 2 m. In short, the transverse coordinates of a hit can be determined from the chamber/module/tray numbers and from knowing the particular x and y strip numbers on that tray. While these parameters have been used to generate the results discussed in this Chapter, all these configurations can be changed by using different input cards when running the program.

The digitisation of hits is done by determining the coordinates of x and y strips of the hit from the procedure described above and determining the z coordinate from the layer number (in the case of horizontally placed iron-plates, which is the standard configuration). Hence the resolution in the z direction is 8.5 cm. The signal read-out is then saved as two bytes of information, containing the layer/chamber/module/tray/strip information for the x strip and y strip respectively. This information can be used to recover the hit coordinates (rounded off according to the various resolutions).

The RPCs are assumed to give nano-second timing (for up/down discrimination). While it may not be possible to have sufficiently good time-resolution between successive hits, the requirement of minimum number of hits for reconstruction ensures that the over-all timing efficiency and hence up/down discrimination is 100%. In this analysis, we have not used any energy information which may be obtained from the pulse height; all calibration is done by calibrating the track length (for muons) and number of hits (for hadrons).

The detector has to be calibrated using muons and hadrons with known energy and direction before it can be used to study atmospheric neutrinos of interest. Before we go on to these results, we present some details of the atmospheric neutrino flux.

6.2 The neutrino source

Atmospheric neutrinos have been simulated using the NUANCE neutrino generator [155]. The generator provides a choice of neutrino fluxes and also allows 3-flavour mixing to be turned on from source to detection point, apart from providing the relevant interaction cross sections. The HONDA flux [156] for atmospheric neutrinos has been used in the simulations. The main CC interactions of the neutrinos in the detector are quasi-elastic (QE) and resonance (RS) interactions at low energies (up to a few GeV) and deep-inelastic scattering (DIS) at higher energies. All CC neutrino interaction events produce the associated lepton (muon in the case of muon neutrinos). The DIS events usually produce a large number of accompanying hadrons (mostly pions) while resonance interactions produce at most one pion along with the lepton. Since the DIS cross-section is roughly proportional to the energy E, the events sample peaks around a few GeV although the flux itself peaks significantly below 1 GeV.

6.2.1 The atmospheric neutrino flux

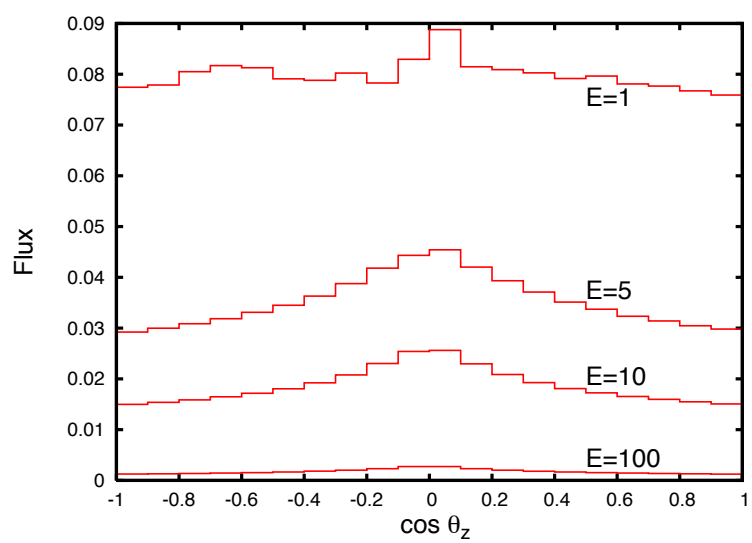

Figure 6.2: The HONDA atmospheric muon neutrino flux, $E\,\mathrm{d}^2\phi/(\mathrm{d}\log E\,\mathrm{d}\cos\theta_z)$ where the flux ϕ is defined to be the number of neutrinos per square cm per steradian per second, averaged over bins of $\cos\theta_z$ of size 0.1 and bins of $\log_{10} E(\mathrm{MeV})$ of 0.02, shown as a function of the zenith angle at different energies, E, in GeV. The flux is clearly dropping very fast with energy, as can be seen by following the different curves for the same zenith angle bin. Muon anti-neutrinos and electron neutrinos and anti-neutrinos exhibit a similar behaviour.

Atmospheric neutrinos, of both e and μ type, have a large range in energy E and path-length traversed L. As can be seen from Fig. 6.2, there is an up-down symmetry in the flux of somewhat higher energy neutrinos (in the absence of neutrino oscillations) so that the up-going neutrino rates in a bin around a zenith angle θ_z can be normalised by the down-going rates [57] in a bin around $\theta_z \leftrightarrow \pi - \theta_z$. This is demonstrated in Fig. 3.3 and has been explained in detail in Chapter 3. Note that $\cos\theta_z = +1$ corresponds to up-coming neutrinos and so θ_z is actually the nadir angle.

6.2.2 Events generation

The NUANCE neutrino event generator is used to generate atmospheric neutrino events inside ICAL using this HONDA flux. A simplified ICAL detector geometry (with both horizontal and vertically oriented iron plates) has been encoded in the NUANCE generator. Since neutrino interactions depend on the density of scatterers in the medium, a unit cell containing only iron and glass has been incorporated. The amount of copper and G10 in the ICAL detector being very small, it is expected that very few events will be generated there, with neutrino interactions with air/gas being negligible. Hence this geometry is adequate to generate events for analysis. All results in this chapter are for NUANCE Version 2.003; a newer Version 3.0 mainly differs in the handling of the transition between the resonance and DIS region and, while improving the quality of the physics inputs, should not seriously affect the results presented here. A basic cut on the neutrino energy, $E > 0.8$ GeV, has been implemented while generating events themselves. When no other cuts are specified, this cut is always to be understood to be in place.

Events are generated using the HONDA flux [156] for fixed values of the oscillation parameters δ_{21} and θ_{12} and input variable oscillation parameters δ_{32}, θ_{23}, and θ_{13}. The last determines matter dependent effects which can be measured from charge-identification; we will only show results with $\theta_{13} = 0$. For neutrino energies greater than 0.8 GeV, neutrino charged-current (CC) events of interest are roughly generated in equal proportions via quasi-elastic, resonant and DIS processes. Typically interesting events have $E > 1$–2 GeV so the proportion of DIS events in the final sample is somewhat higher than the others.

The events are first analysed at the NUANCE output level. Issues of relevance are the muon energy and direction with respect to that of the originating neutrino. This defines the kinematic limitations on the event reconstruction, that is, for the ideal detector. Then the NUANCE data are fed into the GEANT simulated ICAL detector to study the effects of detector-dependent resolutions and cuts; this will determine, ultimately, the sensitivity of the ICAL detector to atmospheric neutrinos.

6.2.3 Muon energy distribution

Fig. 6.3 shows the event distribution in energy with a 5 years' unoscillated data sample. The events are binned in 1 GeV energy bins. The energy distribution of both the initial neutrino and the produced muons are shown; this distribution is not very sensitive to oscillations. Clearly there is a strong correlation between the energy of the muon and the parent neutrino. Furthermore, the muon carries a substantial energy of the parent neutrino, as can be seen from Fig. 6.4.

6.2.4 Muon zenith angle distribution

The zenith angle dependence of those muon neutrinos that give rise to charged current (CC) interactions in the ICAL detector is shown in Fig. 6.5. It can be seen that the oscillated

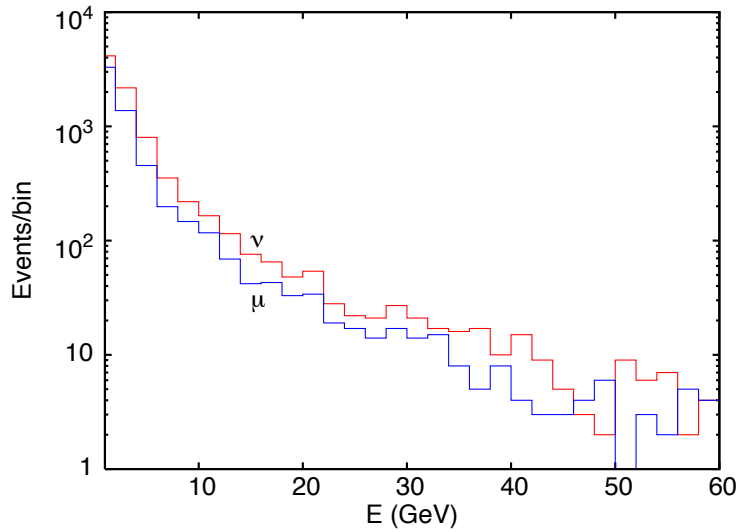

Figure 6.3: Number of events in GeV bins from 5 years' CC atmospheric muon neutrino interactions. The distributions both for the original neutrino and the generated muon, in the absence of oscillations, are shown.

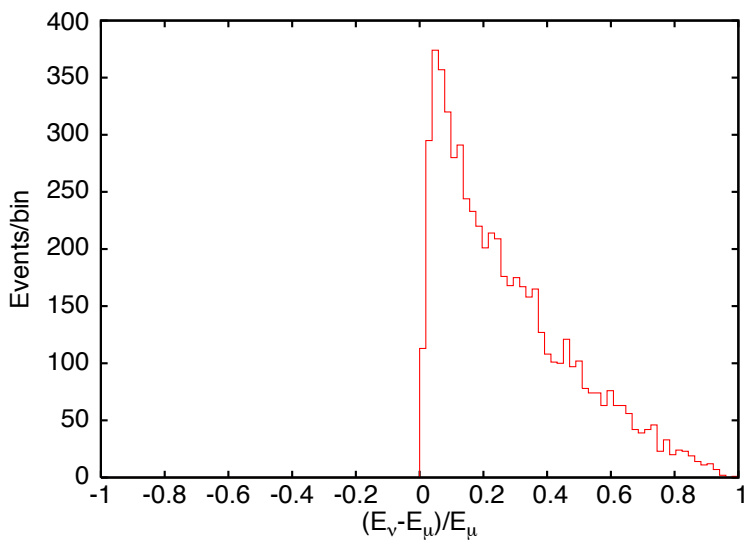

Figure 6.4: The figure shows the events distribution as a function of the fraction of neutrino energy carried by the muon. The data is a 5 years CC muon neutrino sample, without oscillations. Clearly most events fall in a region with small $(E_\nu - E_\mu)/E_\nu$, indicating that the muon carries a substantial fraction of the neutrino energy in most events. Here E_ν and E_μ refer to the energies of the neutrino and muon respectively.

flux is severely depleted in the upward direction ($\cos\theta_z > 0$) as opposed to the unoscillated flux. The transition towards depletion is rather sharp.

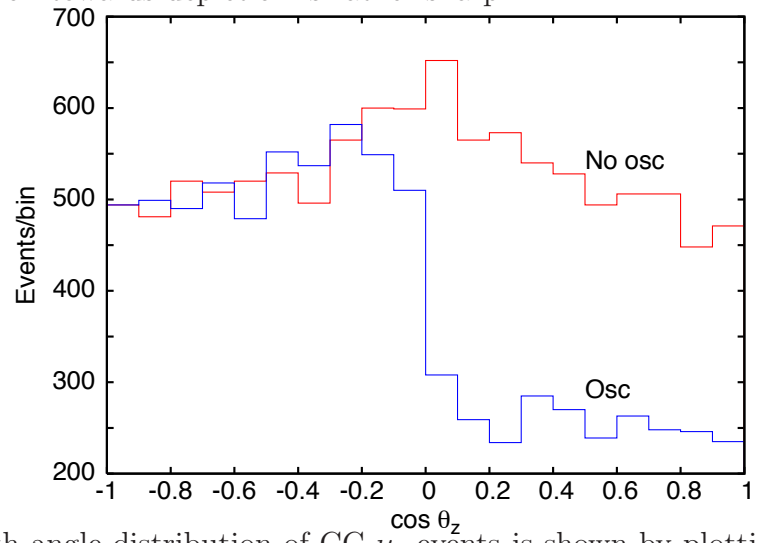

Figure 6.5: Zenith angle distribution of CC ν_μ events is shown by plotting the events rates per bin as a function of $\cos\theta_z$ where θ_z is the neutrino zenith angle. The bin size is 0.1. NUANCE labels "up-going" events as those with $\cos\theta_z > 0$. These events are depleted when (2-flavour) oscillations are turned on, where oscillation parameters $\delta_{32}, \theta_{23} = 2 \times 10^{-3}$ eV^2, 45° have been used.

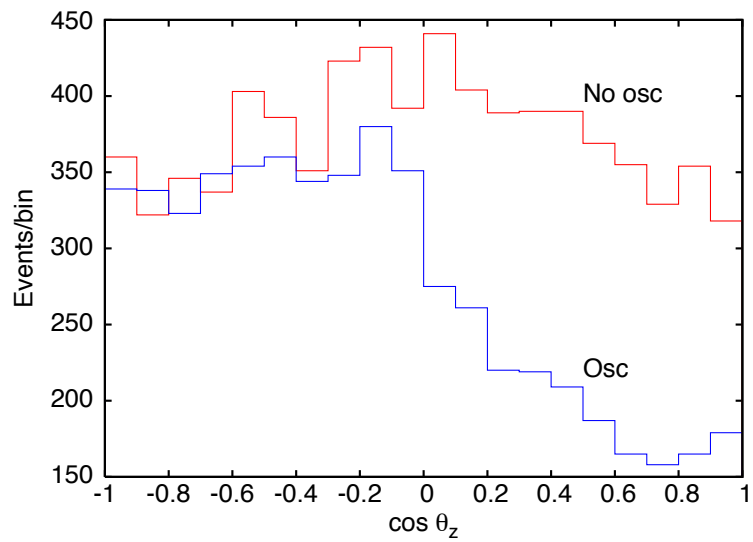

Figure 6.6: The same as Fig. 6.5 for the zenith angle distribution of the muons.

The zenith angle dependence of the muons produced in the CC interaction is shown in Fig. 6.6. A similar behaviour is seen for the muons as for the neutrinos, confirming that the muons do reflect the energy and direction of the initial neutrinos. However, the onset of depletion at $\cos\theta_z \sim 0$ is not as sharply defined as for the neutrinos. This is because of smearing of the energy and direction of muons compared to that of the parent neutrino. In any case, it is reasonable to expect that ICAL is sensitive to oscillations in regions away from the horizontal, viz., to regions where $|\cos\theta_z| > 0.1$.

It is seen that about 85% of the muons are within a cone of $\cos\theta_z = 0.9$ (half-angle of 13°) of the incident neutrino when its energy is at least 1 GeV. Hence, the direction of the muon is roughly the same as that of the original interacting neutrino, although the kinematics of the interaction induces a finite width for the direction resolution, as can be seen from Fig. 6.7.

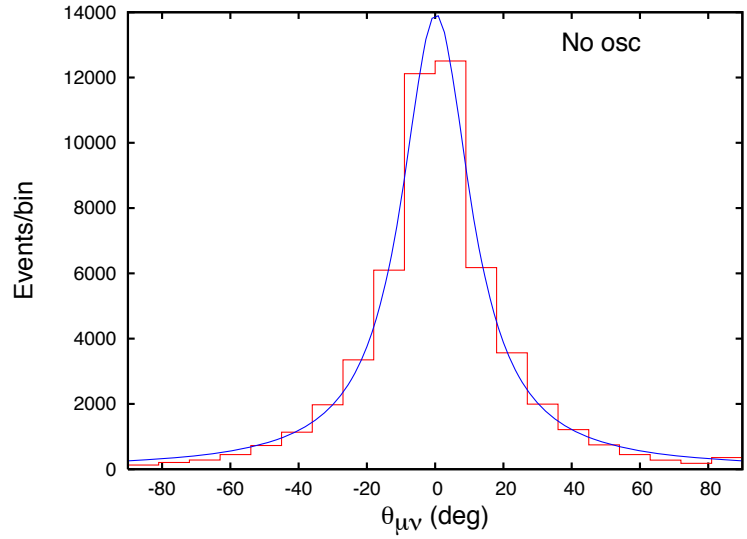

Figure 6.7: Distribution of events in bins of 9 degrees as a function of the relative angle $\theta_{\mu\nu}$ between the incident neutrino and the produced muon in the CC interaction.

In summary, the energy of the interacting neutrino can be reconstructed by summing the energies of the muons and hadrons. Its direction can be deduced from that of the muon, while its particle type (particle or anti-particle) can be determined from the curvature of the track of the produced muon in the CC interaction in the presence of the magnetic field.

6.3 Event tracking and reconstruction

In order to determine how these results get diluted when finite detector resolution is taken into account, we study the same NUANCE events sample, by tracking the final state particles through the simulated ICAL detector and reconstructing their energies and directions. Before we do this, we need to calibrate the detector.

6.3.1 Reconstruction of test events

We first study the tracks of muons and hadrons with fixed energy and direction, both with and without a magnetic field.

6.3.2 Muon energy reconstruction

In the absence of a magnetic field, the energy and direction of muons are reconstructed from the track length in the detector. This requires that the track be fully contained (FC) inside the detector volume. A general formula for fitting a straight line in 3 dimensions is used to fit the track; the track length is calibrated using the known muon energies. It is found that the track length is proportional to the muon energy for almost all energies whose tracks can be contained. The charge of the muon cannot be identified in this case.

The nature of interactions that cause energy loss in matter (primarily iron in this case) are statistical; hence all calibrations arise from Gaussian distributions around a mean. Fig. 6.8 shows the distribution of effective path-length and polar angle for 500 muon triggers with fixed energy $E = 1$ GeV and a polar angle of $\theta = 40°$. The muon energy is calibrated from

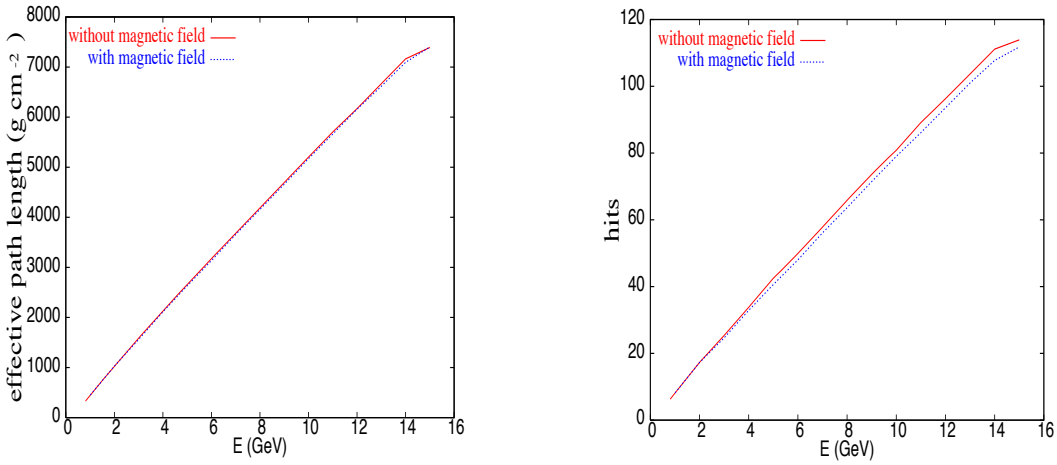

Figure 6.8: The variations of effective path-length (left) and number of hits (right) with energy for fixed θ ($= 40^o$) in ICAL-H for muons (without and with a magnetic field of 1 T in the z direction).

the average path-length according to

$$L_{\rm eff} = \sum_i \frac{d_{\rm tot}}{|\cos\theta|} f_i \rho_i \ ,$$

where $d_{\rm tot}$ is the thickness of one unit layer and $f_i = d_i/d_{\rm tot}$ the density fraction of a component of that layer. Here d_i and ρ_i are the thickness and density of the i-th material constituting the layer. The sum is dominated by the iron layer. The other layers including glass, air, gas, etc., contribute very little due to their smaller densities. It is clear from the figure that the same linear relation holds in the presence of the magnetic field as well.

In the presence of the magnetic field, in addition, the muon momentum can be obtained from the track curvature and its charge from the direction of bending with respect to the external magnetic field. Partially contained (PC) events whose vertices are within the fiducial volume but whose track is not completely contained within can also be analysed in the presence of a magnetic field.

When a magnetic field is applied in a particular direction, the tracks bend in a plane perpendicular to this direction. The length of the track in the direction along the magnetic field is determined from the energy loss formula, while a combination of energy loss and curvature in the external magnetic field determine the nature of the track perpendicular to it. The transverse momentum p_T is found by fitting such a track in that plane. The total momentum of the track is determined from $p_{\rm tot} = \sqrt{p_{||}^2 + p_T^2}$.

Several different methods of track fitting in the magnetic field have been tried. We will discuss two of them here. In one method, only about 30% of the length of the full track is used; this is useful to analyse partially contained (PC) events. In the other method, the entire track length is used for fitting; such a procedure allows fits to totally contained events alone. In particular, fully contained (FC) events are defined as those events with hits within ± 20 cm of the edge in any direction. The energy of muons with fully contained tracks can also be determined by summing individual lengths of track in the iron, as in the case where there is no magnetic field. This serves as a cross-check on the calculations.

Algorithm I directly uses the amount of bending of the track at the vertex to obtain the radius of curvature through geometrical considerations. Algorithm II fits the track to a spiral/helical trajectory and determines its parameters. These parameters are then used to

obtain the radius of curvature. Since Algorithm II fits the entire helix, it can only be used for FC events.

Fig. 6.9 shows a few typical results obtained by using Algorithm I. Herein the distribution of the muon total energy (and the corresponding fits) as obtained by fitting the initial part of the track to a curve to determine the radius of curvature at the production point is shown using a large number of muon triggers with constant $B_z = 1$ T and $p_x = p_y = p_z = 1$, 3, 5, 7 GeV. The energies obtained for the different data sets are $E = 1.73 \pm 0.23$ (1.74) GeV, 5.42 ± 0.61 (5.20) GeV, 8.94 ± 0.85 (8.66) GeV, and 11.69 ± 0.95 (12.12) GeV respectively, where the numbers in brackets are the incident energies. We refer to this as Analysis Set 1.

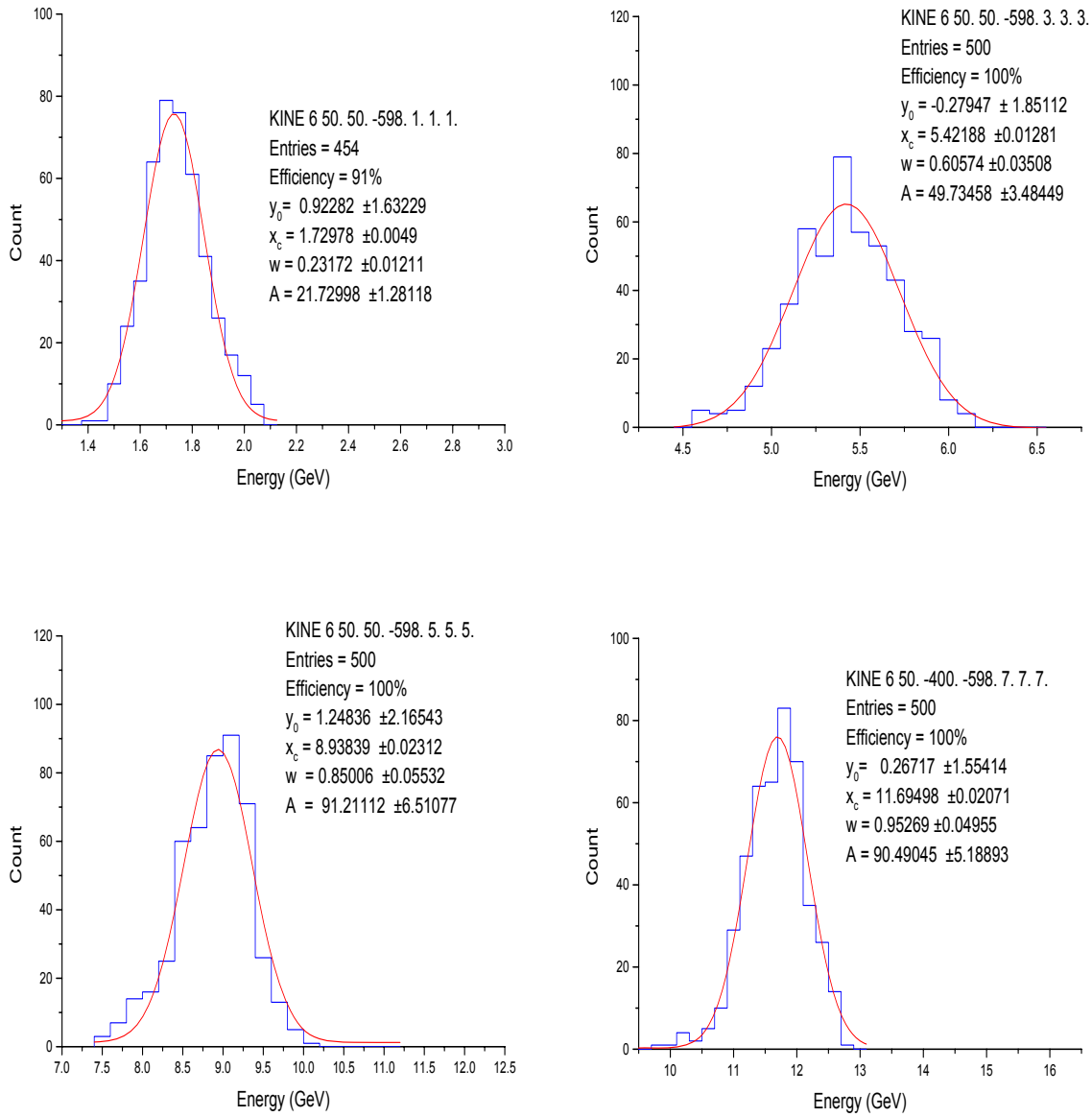

Figure 6.9: Distributions for the total energy for muons using fitting Algorithm I. The incident momenta are given in the KINE statement, which lists, in order, particle id (here muon), (x,y,z) in cm of the production point, and (p_x, p_y, p_z) in GeV.

Algorithm II was used on the same data set to obtain the radius of curvature R_0 at the point of production. For a constant magnetic field, we have

$$p_T = 0.3 R_0\,(\mathrm{m})\, B(\mathrm{Tesla})\ .$$

This technique was implemented in Analysis Set 2 for $p_x = p_y = 2, 3, 4, 5, 7, 10$ GeV. Sample fits to the trajectory for $p_x = p_y = 2, 5, 7, 10$ GeV are shown in Fig. 6.10. The corresponding expected and determined values of R_0 are shown in Table 6.1. Both methods are found to be reliable.

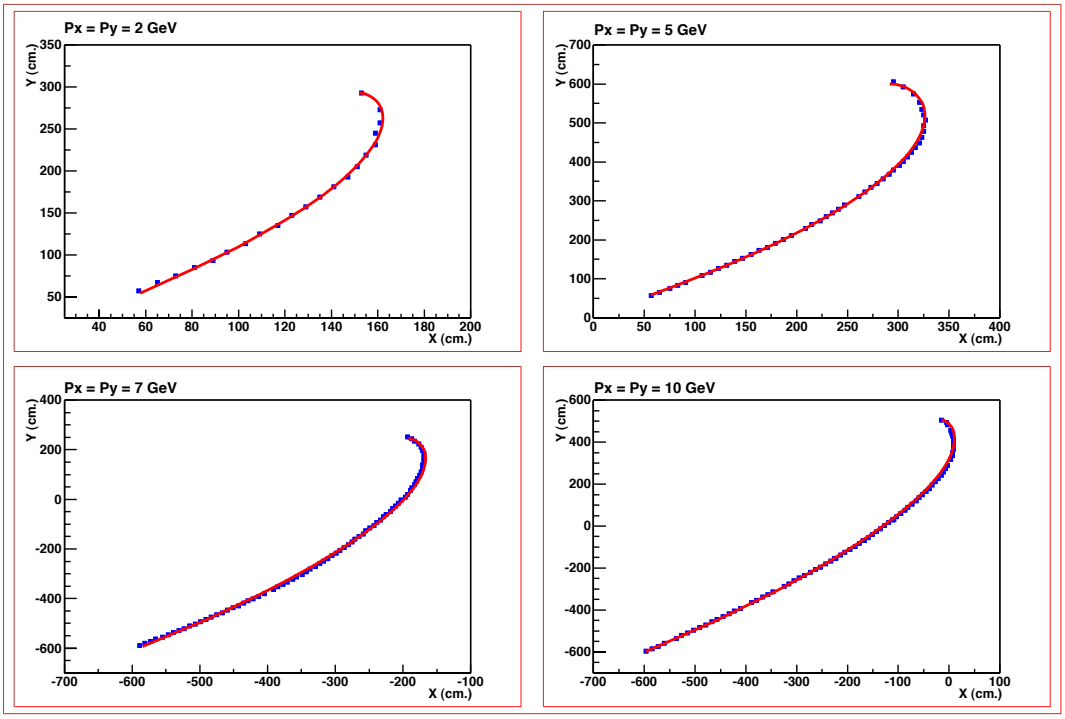

Figure 6.10: Sample fits to transverse tracks with momenta $p_x = p_y = 2, 5, 7, 10$ GeV respectively.

$p_x = p_y$ GeV	p_T GeV	Expected R_0 (cm)	Reconstructed Mean R_0 (cm)
2	2.828	943	959
3	4.243	1414	1439
4	5.657	1886	1908
5	7.071	2357	2370
7	9.899	3330	3283
10	12.142	4714	4635

Table 6.1: Comparison of expected and reconstructed radius of curvature using Algorithm II. For details see the text.

6.3.3 Muon direction reconstruction

In the absence of the magnetic field, the direction of the muon is simply given by the slope of the straight-line fits to the tracks. In the presence of the magnetic field, since the muon is produced *in* the magnetic field, the effect of the field is to bend the muon track perpendicular to the field direction. However, the original muon direction (and hence the neutrino path-length L in Earth) can be estimated from the tangent to the track at the vertex. While Algorithm I again uses a geometric fit to get this slope, Algorithm II uses the analytical

formulae for tangents to helixes to obtain the results. Both methods agree and give angular resolutions of about 10%.

The fits using Algorithm I to the zenith angle distribution for the Analysis Set 1 are shown in Fig. 6.11. The zenith angle was determined to be (53 ± 7), (54 ± 4), (53 ± 3), and (58 ± 8), compared to the expected value of 54.7° $(= \arccos(1/\sqrt{3}))$.

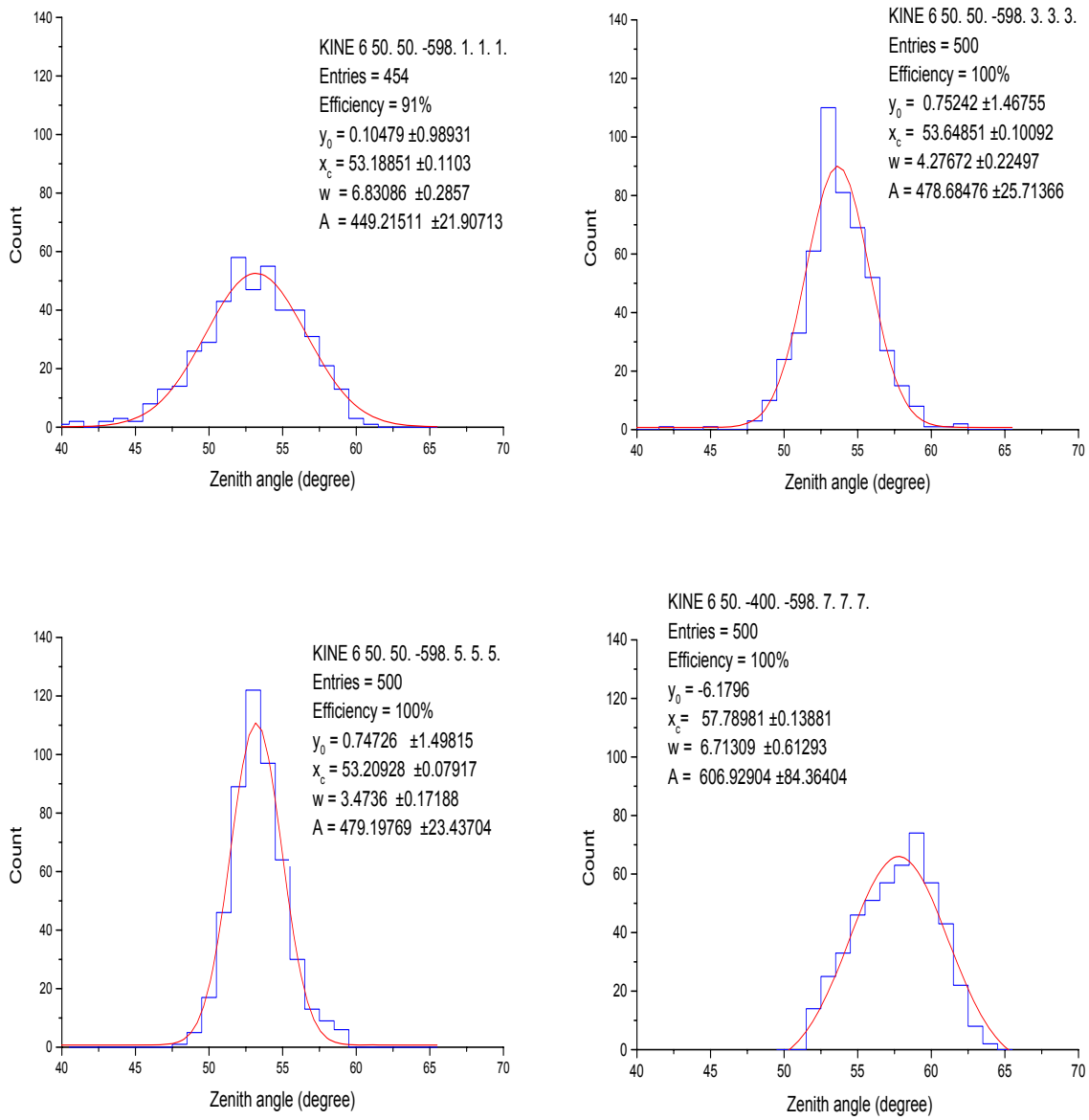

Figure 6.11: Zenith angle distributions for muons. The incident momenta are given in the KINE statement. See Fig. 6.9 for details.

6.3.4 Muon charge identification

Charge identification is crucial for matter effects in a three-flavour analysis. The charge of a particle is determined from the direction of the track curvature in the presence of a magnetic field. Different segments of the track as well as the entire track have been used for this purpose. Both methods give roughly about 94% charge identification efficiency. For muon energies beyond 40–50 GeV, the track curvature is not sufficient to determine its charge.

FC			FC + PC		
No. of selected events	No. with correct charge identification	Charge identification efficiency (%)	No. of selected events	No. with correct charge identification	Charge identification efficiency (%)
2613	2451	93.8	3169	2967	93.6

Table 6.2: Charge identification efficiency for simulated 5-year atmospheric neutrino data samples.

However, the set of such energetic muons from atmospheric neutrinos is small. The 5 year simulated charge identification efficiency for both fully contained and partially contained events from such a sample is shown in Table 6.2.

6.3.5 Hadron energy calibration

The ICAL detector is not very sensitive to individual hadrons. Indeed, it appears that such a detector cannot distinguish different hadrons such as K and π. Many atmospheric neutrino CC events of interest have substantial multi-pion events; *all* the hadrons produced in a single such event are calibrated using hit multiplicity. That is, the total hits (that are rejected as being part of the muon track) are calibrated to the total energy of the hadrons in the event. There is also no directional information in this approach. Hence, while calibrating, care has been taken to average the simulated tracks over all possible directions.

The simulation was done with pions of fixed energy, with random directions. Fig. 6.12 shows the number of hits obtained for different fixed energy of pions for a sample of 1000 events at each energy. It is seen that the number of hits are distributed as a Gaussian for a

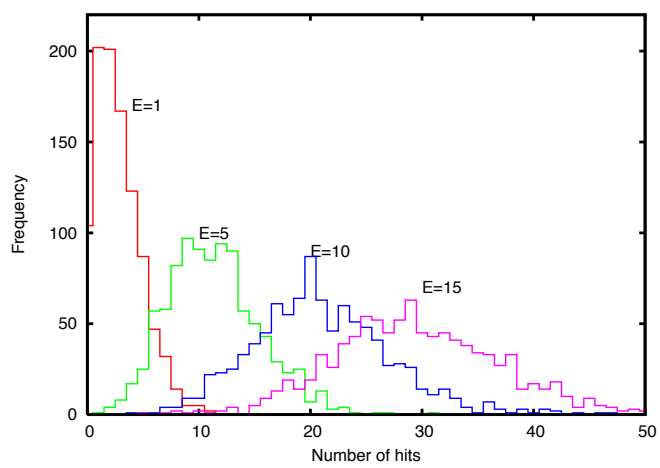

Figure 6.12: The frequency distribution of hits for fixed pion energies of $E_h = 1, 5, 10, 15$ GeV, with 1000 random events per sample.

given energy E:

$$n_h = \frac{N_0}{\sqrt{2\pi}\sigma} \exp\left(\frac{-(x-x_0)^2}{2\sigma^2}\right) .$$

The parameters of interest, σ and x_0, can be determined from the fits to n_h which is shown in Fig. 6.13 as a function of the pion energy.

The data were fitted to a form

$$n_h = n_0(1 - \exp(-E/E_0)) ,$$

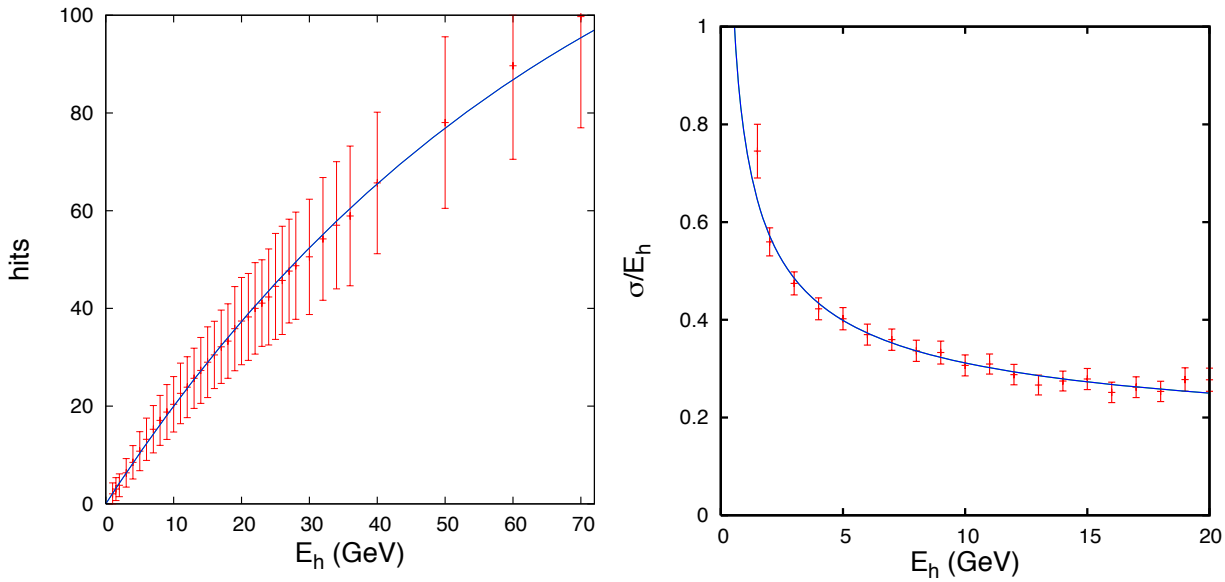

Figure 6.13: Left: The average number of hits as a function of pion energy for 1000 random events per sample of constant energy events. The smooth curve is a best fit to the data. Right: Variation of the width of the Gaussian distribution, σ as a function of the energy. Plotted is the ratio σ/E as a function of E_h, along with best fit curve.

to get $n_0 = 152 \pm 7$, $E_0 = 71.0 \pm 3.5$ GeV. This was used to obtain the resolution function as a function of energy, as shown in Fig. 6.13. The resolution σ for hadrons has an energy dependence,

$$\sigma/E = a/\sqrt{E} + b \ ,$$

with the best fit giving $a = 0.67 \pm 0.03\sqrt{\text{GeV}}$ and $b = 0.10 \pm 0.01$.

To summarise, the ICAL detector simulations indicate that muon energy, direction and charge can be determined with good accuracy, and some estimates made for the energy of the hadrons.

6.4 Atmospheric neutrino analysis with GEANT

We now study the NUANCE generated atmospheric neutrino events with the simulated ICAL detector. We present here results for the up/down ratio of atmospheric CC muon events for the case when $\delta_{32} = 2 \times 10^{-3}$ eV^2 and $\theta_{23} = 45°$.

The NUANCE events are propagated in the simulated ICAL detector. The muon events are separated out for analysis and the remaining hits are analysed as coming from hadrons, in the absence of a track recognition algorithm (a Hough filter analysis is being refined). The calibrations put in place as discussed above are used to determine the track parameters. The relevant parameters (energy, direction, charge) are reconstructed and analysed. The energy of the parent neutrino is determined from that of the final state muon and hadrons. There is no directional information available from the hadron sector. So the direction of the neutrino is approximated by that of the muon. Hence, while the direction of the muon itself is quite well resolved, there is an additional uncertainty/smearing when this is compared to the original neutrino direction.

6.4.1 Data Analysis

Before presenting the data we briefly review the up/down ratio and its sensitivity to the neutrino oscillation parameters. The up/down events ratio for a fixed L/E is determined by the neutrino flux and the cross section of its interaction with the detector. Normally, there are more than one type of interactions possible in which case the total event rate is a sum of that from each interaction channel. The rate can be notionally written as

$$\mathcal{N}(x) \propto \int \mathrm{d}E\, \mathrm{d}L\, \delta(x - L/E)\, \Phi(L, E)\, \sigma(E) \ ,$$

where the flux Φ is the known atmospheric neutrino flux, modified by oscillations, $\Phi_j = \Phi_{0,i} P_{ij}$ where $\Phi_{0,i}$ is the unoscillated flux, i, j are neutrino species, $j = e, \mu$ and σ is the cross section. In the case of 2-flavour oscillation (where there are no matter effects at the energies of interest), the muon neutrino events rates directly depend on the survival probability $P_{\mu\mu}$. Since the down-going neutrinos are almost unaffected, the ratio of the up/down events rate is directly given by $P_{\mu\mu}$. However, the reconstruction of this ratio is limited by the finite detector resolution. This resolution is a function of (L, E) and in particular, for this 2-flavour analysis, is a function of L/E. Events with larger L/E are reconstructed worse than those with smaller L/E. This causes a smearing of the probability distribution since a neutrino event with parameter $L/E = x'$ is reconstructed as an event with $L/E = x$. In order to compare the up/down ratio of reconstructed events with the theoretical expression for the oscillation probability, it is first necessary to know this resolution function. Note that the oscillations are incorporated in both the up-coming and down-going neutrino samples.

6.4.2 L and E resolutions

Resolution functions are normally dependent on detector characteristics alone and are independent of the exposure times in an experiment and other factors. Furthermore, the resolution function is also dependent on kinematic smearing. The neutrino energy and direction are determined from the reconstructed muon and hadron properties. This is limited by kinematics. In order to obtain stable resolution functions that do not depend on exposure time, it is important to generate a large enough data set so that statistical errors are made reasonably small. In particular we have checked that these resolution functions *do not* depend on the a priori unknown oscillation parameters as that will bias the sample.

The L/E resolution depends on the resolution in both E_ν and $(L/E)_\nu$. These resolutions are found by separately dividing the whole E_ν–$(L/E)_\nu$ space into subspaces with very small bins of E and L/E. A large number of events (around 83000) are generated in the energy range 0.8 to 200 GeV with almost equal weightage up to 30 GeV and separately analysed in different E_ν and L_ν ranges. Note that *the same cuts* that were used to determine the resolution function must be applied when analysing the data sample. We begin by considering the fully contained (FC) events.

FC analysis In this mode of analysis, the energy of a particle is obtained from the track length. Only FC events are considered. The cuts employed were motivated by the following considerations.

The L/E resolution has a complicated dependence on L and E. Qualitatively for a fixed energy, the L resolution worsens gradually as we go from vertical to horizontal region and worsens very rapidly close to horizon. Again for a fixed direction, L/E resolution improves with increase in E_ν since the angle between the directions of incident neutrino and the produced muons decreases with increase in E_ν. If one neglects totally the near horizon

events (say between zenith angles 70° and 110°), all the events with L/E below 200 Km/GeV are lost. So in practice we consider only the high energy events at near horizon. This cut can be relaxed gradually as we move away from the horizon. Based on these ideas, numerical study is done to arrive at the cuts for our analysis. Fig. 6.14 gives the selected/rejected region in the E–(L/E) domain.

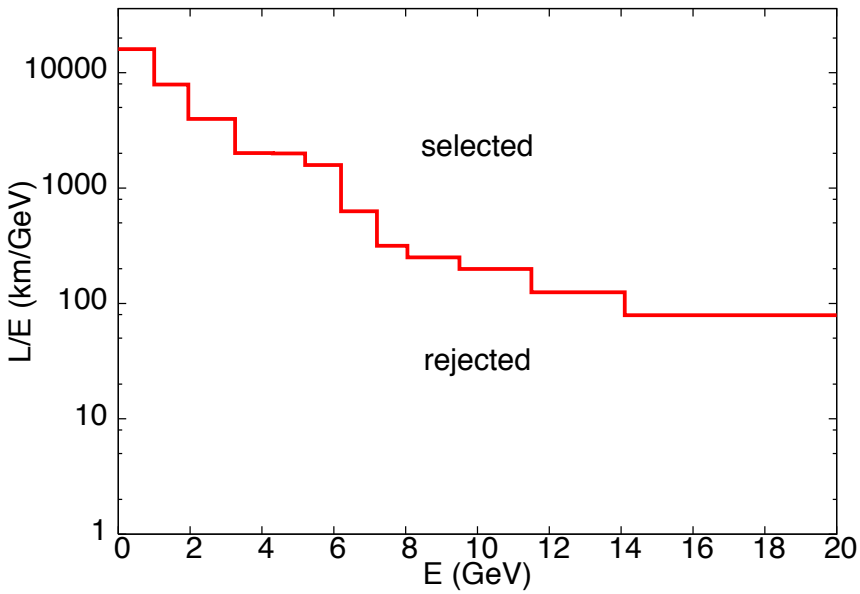

Figure 6.14: Region of acceptance for the choice of cut for FC events.

With these cuts, the total energy resolution is obtained. Although the resolutions used in the analysis were generated in small bins in both E and L/E, a typical energy resolution is shown in Fig. 6.15. The muon direction was reconstructed and a corresponding typical resolution in path length L is also shown in the same figure. This results in a resolution in the variable L/E as shown in Fig. 6.16.

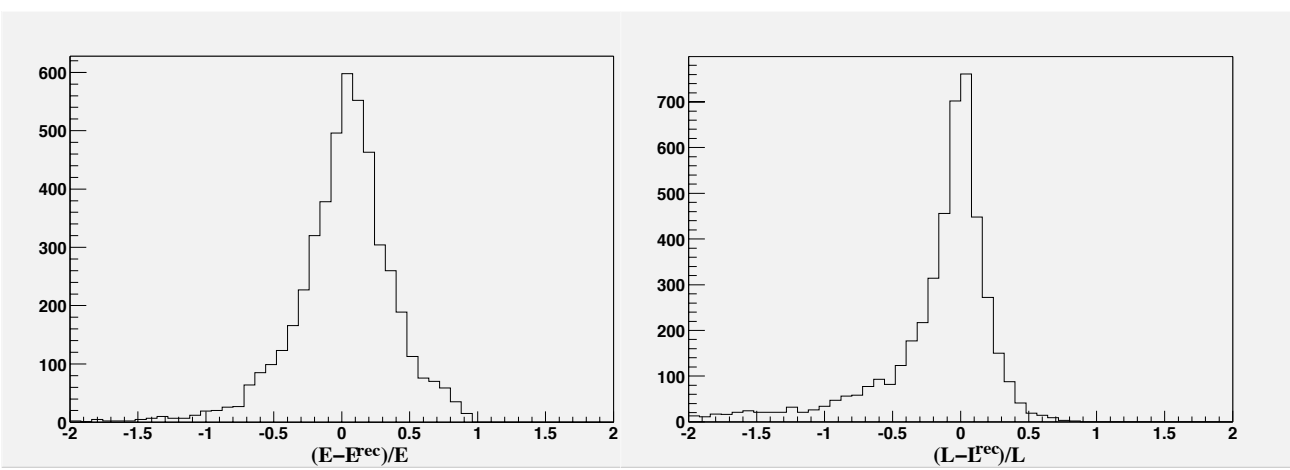

Figure 6.15: Typical resolution functions for energy E and path-length L of fully contained neutrino events.

FC+PC analysis : For partially contained events, the energy of the particle is obtained from the track-curvature in a magnetic field using Algorithm I. The FC events are however

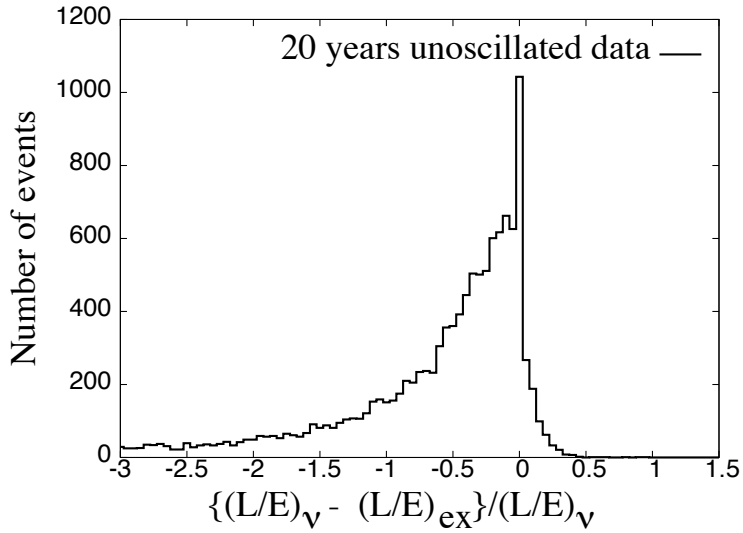

Figure 6.16: Typical resolution functions in L/E for fully contained neutrino events.

analysed as before. This is because the programs using the track-curvature algorithm have not been fully optimised. In particular, reasonable results have been obtained for partially contained events where the tracks have at most 20 hits. Hence only such events have been included in the analysis.

The number of events that survive the cuts is shown in Table 6.3.

Years	Events ($\geq$ 6 hits)	FC events (after cut)	Efficiency (FC)	PC events (after cut)	Total (FC + PC)	Efficiency (FC+ PC)
3	2574	1364	53.0%	164	1528	59.4%
6	5146	2750	53.4%	348	3098	60.2%
10	8571	4581	53.5%	619	5200	60.7%
15	12948	6954	53.7%	951	7905	61.1%
20	17299	9307	53.8%	1255	10289	59.5%

Table 6.3: Efficiency of ICAL for 3, 6, 10, 15, and 20 year data samples for both FC and (FC + PC) events, after applying cuts as described in the text.

6.4.3 The oscillation parameters

The theoretical up/down ratio is determined for a 20 year of NUANCE data, incorporating the resolution functions discussed earlier. A chi-square analysis of the samples (referred to as "data"), generated for different exposure times in the detector, with the "theoretical" ratio thus determines the best-fit oscillation parameters and their precision.

FC Analysis : The up/down events ratio as a function of L/E for FC events is shown in Fig. 6.17 for a sample case with data generated for an exposure time of 6 years. These were binned for the up/down events ratio as a function of L/E. The figure also shows the allowed region of oscillation parameter space obtained from a best-fit to the up/down ratio. Both 90% CL and 99% CL contours are shown, along with the best-fit values of $\delta_{32} = 2.03 \times 10^{-3}$ eV^2 and $\sin^2 2\theta_{23} = 1.0$ for input values 2.00×10^{-3} eV^2 and 1.0 respectively.

(FC + PC) Analysis : The same 6-year data sample was then analysed including both the FC and PC events, the latter analysed as mentioned earlier.

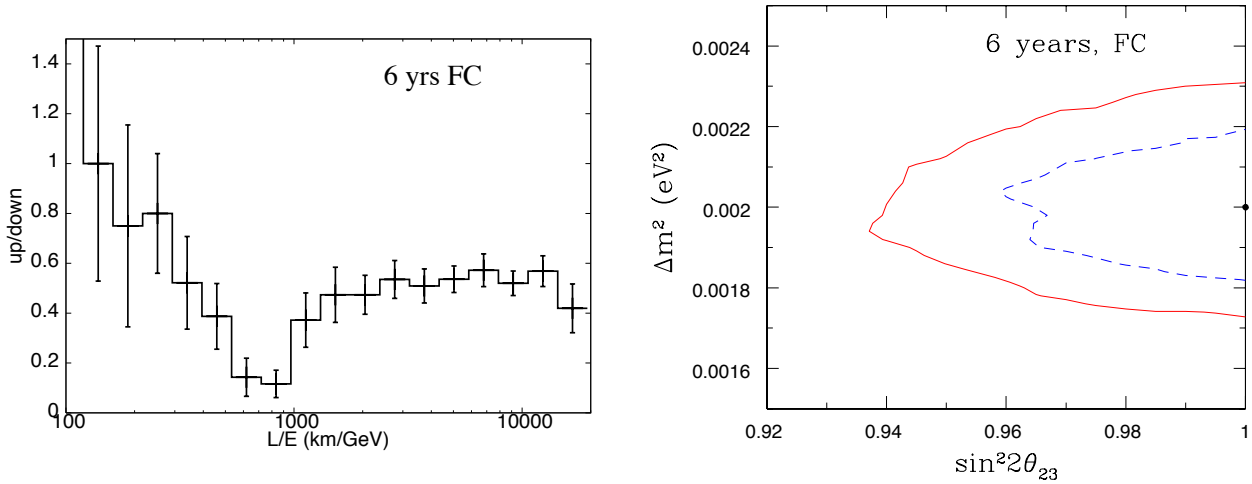

Figure 6.17: The up/down ratio as a function of L/E obtained from GEANT simulated data of a 6 year NUANCE data sample with oscillation parameters δ_{32}, $\theta_{23} = 2 \times 10^{-3}$ eV^2, 45°. The allowed oscillation parameter space is shown on the right, where the 90% CL and 99% CL regions and best-fit value are shown.

The resulting up/down events ratio is shown in Fig. 6.18, with the allowed oscillation parameter space. The best-fit point corresponds to $\delta_{32} = 2.04 \times 10^{-3}$ eV^2 and $\sin^2 2\theta_{23} = 1.0$ for the same input values of 2.00×10^{-3} eV^2 and 1.0 respectively. It may be seen that the allowed parameter space is somewhat larger than with the pure FC sample. This is a clear indication that the PC events analysis needs to be further optimised. PC events crucially add to the statistics in the low L/E bins. Thus an improved analysis in this sector is necessary to improve upon the obtained precision of the parameters.

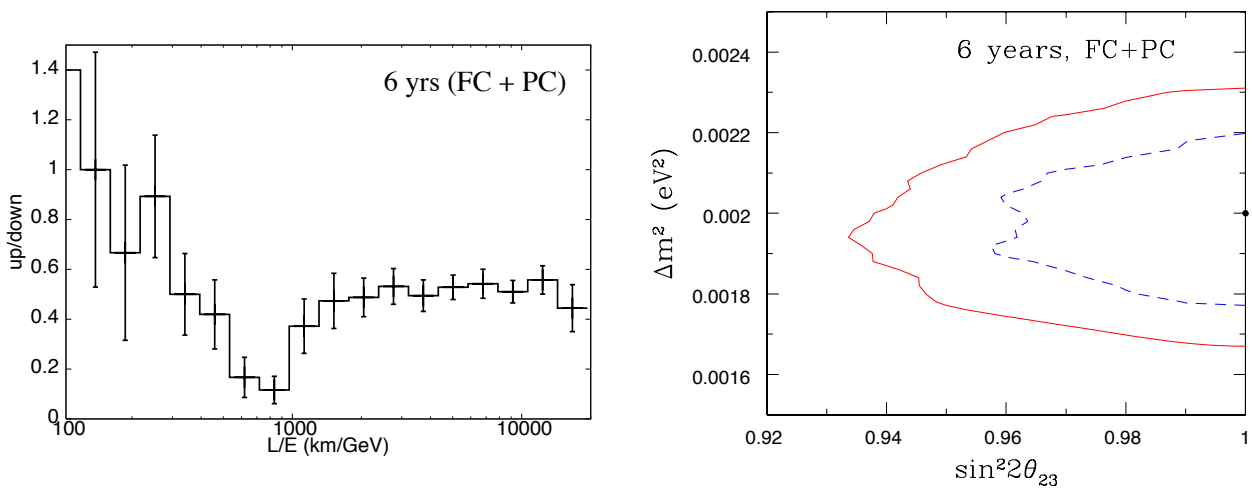

Figure 6.18: As in Fig. 6.17, but for a combined sample of FC and PC events.

A comparison of this result (FC analysis) with the Super-Kamiokande [201] data (from both a zenith angle and an L/E analysis) is shown in Fig .6.19. It is seen that the precision in both δ_{32} and $\sin^2 \theta_{23}$ is significantly better than the existing limits from Super-Kamiokande.

6.4.4 Precision Plots

The precision with which the neutrino oscillation parameters can be determined with ICAL depends on the exposure (both size and time) as well as on the quality of the cuts used in

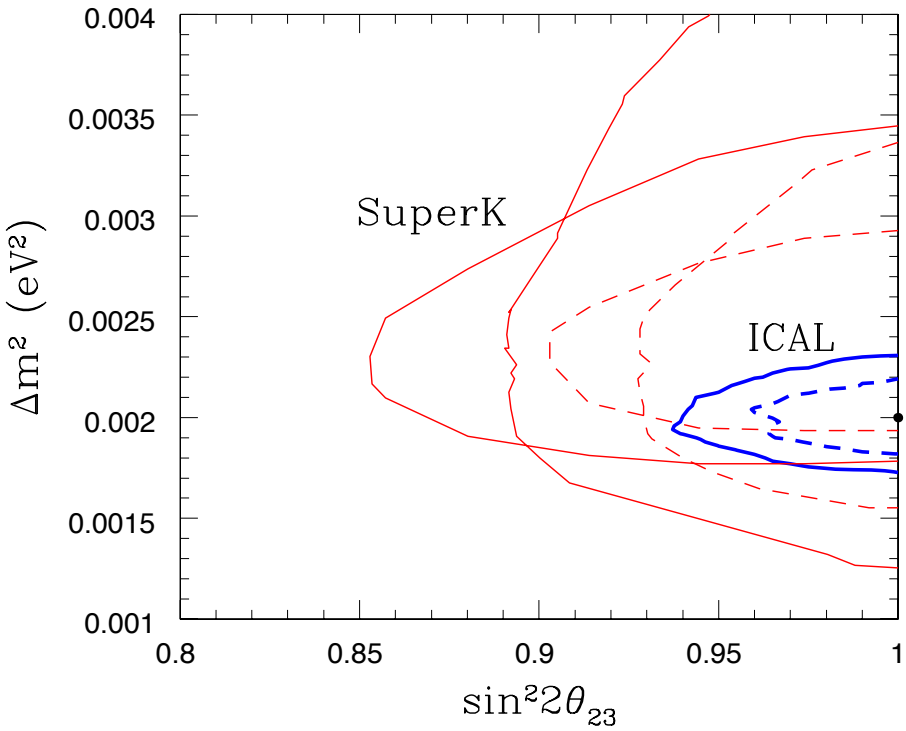

Figure 6.19: The allowed oscillation parameter space obtained from this analysis overlaid with the corresponding contours (at 90% (dashed lines) and 99% C.L. (solid lines)) obtained from the Super-Kamiokande Collaboration using both zenith angle (contours narrow in θ_{23}) and L/E (contours narrow in Δm^2) analyses [201].

the analysis. A figure of merit for the precision at a given confidence level is defined as

$$\text{Precision} = 2\left(\frac{\text{upperlimit} - \text{lowerlimit}}{\text{upperlimit} + \text{lowerlimit}}\right) .$$

The variation of precision of $\sin^2\theta_{23}$ and δ_{32} with years of exposure is shown separately in Figs. 6.20 and 6.21 for FC and (FC+PC) events. Here the limits correspond to 3σ errors. The plots indicate that the precision scales statistically ($\sqrt{N}$) with exposure. The precision obtained, especially for δ_{32} is rather worse than that computed from the physics calculation in Chapter 3. In the former, a separation of ratios of neutrinos and anti-neutrinos was done, in order to increase the sensitivity to the oscillation parameters. Here, a combined sample of neutrinos and anti-neutrinos has been considered. Also, the precision may improve with improvement in the reconstruction of the PC events.

6.5 Cosmic ray muons

Low energy cosmic ray muons form the most significant background to the atmospheric neutrino events of interest. High energy cosmic ray muons, however, are an interesting signal in such a detector. This is because their fluxes, which are not very well-known at very high energies, can be studied at ICAL via the pair-meter technique as discussed in Chapter 4. We will begin by describing the cosmic muon flux background first and address the detection of the very high energy component of this flux next.

Muons are the most penetrating of the cosmic background radiation. The cosmic ray muon flux is known to fall exponentially (actually, to be precise, faster than $E^{2.7}$) with

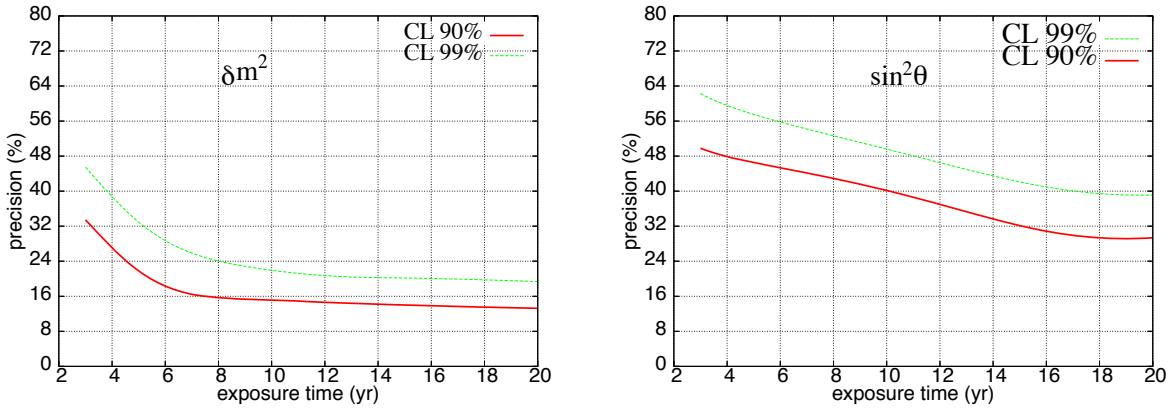

Figure 6.20: Precision in δ_{32} and $\sin^2\theta_{23}$ with FC events, as a function of exposure.

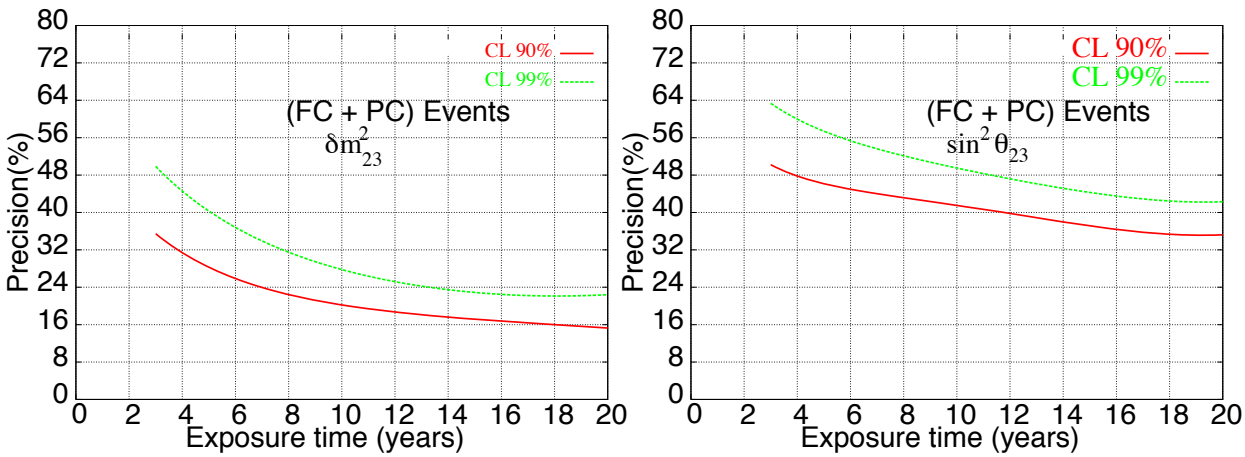

Figure 6.21: Precision in δ_{32} and $\sin^2\theta_{23}$ with FC+PC events, as a function of exposure.

depth. However, due to the large primary flux, there is a substantial cosmic muon flux present even 1 km underground.

Here, we use some simplistic formulae and approaches to get a preliminary estimate of the muon fluxes at the possible PUSHEP and Rammam sites for the proposed ICAL detector.

6.5.1 The surface muon flux

The surface muon flux has been very well-measured [158]. Here we use some well-known analytical formulae to describe the energy and zenith angle dependence of the flux [159].

$$\frac{\mathrm{d}N_\mu}{\mathrm{d}E_{\mu,0}} \approx \frac{0.14E_{\mu,0}^{-2.7}}{\mathrm{cm}^2\ \mathrm{s\ sr\ GeV}} \times \left\{ \frac{1}{1+1.1E_{\mu,0}\cos\theta_z/(115\ GeV)} + \frac{0.054}{1+1.1E_{\mu,0}\cos\theta_z/(850\ GeV)} \right\} . \quad (6.1)$$

This formula is valid when muon decay is negligible (the muon energy, $E_{\mu,0} > 100/\cos\theta$ GeV) and the curvature of the Earth can be neglected ($\theta_z < 70°$). The first term in brackets is from pion decay (dominant contribution) and second from kaon decay. This is the total muon spectrum, with the muon charge ratio μ^+ to μ^-, being slightly more than unity because of the excess of protons over neutrons in the primary spectrum, together with the fact that there are more π^+ than π^- in the forward fragmentation region of proton-initiated interactions.

The angular distribution of muons on the surface is energy dependent. The higher energy ones, of interest here, approach a $\sec\theta_z$ distribution for $E_{\mu,0} > 115$ GeV and $\theta_z < 70°$. While

the above formulae are strictly valid for $\theta_z < 70°$, we use these formulae for all $0° < \theta_z < 90°$, for convenience; roughly 25% of the events are in the bin $70° < \theta_z < 90°$.

6.5.2 Cosmic rays underground

The muons lose energy by ionisation, and by radiative processes including bremsstrahlung, pair production and photonuclear interactions. The total muon energy loss may be expressed as a function of the amount of matter traversed, X,

$$-\frac{\mathrm{d}E_\mu}{\mathrm{d}X} = a + bE_\mu \ ,$$

where a is the ionisation loss, and b is the fractional energy loss by the three radiation processes. Both a and b are mildly energy dependent. The range of muons of energy $E > 1000$ GeV exceeds 2.45 km w.e. (2.65 km. w.e. is about 1 km depth in standard rock of density 2.65 gm/cc). Since both the PUSHEP and Rammam sites have a cover greater than 1 km in all directions, this means that only those surface muons with $E_{\mu,0} > 1$ TeV will reach the ICAL detector. For such high energy muons, the parameters a and b can be considered to be energy independent, with values $a = 2.7 \times 10^{-3}$ GeV/(gm/cm^2) and $b = 4 \times 10^{-6}$ / (gm/cm^2). Then, the muon energy loss equation above can be easily integrated and inverted to give the energy of the muon at slant depth X, in terms of the energy $E_{\mu,0}$ of the surface muon,

$$E_\mu = (E_{\mu,0} + \epsilon)e^{-bX} - \epsilon \ ,$$

where $\epsilon = a/b$. Then the muon spectrum, at slant depth X, in terms of the *observed* muon energy E_μ at that depth is

$$\frac{\mathrm{d}N_\mu(X)}{\mathrm{d}E_\mu} = \frac{\mathrm{d}N_\mu(X)}{\mathrm{d}E_{\mu,0}}\frac{\mathrm{d}E_{\mu,0}}{\mathrm{d}E_\mu} \ ,$$

and can be computed within the approximations used. The spectrum at two constant depths of 3.4 and 4.6 km w.e., corresponding roughly to the vertical overburden at PUSHEP and Rammam respectively, are shown in Fig. 6.22.

6.5.3 The slant depth X

A knowledge of the slant depth X requires a detailed knowledge of the topography of the land around the site. We use two approximations:

1. The depth is a constant, equal to the vertical depth just above the cavern. This equals 1.3 km in PUSHEP and 1.7/1.8 km in Rammam for two possible tunnel lengths.

2. The topography is a "triangle", with height h_0 equal to the vertical depth just above the cavern and half-length l_0 equal to the length of the approach tunnel. The half-lengths are 2.1 km at PUSHEP and 3.85/3.97 km at Rammam for the two tunnel lengths (the second number is not 4.85 since the last 1 km is roughly perpendicular to the 3.85 km stretch). In this case, the slant depth is calculated geometrically as

$$X = \frac{h_0 \sec\theta_z}{1 + \tan\omega \tan\theta_z} \ ,$$

where $\tan\omega = h_0/l_0$ is the "slope" of the mountain and is a function of the zenith angle.

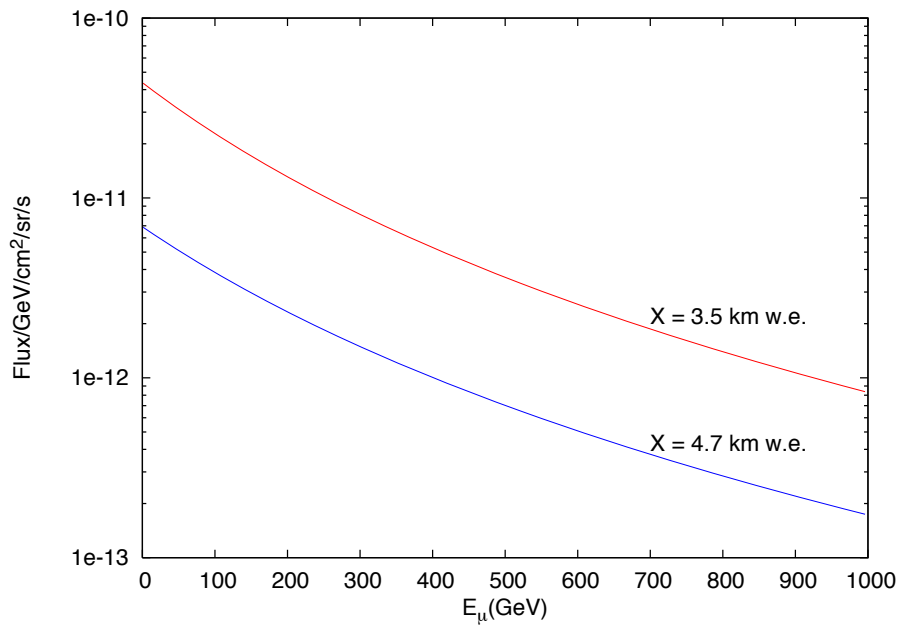

Figure 6.22: Flux of neutrinos at depths X in km w.e. below ground, as indicated. The two values correspond roughly to vertical depths at PUSHEP and Rammam.

6.5.4 The aperture

The aperture of ICAL includes contributions from 5 faces: top, left, right, front and back. The bottom face of ICAL does not contribute since the muons are coming from above. We consider a 32 m $\times$ 16 m $\times$ 12 m ICAL geometry. We also require that, for a cosmic ray muon to be detected, it has to pass through at least 7 layers at ICAL. Since the two possible topographies we have used are symmetric in ϕ, the aperture integration is trivial over this variable. A monte carlo code was used to calculate the aperture. This comes out to be roughly 85% of the geometric aperture, i.e., 5702 $m^2 sr$. However, in the actual calculation, the total flux was numerically integrated (aperture, weighted by flux) since the flux is also zenith angle dependent. The results are shown in the figures below.

6.5.5 Results

Fig. 6.22 shows the muon flux at PUSHEP and Rammam assuming constant depths of 1.3 and 1.7 km respectively. It is possible to compute the flux, depending on the two choices of topography: flat, or "triangular", as described above, so that the flux depends on the slant depth, X, which is in turn zenith angle dependent. The flux times aperture, suitably integrated, gives the total flux/hour at ICAL, for both PUSHEP and Rammam. Fig. 6.23 shows the total flux, integrated in 20 GeV energy bins (for $E_\mu > 1$ GeV, passing through at least 6 iron plates), for PUSHEP and Rammam for the flat topography (constant depth of h_0). The two curves show the contribution from the top and the total contribution in each case. Due to the ICAL geometry, the contribution from the top is about 48%, with that from the two longer sides being about 35% of the total flux. Fig. 6.24 shows the flux for the second assumed topography, that of a triangular cross-section. Note that the shorter tunnel option at Rammam has been used in the calculations.

The total energy integrated fluxes are listed in Table 6.4.

In summary, the energy bin from 1 to 20 GeV, that is most likely to cause any significant background to the neutrino events of interest at ICAL, will contain roughly 320–355

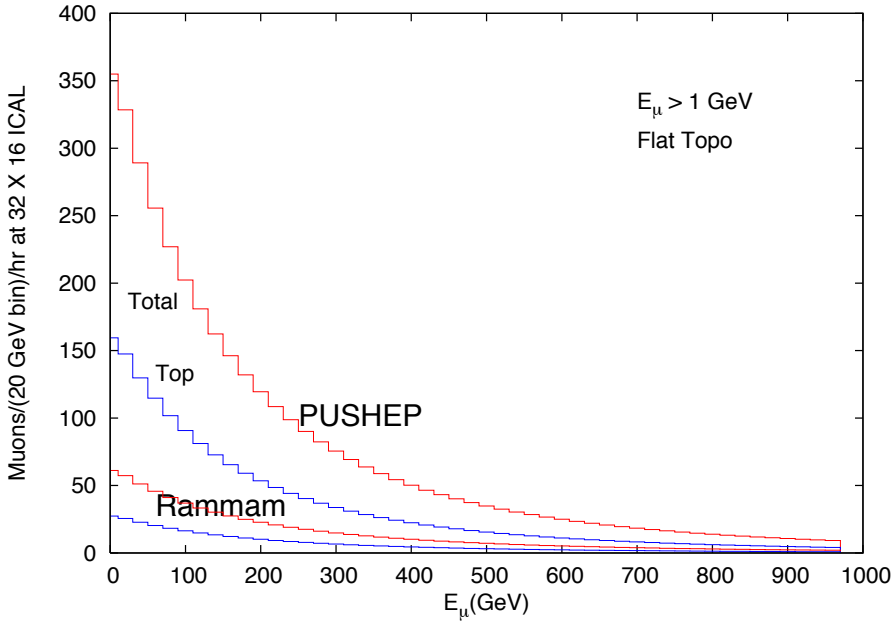

Figure 6.23: Integrated flux per hour of muons at constant depths X in km w.e. below ground, in energy bins of 20 GeV ($E_\mu > 1$ GeV). The two sets of curves correspond roughly to vertical depths at PUSHEP and Rammam. The contributions from the top aperture (32 m $\times$ 16 m) and the total from the top and four sides of ICAL are separately shown.

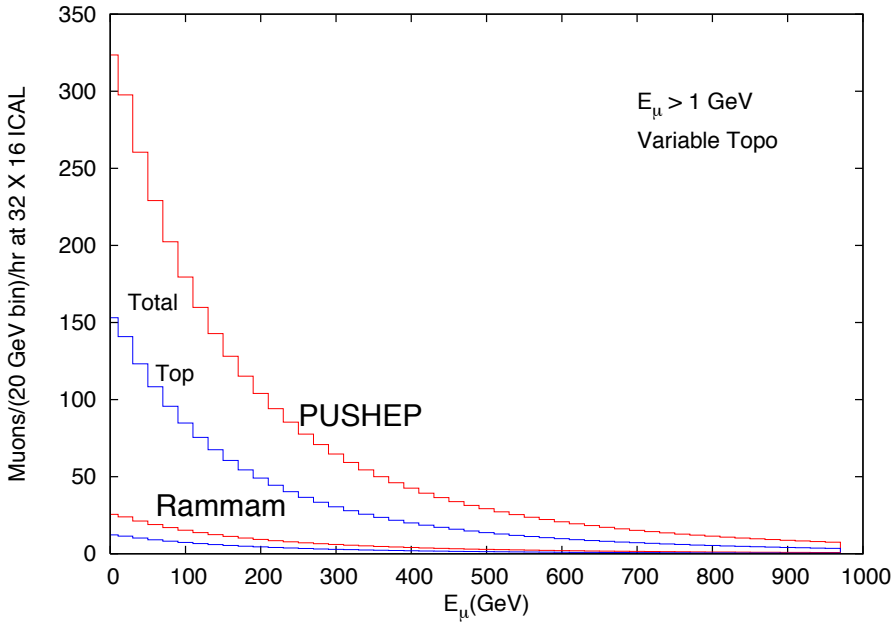

Figure 6.24: As in Fig. 6.23, at triangulated depths X in km w.e. below ground. For more details, see the text.

Topography	Site	Events/hour
Flat	PUSHEP	3774
	Rammam	710
Triangle	PUSHEP	3307
	Rammam	290

Table 6.4: Total energy integrated ($E > 1$ GeV) cosmic ray rates at PUSHEP and Rammam sites at a 32 m$\times$16 m ICAL detector. Two topographies: a flat overburden, and a triangular mountain, are assumed, in the calculation. The event rate is much smaller at Rammam for the triangle topography due to the large access tunnel length.

events/hour at PUSHEP and 25–61 events/hour at the first option at Rammam. The corresponding rate from cosmic ray neutrinos interacting with rock surrounding the cavern to give muons is about 460 events per year at either site. In particular, about 1700 events with $1 < E_\mu < 40$ GeV, and about 600 events with $E_\mu > 40$ GeV are expected in 5 years, with typical oscillations turned on.

6.5.6 Pattern of hits in the ICAL detector

There are relatively fewer cosmic ray events at Rammam. Hence we examine the effect of the cosmic ray background at PUSHEP in order to determine how this flux will affect the neutrino studies.

Fig. 6.25 shows a typical set of cosmic ray muons hitting the top and four sides of ICAL per hour of exposure.

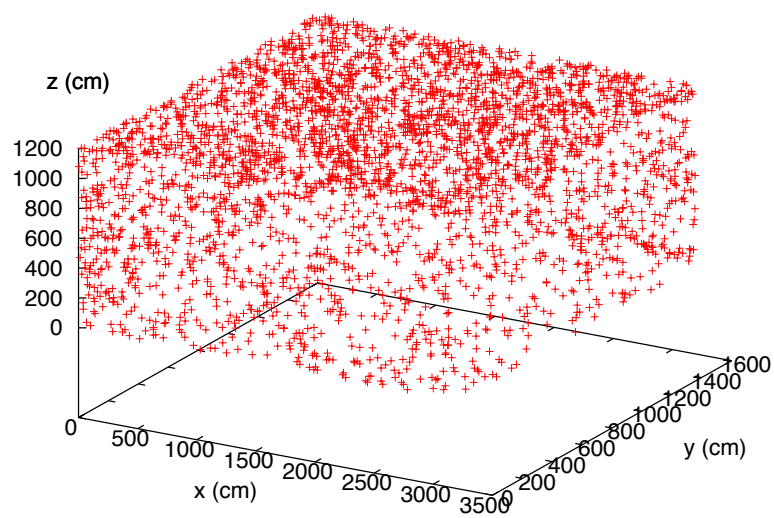

Figure 6.25: Cosmic ray muon events for one hour exposure at ICAL/PUSHEP. Shown are the "vertices", that is, the points of entry of the muons into the detector.

The events at the top look more dense since the entire $0 < \phi < 2\pi$ aperture is allowed, while only half that aperture is available from the sides. In this simulation, all possible events are generated, without the requirment cut of "passing at least 7 iron plates". Fig. 6.26 show the GEANT-based simulation of 1 minute and 10 minutes of cosmic rays through ICAL.

Here a constant magnetic field of 1 T was turned on in the y-direction; however, the effect of this is not visible in the figures due to the high energy of most events.

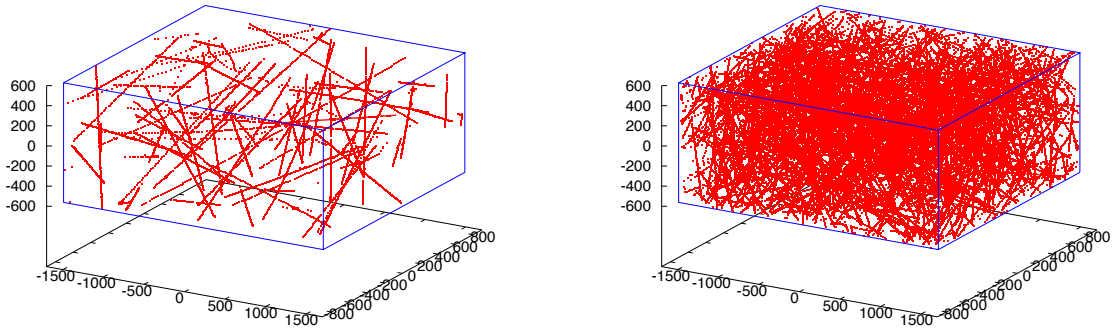

Figure 6.26: Cosmic ray muon events for 1 and 10 minutes exposure at ICAL/PUSHEP.

Clearly, the density of hits will be very high for one hour. Hence, the one hour exposure data of hits is shown in Fig. 6.27 as three horizontal slices: of the top and bottom layers, and the central layer, and as three similar vertical slices through the detector. The "cross-hair" bands shown indicate the size of 100 pixels in each direction. The pixel size assumed was 2 cm each in the x- and y-directions. That is, this is the accuracy to which the location of the hit can be pin-pointed.

It is also clear that most of the tracks are very long, some passing all the way through the detector; that is, the sample is dominated by very high energy events. Close examination (which may not be possible with these figures) also shows that there are hardly any events where the tracks *do not* begin at any surface, i.e., these are unlikely to mimic muon events from charged-current neutrino interactions in the detector (that constitute the signal and are to be used to study neutrino oscillations).

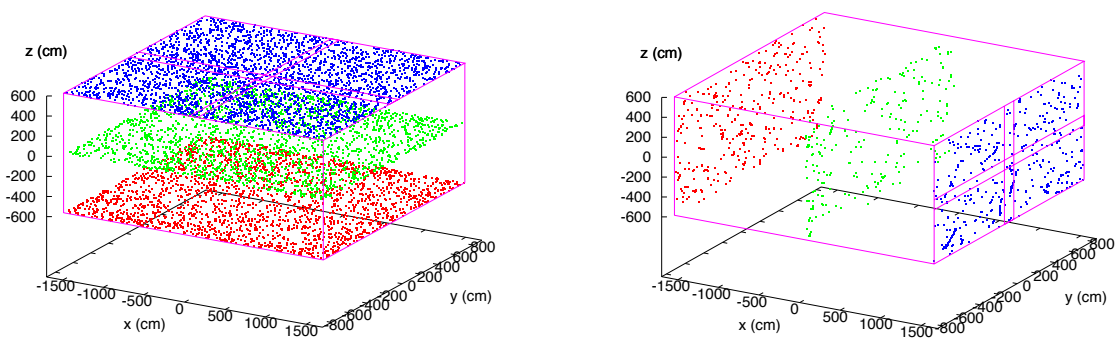

Figure 6.27: Hits in ICAL detector from cosmic ray muons for 1 hour exposure at ICAL/PUSHEP. Shown are hits in typical horizontal and vertical layers.

6.6 Very high energy muons

The PeV cosmic ray muons degrade on their way to the ICAL detector underground and pass through the detector with typically few 10s or 100s of TeV energy. Such muons are not

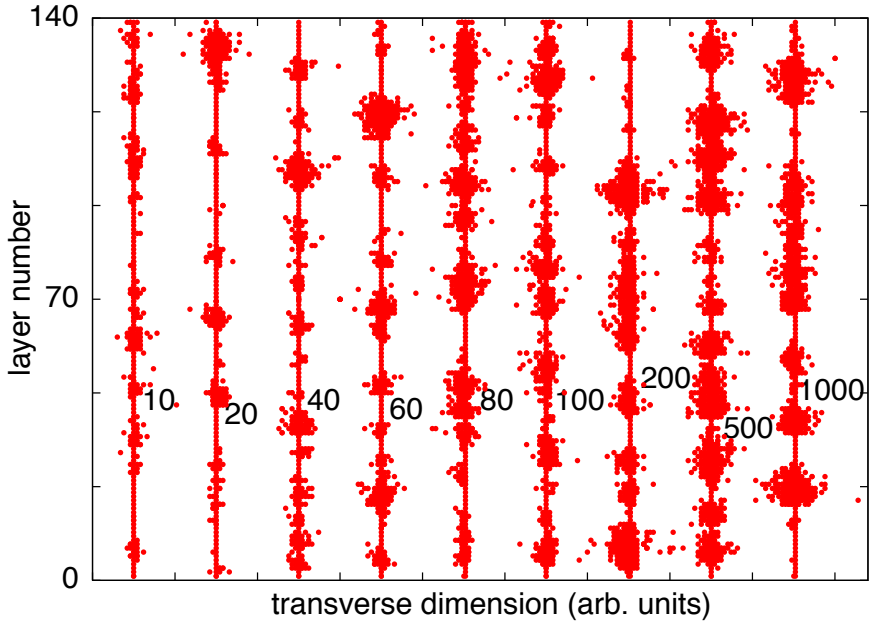

Figure 6.28: Tracks in ICAL of high energy muons vertically passing through the detector. The x-axis indicates a transverse direction while the y-axis is the vertical direction and is labelled by the layer number. The energy of the muons in TeV is indicated next to the tracks.

deflected by the magnetic field of the detector nor are they confined within the detector in any way.

These (still) very high energy muons produce energetic e^+-e^- pairs which produce cascades in the detector. The nature of electromagnetic cascades depends not only on the energy of the pair but also on the thickness of the iron plates (which absorb these particles) and the transverse resolution (strip width) of the detector. However, it is well-known, as discussed in Chapter 4 that these cascades can be used to determine the energy of the muon.

The relative error in the energy measurement is roughly given by $\delta_E \sim \sqrt{1/(\alpha T)}$, where $\alpha = 1/137$ is the fine structure constant and T is the number of radiation lengths traversed by the muon. For ICAL, a vertical muon traverses 477 radiation lengths so that $\delta_E \sim 0.50$. This error improves marginally for slant-going muons.

The tracks through ICAL of vertical muons of very high energy (10 to 1000 TeV) are shown in Fig. 6.28. Small and large cascades are clearly seen; in general, larger clusters at higher energies are visible to the eye.

A zero-th order attempt to calibrate the muon energy was done by counting the total number of hits in the track. Notice that the shower triggers several hits in the same layer, unlike muon tracks at low (few GeV) energy. The calibration is made direction-independent by normalising the track-length to the vertical height of the detector. It was found that this scaling holds over a wide energy range. The number of hits per equivalent "vertical" detector height (477 radiation lengths) is plotted as a function of the incident muon energy in Fig. 6.29. While the behaviour is fairly linear up to about 100 TeV, strong non-linearity sets in beyond 100 TeV. It may therefore be possible to determine the energy of such muons simply by calibrating the total number of hits.

For higher energies, it is not possible to use such a crude analysis. The standard method in this case is to use the pair-meter technique. Here, the energy of the muon is calibrated by counting clusters of different sizes. It is known that the most sensitive clusters are those that carry about (10^{-3}–10^{-2} fraction of the incident muon energy. Higher energy electromagnetic

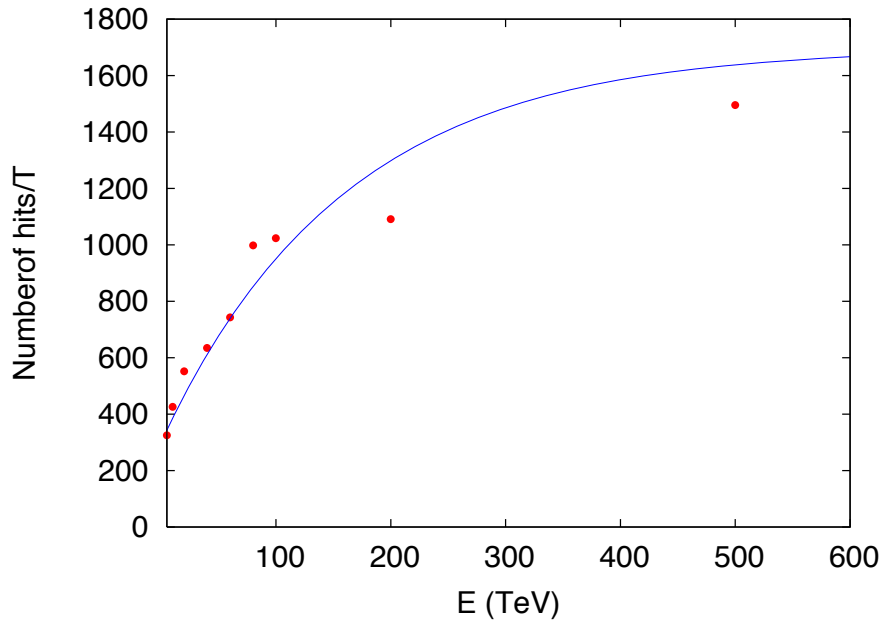

Figure 6.29: Number of hits normalised to the vertical detector height versus the incident muon energy. The x-axis scale begins at 10 TeV and T corresponds to a distance of 477 radiation lengths. Linear behaviour is noticed up to $E_\mu \sim 100$ TeV. Errors on the energy estimates are of the order of 50%; see text for details.

cascades have a much larger transverse spread than lower energy ones. That is, the number and distribution of hits per layer is an indicator of the energy in the shower, as discussed in Chapter 4 and shown in Fig. 4.2. Hence, the hits shown of Fig. 6.28 can be reorganised in terms of number of hits per layer, as shown in Fig. 6.30.

In the figure, typical tracks for muons with energy $E = 10, 100, 1000$ TeV are shown. While the total number of hits does not increase linearly with energy, the number of energetic cascades is very different in the three cases. For instance, there are only medium sized clusters at 10 TeV. For the 100 TeV track, 1 cascade with energy greater than 500 GeV, 4 cascades with energy greater than 100 GeV, and 14 cascades with energy greater than 10 GeV can be seen. This is consistent with the expectation for the track of a 100 TeV muon. This characterisation needs to be quantified further and a more detailed analysis performed.

6.7 Open issues

The gaps are in the following areas:

1. A track recognition algorithm to separate the muon tracks from the hadron hits using Hough transforms is being fine-tuned. A preliminary study involving track fitting as well as some basic recognition algorithms using the Kalman filter technique has begun.

2. Reconstruction of fully contained events seems rather straightforward. However, a clear understanding of partially contained events which is necessary to improve the statistics, especially at small L/E values, is still awaited. Since most high energy events will be partially contained, improper reconstruction of such samples will alter the up/down ratio at small L/E and worsen the fits considerably. A lot of effort is currently going-on to improve our understanding of such events.

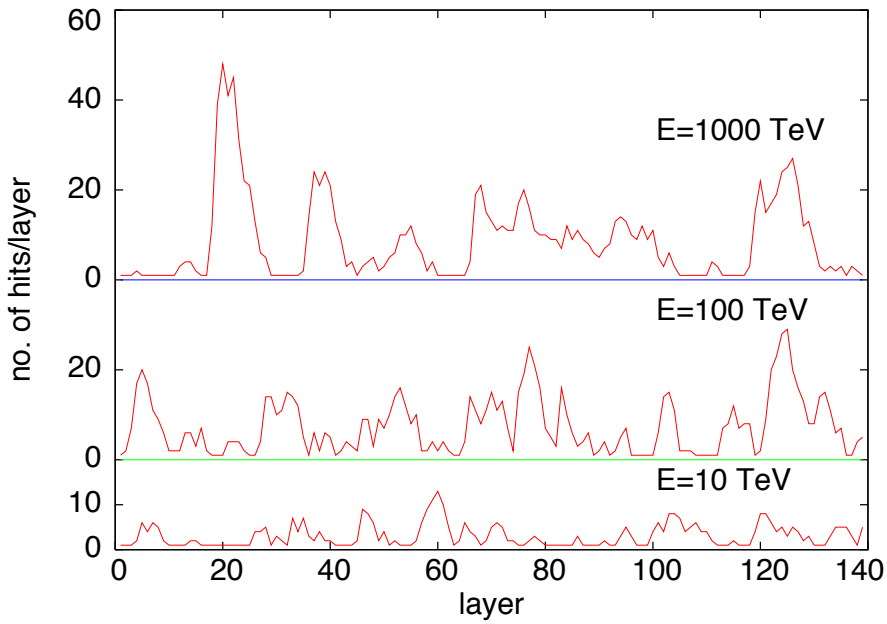

Figure 6.30: Number of hits per layer shown over the track length of vertical muons with energies $E = 10, 100, 1000$ TeV. Cascades are clearly seen as peaks in the number of hits/layer. Larger cascades are more energetic.

3. Inclusion of 3-flavour oscillations and study of matter effects has been studied extensively using the codes described in the physics analysis. However, a GEANT analysis of these phenomena remains to be done. This is important since matter effects at ICAL can be significant due to the large L and E ranges afforded by atmospheric neutrinos and the charge identification possible at ICAL.

4. Efforts are on to optimise the detector configuration. In particular, what has been studied are the effects of a constant magnetic field that periodically undergoes sign-flips (as is the case with a toroidal coil), effects of non-uniform magnetic fields, effect of changing strip width (taken to be 2 cm in x and y, thus limiting the spatial resolution in the transverse direction to be 2 cm), and the effect of a vertically oriented geometry. All these results have been obtained and presented in various meetings of the Simulation group; however, they are still at a preliminary stage and need verification.

5. A study of cosmic ray muons produced by interactions of atmospheric neutrinos in the rock surrounding the detector. Here the ratio of interest is that of the up-coming event rate to the theoretically predicted rate. This is because the down-going neutrino-induced events will be swamped by the cosmic ray muon background. Although such a ratio has theoretical uncertainties due to flux, etc., again, a clear dip is seen in this ratio, signalling that it is sensitive to oscillations. However the analysis for extraction of the oscillation parameters is yet to be completed.

6. A major issue, yet to be studied, is the mis-identification of pions as muons from neutral current (NC) as well as a subset of CC events and electron CC events. This will contribute to the background.

7. Analysis of cascades with very high energy muons needs further characterisation.

The simulations group is currently engaged in a study of these issues.

Chapter 7

A tale of two sites

An important component of the INO feasibility study would be to find an appropriate location with sufficient rock overburden to satisfy the physics objectives. This section briefly outlines the results of the various surveys undertaken in many places all over the country[1].

The site survey group studied the topographic material, discussed with the scientists of the Geological Survey of India and the engineers involved in many underground projects, regarding many possible sites in the Western Ghats of South India and the lower Himalayan region in West Bengal. Based on a set of criteria evolved for the purpose, two particular sites located at *Singara in the Nilagiris* and *Rammam in Darjeeling* were identified as the possible sites. [2]

A Site Selection Committee (SSC) was authorised to prioritise these sites with the available information. The SSC has now recommended that the site at PUSHEP in the Nilagiri mountains in South India is the preferred site for locating INO underground laboratory.

An engineering task force is now being formed to prepare the Detailed Project Report for the site.

For completeness, we first outline the set of criteria which were used to determine the suitability of the sites surveyed for the location of INO and then present a summary and comparison of the two possible sites.

7.1 Site requirements

In order to have some uniform criteria to prepare a report on possible sites for INO, the following criteria were suggested[3]:

The recommended evaluation criteria may include the following factors :

1. **History of the site:** This mainly translates to the issue of availability of the site on a long-term basis. It should be noted that the underground facility will be used for decades in future to conduct many experiments in physics and other sciences.

2. **Cost factors**: This includes both construction costs and operating costs. Existing underground projects like hydro-electric plants are better since many of the facilities such as access roads and housing would already be present and save costs.

[1]The details of the site surveys are given in a separate volume: Volume II Site Surveys

[2]Apart from these, another exciting possibility appears to be the 8800 meters long *tunnel under Rohtang Pass near Manali*. Some details of this site is given in the Appendix G.

[3]These criteria were gleaned from our own experience as well as by looking at similar studies in other locations, especially the documents related to the proposal for a National Underground Science Laboratory in the US (see http://int.phys.washington.edu/NUSEL/ for more details). We have benefitted much from these earlier or ongoing projects

3. **Risk Factors and Safety issues:**

   - Rock conditions risk: This risk factor includes multiple considerations relative to the risk of capital and operating cost overruns due to unexpected rock conditions. Forecasting based on known stress conditions may help in anticipating such a risk.
   - Environmental Risk: The time and expense required at various sites to determine what is safe and environmentally sound.
   - Seismic Risk: Although engineering can control seismic risk, there is an additional cost involved in installing detectors in a seismically active region. In addition, there is a risk of a more intense than expected earthquake or an engineering or installation mistake that leads to failure in an earthquake of expected magnitude.
   - Mechanical Systems Risk: Sites with heavy equipment, hoisting or other machinery have an operating cost risk due to the possibility of failure of significant mechanical systems.

4. **Depth:** Apart from a reasonable overburden in all directions, a complete 3D topo map of the region must be prepared for evaluating backgrounds. Rock density, suitability for low radioactivity experiments, are other considerations.

5. **Neutrino Beam:** Though this is still some way into the future, distances to various neutrino factories and any particular advantage that may be there due to physics reasons is an important factor.

6. **Time to Install First Detectors:** This is perhaps the most important factor for ICAL to be competitive.

7. **Accessibility:** Access to the laboratory by air/train/road throughout the year is an important factor. The perceived ease of personnel access to the laboratory is important both as a substantive factor and as a quality-of-life factor. Ideally, the laboratory should be available 24 hours a day, seven days a week.

7.2 Summary of the sites

Details of the location, geology and physics prospects at both PUSHEP and Rammam sites are available. The topographies are well-known as well as the type and quality of the rocks. Some highlights of the two sites are presented below, followed by a comparative study of the two locations.

PUSHEP Site

This site is located in Singara in South India (Lat. North 11.5° and Long. East 76.6°). There are three airports (two international) located at Bangalore, Coimbatore and Calicut within a few hours of driving distance. Situated in the southern peninsular shield, it offers one of the best tunnelling medium for the creation of an underground facility.

If located here, the INO site will be an extension of an almost-operational underground Hydel project located about 6.5 km from a town called Masinagudi (90 km south of Mysore) at the edge of the Mudumalai sanctuary near the borders between Tamil Nadu, Karnataka and Kerala states. It is called the Pykara Ultimate Stage Hydro Electric Project (PUSHEP) and is being executed by the Tamil Nadu Electricity Board (TNEB). The powerhouse is

located in a cavern 500 m underground, accessed by a 1.5 km long tunnel. The intake and tail-race tunnels as well as the transformer are all housed underground as well. In all, nearly 13 km of tunnels have been constructed for this project. Fig. 7.1 gives a panoramic view of the PUSHEP site.

Figure 7.1: A View of PUSHEP location from Glenmorgan.

The underground cavern that houses the generators is 20 meters wide, 39 meters high and 70 meters long, so its dimensions are similar to the requirement of INO for locating the iron calorimeter detector. The transformers are located in a smaller cavern and there are a few more caverns of smaller size. The proposed INO tunnel portal is to be located close to the existing portal of the PUSHEP access tunnel. The proposed laboratory cavern will be located under the 2207 m peak, about a km away from the PUSHEP caverns; however, the entire area is composed of similar (monolithic) charnockite rock. The prior existence of a number of tunnels and caverns is important and useful for future forecasting. In fact, a number of geological features such as shears, dykes and joints in the INO tunnel/cavern area have been mapped from both surface projections and from the existing PUSHEP tunnels. The site is also conveniently located in seismic zone-2, which implies a minimum seismic activity zone in India. A panoramic view of the peak directly above the projected site is shown in Fig. 7.2.

Rammam site

The INO site near the Rammam hydel project is located in the Eastern Himalayas at Lat. North 27.4 Long. East 88.1 in the district of Darjeeling in the state of West Bengal. It is at an elevation of 1450m and is about 140 km away from Bagdogra airport and the city of Siliguri. Bagdogra is connected by air to both Kolkata (1 hr flight time) and Delhi airports. Siliguri is connected by train to Kolkata (overnight journey) and to Delhi. It takes about 5–6 hours by car to reach Rammam from Bagdogra/Siliguri. There are three alternate routes.

Figure 7.2: Panoramic view of the mountain peak (2207 meters) at PUSHEP. The laboratory cavern will be located directly under the this peak.

The scenic hill town of Darjeeling, the district headquarters is closer - about 70 km away (2.5 hrs) and again connected by two alternate routes.

The Rammam hydel project presently has an installed capacity of 4×12.75 MW. It uses the water from the Rammam river and in its extension plans will utilise the water from the other river Lodhama. Digging of the Lodhama interconnection tunnel is going on right now.

The proposed portals of the access INO tunnel and adit are located adjacent to the metalled road leading to the Powerhouse (about 4km south) of the hydel project. They are within the hydel project settlement and connected through a network of metalled/non-metalled road. Figs. 7.2 and 7.4 shows photographs of the area at the proposed portal location. Multiple locations and depths for the laboratory are possible. The area is in seismic zone 4. Hence extra precautions needs to be taken during the construction stage. But there are a number of long tunnels and large caverns already built in and around this area. So it does not seem to be a very difficult problem.

7.3 Comparison of PUSHEP and Rammam

The atmospheric muon background flux at these two sites may be obtained from Fig. 7.5 where the depth is measured in metre-water-equivalent, MWE (depth times the density of matter). Corresponding depths of some well-known labs are indicated in the figure for comparison. Other features of INO at PUSHEP and Rammam are summarised in Tables 7.1 and 7.2.

Figure 7.3: INO tunnel portal location at Rammam Site.

Figure 7.4: Panoramic view of the Rammam river valley.

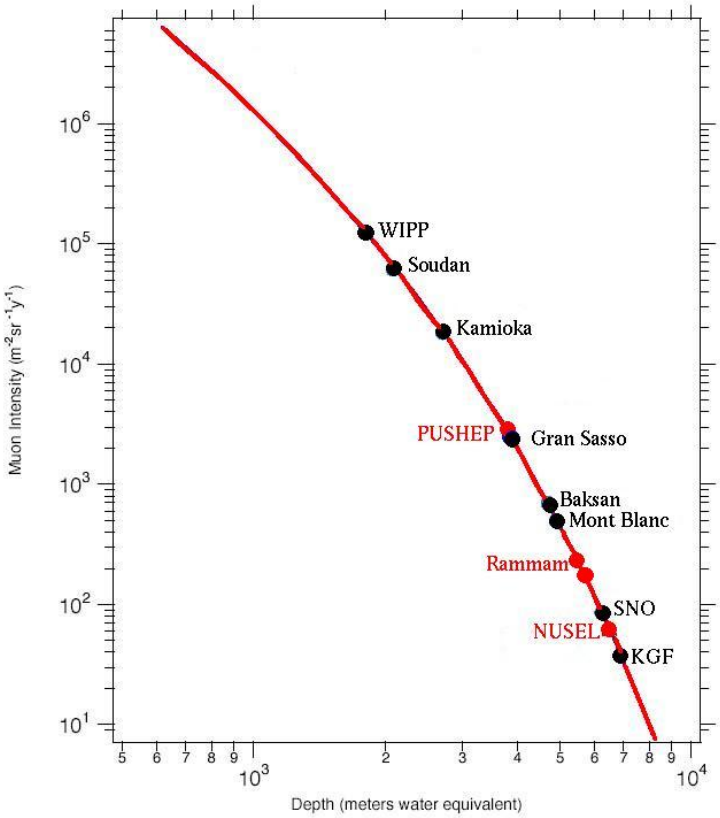

Figure 7.5: Atmospheric muon background as a function of depth. The best locations for INO correspond to backgrounds as in Gran Sasso or better.

7.4 Tunnel and Cavern Complex

The description given below provides a feasible baseline access and laboratory designs that satisfies the scientific needs of INO. These may change depending on detailed geological mapping of the site and as the INO needs are fully developed. No finality in design is presumed.

7.4.1 Surface laboratory and Portal

Once the location of the portal is decided at a chosen site for INO, an important next step is the extent and availability of land for surface laboratories, if any. Factors that need to be kept in mind are the surface laboratory location, ventilation equipment, cavern cooling plant(if necessary), visual and environmental impact as the location may be close to a reserve sanctuary and parking facilities. A dumping yard for the rock material excavated should be close by. At present the dumping yard of PUSHEP project is being cleared and should be available for INO if negotiations are successful. A similar dumping yard at Rammam is also being looked into.

7.4.2 Design of access tunnel

There are two feasible options for the design of tunnels. Single tunnel or two tunnel access. The main factors that will dictate the appropriate option will be cost and safety issues.

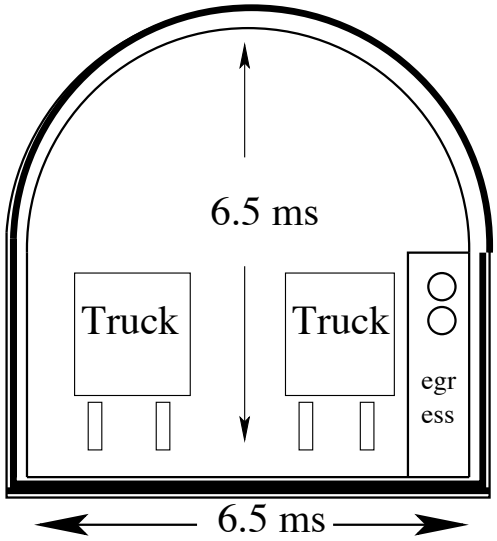

SINGLE TUNNEL

CROSS SECTION

Figure 7.6: A schematic of the two-way single tunnel shown in cross-section.

Single tunnel approach

Single tunnel approach is cost effective. Further saving may be effected by having single lane traffic with space for emergency vehicle parking and turnarounds every few hundred meters. Emergency exit may be provided by a pedestrian walkway separated by concrete wall from the traffic lane. Fresh air through ventilation ducts flows through the pedestrian tunnel which may also contain the exhaust ducts, electrical wiring, water mains and other such facilities that extend up to laboratory cavern. Fire proof doors between the traffic lane and the pedestrian walkway may be provided where the vehicular turnarounds are located.

Similar design requirements may be used for a wider tunnel allowing two lane traffic along with a pedestrian walkway containing all the ducts.

The main disadvantage of a single tunnel is that all services are located in a single tunnel even though it is cost effective.

The tunnel cross section for a single lane tunnel may be 5 meter wide by 5 meter high. On the side it contains a 1 meter wide pedestrian walkway separated by a concrete wall. For two lane traffic the PUSHEP tunnel design, with a cross section of 6.5 meters and height 6.5 meters with D-shape, is adequate. There is enough space for locating all the ducts. A cross-section view of the INO tunnel with this possibility is given in Fig. 7.6.

Two parallel tunnel approach

Traffic lanes may be separated by two parallel tunnels of smaller cross-section. The two are interconnected every few hundred meters with fire safe doors. Ventilation and exhaust ducts may be installed separately in the two tunnels. Power and other services can be divided between the two tunnels. No separate pedestrian walkway is necessary.

The main disadvantage is the cost but future expansions are not impeded and much better than single tunnel design from safety point view. The cross section is about 4 meters

wide and approximately the same height for each tunnel.

7.4.3 Cavern complex

The orientation of the cavern complex is tentatively fixed as running from North to South in PUSHEP extrapolating from the Geo-technical data available at present. The exact location and orientation of the underground complex depends on the detailed data that will be obtained and monitored as the tunnel construction progresses in the chosen site.

The present design parameters of the Cavern complex is as follows:

1. A single experimental hall measuring 22m wide, 70-120m long and 25-30m in height. This is more than adequate for housing ICAL which may have the dimensions 15m by 32m by 11.9 m and possibly other experiments with smaller dimensions. The length of the 70 (120)m allows for the expansion of ICAL detector from presently designed 35 ktons to 50 (100).

2. Smaller cavern for locating control facilities (fully air conditioned). The main experimental hall has adequate space at present to house these and a separate cavern may not be necessary.

3. Common area where the experimental hall is connected to the main access tunnel. This provides space for parking, storage, rest rooms, etc.

4. Refuge cavern at a lower level than the experimental cavern to house a drainage reservoir(in case of water leakage), fire control measures, and refuge in case of accidents.

5. All the caverns are to be connected by smaller interlinked tunnels providing exit distances less than 20-30 meters for immediate exit under emergency conditions.

A schematic view of the Cavern complex based on the present design of PUSHEP powerhouse complex is given in Fig. 7.7. A top view of the same is shown in Fig. 7.8.

7.4.4 Basic Services

Any laboratory-tunnel design will have to take into account basic services to be provided at the INO laboratory:

- Adequate power, water, emergency systems and drainage all 24 hours and throughout the year both on the surface and at underground facilities.

- Climate control measures at the cavern complex up to laboratory standards.

- Fire protection and other emergency services.

- Communication facilities for data transfer at reasonable speeds and analysis both from the underground and surface laboratories.

- Heavy components of material making up the detector have to be transported and assembled in the cavern. Mechanical outfitting like overhead cranes, scaffolding etc.

- Maximum occupancy for about 50-100 personal with unlimited access to the underground facilities.

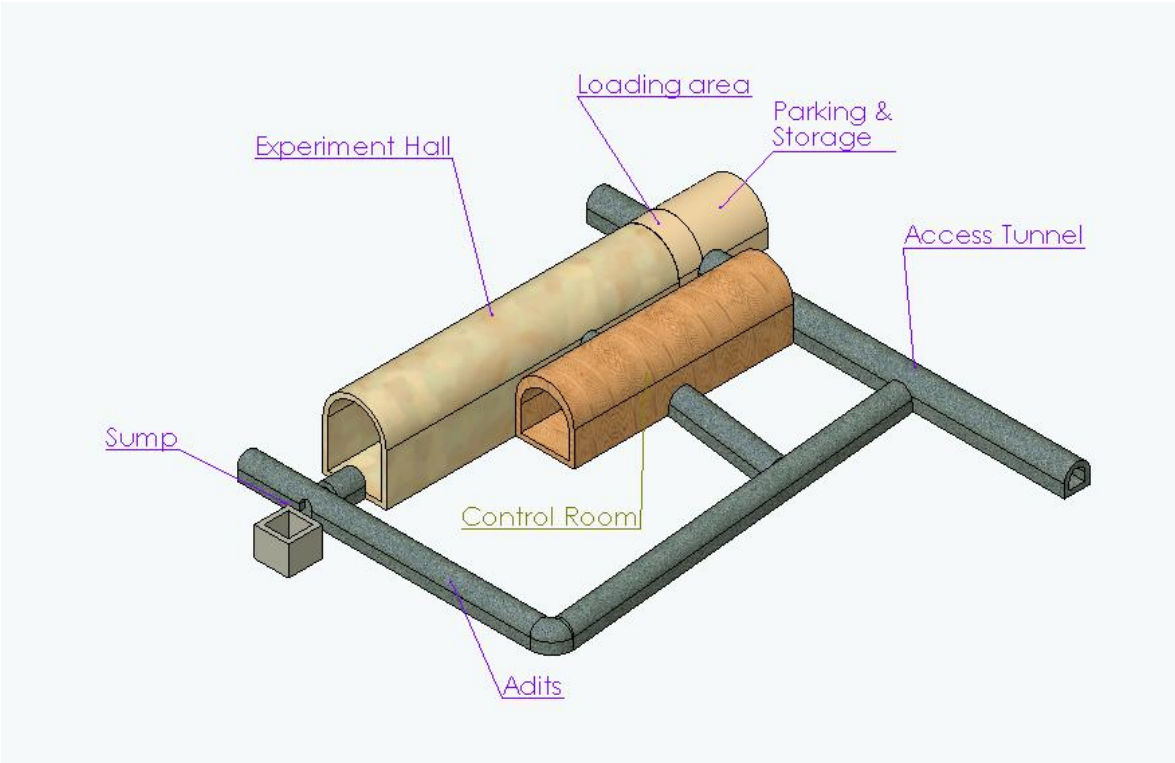

Figure 7.7: An artist illustration of the Laboratory Cavern Complex

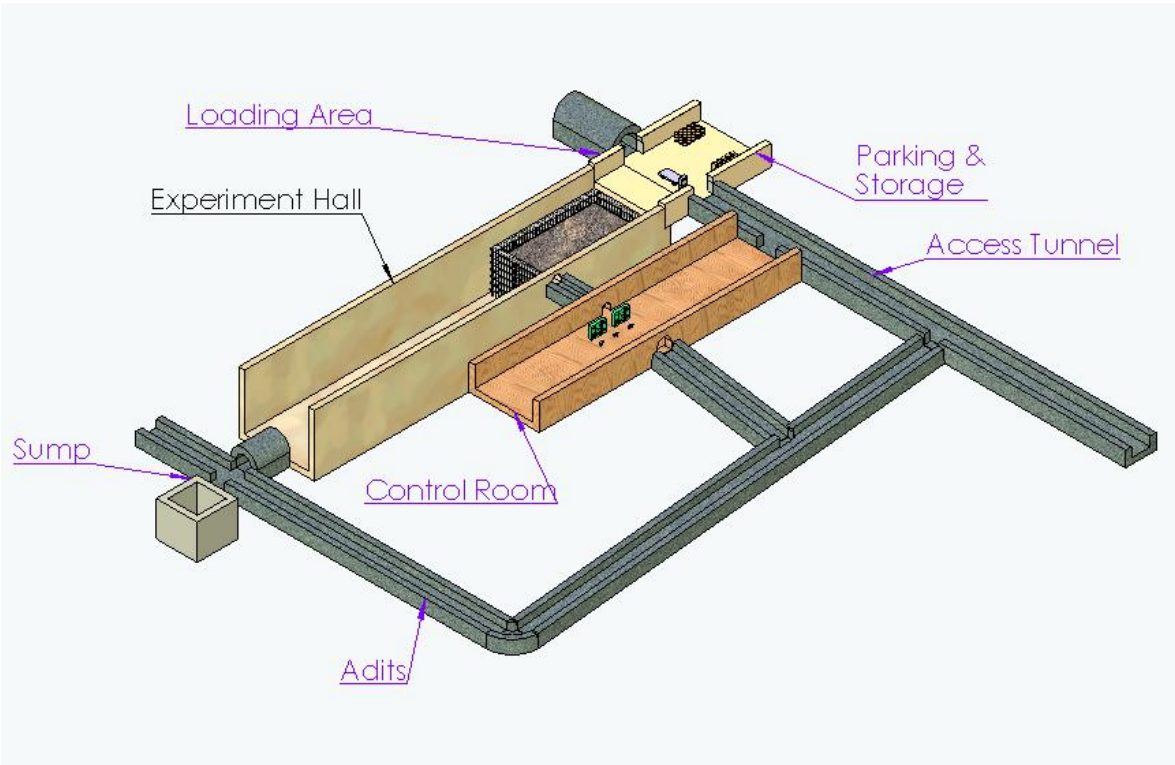

Figure 7.8: Top view of the laboratory cavern with a single detector module

Criteria	PUSHEP	Rammam
1. Site History:	Singara project since 1930s; PUSHEP built to last 100 yrs	Operating since 1995
2. Transportation: Site access:	Masinagudi (7 km) Ooty (30 km) Mysore (90 km) Coimbatore (100 km) Calicut (120 km) Bangalore (250 km)	Lodhama (5 km) Darjeeling (70 km) Siliguri (140 km)
Nearest Railhead:	Mysore (North) (90 km) Coimbatore (South) (100 km) Calicut (West) (120 km)	New Jalpaiguri (150 km)
Nearest Airports:	Coimbatore (domestic) Calicut (domestic) Bangalore (Int'l)	Bagdogra (domestic) Kolkata (Int'l)
3. Geo-technical Data: Rock type: Specific gravity: Q-factor of tunnel. medium: Horizontal/vertical stress ratio (1–2 is desirable): Seepage: Geological adversities: Geological mapping: Stand up time: Support measures: Rock radio-activity:	Charnockite (Monolith) 2.62–2.9 4-45: Good to very good Approximately 1.6 Moist to Dry No known adversities Shears, dykes, joints are mapped from both surface projections and underground tunnels 90 days to infinity PCC lining, shotcreting, rock bolting 0.005 mR/hr—very low	Gneiss 2.79–2.84 Fair to very good Not available Moist No known adversities Shears, joints are mapped from surface studies 1–90 days shotcreting, rock bolting Not available
4. Neutrino beam base-line: CERN (Magic baseline) JHF Fermi Lab	7,100 km 6,600 km 11,300 km (with 3,700 km of core)	7,100 km 5,000 km 10,600 km (no core)

Table 7.1: Comparison of various features at PUSHEP and Rammam, to be continued in Table 7.2.

Criteria	PUSHEP	Rammam
5. Laboratory Features:		
Lab Location:	Below 2207 m at ≈ 900 m above MSL	Below 2880 m at ≈ 850 m above MSL
Lab Access:	Horizontal two way heavy equipment transport	Same
Tunnel Option:	Tunnel Length (km); Vertical Cover (m); All-round cover (m)	
Option-1	1.87; 1313; $\geq$ 1000	3.25; 1400; $\geq$ 1250
Option-2	2.13; 1299; $\geq$ 1000	3.85; 1680; $\geq$ 1500
Option-3	2.38; 1340; $\geq$ 1000	4.85; 1780; $\geq$ 1650
Gradient:	1:15 (reverse)	Horizontal
6. Risk Factors:		
Seismic Risk:	Zone-2 No discernible faults	Zone-4 No faults on alignment
Environmental Risk:	Reserve Forest Portals are inside TNEB/private land	Reserve Forest Portals are inside WBSEB/Govt. land
Civil Unrest/Terrorism:	None so far	None so far
7. Time Scale :		
Pre-Construction Stage:	≤12 months	$\leq$ 12 months
Tunnel/cavern excavation with support measures:	About 22 months (Option 2)	About 41 months (Option 3)
Mechanical Outfitting:	12–18 months	12–18 months
8. Cost Saving Factors:		
Facilities already available:	Housing, guest-house, access road, security guest-house at Ooty	Housing, guest-house, access road, security
9. Academic Institutions:		
Educational Inst.:	Bangalore, Mysore, Coimbatore, Calicut	Siliguri, Darjeeling
Research Inst.:	Bangalore, Mysore, Coimbatore, Ooty (TIFR RAC/CRL)	Darjeeling, Kolkata
10. Environmental Factors:		
Weather:	Moderate (min. 12–25°C)	Moderate (min. 5–20°C)
Rainfall/year:	Low (100–150 cm)	Mod. heavy(300–400 cm)
Access:	24 hrs/365 days	Almost all days
Biosphere:	Wildlife sanctuary	Wildlife sanctuary

Table 7.2: Comparison of various features at PUSHEP and Rammam, continued. The time factors for driving tunnels and cavern construction are based on L&T estimates and are to be regarded as approximate guide-lines.

Chapter 8

Cost and Time Schedules

We provide some preliminary estimates of the cost and time scales for various tasks. No detailed estimates are available at present and the figures mentioned in this chapter are very preliminary estimates. The total cost for this project can be divided into three broad categories

- The cost of building the underground tunnel, cavern and the surface laboratory.
- Cost of iron.
- Cost of active detector modules (RPCs), detector electronics, gas system, magnetisation, etc.

It should be noted that the underground cavern is planned as a national facility for conducting experiments in science and engineering in general and not limited to the proposed neutrino physics experiment(s) alone. Thus the expenditure related to the construction of the laboratory should be considered as the cost for creating such a facility.

The major portion of the ICAL detector cost is the expenditure on the 6 cm thick iron plates. The plates will be used without any modification and may be retrieved at the end of the experiment without any degradation. Hence this part of the cost should be considered as a recoverable expenditure.

The last major cost associated with this experiment is the cost of active detector modules, pickup strips, electronics, gas circulation systems, etc. We consider this alone to be the cost specific to the proposed experiments with the ICAL detector.

8.1 Cost factors: INO Laboratory

The cost factors include the following items; details are listed in Table 8.1:

- Site: Each of the site-related activity involves construction of tunnels, laboratory cavern and support structures. The actual cost depends on the nature of rock, availability of labour and ease of access[1].

  The approximate cost for the construction at the PUSHEP site is Rs. 35 crore, which includes an access tunnel (7m dia., 'D' shaped) of length 2.2 km and a cavern of dimensions 150 m $\times$ 20 m $\times$ 25 m (height).

  The corresponding figure for construction at Rammam is Rs. 85 crore, which includes a main access tunnel (7m dia., 'D' shaped) of length 4.85 km, an adit (7m dia., 'D'

[1]The figures given here are based on the budget estimate given by *M/S L & T Limited*

No.	Item	Cost (Rs. crore) for PUSHEP	Rammam
	LAB CONSTRUCTION (surface and underground)		
1.	Tunnel and cavern excavation	35	85
2.	Civil work surface and underground	35	35
	(i) the access tunnel		
	(ii) the cavern		
	(iii) surface laboratory		
	(iv) hostel buildings		
	(v) housing/accommodation		
3.	facilities in the cavern	20	20
	(i) overhead crane		
	(ii) air circulation in tunnel		
	(iii) air-conditioning the lab		
	(iv) electrical work		
	Total cost of lab construction	90	140

Table 8.1: Estimated cost of INO underground laboratory at the two possible sites in PUSHEP and Rammam.

shaped) of 2 km and a cavern of the same dimensions as for the PUSHEP site. The adit provides an escape route.

It is to be noted that the higher cost of construction at Rammam is due to the length of the main access tunnel which is more than twice the length of the tunnel at PUSHEP. In addition there is an adit of 2 km at Rammam due to the long length of the tunnel. This additional cost will allow for more depth at Rammam compared to that at PUSHEP. If on the other hand we restrict the depth at Rammam to that of PUSHEP then the cost of tunnel construction at both places may be comparable. The site at Rammam also provides an opportunity of stopping at some desired depth for the proposed experiment and extending it later for future ones.

- Civil Work: Additional civil work will be needed near the access to the tunnel portal, for the construction of structures to house the surface laboratories and buildings to house people who will work in the laboratory. Substantial saving may be achieved if such facilities like guest house and living quarters are readily available.

  The total cost of such civil work is approximately Rs. 35 crore; a break-up of this estimate is shown in Table 8.1. Furthermore, facilities such as overhead-crane for lifting equipment and steel plates into place, air-circulation and air-conditioning in the lab and tunnel are required. The estimated cost for this is roughly Rs. 20 crore.

The total estimated cost of building the laboratory is therefore expected to be around Rs. 90 crore[2] in PUSHEP and about Rs. 140 crore in Rammam. The extra cost at Rammam site is for reaching more depth and for providing an escape adit. Note that the underground laboratory will a national facility and can be used for other types of experiments also.

[2]Note: 1 crore = 10 million. At present conversion rates, 1 US-D $\sim$ Rs. 45, 1 Euro $\sim$ Rs. 58.

8.2 Cost factors: ICAL detector

We give an estimate for a 50 kton module of the ICAL detector which is an optimum target mass required for the detector. However, based on the physics needs and the goals outlined in the chapter 3 on physics issues, the final detector mass may go up to 100 ktons. The cost of the detector will go up proportionately. The laboratory construction cost outlined above, however, will remain the same. The cavern design already takes into account a possible expansion of ICAL up to three times the present design.

The cost factors are listed in detail in Table 8.2:

No.	Item	Cost (Rs. crore)
I	COST OF IRON	
1.	Iron (at Rs. 60 per kg)	300
II	OTHER DETECTOR-RELATED COST	
2.	Magnetisation	20
3.	Detector	120
	(i) RPC	
	(ii) strip plates	
	(iii) front-end electronics	
	(iv) power supply	
	(v) gas circulation system	
4.	Electronics and DAQ	25
5.	Contingencies	40
Total detector-related cost (excl iron)		205
	TOTAL	505

Table 8.2: Estimated cost of one ICAL detector module at INO. This cost is the same at both sites. Note that the cost of iron is substantial but it can be re-used.

- Iron: A total of 50 ktons (or more) of iron rolled into plates is required for ICAL. Normal mild steel costs around Rs. 60 per kg and has a saturation magnetic field of about 1–1.4 Tesla. The cost of iron is expected to be around Rs. 300 crore. Here we have not taken into account possible cost increase in case any special modification in the composition of steel is required for magnetisation purposes. It may be noted that there is no degradation of iron—once the experiment is finished, it can be reused. *Even though this is one of the biggest components of the total expenditure of ICAL, it is a recoverable expenditure.*

- Magnetisation: Approximately around Rs. 20 crore, including the cost of copper coils and machining.

- Detector: Approximately around Rs. 120 crore for the detector elements including glass plates, strip plates, front-end electronics, power supply, gas system. The cost of the gas mixture is a major recurring expenditure and is not included here.

- Electronics and Data acquisition: Approximately about Rs. 25 crore for DAQ, trigger, external veto, etc.

The total estimated cost of building the laboratory along with 50 ktons of ICAL detector is therefore expected to be around Rs. 595 crore in PUSHEP

and about Rs. 645 crore in Rammam, of which Rs. 300 crore (for the iron) is recoverable and Rs. 40 crore has been added for contingencies.

The figures given above do not include the operating cost at either of these sites, or the recurring expenditure. This again is site dependent.

8.3 Time Scale

The project may be executed in three phases once the approval is given in principle:

- Phase 1 of approximately 12–18 months duration: Site investigation to draw up detailed design reports for tunnel and cavern complex. This could be faster if all the permissions are easily available and and the work entrusted to reputed engineering group/s.

  During this period, detailed design reports on the detector structure, RPCs, pick-up electrodes, front-end electronics, power supply systems will be ready.

- Phase 2 will include tunnel and cavern excavation and related support measures. The estimated time for PUSHEP is 22 months and for Rammam is 41 months[3]. The estimate for Rammam is for reaching a depth of 1780 m (option 3). A depth similar to the PUSHEP site can be completed on a comparable time scale.

  The basic design of RPC as already available will be frozen by this time. Tenders for the supply of iron, magnet coils, cables, etc., will be issued. The procedure for making detector elements, electronics, gas mixing units will be in place and the production process may begin.

- Phase 3 of approximately 12–18 months duration: Laboratory outfitting, transport of detector components and material and assembly begins. The first module may be completed early and data taking may begin. This phase ends with the laboratory occupancy and data taking by the second module.

[3]Based on L& T estimates

Chapter 9

Laboratory Management

The India-based Neutrino Observatory initiative started as a joint multi-institutional collaborative project. Since it is expected that various institutions (including research institutes and university departments) within India and abroad will participate in its scientific activities, the member institutions will have a major role in the running of this centre. The preferred model is that this centre functions in a manner similar to CERN (which is governed by a council with members from participating countries) or Fermilab (which is governed by representatives from participating universities).

The current INO initiative already has such a model in place. Presently there is an INO advisory council in which all the Directors of the nodal DAE institutions as well as a nominee of the DAE and the scientific coordinator of INO are members. This structure may be followed in future too, albeit in an expanded form, by including more members from other funding agencies such as DST and UGC.

It is, however, going to be a major project where one needs to take important decisions on a day-to-day basis for the timely completion and smooth operation of the project. It would be desirable to run this project with a base of its own. We, therefore, propose that a centre be created close to the underground facility to coordinate the activities of the INO laboratory. The exact location of this centre may be decided on after identifying the final site of the underground laboratory.

Most of the members of the INO project will come from participating research institutes and universities in India and abroad. Many members who are already working for INO are distributed in many institutions. However, many more will be required. Creation of such a resource requires a firm commitment from both the participating institutions and INO to create joint positions dedicated to INO related work. While the funding for creating such positions may come from INO, there should be a firm commitment from the participating institutions to host such positions and to provide facilities needed for them. In addition, a reasonable number of in-house full time researchers, technical and administrative support staff, directly affiliated to the INO centre are required.

The Neutrino Collaboration Group (NCG) will have a clear line of command for efficient functioning of the laboratory. The proposed structure is shown in Fig. 9.1. The responsibilities are distributed among many groups with clear mandate. Some of the structure envisaged already exists as laid out in the MoU (see Appendix F) and may be continued even after the MoU expires. Interaction outside of INO will be discussed later.

The Director, INO, will convene meetings and directly interact with the NCG and the Program Management Committee (PMC) which will also function as the INO users committee. The Director will also interact with the funding agencies through the governing council. Indeed this structure already exists as is clear from the MOU. The NCG is further subdivided according to specific tasks like detector, simulation, site, etc. An engineering group

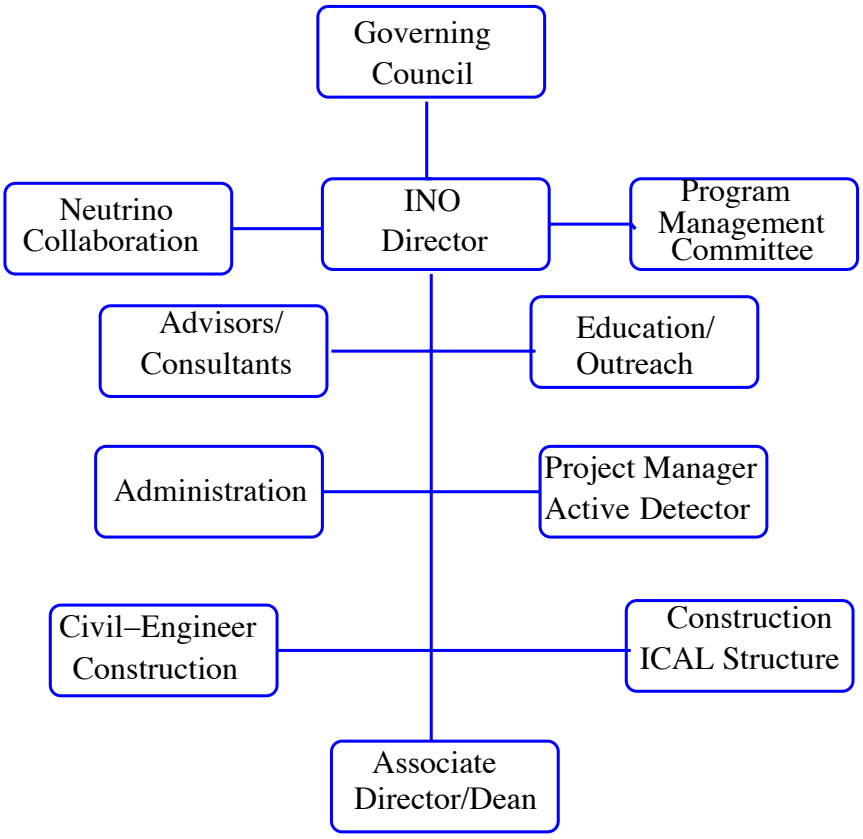

Figure 9.1: Proposed management structure of INO. The groups in the top half already exist while the ones in the bottom half need to be created soon.

and a group of technical advisors will be needed once the project is approved, to design and execute the plans. The management groups, both for routine administration and research programme will come into existence when INO starts functioning.

The proposed engineering group as shown in Fig. 9.2 is further subdivided into Design, Civil, Operations and Safety groups.

Figure 9.2: The proposed INO Engineering Support group which needs to be created.

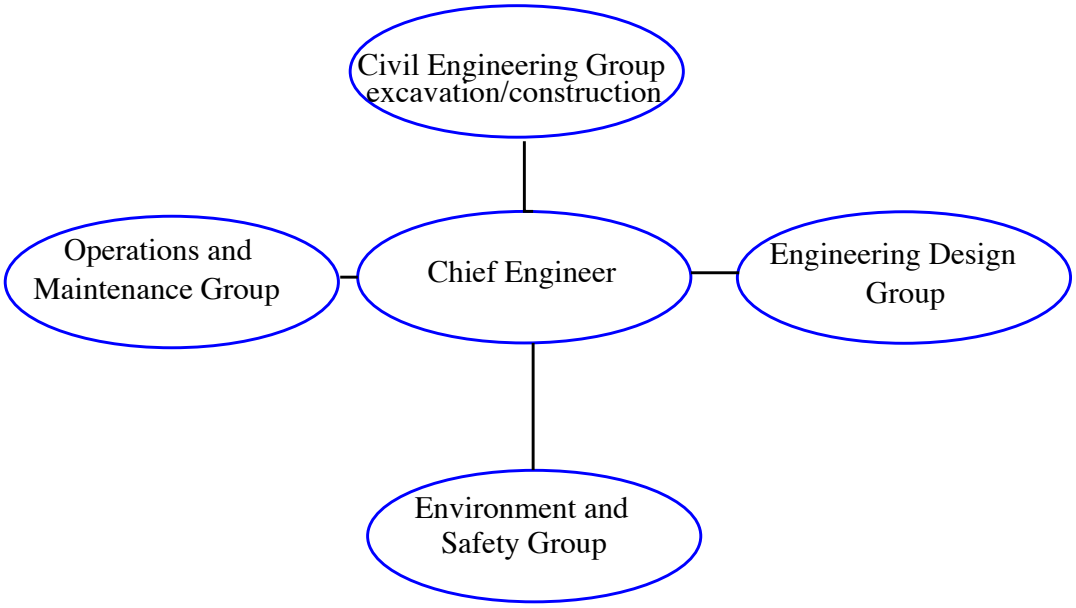

At the pre-construction stage, the engineering group, along with technical advisors, will make precise the design requirements and cost-estimates, drawing time schedules, calling for tenders and contracting work. This group will also be responsible for executing plans as per time and cost schedules, and providing emergency solutions under unforeseen conditions at the construction stage. Apart from these INO may also employ research consultants and other such advisors as needed. Some of these groups may be wound up once the specific tasks are completed like the excavation group and design group. The Running stage involves a clear management philosophy to achieve desired goals by combining a clear line of command and accountability. A single managing entity with an administrative structure and broad involvement of NCG and the scientific community is a good starting point. The Research group under an Associate Director, and a full fledged administrative set up, will come into existence once the construction phase is over. In Fig. 9.3 we show a sketch of the proposed administrative set up.

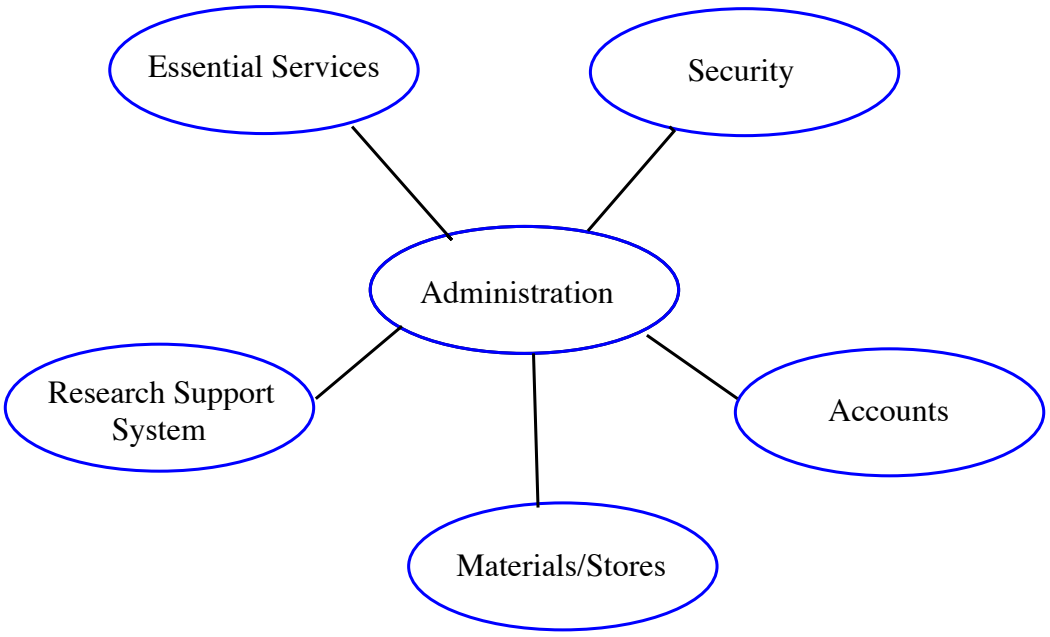

Figure 9.3: The proposed administrative set up for INO.

In Fig. 9.4 we have shown a sketch of the proposed research set up. This is indeed the most important arm of INO and detailed planning is needed to ensure that the groups under this category are enabled to achieve the goals of ICAL in the first phase and of INO in general.

We have so far discussed the local interaction among various groups within INO. However, an extremely important aspect of the proposal is the INO–industry interface. The scale on which INO is conceived is huge and the role of industry—be it in the construction of the laboratory, equipping the laboratory, building the massive steel structure for ICAL, electronics components, etc.,—is going to be a crucial aspect.

Furthermore, the spin-off benefits to the industry may also be considerable. For example, in the Indian context, there is already considerable expertise in building detector components and this will be further buttressed by the RPC development for ICAL. The capacity that will be built for designing and manufacturing detector components for ICAL and further extensions of INO may provide the seed to start large scale manufacturing of detector components. This will cater to the needs of not only the Indian scientific community but also will have worldwide applications. This will strengthen international collaborations which

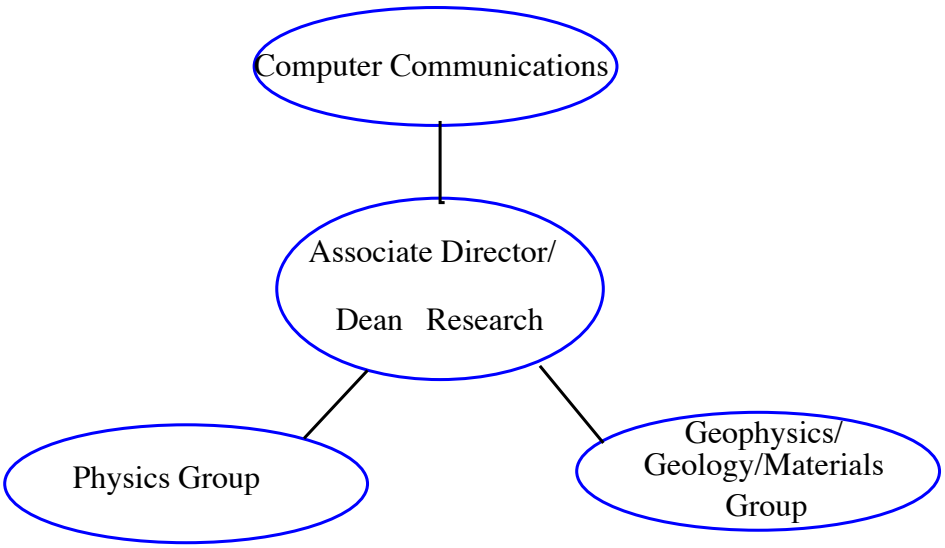

Figure 9.4: The proposed research group organisation at INO.

will generate a feed-back loop as shown in Fig. 9.5.

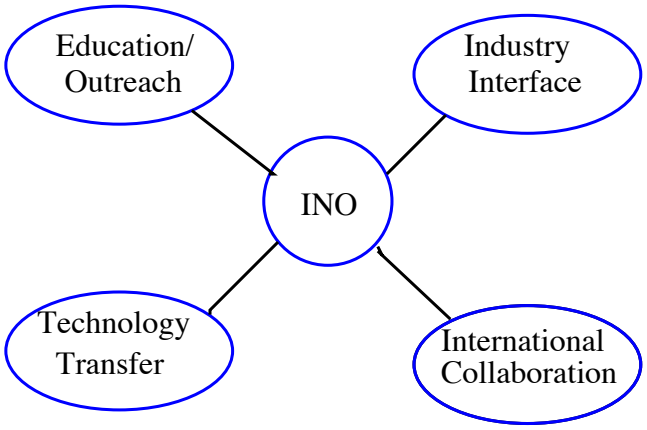

Figure 9.5: Anticipated wide-area interaction at INO and its wider impact.

INO being the first of its kind in the country, we can draw upon the experience of people in the NCG who have been part of large collaborations before where many institutions have come together to create a common facility.

Chapter 10

Ideas for Human Resource Development

INO will require a substantial investment in human resources. It needs a large number of physicists and engineers who will ultimately be the backbone of INO and contribute to its success. Innovative ideas are needed in the recruitment and training of these physicists and engineers. A discussion of this issue, within the Indian context, is presented in this Chapter.

Some of the INO members have already started giving lectures to students in colleges, universities and other institutions, exposing them to recent discoveries in neutrino physics and to the possibility of doing front-line neutrino experiments in India. The typical response from the brighter and the more daring students has been to ask what should they do in order to join this experimental project. So it is clear that there is no dearth of capable student power willing to undertake any major scientific project. But we do not have a suitable mechanism as yet, to exploit this abundant resource available in the country. This will be one of the high-priority items before us.

Human Resources Needs: The human resources needed for a large project like INO are varied: broadly they are classified as:

- Construction and installation: Mainly civil and mechanical engineers and scientists will be involved in the installation of the detector and data systems. While the civil and mechanical works will be entrusted to appropriate external agencies, INO will need its own engineers to ensure all design requirements are met.

- Maintenance and operations: After the installation of the detector, approximately about 15 engineers/scientists will be needed to ensure continuous running of the detector throughout the day.

- End user groups: This group consists of physicists— faculty/students/post-docs— who are members of the INO collaboration. A collaboration of this type needs at least 50 people including about 30 scientists. At any time about 15 members of this group will be present on site conducting experiments and analysing data. Apart from these, there must be opportunities for students and visiting scientists to pursue projects at the site.

The required human resources, scientific, may be generated in about four to five years time. Some ideas for generating the required human resources are outlined below.

INO Training School: One solution is to start a Training School that can train about 15 M.Sc/B.Tech/B.E students every year at an all-India level, so that in 5 years we would

have about 75 well trained experimental physicists. We think this would be better than the present dependence on the meagre supply from the existing Ph. D. programmes in our Institutes and Universities. The difference is that the trainees would be promised jobs in the various institutions (BARC, HRI, IMSc, IOP, SINP, TIFR, VECC, and Universities) that participate in the Neutrino Project or at the INO centre. They may be selected on the basis of their successful performance in the Training School (which may last a year or less). In this we are borrowing the concept from the BARC Training School. The Department of Atomic Energy (DAE) has in fact started more Training Schools at CAT, Indore and at their other centres. It may even be possible to use their Training Schools to recruit the number that we want or to share their infrastructure if DAE agrees. Otherwise we may have to organise everything separately.

Topics to be taught in the Training School could be the following:

- Particle and nuclear physics,
- Detector physics and technology,
- Electronics,
- Computer simulation, Monte Carlo techniques,
- Data handling and data analysis, etc.

Some experience in teaching these subjects already exists in the country because of the SERC Schools in Experimental HEP that were conducted in the past few years. This can be used in designing a very good course.

Some of these students may join other on-going or future experimental HEP projects such as CMS. So the Training School may be for all of Experimental HEP including the Neutrino Project. This is an alternative.

Actually the best training will be achieved through hands-on experience in existing experiments or detector-development activities, rather than class-room teaching. Nevertheless we are calling it a Training School mainly because we want to emphasise that we have to make this conditional offer of a regular job on the basis of a successful completion of training.

Another possibility is to use the universities for this training programme. Several Indian universities are already involved in high energy physics and nuclear physics experiments using accelerators in India and abroad. Some of these universities may be requested to start a joint training programme in experimental high energy and nuclear physics. This will be a very good way of involving our universities in INO activities. However even in this alternative, there must be suitable mechanism to offer jobs to those students after a successful completion of the training course. This promise of a career in a world class experiment is the only way of attracting talented students in bigger numbers which is essential for the success of any big science project.

Direct Recruitment: As already mentioned, the best training could be imparted through hands-on experience in existing experiments on detector development activities, rather than class room teaching. About a dozen people must be recruited immediately. This can be repeated every year. Both physicists and engineers must be recruited.

Initially we may start with the following number of new recruits:

- 4 at Mumbai (TIFR + BARC)
- 4 at Kolkata (SINP + VECC)

- 2 at Bhubaneswar (IOP)
- 2 at Chennai (IMSc)
- 2 at Allahabad (HRI)

Similar numbers could be added at the other centres as well as in a few selected universities.

About 12 full-time research workers doing INO work under the guidance of senior physicists at the above centres must be recruited immediately. At the rate of Rs 10,000 per month per person, this works out to a sum of only about Rs 15 lakh per year, but the benefit to INO work and for human resource development in the country will be enormous since these bright youngsters will be working in a front-line experiment in the country. The above suggestion is about pre-Ph.D level researchers, but a similar number must be recruited at the post-doctoral level also.

The tenure may be initially for one year, but on evaluation of the candidate's capabilities and achievement, a regular tenured job at one of the participating institutions or at least a 5-year contract must be offered at the end of the year. An All-India advertisement for this INO recruitment must be placed as soon as possible.

INO Fellowships at various institutions: INO Fellowships may be made available at selected university departments, IITs and other engineering institutions. These may be for M. Tech and similar Masters level programmes and may be for 2 years. While holding this INO Fellowship, the candidate shall be required to do his/her thesis work on an INO-related piece of research or development and also give an undertaking to continue work in the INO project for at least 3 years after completion of his/her M. Tech. or other Masters level degree.

Ph. D. degree for instrument-building: We have to nurture the culture of original instruments-building. New discoveries in Science are not possible without building new instruments. Unfortunately the blind adherence to a career-path: B. Sc. $\rightarrow$ M.Sc. $\rightarrow$ Ph. D. has forced young people to look for the shortest path to reach Ph. D. and in the process we have failed to inculcate in them in real experimental culture that has to involve construction of experimental equipment. Students generally seek avenues of research where the required equipment is readily available or can be bought. This is because the time and effort involved in building an equipment is not recognised by academic bodies empowered to grant research degrees. We have to identify those enlightened university bodies which recognise the importance of instruments-building activities so that a candidate can be given a Ph. D. degree on the basis of his/her contribution to this activity. This is essential for successfully recruiting and retaining the best scientific and engineering talent in the INO project.

Mobilisation of the Universities: We now come to the most crucial part of the HRD problem: the mobilisation of our universities. There are more than 300 universities in the country. It is clear that Universities are the source for the human resources that needs to be tapped. That is where the HRD problem must be attacked. But how?

A solution was provided by Praveer Asthana and D P Roy in the DST-DAE Meeting on the Road Map for High Energy Physics and Nuclear Physics held at Mumbai on 7-8 April 2006. As most of us are aware, universities are depleted of staff, due to lack of funds and various other reasons. In many university departments, nearly half of the posts are vacant. While this is a calamity,it is also an opportunity because it can now be used to recruit

people for working on INO and other major projects. Young people may be inducted into the departments and they must be attached to the particular project such as INO. Their remuneration for the next 10 or 15 years must be covered by DST and DAE. After that, the university itself must support this staff. This, in brief, is the solution to the HRD problem.

But considerable amount of spadework is needed before this can be achieved. First of all, UGC has to be brought into the picture. Clearly, our Road Map for HRD must involve UGC in addition to DST and DAE. All the details of this recruitment and the terms of appointment must be worked out in dialogues with the concerned universities. We must choose the universities where such negotiations are likely to succeed. Once successful models are created, other universities are bound to follow.

In summary we have given a few ideas on the HRD required for INO. These are not mutually exclusive. One or more of them or a suitable combination of them could be used for INO. The availability of human resources has been a major concern in initiating any major scientific project or activity in the country. Hence we emphasise the importance of starting human resource development activity as an essential component of INO. In particular the training school as envisaged can address the human resource needs of INO and other projects of this nature. Finally, it is essential to mobilise the universities through a joint effort by UGC-DST-DAE, by recruiting research-cum-teaching faculty against the vacant posts in various universities. It is hoped that the HRD for INO will become a trend-setter for other major scientific projects in the country.

Chapter 11

Education and Outreach

The particle detectors developed by high energy and nuclear physicists over the years have found wide application in areas such as medical imaging, material science, industrial control and in geological survey. The primary motivation of the India-based Neutrino Observatory is to build and operate an underground laboratory and to set up experiments in the field of neutrino physics. Detector development is, however, expected to be a major part of the over-all activities of this centre. It can therefore play a major role in the development of detector technology and in the transfer of this technology to industry for its potential large scale utilisation in other areas, especially in the area of medical imaging. We discuss the possible impact of INO in this area, highlighting, when possible, the Indian situation.

International collaboration: Indian groups are now participating in several international high energy physics experiments at various laboratories around the world. Apart from exciting physics that these experiments offer, there is scope for development of the latest detector technologies through these collaborations. However, there needs to be a focussed approach from our side with a well-coordinated group of people working on detector development, if we aim to get the full benefit from such collaborations. The INO centre can certainly play the role of coordinating such activities through joint R & D efforts on detector development with other laboratories around the world.

In fact, the INO collaboration has already started working towards this and currently we are collaborating with the LNGS at Gran Sasso in Italy and CERN at Geneva in Switzerland for joint development of RPC detectors. Similar activities in other detector areas as well as in related technologies like electronics and on-line monitoring systems can aid in developing the technological base of the country to a large extent.

Education: It is hoped that the INO centre will eventually play the role of a national high energy physics centre in India similar to the HEP Centre in China, KEK in Japan and CERN in Europe. Apart from being a premier experimental facility in the country, the laboratory will also become a nodal centre for initiating collaborations and educational outreach programmes with the leading HEP and nuclear physics laboratories in the world. In fact, the Nobel Laureate Gerard `t Hooft, during his visit to India in 2003, felt that "experimental work is imperative" and further pointed out that the "Indian scientists need to do more experimental work to support their research lest they continue to produce Nobel Laureates only sporadically"[1].

An immediate impact of such a centre will be in the field of physics education in particular and science education in general. In particular the contribution to the culture of doing

[1]The interview with `t Hooft was published in *The Hindu*, January 30, 2003

experiments, small or big, will be enormous. The training and educational programmes directed at the students, technicians and educators will in the long term have a positive influence on the educational scene as it has elsewhere in the world.

Impact of detector technology development: Detector development is expected to be a major part of the overall activities of this centre. The benefits due to such detector development activities can reach the common public only through the participation of the industry in a major way. The purpose of a basic research laboratory like INO will be to develop and prototype the detector systems in the laboratory and then pass it on to the industry for its commercial utilisation. However, for doing so, it is important to have a close interaction with the industry. INO will therefore interact with the relevant industry from the very beginning.

The best illustration of such a collaboration is in medical imaging which is widely used around the world and is a direct result of the R & D in detector development. Some details are given below—we also outline how this field can benefit from detector R & D at INO centre.

Medical imaging: Today, there are estimated to be around 10,000 particle accelerators in the world, over half of them used in medical treatment. About 20 million people around the world undergo radio pharmaceutical diagnosis each year, using Positron Emission Tomography (PET) scan whose development owes much to the detectors used by the experimental high energy and nuclear physics community in the world. High energy physics laboratories around the world have dedicated programs to develop new detectors for medical imaging and improve the performance of the existing detectors in this field.

In India the use of medical pharmaceuticals for cancer diagnosis and treatment is in its infancy. However, we need a large number of such facilities in the country as soon as possible. It is therefore important to develop a large pool of experts in the country, both in the area of accelerator and detector technologies, who can help in developing and transferring these technologies for its use in the area of medical treatment. While in the area of particle accelerators, there are centres like Centre for Accelerator Technology (CAT), Indore, Variable Energy Cyclotron Centre (VECC), Kolkata, Nuclear Science Centre (NSC), New Delhi, etc., there is no such centre for the purpose of in-house development of particle detectors.

The use of methods developed in nuclear and particle physics is increasing rapidly in medical diagnostics. The technique of position sensitive detection (PSD) employed in medical imaging is one such. Most of the modern medical-imaging gadgets rely on this technique of detection. Multiwire proportional chamber (MWPC), a position sensitive detector which was invented by Georges Charpak (Nobel Laureate 1992) for tracking of charged particles in particle physics experiments, is widely used in medical-imaging systems. The state-of-the-art computer tomography (CT) systems, which can obtain a series of 2D 'slices' through the body, and a whole host of other physics-based techniques that are routinely used for anatomical imaging of body without the need for a scalpel, are based on PSD.

In this context, the training imparted in the development of RPC position sensitive detector at INO, and the transfer of such a technology, can lead to development of imaging systems for medical applications.

Positron emission tomography, a functional imaging technique, is also a spin-off of research in particle physics. It is a technique used in clinical medicine and biomedical research to create images that show anatomical structures as well as physiological functions of tissues, i.e., functional imaging is the major modality. Radioactive nuclei are introduced to the body as labels on tracer molecules designed to probe physiological processes. These radioactive

nuclei emit positrons that annihilate with electrons in the tissue. An annihilation event mostly results in two gamma photons being emitted at almost exactly 180 degrees and with an energy of 511 keV each. The gamma photons are detected in coincidence in a detector ring so that two detected gamma photons represent a straight line along which the event took place. An assembly of such lines is gathered and processed with the aid of image processing tools to finally produce an image of the activity and thereby of the functionality.

An extension of PET is TOFPET (Time-Of-Flight Positron Emission Tomography) in which the time difference between the arrival of coincident photons is measured. In PET this information is ignored and the annihilation is equally probable to have occurred along the full extension of the line between the detectors. Incorporating this information gives more weight to the more probable locations of the emission point for each event. The localisation of the emission point is made to within 4-10 cm, depending on the time resolution of the system. Including these data reduces statistical uncertainty in the reconstructed image and thus one obtains better images.

It is easy to see an analogy of PET/TOFPET technique/setup with the detector setup at INO, where layers of scintillation counters (surrounding the main detector) will be used to identify muons entering the detector from outside as well as to identify partially confined events with vertex inside the detector. Training in extracting and analysing genuine/correlated events in such a detector setup will help develop better insight to PET.

Information integration: Digital data handling in diagnostic systems is an integral part of medical imaging. Modern diagnostic systems mostly produce digitised image data. With these advancements, researchers are now striving to enhance the clarity of images, collect more quantitative data, monitor physiological processes, merge existing techniques and find more intelligent ways of displaying and using the information generated.

Whatever the modality, a typical scan now yields more information than ever before. This is particularly true for multislice CT scanners in which the X-ray source and the detectors are both rotated around the body of the patient. The multislice approach has improved the spatial resolution of CT scans, making it increasingly attractive for a wider range of diagnostic and screening tests. However, the rise in data per CT scan, and the greater use of machines, means that there is a dramatic increase in the amount of data they generate. Computer networks and existing software for the manipulation of images are inadequate to cope with the sheer volume of data now being generated. The end result is that there is often a delay before a doctor can view the results of a scan.

The problem of data overload is only going to get worse according to latest survey. This calls for a need to develop ways of controlling data acquisition during the scan to optimise the quality of the data produced. This is called 'intelligent acquisition', which will significantly increase the performance and functionality of image processing and analysis. They may also lead to cost-effective solutions.

Towards this end, the training in 'data analysis' that would be imparted at INO, is a promising step in generating human resource for 'information integration'.

Chapter 12

INO as a Facility for the Future

The science that can be done in a deep underground laboratory spans an impressive range of fields and disciplines. In the earlier chapters we have emphasised the capabilities of a specific detector like ICAL. However, we note that experimental observation of any aspect of neutrino physics needs a deep underground set-up or massive shielding in order to reduce the background. No matter what the main physics goal is, it is always possible to incorporate changes and additions in such a set-up in order to look at a different class of outstanding problems possibly requiring more than one type of detector/s. We list some of these other other possibilities below.

12.1 Low Energy Neutrinos

Solar Neutrinos: The current and planned solar neutrino detectors are all situated at latitudes above 35 degrees. These detectors have very small exposure times (about ten days in a year) to solar neutrinos travelling at night through the core of the Earth. The MSW phenomenon can play an important role in the regeneration of neutrinos in Earth's core assuming the range of parameters responsible for neutrino oscillations. To study this, it is important to build a solar neutrino detector as close to the equator as possible. India offers a possibility geographically, as well as in terms of scientific expertise, engineering expertise, manufacturing, and tall mountains which provide good shielding. Such a detector will allow one to check the parameter range for time-of-night variation.

While many aspects of solar neutrinos, especially the low energy spectrum, have been well investigated, there are some areas which will remain uninvestigated. For example, the higher energy tail of the solar neutrino spectrum, in the range of 13–17 MeV, where hep neutrinos contribute, cannot be well studied at Super-K or SNO, which is the largest instrument presently operating, because of limited statistics. An improvement may be brought about by a detector whose mass is in the megaton range.

Reactor Neutrinos: Furthermore, if such a low energy detector has a low threshold of a few MeV, it may be capable of detecting reactor neutrinos. Many new reactors (at Koodankulam, Tarapur and Rajasthan) producing about 1000 MWe of electrical energy (a factor of three more in thermal energy output) or more are being constructed/planned in India. Still larger reactors or a collection of them may be needed to have sufficient flux of neutrinos for a near detector. Such a detector must have a low threshold in order to detect these neutrinos; the reactor neutrino spectrum peaks at about 4 MeV. While this is an energy range that is of definite interest to solar neutrino studies as well, the lowering of the threshold to include such neutrinos may be technically difficult and cost-wise prohibitive in a very large detector.

This is because the radio-active purity of the detector material becomes relevant at such energies.

Supernova Neutrinos: On the other hand, a detector with an energy detection threshold of 10 MeV or more will not make huge demands on purity of the detector material and may be cheaper. Such a detector will not be suitable for reactor neutrinos. Nevertheless, it can "clean-up" the higher energy tail of solar neutrinos. More importantly, such a detector will be capable of detecting *supernova neutrinos*. Neutrinos from just one collapse, that of supernova SN1987a, have been observed so far. While the number of events were sufficient to qualitatively confirm the mode of stellar collapse, the statistical significance of these events was too small to look for effects of mixing and oscillations. While current detectors are much larger than those which observed the events from SN1987a, future planned detectors also need to be much larger in order to acquire enough statistics in various detection channels to make a detailed analysis of such events possible. In particular, even a low-energy detector with mass in 100 kton range instead of megaton range may detect 500–1000 events for a supernova explosion similar to the SN1987a. This is an exciting possibility. The detector material could be either water, heavy water or scintillator, perhaps even a combination of these.

Global radioactivity in the Earth: Radiogenic heat from radioactive materials inside the Earth plays an important role in Geo-dynamics. The observed heat outflow on the surface of the Earth is 40 TW and 40% of this (16 TW) is the estimated radiogenic contribution. Most of the radiogenic heat (90%) is believed to arise from the decays of U^{238} and Th^{232}.

Models of the Earth disperse 50% of U and Th in the mantle (2900 km thick) and concentrate the remaining 50% in a thin crust (35 km thick) under the continents, while the much thinner oceanic crust (6.5 km thick) is left poorer in U and Th. The continental crust is much thicker (about 75 km) under the Tibetan plateau. A practical way of studying this distribution is to detect anti-neutrinos through the reaction $\overline{\nu}_e p \to e^+ n$ since all the anti-neutrinos essentially reach the surface. Such detectors, however, have to have a very low threshold, less than an MeV.

But, all this is theory! An exciting possibility of *directly measuring* the amount of U and Th by their β-activities has opened up through the development of neutrino physics. This can be done by detecting the $\overline{\nu}_e$ emitted in β-decays of U and Th. An earlier proposal (1984) by Krauss, Glashow and Shramm [160] was revived in the current context of neutrino detectors by Raghavan *et al.* [161] in 1998. See also the recent papers in Ref. [162] on this subject.

In particular, Raghavan *et al.* [161] pointed out that BOREXINO in Italy and KamLAND in Japan may be used for measuring the amount of U and Th quantitatively. Italy being on a continental crust, and Japan being on an oceanic crust, a confrontation with the above theoretical model prediction is possible. For the first time, the global U/Th distribution predicted by current geochemical models appears to be testable by experiment. In such an experiment, $\overline{\nu}_e$ from nuclear fission reactors on the surface of the Earth will provide a known background and hence can be used for calibration.

The amounts of U and Th can actually be measured individually by a spectral signature, thus leading to the first global transuranic chemical analysis of the interior of the Earth. Geo-neutrinos have already been observed in the KamLAND experiment [26]. The low-energy component of the observed $\overline{\nu}_e$ spectrum in the KamLAND detector has a significant contribution from the radioactive decay of U and Th in the Earth. Mohanty [163] has analysed the spectral signature and determined the relative abundance of Th to U which

has important information on the age of the Earth. In the context of INO laboratory it should be noted that *the flux of Geo-neutrinos near the Himalayas is 86% larger than the flux in Kamioka* [164] which makes it an interesting location for the INO laboratory. It is also expected that the Geo-neutrinos flux will be significantly larger in the Deccan though there are no precise numbers yet. Unlike KamLAND, there is no significant background due to neutrinos from reactors at this location. It may also be noted here that the flux of Geo-neutrinos from ^{40}K is higher than that from U and Th , but, since $E_\nu \leq 1.31$ MeV, it populates the low energy regions.

Raghavan [165] has drawn attention to the possibility of directly detecting the existence of a natural fission reactor at the centre of the Earth, that had been proposed as the energy source of the Earth's magnetic field. The experimental study of Geo-neutrinos may yield other surprises. A fantastic natural nuclear fission reactor that operated two billion years ago at the Oklo mine in Gabon, Africa, was accidentally discovered [166] some time ago. There may be other natural fission reactors somewhere that may still be running and future $\overline{\nu}_e$ detectors may reveal their existence!

One must also mention the possibility of neutrino exploration of the Earth [167]. Neutrino factories and very long baseline neutrino experiments can lead to tomography of the Earth.

Beta decay and neutrino-less double beta decay: A *direct* measurement of, or limit on, the neutrino masses has to come from a different class of experiments.

The end-point of the energy spectrum of the electrons in the beta decay of an appropriately chosen nucleus is sensitive to the neutrino mass. If we invoke our current understanding of flavour mixed eigenstates with nearly degenerate masses, then it is clear that bounds from beta decay are on a combination of masses, weighted by the appropriate entry in the neutrino mixing matrix. At present only upper limits are available: The most stringent upper limit for neutrino mass from beta decay is ~ 2.2 eV. The corresponding upper limits from the muon and tau decay processes are 0.27 MeV and 18.2 MeV respectively. Since neutrino oscillation data clearly show that the mass differences among the three neutrinos are very small, 2.2 eV can be regarded as the upper limit for all the three neutrino masses.

Double beta decay is a novel phenomenon that distinguishes Dirac neutrinos from Majorana neutrinos [168, 169]. Being electrically charge-neutral, among the particles of the Standard Model, neutrinos are the only fermions that can have Majorana behaviour, viz., be their own antiparticles. The possibility that neutrinos may be identical to anti-neutrinos has profound implications for neutrino physics and for models of neutrino masses and mixing. If neutrinos are Majorana particles, neutrino-less double beta decay ($0\beta\nu\nu$) can occur, when two electrons but no neutrinos are emitted. Such a non-zero $0\beta\nu\nu$ rate not only requires neutrinos to be Majorana particles but also requires that the relevant neutrino mass matrix element M_{ee} be non-vanishing; thus this process is a sensitive probe of the nature of the neutrino as well as this matrix element. Recently it has been claimed that such a non-zero rate has actually been measured at the Heidelberg-Moscow experiment. Future planned detectors may refine the results and improve the error estimates. A proposal to locate a double-decay experiment at INO is given in Appendix E.

Nucleon Decay: One of the most important quests in all of physics remains the search for nucleon decay. The observation (or lack thereof) provides tests of elementary particle structure at the unification scale, not accessible to accelerator experiments. The present best limits on the mode $p \to e^+\pi^o$ are at a lifetime of 3×10^{34} years (from Super-K). Many supersymmetric (SUSY) models favour nucleon decay modes with K mesons, which have atmospheric neutrino background, for which the limit from Super-K will be roughly the

same. Current expectations from theory range over several orders of magnitude above this limit, but nucleon decay could well be found at a life time longer than 10^{35} years. This cannot be done by the present ICAL detector, since to set new limits we need megatons of target mass, but it remains a possibility as a future experiment at INO.

12.2 Neutrino Astronomy

Cosmic ray composition: The origin of high energy cosmic rays is unknown. Such cosmic rays, with energies exceeding 10^{20} eV, have been detected. Some of the proposals that attempt to understand the sources of high energy cosmic rays involve the possible role of neutrinos.

Ultra High Energy Neutrino Astronomy: Our current knowledge of the Universe almost entirely comes through the detection of photons, namely, the conventional astronomy. A major disadvantage of this conventional astronomy is that the hot and dense mass which forms the central regions of stars, active galactic nuclei (AGN) and other astrophysical energy sources, are completely opaque to photons. Therefore we cannot investigate the properties of these regions by direct observations of photons. In order to observe the inner workings of astrophysical objects and to obtain a description of the Universe over a large range of energies, we may have to rely on neutrinos. Although astrophysical sources of very high energy neutrinos have not been observed directly, their existence may be inferred from the properties of cosmic rays. Ultra high energy neutrino astronomy thus offers probably the only way of observing astrophysical sources and may give us information on the acceleration mechanism of the highest energy cosmic rays in particular, and energy generation mechanisms in the central regions of the most energetic astrophysical objects.

Other outstanding problems are the search for non-baryonic dark matter and monopole searches. The opening up of a new window to the Universe is likely to throw up new, unexpected phenomena. This has happened many times throughout history. Neutrino astronomy is an exciting new field with plenty of scope for surprises.

12.3 A low energy accelerator for nuclear astrophysics

Recently a proposal has been made by Saha Institute of Nuclear Physics to set up a *Centre for Study of Nuclear Astrophysics* which will be devoted to the study of the synthesis of elements and the evolution of cosmic sites where such a synthesis may occur. As part of this centre, a low energy high current Tandem Accelerator with a maximum terminal voltage of 3 MV will be set up. This will be used initially with the existing high efficiency gamma, charged-particle and neutron detectors. Subsequently, a recoil separator and sophisticated detector systems are proposed to be purchased as part of this Centre. The entire experimental facility will be set up at a suitable site that will permit the study of some of the thermonuclear reactions.

Nuclear astrophysics encompasses the study of such a wide range of low energy nuclear reactions that a 3 MV accelerator alone will not be sufficient to study reactions that occur in the stellar interiors. Many of these reactions, for example in the CNO cycle, are needed to be studied with projectiles having energies in the region of about 100 KeV. The main problem with most of the charged particle reactions in the energy regime of astrophysical interest is one of extremely low cross sections, typically in the nano- to pico-barn range. Low-energy studies of thermonuclear reactions in a laboratory on the surface are hampered by the cosmic ray background. Conventional passive or active shielding around the detectors can partially

reduce the cosmic ray background. But some reactions, where this partial reduction of background is not sufficient, require an underground accelerator facility.

It is thus proposed that the underground laboratory that is being planned for INO may also fruitfully house a very low energy accelerator, with a terminal voltage of a few hundred KV. A few such facilities exist in the world, most notably the LUNA project at Gran Sasso, Italy, but this will be the first of its kind in India devoted to the study of very low energy nuclear reactions of interest in nuclear astrophysics.

12.4 Others

While underground laboratories are germane to neutrino physics and astrophysics, the science that can be done in such laboratories spans an astonishing range. We have not attempted a detailed study of such possibilities, but mention a few of them[1].

Perhaps, the most important use of a deep underground laboratory outside of neutrino physics and astronomy may be for *geo-sciences*. The laboratory would offer a unique opportunity for geo-science in developing a sharply focussed understanding of subsurface physical characteristics and environmental conditions. It can be used to investigate the properties of weak and fractured rocks, flow paths, fractures, deformations caused by stress releases and investigate the data against model predictions. Geophysical equipment is set up in LNGS at Gran Sasso to investigate deformation events of tectonic interest. These are then correlated to earthquakes. There exists a possibility of studying the location and time of earthquake occurrence by observing rock micro fracturing processes which occur in the focal area during the pre-seismic period. Indeed the list of possible geological investigations is quite long.

The LNGS at Gran Sasso also provides a facility that can accommodate some of their low counting rate capability for *materials applications* and *detector development*. Underground facilities offer opportunities for ultra-pure chemical manipulations of materials. An underground facility with sensitive equipment could be used for *monitoring nuclear tests*. Such a facility already exists in Gran Sasso.

The investigation into the distribution, diversity, and activity of *microbial communities in subsurface environments*, where pressures could approach that at ocean ridges, is yet another area where there is a window of opportunity.

[1]Some of the material mentioned in this section is from "Underground Science" by Bahcall *et al.* which appears as Appendix A of the report for a National Underground Science Laboratory in the US (NUSEL). See http://int.physics.washington.edu/NUSEL/ for more details.

Chapter 13

Acknowledgements

We are grateful to all the participants of the Working Group on INO who contributed to the idea during the Sixth Workshop on High Energy Physics Phenomenology (WHEPP-6) held at Chennai during January 2000. Urjit Yajnik was the organiser of this group and helped prepare the report [3]. We are especially grateful to John Learned (Super-K Collaboration) for his enthusiasm and contribution in preparing the first working group meeting report. We thank R.S. Raghavan (Borexino collaboration) for putting us in touch with A. Bettini, Director of LNGS at Gran Sasso, and paving the way for the beginning of the collaboration on detector development for ICAL. They have been instrumental in providing many inputs as also sustained encouragement for us.

We would like to acknowledge the help, guidance and support provided by Carlo Gustavino, Marco D'Incecco, Tomoasso Tabarelli de Fatis and their group at Gran Sasso for help in the development of RPC detectors, the design of the gas mixing unit and simulation-related work. We also thank Adam Para of Fermi National Accelerator Laboratory for helping us with some of the material used in the initial stages of the RPC R & D work.

We are grateful to Dave Casper for making the NUANCE neutrino generator software freely available, and answering a long list of questions on its use.

We thank B.N. Karkera, BARC, for his help in procuring magnetic steel for the detector prototype. We would like to acknowledge the help of Shri K. Narayanan and Ch. Sambi Reddy of the R&D group of BHEL, Tiruchirapalli, in the dismantling of the MHD magnet.

We thank Vinod Sahni, Director, CAT, and Director of Physics Group, BARC, for his invaluable contribution in the formulation of the MoU which made the smooth functioning of INO in the various participating institutes possible. We thank S. Kailas, Associate Director of Physics Group and Head, Nuclear Physics Division, BARC, for his enthusiastic support and cooperation. We are grateful to S.S. Jha, former director of TIFR, for his encouragement and support.

The site survey groups at Chennai and Kolkata have benefitted from help from various agencies and persons. We thank the Geological Survey of India (GSI) for carrying out the survey work and for waiving the charges for the work undertaken by them both at PUSHEP and Rammam.

We thank the geologists at the GSI, Chennai, and Suryanarayana Rao, the Regional Director, for his interest. We are especially grateful to V. Balachandran (Director, Engineering Geology), R. Srinivasan and C. Thanavelu (Senior Geologists), for suggesting the site at PUSHEP and preparing various reports, apart from advising the group on all matters related to the site.

We are grateful for the support and permissions given by the Chairmen of the Tamil Nadu Electricity Board (TNEB), past and present, as well as other officers, to visit the site and conduct our studies. The Engineers of the TNEB at PUSHEP, Masinagudi, have been

of great help. The Chief Engineer, V. Jayaprakasam (now retired), was extremely supportive and encouraging from the very first site visit by the group. We are particularly grateful to Esakkimuthu, who knows the PUSHEP region like the back of his hand, for accompanying the site survey group on many trips in and around the project site while educating them on everything connected with building tunnels and caverns (and sometimes elephants). In particular we thank Esakkimuthu for adopting INO as his own mission.

Special thanks to the team from the Engineering Geology Division, GSI, Eastern Region,, that worked at Rammam, for the cooperation and help they provided. We thank the National Institute of Rock Mechanics (NIRM) for a site visit, for doing numerical modelling for in-situ stress measurements and promising to do the stress tests as and when required. We also thank M/S L& T and Hindustan Construction Company for providing realistic estimates of the time and cost for the tunnel and the cavern. Lastly our special thanks to the Government of West Bengal, without whose help we could not even think of making Rammam a possible INO site. All the relevant departments helped a lot throughout, in particular the Department of Power and the West Bengal State Electricity Board, Department of Science and Technology, Department of Forest and Department of Land and Land Reforms. We hope to get continued help from the Government for this project.

We thank Thushar Prabhu of IIA for initial help in identifying Rohtang Tunnel as a possible site for INO, R. Balasubramanian, Director, IMSc, for not only arranging our visit through the Chairman of AEC but meeting the Director-General of the Border Roads Organisation (BRO) to set up subsequent meetings. We are grateful to General Ranjit Singh, Director General, BRO, V.T. Velayudhan, Additional Director General, BRO, and Amit Srivastava, Dy. Director (Tunnels), BRO, for their help in providing the details of the tunnel as well as identifying possible locations for the laboratory cavern.

The photographs reproduced in this report were taken during site surveys at PUSHEP and Rammam sites. The pictures of Rohtang Pass were provided by David Clarke from Australia. We thank David Clarke for his kind permission to reproduce these beautiful photographs.

We are grateful to the Directors of BARC, HRI, IMSc, IOP, SINP, TIFR and VECC for their strong support from the beginning. Finally, the National Neutrino Collaboration Group is grateful to the Department of Atomic Energy for supporting the feasibility study for establishing the India-based Neutrino Observatory.

Appendix A

Neutrino Experiments in India

Historically, the Indian initiative in cosmic ray and neutrino Physics experiments goes back several decades. In fact the first atmospheric neutrino induced muon events were recorded at the Kolar Gold Fields (KGF) underground laboratory nearly thirty five years ago. The KGF experiments spanned several decades involving a systematic study of cosmic ray muons and neutrinos, and other exotic processes at great depths underground. The experience gained here makes it possible to mount a large scale experiment proposed in this report.

Figure A-1: The Gifford shaft at KGF Champion Reef Mine provided access to various levels of the KGF underground laboratory.

Primary Cosmic Radiation (PCR), the only source of high energy elementary particles until the advent of accelerators in early 60's, was the subject of intense study at a number of laboratories around the world including those in India, and in particular at TIFR. The detection medium used to be nuclear emulsions flown at balloon altitudes (Hyderabad) and triggered cloud chambers operated at mountain altitude (Ooty), to study the composition of primary cosmic rays and secondary hadron interactions respectively. This was closely followed by extensive air shower (EAS) studies using a network of scintillation detectors arranged in an array at both sea level and at mountain altitudes. This lead to the study of hadron collisions at ultra high energies, which are not available from the accelerator beams,

by a detailed simulation and comparison with the EAS data on electrons, muons and hadrons. A different path was taken in the study of cosmic ray muons in early 1950's. The Kolar Gold Fields (KGF) provided an ideal environment to study muons at different depths underground and thereby allowed the study of their energy spectrum and angular distributions up to very high energies, much beyond what was possible with magnet spectrometers operated at sea level. The KGF work covered high energy atmospheric muons and neutrinos, search for new particles, bound nucleon decay and GUT monopoles, in addition to extensive air shower study.

The KGF mines were endowed with some of the following features conducive for large scale experiments underground. (a) The terrain is fairly flat and uniform resulting in good accuracy of depth estimate up to large zenith angles; (b) The density (3.03 gm/cm^2), and chemical composition (Z^2/A) of the rock were well determined and are uniform through most of the mines. (c) The availability of a large network of ventilated sites at regular intervals down to deepest point of about 3 km underground and their easy accessibility was a major advantage in these mines. (d) Location near the equatorial latitude resulted in a smaller low energy neutrino background in the search for proton decay.

With such advantages, a series of experiments were undertaken spanning a period of about fifty years. They are all listed below in chronological order with brief statements about the detectors used and results with emphasis on relevance to large-scale neutrino experiments.

1. The earliest experiments were conducted by Sreekantan and Naranan in the fifties to measure the cosmic ray intensities underground at shallow depths [170].

2. In 1961 and 1962 Miyake, Narasimham and Ramanamurthy did pioneering work by measuring the cosmic ray muon intensities using scintillators, photo-multipliers and Geiger counters. Lead was used as absorber. Their studies covered a set of six depths from 270 m (corresponding to 826 hg/cm^2 since 1 m of KGF rock$\sim$3.03 hg/cm^2) to 2760 m underground. Apart from deriving the vertical intensities of muons at these depths, and consequently the energy spectrum of muons up-to $\sim$ 50 TeV, this experiment provided a very crucial result. For an exposure of 180 m^2.days, there was no count at all at the depth of 2760 m [171]. The authors concluded from this result that proton's life-time was $> 10^{28}$ years and showed that the background from cosmic ray muons at such large depths was low enough to look for atmospheric neutrinos without much background from other cosmic rays. These experiments were continued by the Bombay $-$ Durham collaboration after augmenting the setup by adding neon flash tubes to track charged particles [1].

3. In 1965, the neutrino experiment at the depth of 2300 m was started by the Bombay-Durham-Osaka collaboration at first with two telescopes looking in the horizontal direction and providing the projected zenith angle of charged particles through neon flash tubes. Three more telescopes providing spatial angles of tracks and two magnetic spectrographs were added later on. All these detectors used neon flash tubes for track recording and a scintillator-photo-multiplier combination for triggering.

   This experiment recorded the first ever cosmic ray neutrino event underground in early 1965 and measured the rate of muons from neutrino interactions in the rock surrounding the detectors [172].

   The charged current cross-section at neutrino energies beyond those delivered by the CERN proton synchrotron and the improvement on the limit of the W-boson mass were the highlights of these measurements. Also this experiment gave the first indications of "Kolar Events" to be discussed later.

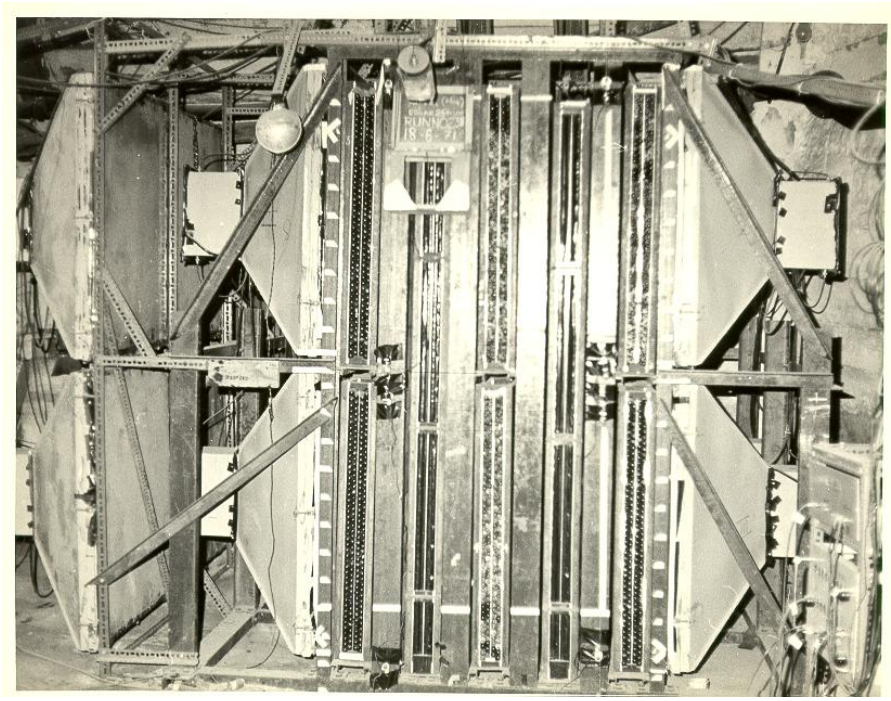

Figure A-2: Neutrino Detectors at the depth of 2.3 Km at KGF.

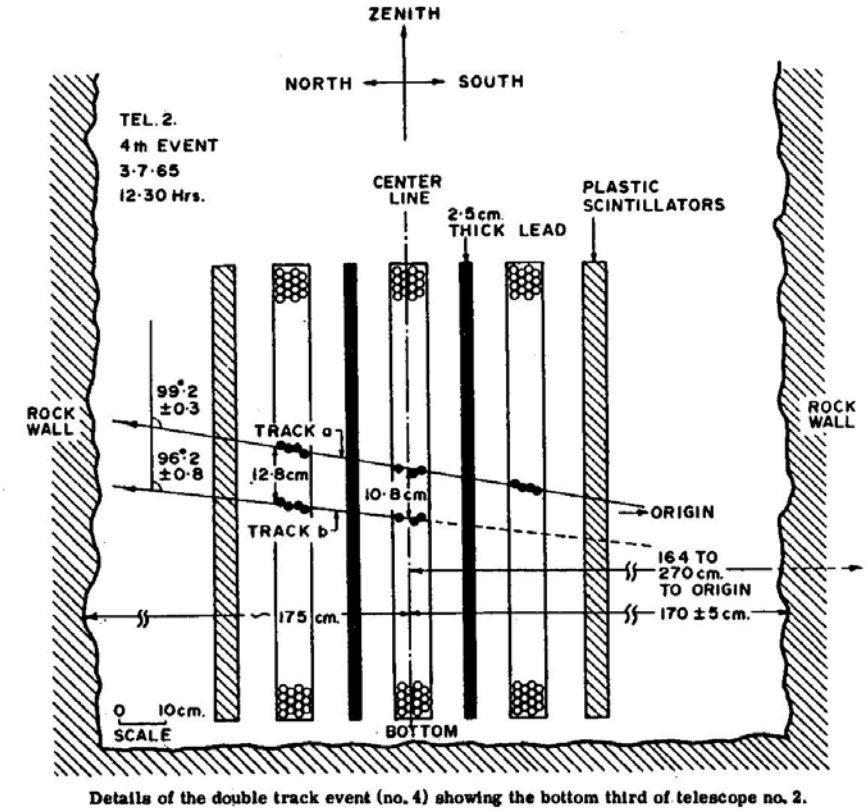

Figure A-3: An expanded view of a section of Telescope 2 in which an inelastic collision in rock of an upward moving neutrino was recorded. The black dots are the fired NFT's.

4. The question of origin of cosmic ray muons was addressed by a series of experiments at the depths of 754, 1500, 3375 and 6045 hg/cm^2 which measured the zenith angular distribution of muons during the period 1968 to 1972. It was clearly established by these experiments that for muon energies up-to several TeV the muons from the decays of pions and kaons were much more numerous than "prompt muons" (muons produced directly or through the decay of very short-lived particles) [173].

   The angular distribution recorded in this series has been combined with earlier experiments done at KGF to derive a very comprehensive depth-intensity relation for underground muons spanning the depth range of 700−10,000 hg/cm^2.

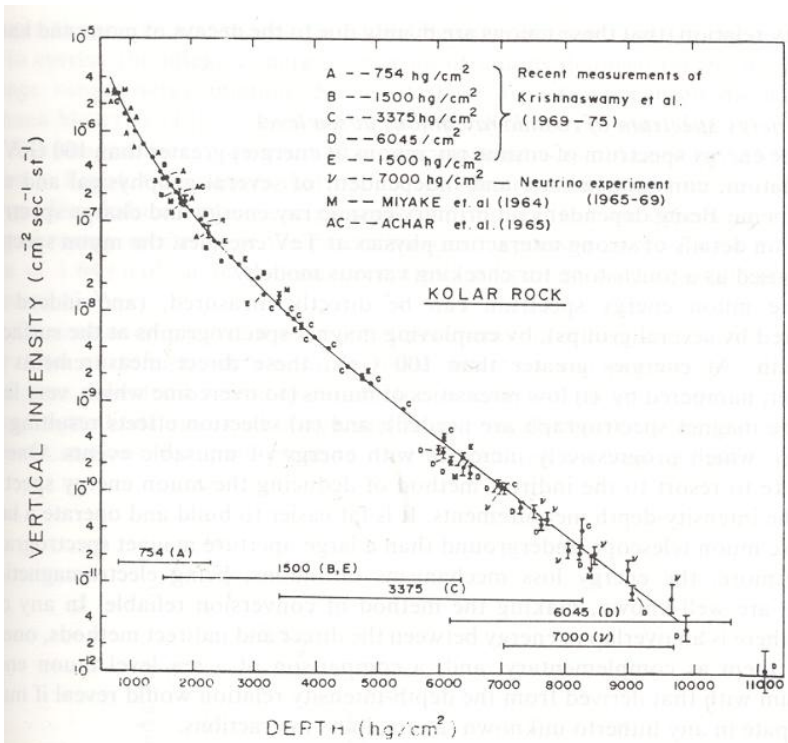

THE CONSOLIDATED DEPTH-INTENSITY RELATION FROM ALL WORKS DONE UNDER KOLAR ROCK

Figure A-4: Depth vs intensity plot from all experiments conducted at KGF until 1970. Many points in this plot were extracted from angular distributions assuming that only pions and kaons are the parents of muons.

5. After this series, an experiment to search for new particles was done at the depth of 3375 hg/cm^2. A telescope recording the spatial zenith angles and triggered by proportional counters as well as the magnetic spectrograph from the earlier neutrino experiment was used. In this experiment more evidence was found for "Kolar Events".

   In this special class of events, all events had two or more tracks with at least one of them fully penetrating the whole detector. All tracks originated presumably from a vertex located either in the air or the low density materials in the periphery of the detector. Finally, the opening angles of the tracks from the vertex were unusually large. All these features suggested the possible decay of a heavy particle at the vertex with a lifetime of $\approx 10^{-9}$ s, as indicated by the typical decay lengths in these events.

6. In 1978, Bhat and Ramanamurthy [174], after measuring the intensity of stopping muons at different depths, obtained the angular distribution of muons at the depth

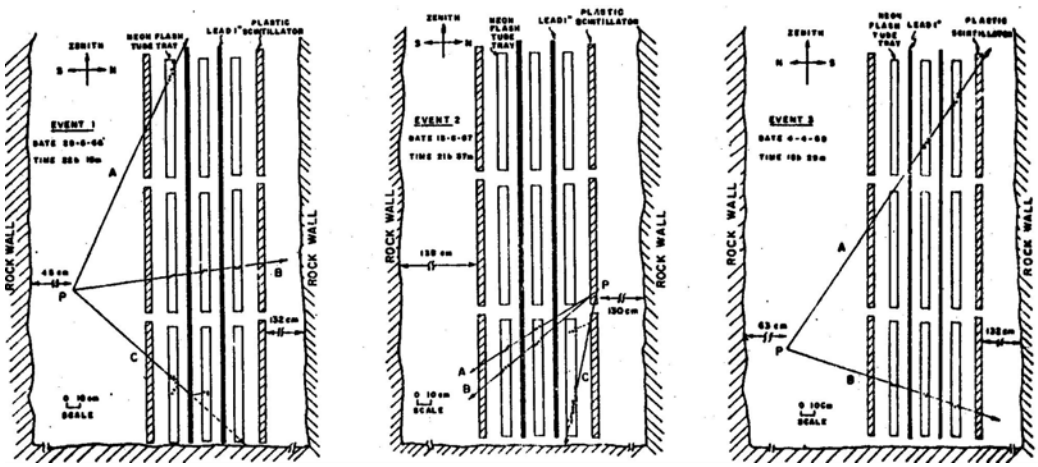

Figure A-5: Multi-track (Kolar) events recorded in KGF neutrino-detectors.

of 417 hg/cm^2. From all these measurements they showed that the intensity of stopping muons is exactly as predicted by the depth-intensity relation for muons and that the fraction of the locally produced component in them had a much flatter angular distribution.

7. From 1980 to 1992, the first pioneering experiment on proton decay was conducted at KGF. Phase I experiments were started at the depth of 7000 hg/cm^2 with a 140 ton detector. Phase II experiments began in 1985 with a 350 ton detector at a depth of 6045 hg/cm^2. Later on the Phase III detector, intended solely for monopole detection, was installed at a depth of 6045 hg/cm^2. All these detectors used proportional counters in an orthogonal geometry sandwiched between iron absorbers for tracking and also had ionisation (dE/dx) measurement in each counter for energy determination.

   This experiment used the latest automatic monitoring and recording techniques then available. The early results from these experiments provided an incentive for the construction of many large scale detectors around the world. Apart from giving a lower limit of a few $\times$ 10^{31} years for the life-time of bound nucleons, this experiment produced a wealth of information on single and multiple−muon events at the highest energy of ∼7-10 TeV, upper limits on the flux of GUT monopoles, rates of atmospheric neutrino interactions inside the detector and in the surrounding rock etc. [175].

The decision by the Bharat Gold Mines Limited and the ministry of mines to close the deeper levels of the KGF mines progressively from 1990 onwards, due to financial reasons, necessitated the termination of the underground experiments by about 1992. The experimental areas became unusable and the experiments closed formally a year later.

Several other low energy laboratory neutrino experiments were also conducted elsewhere in India. Notable among them is the search for the 17 keV neutrino [176]. A Canadian group had claimed to have found evidence for such a massive neutrino in measurements of the tritium beta spectrum and this had made headlines in early eighties. The null result of Datar *et al.* [176] was confirmed by several concurrent experiments all over the world. This was followed by experiments which put limits on the mixing of heavy neutrinos of mass ranging from tens of keV to ∼ a few MeV. Recently a couple of low energy nuclear

Figure A-6: The proton-decay detector at KGF.

physics measurements relevant to solar neutrino physics have been performed at Variable Energy Cyclotron Centre, Kolkata and at the ^{7}Be radioactive ion beam facility at the Nuclear Science Centre, New Delhi.

There are two important issues to be kept in mind when discussing the possible resurrection of an experimental Indian neutrino physics programme: one is that the expertise that was generated when KGF was operational is still available, and the second is that a great deal of potential can be tapped from the experimental nuclear and particle physics community in the country.

Appendix B

Introduction to Neutrino Oscillations

The "Standard Model"(SM) of particle physics is a description of the way particles of matter interact. The SM has twelve building blocks of matter, six leptons and six quarks, and their antiparticles.

$$\begin{aligned} Leptons: &\quad \begin{pmatrix} \nu_e \\ e \end{pmatrix}, \begin{pmatrix} \nu_\mu \\ \mu \end{pmatrix}, \begin{pmatrix} \nu_\tau \\ \tau \end{pmatrix} \\ Quarks: &\quad \begin{pmatrix} u \\ d \end{pmatrix}, \begin{pmatrix} c \\ s \end{pmatrix}, \begin{pmatrix} b \\ t \end{pmatrix} \end{aligned} \tag{B-1}$$

The quarks have fractional charge and interact primarily through the colour force though they experience all other basic interactions. Their binding through the colour interaction is what gives rise to the proton, the neutron, nuclei and all other hadrons. The charged leptons do not interact via the colour force, but experience the other three forces of nature, electromagnetic, weak and gravity. The other building blocks of SM are the gauge bosons that mediate the various interactions, namely, the gluons, the photons and the $W^{\pm}$ and the Z boson.

Within the SM, the three neutrinos (and their antiparticles) are massless. Neutrinos interact with matter only through the weak force (and gravitational force). It is precisely this lack of interaction strength that makes the neutrinos elusive. Because the lepton flavour or family number is conserved, an electron neutrino cannot change into a neutrino from another family. The predictions of SM have stood up to increasingly precise tests in laboratory experiments. Precisely this fact makes the observation of neutrino mass and oscillation a fundamental issue central to neutrino physics and of course the Standard Model.

The discussion of neutrino oscillation can proceed without any further help from SM since it involves only the basic quantum mechanics of time evolution of energy eigenstates as shown in the next section. We do not give explicit references in this section. However, much of the material contained in this section is already part of the popular folklore. See for example [17] and [177]

Neutrino Oscillations

The recent observations on neutrinos all fall in line if neutrinos of one flavour (say, the electron-type) are assumed to oscillate to those of another flavour (say, the muon-type). This merits close examination because the oscillation mechanism is truly the tip of the iceberg: it is possible only if neutrinos are massive. In fact, through neutrino oscillations, quantum mechanics has permitted us to probe the smallest masses measured so far. More importantly, in the Standard Model(SM) neutrinos must be massless. The results from

neutrino experiments are thus setting the stage for an *extension of the Standard Model itself*. Massive neutrinos also have major ramifications on cosmology, the early Universe, and astrophysics.

Vacuum oscillations

We begin with a discussion of oscillation between two neutrino flavours, say electron neutrino and muon neutrino. This is really a toy model, for illustration, since by now we know that there are at least three neutrino flavours. The formalism is applicable in general to any two flavours of neutrinos. The idea of neutrino oscillations [178, 48] is rooted in quantum mechanics. The time evolution of a stationary state $|\psi_k\rangle$ (in units such that $\hbar = c = 1$) is:

$$|\psi_k(t)\rangle = |\psi_k\rangle \;\; \exp\,(-i\; E_k t), \tag{B-2}$$

where E_k is the energy eigenvalue corresponding to $|\psi_k\rangle$. Thus, the stationary state vectors at different times differ simply by an overall phase change. The time evolution of an arbitrary, *i.e.,* non-stationary, state, $|\psi\rangle$, is more complicated. For such a state we can write at $t = 0$:

$$|\psi(0)\rangle = \sum_k \; a_k \; |\psi_k\rangle,$$

where a_k are constants. Using Eq. B-2 one finds:

$$|\psi(t)\rangle = \sum_k \; a_k \; |\psi_k\rangle \; \exp\,(-iE_k t).$$

For neutrinos, the basic assumption is that the familiar electron and muon neutrinos (ν_e and ν_μ) – the *flavour* eigenstates – are not the mass eigenstates (*i.e.,* the stationary states) ν_1 and ν_2, but their superpositions:

$$|\nu_e\rangle = |\nu_1\rangle \; c \; + \; |\nu_2\rangle \; s; \qquad |\nu_\mu\rangle = -|\nu_1\rangle \; s \; + \; |\nu_2\rangle \; c,$$

where $c = \cos\theta$ and $s = \sin\theta$. For two flavours a single angle, θ, suffices to completely specify one basis in terms of the other.

Consider now the state vector of a ν_e produced at $t = 0$. Thus, initially $|\psi(0)\rangle = |\nu_e\rangle = c|\psi_1\rangle + s|\psi_2\rangle$. If the stationary states $|\psi_1\rangle$ and $|\psi_2\rangle$ correspond to energies E_1 and E_2, respectively, then at a later time the state vector will be:

$$|\psi(t)\rangle = c|\psi_1\rangle \; \exp(-iE_1 t) \; + \; s|\psi_2\rangle \; \exp(-iE_2 t).$$

The probability, $P(\nu_e, 0; \nu_\mu, t)$, of the state $|\psi(t)\rangle$ (originating as a ν_e at $t = 0$) appearing as a ν_μ is $|\langle\nu_\mu|\psi(t)\rangle|^2$ and can be expressed as:

$$P(\nu_e, 0; \nu_\mu, t) = c^2 s^2 | - \exp(-iE_1 t) \; + \; \exp(-iE_2 t) \; |^2.$$

To make the notation simple here after we denote the probability $P(\nu_e, 0; \nu_\mu, t) = P_{e\mu}$ and similarly for other flavours. The neutrinos are expected to have small masses, m_i, and are in the ultra-relativistic regime ($E_i \simeq p + m_i^2/(2p)$) where p ($\gg m_i$) is the magnitude of the neutrino momentum[1]. In this situation:

$$P_{e\mu} = 4c^2 s^2 \sin^2\left(\frac{\delta_{21}}{4p} t\right) = \sin^2 2\theta \sin^2\left(\frac{\pi x}{\lambda_{21}}\right), \tag{B-3}$$

[1]Here, we assume that all neutrinos share the same momentum p. To include the effect of momentum spread one must consider a neutrino wave-packet. In most situations, such an analysis makes no practical difference [179] from the above.

where $\delta_{21} = (m_2^2 - m_1^2)$ is the **mass-squared difference** and

$$\lambda_{21} = 2.54\text{m}\left(\frac{E}{\text{MeV}}\right)\left(\frac{\text{eV}^2}{\delta_{21}}\right), \tag{B-4}$$

is the so-called **oscillation length** expressed here in terms of the neutrino energy $E \approx p$. We use x and t interchangeably, since the neutrinos move with essentially the speed of light ($c = 1$). On the right hand side of Eq. B-3 the first factor is a consequence of the 'mixing' while the second factor leads to the 'oscillatory' behaviour.

From Eq. B-3, we have

$$P_{ee} = 1 - P_{e\mu} = 1 - \sin^2 2\theta \sin^2\left(\frac{\pi x}{\lambda_{21}}\right).$$

It is seen from the above that P_{ee} can be less than or equal to unity. The essential ingredients for this are twofold:

1. The neutrinos must be massive and *non*-degenerate.

2. The mass eigenstates of the neutrinos – $\nu_1,\ \nu_2$ – must be different from the flavour eigenstates – $\nu_e,\ \nu_\mu$.

Matter effects

Neutrinos passing through matter, unlike their propagation in vacuum, interact with electrons in matter. While both charge and neutral current weak interactions contribute to the interactions of electron type neutrinos, only the neutral current contributes in the case of other flavours. In the computation of the matter mixing angle, we can ignore the neutral current weak interactions which are the same for all flavours and hence do not affect oscillation probabilities. The additional interaction felt by the electron type neutrinos in the presence of matter is given by [50],

$$V \simeq \sqrt{2} G_F n_e, \tag{B-5}$$

where n_e is the electron density in matter, and G_F is the Fermi coupling. In deriving the above, the electron is assumed to be non- relativistic. In the presence of such interaction, the mass eigenstates are modified and the mass eigenvalues in the presence of interaction are given by,

$$M_{1,2}^2 = \frac{1}{2}\left[m_1^2 + m_2^2 + A \pm \sqrt{(\delta_{21}\cos 2\theta - A)^2 + {\delta_{21}}^2 \sin^2 2\theta}\right] \tag{B-6}$$

where $A \simeq 2\sqrt{(2)} G_F n_e E$. The mass eigenvalues and eigenstates are now a functions of the density n_e and the energy E of the neutrino. The relation between mass eigenstates and flavour eigenstates takes the form

$$|\nu_\alpha^m\rangle = \sum_i (U_m)_{\alpha i} |\nu_i\rangle \tag{B-7}$$

where

$$U_m = \begin{pmatrix} \cos\theta_m & \sin\theta_m \\ -\sin\theta_m & \cos\theta_m \end{pmatrix} \tag{B-8}$$

and θ_m is the new mixing angle in the presence of matter given by,

$$\sin^2 2\theta_m = \frac{\delta_{21}^2 \sin^2 2\theta}{(\delta_{21}\cos 2\theta - A)^2 + \delta_{21}^2 \sin^2 2\theta}. \tag{B-9}$$

Notice that for θ_m to be non-zero requires that θ be non-zero, i.e.,vacuum mixing is essential. The conversion probability in the presence of matter is given by,

$$P_{e\mu} \equiv P_{\nu_e \to \nu_\mu} = \sin^2 2\theta_m \sin^2 \frac{\pi L}{\lambda_{21}^m}, \tag{B-10}$$

where

$$\lambda_{21}^m = \frac{\pi E}{1.267 \delta_{21}^m} \tag{B-11}$$

is the oscillation wavelength in the presence of matter and

$$\delta_{21}^m = M_2^2 - M_1^2 = \sqrt{(\delta_{21} \cos 2\theta - A)^2 + {\delta_{21}}^2 \sin^2 2\theta}.$$

Substituting for θ_m, and averaging over the production region, the conversion probability is given by

$$P_{e\mu} = \frac{1}{2} \frac{\delta_{21}^2 \sin^2 2\theta}{(\delta_{21} \cos 2\theta - A)^2 + \delta_{21}^2 \sin^2 2\theta}, \tag{B-12}$$

which is precisely the Breit-Wigner expression for resonance if $\delta_{21} \sin 2\theta$ is interpreted as the width. It is easy to see that the states are maximally mixed at resonance with $\theta_m = \pi/4$ even when the vacuum mixing angle is very small.

Remarks :

For neutrino propagation in non-uniform matter the evolution of mass eigenstates is given by,

$$i \frac{\mathrm{d}|\nu_i\rangle}{\mathrm{d}t} = \begin{pmatrix} M_1^2/(2E) & -i\mathrm{d}\theta_m/\mathrm{d}t \\ i\mathrm{d}\theta_m/\mathrm{d}t & M_2^2/(2E) \end{pmatrix} |\nu_i\rangle \tag{B-13}$$

and

$$|\nu_\alpha^m\rangle = \sum_i (U_m)_{\alpha i} |\nu_i\rangle$$

which will give the corresponding evolution for the flavour eigenstates. The off-diagonal terms introduce transitions between the two mass eigenstates.

There are two possible cases of interest— adiabatic and non-adiabatic. In the adiabatic case the states evolve almost independent of each other and we may ignore the off-diagonal terms. This is the adiabatic limit which may be stated quantitatively as

$$\frac{d\theta_m}{dt} \ll \frac{|M_2^2 - M_1^2|}{2E}. \tag{B-14}$$

Consider now the propagation of electron neutrinos produced in high dense regions to regions of very low matter density. In these two limits we have

$$\begin{aligned} A \;\to\; \infty : &\quad \theta_m = \pi/2, \quad \text{so that } |\nu_e\rangle = |\nu_2\rangle \;, \\ A \;\to\; 0 \;: &\quad \theta_m = \theta, \quad \text{so that } |\nu_e\rangle = \cos\theta |\nu_1\rangle + \sin\theta |\nu_2\rangle \;. \end{aligned} \tag{B-15}$$

Thus the probability of an electron neutrino remaining electron neutrino is given by,

$$P_{ee} = \sin^2 \theta \tag{B-16}$$

which can be very small if θ is small. This is the essential content of the so called MSW effect. While extreme densities are not always realised, it is sufficient to have reasonably high

dense matter as in the solar core to satisfy the resonance condition during the propagation of electron neutrinos in solar matter.

The other extreme possibility is the purely non-adiabatic case. Here the off-diagonal terms are kept in the evolution of mass eigenstates and hence transitions between them do take place. The probability for an electron type neutrino to remain electron neutrino is then given by the so called Landau-Zener probability,

$$P_{LZ} = \exp\left[-\frac{\pi\delta_{21}\sin^2 2\theta}{4E\cos 2\theta}\beta\right] , \tag{B-17}$$

where

$$\beta = \left[\frac{\mathrm{d}\ln\rho}{\mathrm{d}r}\right]_{res}^{-1} .$$

The survival probability depends on the Energy E of the electron neutrinos. Typically low energy neutrinos are suppressed more than the high energy ones.

However, the propagation may not be purely adiabatic or non-adiabatic and the survival probability, in general, is given by,

$$P_{\nu_e\to\nu_e} = \frac{1}{2}[1 + (1 - 2P_{LZ})\cos 2\theta_m \cos 2\theta] . \tag{B-18}$$

Three flavour oscillation

The LEP experiments established that there are three light neutrinos which is also supported by the requirements of nucleosynthesis in the early Universe. The ν_τ has been directly experimentally detected recently. A natural question then is how do experiments constrain three-neutrino mixing? The results of the previous sections are readily generalised to the case of three or more flavours. Here, for the purpose of illustration, we focus on three neutrinos. The 3×3 neutrino mass matrix M_ν can be diagonalize according to[2]

$$U^\dagger M_\nu^2 U = \mathrm{diag}(m_1^2, m_2^2, m_3^2), \tag{B-19}$$

where U is the Maki-Nakagawa-Sakata [48] unitary matrix which is defined below. The neutrino flavour states $|\nu_\alpha\rangle(\alpha = e, \mu, \tau)$ are linear superpositions of the neutrino mass eigenstates $|\nu_i\rangle(i = 1, 2, 3)$ with masses $m_i : |\nu_\alpha\rangle = \Sigma_i U_{\alpha i}|\nu_i\rangle$ where U is the 3×3 unitary matrix given by the following popular parametrisation:

$$U = \begin{pmatrix} c_{12}c_{13} & s_{12}c_{13} & s_{13}e^{-i\delta} \\ -c_{23}s_{12} - s_{23}s_{13}c_{12}e^{i\delta} & c_{23}c_{12} - s_{23}s_{13}s_{12}e^{i\delta} & s_{23}c_{13} \\ s_{23}s_{12} - c_{23}s_{13}c_{12}e^{i\delta} & -s_{23}c_{12} - c_{23}s_{13}s_{12}e^{i\delta} & c_{23}c_{13} \end{pmatrix} . \tag{B-20}$$

where $c_{12} = \cos\theta_{12}$, etc., and δ is CP violating (Dirac) phase. If the neutrinos are of Majorana type, there will be two more phases which, however, cannot be measured in oscillation experiments and can be ignored.

Oscillations in vacuum and matter

The probability of a neutrino of flavour α to be observed with flavour β after a distance of travel L in vacuum is given by

$$P_{\alpha\beta} = \delta_{\alpha\beta} - 4\sum_{i>j} Re[U_{\alpha i}U_{\beta i}^* U_{\alpha j}^* U_{\beta j}]\sin^2(\frac{\pi L}{\lambda_{ij}}) + 2\sum_{i>j} Im[U_{\alpha i}U_{\beta i}^* U_{\alpha j}^* U_{\beta j}]\sin(2\frac{\pi L}{\lambda_{ij}}), \tag{B-21}$$

[2]For Majorana neutrinos the l.h.s of Eq. 3.2 reads $U^T M_\nu U$.

where U is defined in Eq. B-20, δm^2_{ij} is in eV^2, L is in metres, neutrino energy E is in MeV, and the oscillation length λ_{ij} is as defined in Eq. B-4.

In matter (especially of varying density), the above formula is drastically changed because of the famous Mikheyev-Smirnov-Wolfenstein (MSW) effect. For illustration, here we consider the propagation of the neutrinos through solar matter. The formalism may however be adopted for other situations easily. Let a neutrino of flavour α be produced at time $t = t_o$ in the solar core. Its state vector is $|\Psi_\alpha(t_o)\rangle = |\nu_\alpha\rangle = \sum_i U^c_{\alpha i}|\nu^c_i\rangle$ where $|\nu^c_i\rangle$ are the mass eigenstates with mass eigenvalues m^c_i and mixing matrix elements $U^c_{\alpha i}$ in the core of the Sun. The neutrino propagates in the Sun adiabatically up to t_R (the resonance point), makes non-adiabatic Landau-Zener transition $i \to j$ at t_R with probability amplitude M^{LZ}_{ji}, propagates adiabatically up to t_1 (the edge of the Sun) and propagates as a free particle up to t_2 when it reaches the Earth.

The state vector at t_2 is

$$|\Psi_\alpha(t_2)\rangle \;=\; \sum_{i,j} |\nu_j\rangle M^{LZ}_{ji} U^c_{\alpha i} \exp\left(-i\int_{t_R}^{t_2} \epsilon_j(t)\mathrm{d}t - i\int_{t_o}^{t_R} \epsilon_i(t)\mathrm{d}t\right) \tag{B-22}$$

where $\epsilon_i(t)\,\{= E + m^2_i(t)/2E\}$ are the matter-dependent energy eigenvalues in the Sun up to t_1 and vacuum eigenvalues for $t_1 < t < t_2$. The probability for detecting a neutrino of flavour β on the Earth is

$$\begin{aligned} |\langle\nu_\beta|\Psi_\alpha(t_2)\rangle|^2 \;&=\; \sum_{iji'j'} U^*_{\beta j} U_{\beta j'} M^{LZ}_{ji} M^{LZ^*}_{j'i'} U^c_{\alpha i} U^{c^*}_{\alpha i'} \\ &\quad \exp\left\{-i\int_{t_R}^{t_2} (\epsilon_j - \epsilon_{j'})\mathrm{d}t - i\int_{t_o}^{t_R} (\epsilon_i - \epsilon_{i'}\mathrm{d}t\right\} \end{aligned} \tag{B-23}$$

Next comes the crucial step of averaging over t_0 and t_2 and the assumption that the oscillations are rapid enough so that the averaged exponential in this equation can be replaced by $\delta_{ii'}\delta_{jj'}$. Calling this averaged probability as $P_{\alpha\beta}$ (The probability for a ν_α produced in the Sun to be detected as a ν_β on the Earth at daytime), we get

$$P_{\alpha\beta} = \sum_{ij} |U_{\beta j}|^2 |M^{LZ}_{ji}|^2 |U^c_{\alpha i}|^2 \tag{B-24}$$

which reduces, in the case of two generations, to the result given in Eq. B-18. The above result is applicable to the case of solar neutrinos when there is no intervening matter. This however will change if we consider the so-called night effect when the neutrinos pass through the Earth matter. We will discuss the night effect next.

Neutrinos passing through the Earth

Neutrino oscillation is a complex phenomenon depending on many unknown parameters (six parameters for three flavours ν_e, ν_μ and ν_τ) and a considerable amount of experimental work and ingenuity will be required before the neutrino problem is solved.

Whenever physicists are confronted with a beam of unknown properties, they pass it through different amounts of matter. Nature has fortunately provided us with such opportunities: (a) Neutrinos produced in the solar core pass through solar matter ; (b) solar neutrinos detected at night pass through Earth ; (c) solar neutrinos detected during a solar eclipse pass through the moon ; (d) solar neutrinos detected at the far side of Earth during a solar eclipse pass through the moon and Earth ; (e) upward going atmospheric neutrinos pass through the Earth. To these we may add two more experiments of the future : (f)

Long-base-line experiments of accelerator and reactor produced neutrinos and (g) detection of geophysical neutrinos

It is possible to treat these effects analytically. The analytical formula for (a) was already given in Eq. B-24. We shall now derive the formulae for (b) the night effect. We note that a general formula may be written down for many slabs of matter intervening the flight path of neutrinos.

Starting with $|\Psi_\alpha(t_2)\rangle$ on the surface of the Earth given by Eq. B-22, we multiply the right hand side by $\sum_k |\nu_k^E\rangle\langle\nu_k^E|(=1)$ where $|\nu_k^E\rangle(k=1,2,3)$ is the complete set of matter dependent mass eigenstates just inside the Earth. If the neutrino propagates adiabatically up to t_3 on the other side of the Earth (we shall soon correct for non-adiabatic jumps during the propagation), the state vector at t_3 is

$$\begin{aligned} |\Psi_\alpha(t_3)\rangle &= \sum_{i,j,k} |\nu_k^E\rangle\langle\nu_k^E|\nu_j\rangle M_{ji}^{LZ} U_{\alpha i}^c \\ &\quad \exp\left\{-i\int_{t_2}^{t_3}\epsilon_k \mathrm{d}t - i\int_{t_R}^{t_2}\epsilon_j \mathrm{d}t - i\int_{t_0}^{t_R}\epsilon_i \mathrm{d}t\right\} \end{aligned} \tag{B-25}$$

This expression automatically contains $\langle\nu_k^E|\nu_j\rangle$ which is the probability amplitude for non-adiabatic transition $j\to k$ at the vacuum-Earth boundary and we shall call it M_{kj}^E :

$$M_{kj}^E = \langle\nu_k^E|\nu_j\rangle = \sum_\sigma \langle\nu_k^E|\nu_\sigma\rangle\langle\nu_\sigma|\nu_j\rangle = \sum_\sigma U_{\sigma k}^E U_{\sigma j}^* \tag{B-26}$$

where ν_k^E and U^E are mass eigenstates and mixing matrix just inside the Earth.

Averaging the probability $|\langle\nu_\beta|\Psi_\alpha(t_3)\rangle|^2$ over t_R results in the desired incoherent mixture of mass eigenstates of neutrinos reaching the surface of the Earth. Calling this average probability as $P_{\alpha\beta}^N$ (the probability for ν_α produced in the Sun to be detected as ν_β in the Earth at night), we can write the result as

$$P_{\alpha\beta}^N = \sum_j P_{\alpha j}^S P_{j\beta}^E \tag{B-27}$$

where $P_{\alpha j}^S$ is the probability of ν_α produced in the Sun being detected as ν_j (mass eigenstate) as it enters the Earth and $P_{j\beta}^E$ is the probability of ν_j entering the Earth to be detected as ν_β after it propagates through the Earth. These are given by

$$P_{\alpha j}^S = \sum_i |M_{ji}^{LZ}|^2 |U_{\alpha i}^c|^2 \tag{B-28}$$

$$P_{j\beta}^E = \sum_{k,k'} U_{\beta k}^{E*} U_{\beta k'}^E M_{kj}^E M_{k'j}^E \exp(-i\int_{t_2}^{t_3}(\epsilon_k - \epsilon_{k'})\mathrm{d}t) \tag{B-29}$$

It is important to note that the factorisation of probabilities in Eq. B-27 (which has been derived here as a consequence of the averaging over t_R), is valid only for mass eigenstates in the intermediate state. An equivalent statement of this result is that the density matrix is diagonal only in the mass-eigenstate representation and **not** in the flavour representation.

During the day, put $t_3 = t_2$ so that $P_{j\beta}^E$ becomes $|U_{\beta j}|^2$ and so Eq. B-27 reduces to Eq. B-24. One can justify the averaging over t_0 and t_2 by the facts that the neutrinos are produced over an extended region in the solar core and they are detected over an extended region or time since the detector is moving with the Earth. While averaging over t_0 and t_2 is equivalent to averaging over t_R as far as $P_{\alpha\beta}$ is concerned, it is not so for $P_{\alpha\beta}^N$, but we have

adopted the latter method (of averaging over t_R) for $P^N_{\alpha\beta}$ because of its simplicity in giving us the factored probability expression in Eq. B-27.

However, two points have to be made : (i) For $P^N_{\alpha\beta}$, it is not justified to average over t_2 or t_3 since we would like to detect the neutrinos during a narrow time-bin in the night. (ii) Averaging over t_R (as we have done) may be partially justified since the result may be effectively the same for energy-integrated rates. However, this argument does not apply for Borexino, where the monochromatic Be^7 neutrino line spectrum will be detected.

Next we show how to take into account non-adiabatic jumps during the propagation inside the Earth. Consider ν propagation through a series of slabs of matter, density varying inside each slab smoothly but changing abruptly at the junction between adjacent slabs. The state vector of the neutrino at the end of the nth slab $|n\rangle$ is related to that at the end of $(n-1)$th slab $|n-1\rangle$ by $|n\rangle = F^{(n)}M^{(n)}|n-1\rangle$ where $M^{(n)}$ describes the non-adiabatic jump occurring at the junction between $(n-1)$th and nth slabs while $F^{(n)}$ describes the adiabatic propagation in the nth slab. They are given by

$$M^{(n)}_{ij} = \langle \nu^{(n)}_i | \nu^{(n-1)}_j \rangle = (U^{(n)\dagger} U^{(n-1)})^*_{ij} \tag{B-30}$$

$$F^{(n)}_{ij} = \delta_{ij} \exp\left(-i \int_{t_{n-1}}^{t_n} \epsilon_i(t) \mathrm{d}t\right) \tag{B-31}$$

where the indices (n) and $(n-1)$ occurring on ν and U refer respectively to the nth and $(n-1)$th slabs at the junction between these slabs. Also note that $M^{(1)}$ is the same as M^E defined in Eq. B-26. Defining the density matrix at the end of the nth slab as $\rho^{(n)} = |n\rangle\langle n|$, we have the recursion formula

$$\rho^{(n)} = F^{(n)} M^{(n)} \rho^{(n-1)} M^{(n)\dagger} F^{(n)\dagger} \tag{B-32}$$

Starting with $\rho^{(0)} = |\nu_j\rangle\langle\nu_j|$ (i.e. ν_j entering the Earth), we can calculate $\rho^{(N)}$ at the end of the Nth slab using Eq. B-32. The probability of observing ν_β at the end of the Nth slab is

$$P^E_{j\beta} = \langle \nu_\beta | \rho^{(N)} | \nu_\beta \rangle = (U^{(N)} \rho^{(N)*} U^{(N)\dagger})_{\beta\beta} \tag{B-33}$$

This formula (which reduces to Eq. B-29 for $N = 1$) can be used for the Earth modelled as consisting of $(N+1)/2$ concentric shells, $N =$ odd, with the density varying gradually within each shell.

Many interesting physical effects are contained in the analytical formulae already presented. As an example, we shall mention what we may call "vacuum oscillations in matter". For $\theta_{13} \approx 0$, we get the following simple formula relating the survival probability in the night and day :

$$P^N_{ee} = P^D_{ee} + \left(1 - 2P^D_{ee}\right)\left(P^E_{2e} - \sin^2\theta_{12}\right)\frac{1}{\cos 2\theta_{12}} \ , \tag{B-34}$$

where

$$\begin{aligned} P^E_{2e} &= \sin^2\theta^E_{12} + \sin 2\theta^E_{12} \sin 2(\theta^E_{12} - \theta_{12}) \sin^2 \frac{1}{4E} \int_{t_1}^{t_2} \left[m^2_2(t) - m^2_1(t)\right] \mathrm{d}t \ , \\ &\approx \sin^2\theta_{12} + 2(\theta^E_{12} - \theta_{12}) \sin 2\theta_{12} \sin^2 \frac{\delta_{21} L}{4E} \ . \end{aligned} \tag{B-35}$$

Here ω_E is the mixing angle just below the surface of the Earth and L is the distance the neutrino travels inside the Earth. In arriving at the approximate expression for P^E_{2e} given in Eq. B-35, we have assumed that $\delta_{21} \gg A$ $(\equiv 2\sqrt{2}G_F N E)$, N being the electron number density inside the Earth. Under this approximation of small matter effect, P^E_{2e} and hence P^N_{ee}

will exhibit vacuum type oscillations as a function of the distance travelled within Earth, but their amplitude will be controlled by matter density (since $(\omega_E - \omega)$ is of order A/δ_{21}). Such regular oscillations were indicated in the numerical calculations for appropriate choice of parameters and their interpretation is clear from the analytical formulae.

Appendix C

Structural Stability of the ICAL Detector

The design capacity of the ICAL has been worked out in detail and a separate report is available. The study assumes a detector with one hundred and forty 60 mm thick steel plates stacked vertically, with 16 m × 16 m plates (single module) in plane and spaced with a 25 mm gap in between as discussed in the detector chapter[1].

The bending stress and deformation of steel plates and glass plates has been checked and found to be adequate when steel spacers spaced at 2 m centre-to-centre are included for support, as shown in Fig. C-1. The bearing width of the steel spacer and the concrete foundation has also been checked. The total load on the rock cavern due to the arrangement has been checked for the bearing capacity and is found to be adequate. The detailed calculations for the horizontal structure is given below:

1. Capacity of steel plate:

Self weight/(plan area) of the 60mm steel plate	$W_s = 7800\ (\mathrm{kg/m^3}) \times 60\ \mathrm{mm} \times 10\ (\mathrm{m/s^2})$
	$W_s = 0.0047\ \mathrm{N/mm^2}$
Maximum moment/width due to self weight	$M_s = W_s L^2/8$
	$= 2350\ \mathrm{N\ mm/mm}$

The sectional modulus Z_s is given in terms of the moment of inertia I, mass per unit length m_l and Y the distance to the extreme fibre. Thus the bending stress in the steel plate is given by,

$$Z_s = \frac{I/m_l}{Y} = \frac{t^2}{6},$$

where $t = 60$ mm is the thickness of the plate. Thus

Bending stress in steel plate	$M_s/Z_s = (2350 \times 6)/60^2$
	$= 3.92\mathrm{MPa}$
	$\ll 250$ MPa (maximum).

[1]The details given in this appendix are based on the preliminary report on the *Design capacity of magnetised iron calorimeter detector* given by Prof. V.Kalyanaraman, Structural Engineering Division, Department of Civil Engineering, IIT Madras, at Chennai.

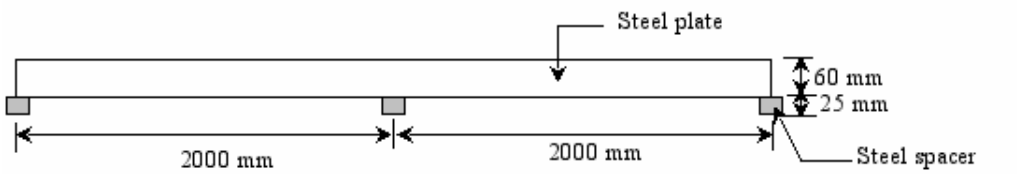

Figure C-1: Schematic of steel structural supports for ICAL where each plate is taken to be 4 m wide.

2. Bending deformation:

Modulus of elasticity (for steel/glass)	$E_{s/g}$
Area moment of inertia (for steel/glass)	$I_{s/g}$=$t^3/12$
Maximum deformation of steel plate	$\delta_{max} = W_s L^4/185 E_s I_s$
	$= 0.1129$mm
	$<<$ 6.15mm (span/325)

3. Stress on glass plate supported by steel plate:

Young's modulus- steel	$= 2 \times 10^5$ N/mm^2
Young's modulus- glass	$= 70 \times 10^3$ N/mm^2

since maximum curvature of the glass and steel plate are equal

Maximum moment per unit width in th glass plate	$M_g = M_s \times E_g \times I_g/(E_s \times I_s)$
	$= 30.46$ N mm/mm
Stress on glass plate	$= M_g/Z_g = (30.46 \times 6)/20^2$
	0.457 MPa $\ll$ 30 MPa

Figure C-2: Bending deformation of glass and steel.

4. Bearing width of 25mm thick steel spacers:

Allowable bearing strength in steel	= 185 MPa
Assuming a factor	= 2.5
Permissible bearing stress in steel	= 74 MPa
Maximum force on 25mm steel spacer	$= 139 \times 0.0047$
	$= 0.6533$ N/mm^2

Allowing 10 percent increase for self weight of 20mm glass plates and spacers

Total reaction	$= 0.7186$ N/mm^2
Total reaction per unit length of spacer plate	$= 2000 \times 0.7186$
	= 1437 N/mm
Required bearing width of 25mm spacer plate	=Total reaction/Permissible bearing stress
	= 1438/74
	= 19.4 mm
Recommended width of 25mm spacer plate	= 50mm

5. Bearing capacity of concrete:

The entire detector will be supported by concrete at the bottom.

Grade of concrete	=M30
Assuming a factor	= 2.5
Total reaction on concrete due to 60mm steel plate	$= 140 \times 0.0047$
	$= 0.6583$ N/mm^2
Allowing 10 percent increase for self weight of 20mm glass plate	$= 0.06583$ N/mm^2
Total reaction on concrete	$= 0.724$ N/mm^2
Total reaction on concrete per unit length	$= 2000 \times 0.724$
	= 1447.6 N/mm
Bearing width of concrete for dispersion of load at 30°	$= 2 \times 103.92 + 50$
	= 257.8 mm
Bearing stress in concrete	= 1447/258
	= 5.6 MPa $<$ 7.5 MPa

Permissible bearing strength for M30 grade concrete

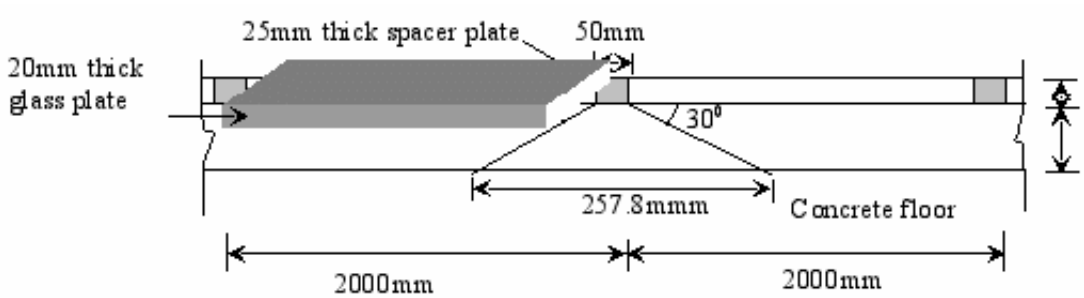

Figure C-3: Bearing width of the concrete floor.

6. Bearing stress on rock:

Assuming uniform distribution of the load on rock supporting the concrete pad

Stress on rock $= 0.724 \times 1000^2/1000 = 724$ kN/m$^2 \ll 3240$ kN/m^2

Permissible bearing strength of rock assumed to be granite.

Some field tests may be needed to confirm the bearing strength of concrete.

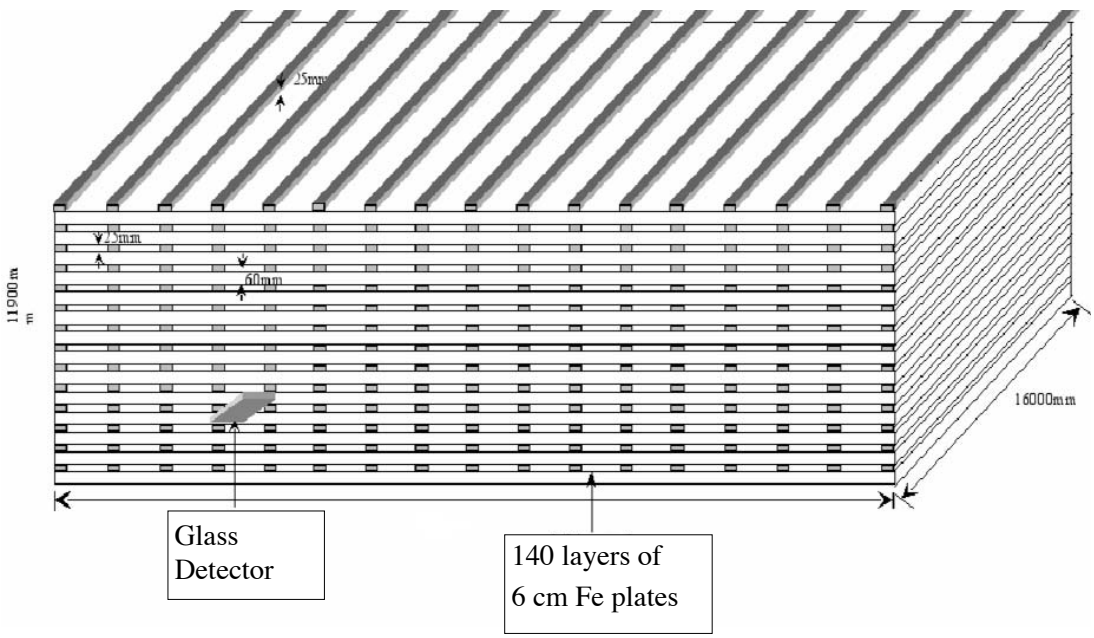

Figure C-4: Schematic view of ICAL including structural supports.

Appendix D

ICAL as an End Detector for a Beta Beam Experiment

Introduction

A high intensity source of a single neutrino flavour with known spectrum is most desirable for precision measurements, the consensus direction for the future. In recent years this has spurred much interest in the development of novel neutrino sources.

The Beta Beam [180] is an especially attractive option in this direction. It relies on intense accelerated beams of β-unstable ions. The decay of these ions in a storage ring with long straight sections produces pure and intense ν_e ($\bar{\nu}_e$) beams of known spectrum. Beta Beams are particularly effective [181, 182, 183] to explore the θ_{13} and δ (CP phase) parameters of the leptonic mixing matrix [184]. It has been proposed to produce ν_e beams using highly accelerated ^{18}Ne ions and $\bar{\nu}_e$ from ^{6}He [182]. Using the SPS accelerator at CERN, it will be possible to access $\gamma \sim 100$ for completely ionised ^{18}Ne and $\gamma \sim 60$ for ^{6}He. The ratio between the two boost factors is fixed by the necessity of using the same ring for both ions. Higher values of γ, as required for longer baselines to INO from CERN, for example, can be achieved by upgrading the SPS with superconducting magnets or by making use of the LHC. The reach of the LHC will be $\gamma = 2488$ (^{6}He) and $\gamma = 4158$ (^{18}Ne) [185].

The β-beam

The Beta Beam contains a single neutrino flavour. The energy spectrum and intensity are well understood and it is virtually *systematic* free. In the rest frame of the spin-less parent ion, the neutrino is isotropically emitted. Strong collimation is ensured by the large Lorentz boost of the parent ions. $\bar{\nu}_e$ are produced by the super-allowed β^- transition

$$^{6}_{2}He \rightarrow ^{6}_{3}Li + e^- + \bar{\nu}_e. \tag{D-1}$$

The half-life of $^{6}_{2}$He is 0.8067 s and the Q value of the reaction is E_0 =3.5078 MeV.

Neutrino beams can be produced by the super-allowed β^+ transition

$$^{18}_{10}Ne \rightarrow ^{18}_{9}F + e^+ + \nu_e, \tag{D-2}$$

having half-life 1.6s and Q value E_0 =3.4 MeV. According to feasibility studies [186, 187] the number of useful decays in case of neutrinos (anti-neutrinos) could be 1.1×10^{18}/year (2.9×10^{18}/year) for a low gamma configuration.

For the long baselines suitable for a rich physics harvest, the ICAL detector being examined for the INO could provide a favourable target. The base ICAL design is a 50 kton

Fe detector with an energy threshold around 800 MeV. For this preliminary analysis the detector is taken to be of perfect efficiency and with no backgrounds[1]. ICAL will be a good choice for a very long baseline β-beam experiment, with a source at CERN, Geneva (L = 7177 km (PUSHEP)).

Simulation for the ICAL design has shown excellent charge identification (95%) and energy determination (10 – 15%) capability for muons with a few GeV energy. To shed light on θ_{13} and the sign of δ_{32}, we focus on the muon neutrino appearance mode, i.e., $\nu_e \to \nu_\mu$ and $\bar{\nu}_e \to \bar{\nu}_\mu$ transitions.

The fluxes and cross sections

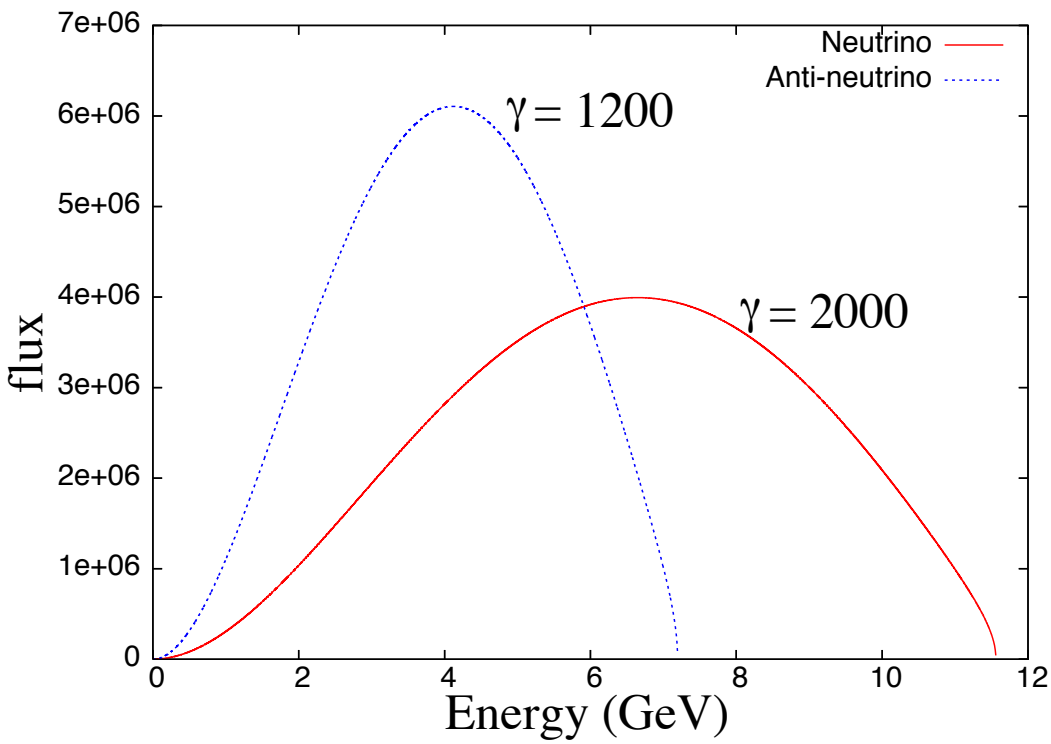

Figure D-1: Boosted spectrum of neutrinos (solid line) and anti-neutrinos (broken line) at the far detector assuming no oscillation. The flux is given in units of $\mathrm{yr}^{-1}\mathrm{m}^{-2}\mathrm{MeV}^{-1}$.

The expected energy spectra are readily calculated and for ν_e (γ = 2000) and $\bar{\nu}_e$ (γ = 1200) these are shown in Fig. D-1. We separately include the contributions to the neutrino-nucleus interaction cross section from the exclusive channels of lower multiplicity (quasi-elastic scattering and single-pion production), and incorporate all additional channels as part of the deep-inelastic scattering cross section :

$$\sigma_{CC} = \sigma_{QE} + \sigma_{SP} + \sigma_{DIS}. \tag{D-3}$$

At low energies, quasi-elastic [188] events are dominant and the cross-section grows rapidly for $E_\nu \leq 1$ GeV, while at higher energies ($E_\nu \geq$ a few GeV), mostly deep-inelastic scattering [189] occurs and the growth is linear in the neutrino energy. At intermediate energies, there are sizeable contributions from both, as well as from resonant channels dominated by the Δ (1232) [190].

[1]Backgrounds are strongly suppressed from the directionality requirement.

Precision measurement of θ_{13}

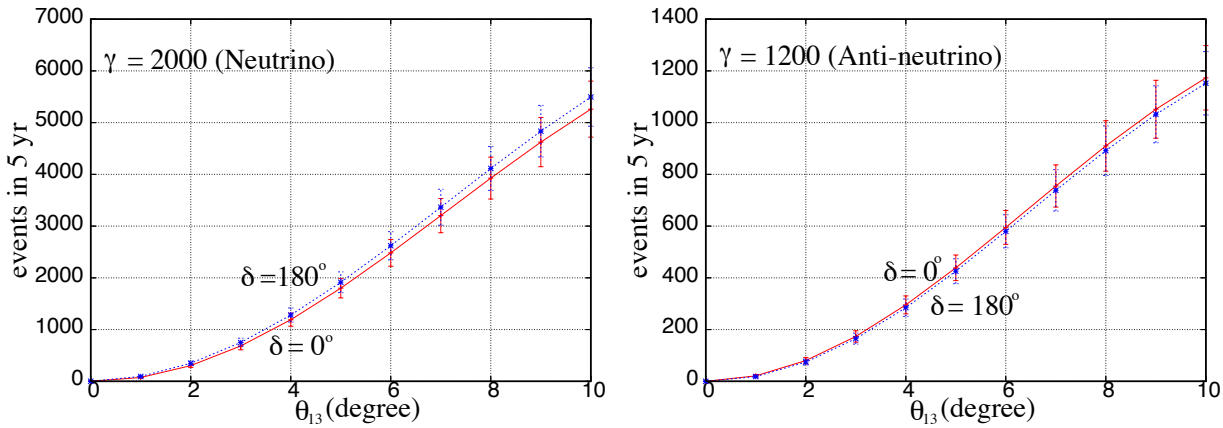

Figure D-2: The number of events as a function of θ_{13} for ν (left) and $\bar{\nu}$ (right) for a 5-year run. Here, δ_{32} is chosen positive (negative) for ν ($\bar{\nu}$). Note the insensitivity to the CP phase δ.

The current bound on θ_{13} from the global oscillation analysis is $\sin^2\theta_{13} < 0.05$ (3σ) [52, 191]. It is seen from Fig. D-2 that for a five-year exposure, ICAL will record a substantial number of events even for $\sin^2\theta_{13}$ as small as 0.0003. Results are presented for two limiting choices of the CP phase δ. The CERN to INO distance is near the 'magic baseline' ($\sim$ 7000 Km) where matter effects are largest and the effect of the CP phase almost negligible. This makes it possible to evade the '$\theta_{13} - \delta$ degeneracy' problem which plagues experiments at other baselines. For mass-squared differences and mixing parameters we use the values from Ref. [192] [2]. We follow the convention $\delta_{ij} = m_i^2 - m_j^2$. In this calculation, we have assumed an uncertainty of 2% in the knowledge of the number of ions in the storage ring. We have included a 10% fluctuation in the cross section. The statistical error has been added to the above in quadrature. We have neglected nuclear effects. For the baselines under consideration, the neutrino beam passes through the mantle of the earth where to a good approximation the density can be considered to be constant. The plots presented here are obtained by numerically solving the full 3-flavour neutrino propagation equation based on the framework of Barger *et al.* [193].

Fig. D-3 shows the 3σ uncertainty in the measurement of θ_{13}. Since the slope of any curve in Fig. D-2 and the size of the error bars is not the same on both sides for a chosen θ_{13}, the uncertainty in the positive direction (upper curves) is different from the one in the negative direction (lower curves).

Determination of the sign of δ_{32}

The sign of δ_{32} is an essential missing piece of information to determine the structure of the neutrino mass matrix. At longer baselines matter effects are sizeable and measurement of the neutrino mass hierarchy becomes possible.

The left panel of Fig. D-4 shows the number of events as a function of θ_{13} for the neutrino case, taking the direct ($m_3^2 - m_2^2 > 0$) and inverted ($m_3^2 - m_2^2 < 0$) hierarchies. The right panel shows the same for anti-neutrinos. It is clear from the huge difference between the

[2] $|\delta_{32}| \simeq 2.1 \times 10^{-3}$ eV^2, $\theta_{23} \simeq 45°$, $\delta_{21} \simeq 7.9 \times 10^{-5}$ eV^2, and $\theta_{12} \simeq 33.2°$ [192].

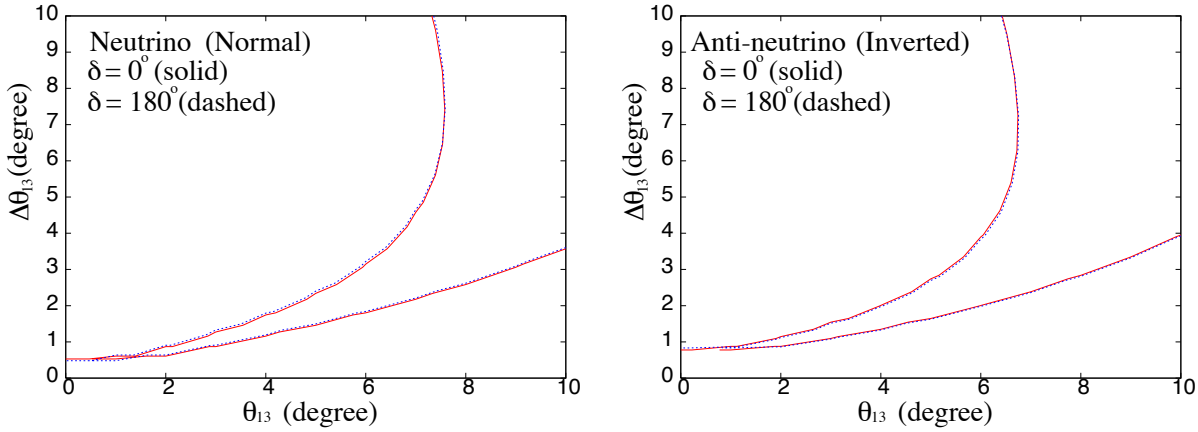

Figure D-3: The 3σ uncertainty in the measurement of θ_{13} for ν (left) and $\bar{\nu}$ (right) from a 5-year run.

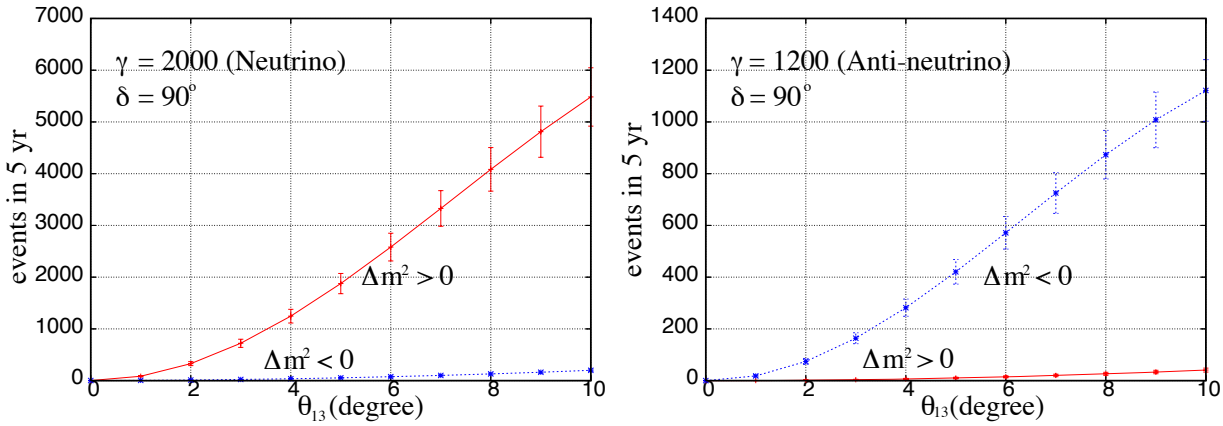

Figure D-4: The number of events as a function of θ_{13} for $\delta_{32} > 0$ (solid curve) and $\delta_{32} < 0$ (broken curve). The left (right) panel is for neutrinos (anti-neutrinos).

two alternatives that Beta Beams at these baselines can settle the issue of the neutrino mass hierarchy.

Conclusions

The ICAL detector has the potential of yielding precise information on the mixing angle θ_{13} and the sign of δ_{32} when used as an end-detector for a high γ Beta Beam. The CERN-INO distance matches the 'magic' baseline, so results are insensitive to the CP phase δ.

Appendix E

Double Beta Decay Experiment at INO

Neutrino physics is one of the present day thrust areas in experimental as well as theoretical physics. The terrestrial and extraterrestrial searches for neutrino mass through the study of atmospheric, solar, reactor and supernova neutrino sources have finally succeeded in establishing that neutrino have mass. The present experimental evidences regarding the neutrino mass strongly suggest physics beyond the standard model of particles. The possibilities include extensions of the Standard Model, super-symmetry and grand unified theories etc. Further, the mass and nature (Dirac or Majorana) of neutrinos play an important role in astrophysics and cosmology, namely, in the understanding of stellar evolution, supernova explosion, nucleosynthesis, galaxy formation and dark matter. However, these two properties of the neutrino can be best extracted through the study of nuclear (single) beta decay and double beta decay (DBD). The topic has an interdisciplinary character covering nuclear and particle physics, astrophysics and cosmology supplemented by experimental and theoretical studies of neutrino interactions.

Neutrino-less double beta ($0\nu\beta\beta$) processes have a great potential to explore some of the fundamental questions associated with neutrino physics beyond the Standard Model, which is believed to be the correct description of all fundamental particles and their interactions except gravitation. Neutrino-less double beta decay is perhaps the only experiment that will tell us about the true nature of neutrino- whether it is a Dirac or a Majorana particle. The $0\nu\beta\beta$ decay will provide the information on absolute effective mass of the neutrinos and will tell us if the total lepton number, one of the fundamental conserved quantities of the Standard Model, is violated. In addition, this would constrain several parameters of the super-symmetric models, composite models, left-right symmetric models and several other extensions of the standard models, more severely than any of the proposed next generation colliders.

As the double beta decay is a second order weak interaction process, best choice to study DBD is one where the single beta decay branch is forbidden either energetically or due to spin-isopin/parity. There are several candidates where double beta decay ($\beta - \beta$ i.e. $\beta^-\beta^-$) can occur. Other possibilities like $\beta^+\beta^+/\beta^+$EC/ ECEC are also feasible, but in all these cases even the corresponding 2ν modes have not been observed due to the reduced phase space. The half-lives of $2\nu\beta\beta$ emitters have been measured for more than ten nuclei.

In order to translate the results of $0\nu\beta\beta$ into coupling constants or effective neutrino mass, representing physics beyond the Standard Model, it is essential to have an accurate knowledge of associated nuclear wave functions. The present estimates of nuclear transition matrix elements (NTME) are believed to have a large uncertainty (10-50 percent). In spite of the rapid growth in computational power, very few nuclei can be studied with reasonable

accuracy using the shell model. The quasi-particle random phase approximation (QRPA) has been used for calculation of NTME. These calculations indicated that the particle-particle part of the effective nucleon interaction in the proton-neutron channel was decisive for the reproduction of the experimental $2\nu\beta\beta$ decay for NTMEs for many nuclei. Recently it has been observed that the neutron-proton interactions vis-a-vis the deformations of the ground states play an important role in arriving at the nuclear matrix elements.

International scenario

The DBD search is entering a new era of large scale interdisciplinary as well as sensitive experimentation on one hand and theoretical computations with reliable nuclear and particle inputs on the other. The existing and planned proposals worldwide show a rich diversity of approaches with many novel techniques involving different areas of research [194]. The results of these experiments will not only be of fundamental importance for neutrino physics but also for dark matter searches and hence will provide crucial inputs to certain key problems as well as help to discriminate between different theoretical models of modern astroparticle physics and cosmology. The majority of experiments, based on direct counting methods, aim to measure the characteristic properties of $0\nu\beta\beta$ decay such as emission of two simultaneous electrons from the same vertex inside the source and/or the constancy of the sum energy of the two emitted electrons. The presently running experiments have typical source sizes less than 100 kg and have put a limit on the half-life for $0\nu\beta\beta$. Many of the proposed experiments, either new or upgrades of the presently running counterparts, are expected to have much better sensitivity primarily due to larger source sizes (approximately a ton). Of various existing and proposed experiments, the CUORE experiment (^{130}Te) [195], the only low temperature bolometric detector so far, and the Ge experiment [196] have the desired energy resolution (0.5 percent and 0.2 percent, respectively).

So far only the Heidelberg-Moscow experiment has reported a positive evidence for the neutrino-less double beta decay in ^{76}Ge[197]. However, this result is based on very low statistics and needs to be confirmed. More recently, the CUORICINO experiment has placed a lower limit on $0\nu\beta\beta$ in ^{130}Te ($T_{1/2} \geq 1.8\times10^{24}$ yr, $m_\nu \leq 0.2-1.1$ eV)[198]. Measurements in several nuclei are invaluable for establishing the existence of the $0\nu\beta\beta$ decay at this effective neutrino mass range and for reducing the uncertainty arising from nuclear matrix elements. Moreover, the neutrino-less double beta decay experiments can be suitably modified for solar neutrino flux measurement and dark matter search.

A group of experimentalists and theoreticians have recently begun to explore the possibility of setting up of a $0\nu\beta\beta$ decay experiment at the INO site. A one-day workshop on *Double Beta Decay (DBD05)* was held at IIT, Kharagpur on March 13, 2005, where various existing and proposed experiments worldwide were reviewed. One of the main considerations for $0\nu\beta\beta$ candidate is a high Q value since the decay rate is proportional to Q^5 and the interference from natural radioactive background is less at higher energies. Both the source and detector have to be large in size, since the expected events are rare due to a large half-life. Thus candidates having a large isotopic abundance are favourable. If the source itself can serve as a detector, then the experimental setup is simplified. As a result of these discussions, ^{124}Sn (Q = 2.28 MeV, 5.8 percent abundance) and ^{150}Nd (Q = 3.37 MeV, 5.6 percent abundance) were identified as possible choices. As mentioned earlier, a crucial criterion for detector design is high energy resolution for a precision measurement of the sum energy of two electrons emitted in $0\nu\beta\beta$ process. For this purpose, a bolometric detector is ideally suited. Of the two candidates (namely, ^{124}Sn and ^{150}Nd), at present, only Sn can be made into a bolometric detector. Tin becomes super-conducting below 3.7 K and

is non-magnetic. Thus at temperatures below 100 mK the specific heat of Sn is very low, having only lattice contributions, and can be used as a bolometric detector. Subsequently, in the second workshop held at University of Lucknow (Nov. 4-5, 2005) the community decided to focus on the *Feasibility Study of Neutrino-less double beta decay in* ^{124}Sn. The main objectives of this feasibility study are:

- To make a bolometric detector of ^{nat}Sn of mass 0.5-1 kg operating at 30mK.
- To simulate the response function of bolometric Sn detector, to build a background model, identify the origins of the interfering radiation background and evolve techniques to minimise the same.
- Theoretical calculation of nuclear transition matrix elements, which are needed to extract parameters of various gauge field theoretical models beyond the Standard Model.

The proposal being multidisciplinary in nature involves several scientific and engineering challenges. The R&D for development of a Sn bolometer will be carried out at TIFR, Mumbai using a refurbished dilution refrigerator. Specialised techniques for low noise, small signal processing essential for mK bolometry need to be developed.

In double beta decay experiments the expected events are rare, since the half-life for the decay is $\geq 10^{25}$ years. It is therefore important to identify and to suppress unwanted background events in order to improve the sensitivity of a $0\nu\beta\beta$ experiment.

The background producing sources relevant to such experiments can be divided broadly into two categories. The first one is cosmogenical, which are produced by the interaction of cosmic rays with the atmospheric molecules and the materials available around the experimental setup. This is significantly reduced in underground laboratories like the INO cavern. The second type of background sources, which are most crucial for sensitivity, are the decay of radioactive nuclei present in the materials of the detector and its surroundings. Therefore, both the detector and shielding materials should have minimum radioactive contamination. Since it is nearly impossible to eliminate all the sources of background, a detailed simulation of the background in the detector becomes an important part of a $0\nu\beta\beta$ experiment. The goal is to build a response function of detectors as well as develop a model for the background. Both the experimental as well as simulation studies for radiation background will be taken up at IIT Kharagpur.

The shell model is the best choice to study the nuclear double beta decay. However, it is not possible to employ the shell model in medium and heavy mass nuclei, as the number of basis states becomes quite large. On the other hand, most of the $\beta\beta$ decay emitters and ^{124}Sn in particular lie in this region. The QRPA and PHFB are convenient models to study the vibrational and deformed nuclei respectively. The deformed Hartree-Fock (DHF) is another choice to study the vibrational as well as deformed nuclei. Calculations of the nuclear transition matrix elements for the DBD processes and for ^{124}Sn, in particular, using different models are already in progress at IIT (Kharagpur) and the University of Lucknow.

We would also undertake the R&D on Sn enrichment ($> 50\%$) and sensor development work in parallel. Our goal would be to make a detector having approximately 1 kg equivalent of enriched ^{124}Sn and install it in a low background area.

Apart from the INO collaboration, the following persons are currently part of the double beta decay working group: P.K. Raina, S.L. Sharma, A.K. Singh (IIT Kharagpur), V. Nanal, R.G. Pillay (TIFR, Mumbai), P.K. Rath, R.B. Singh (Univ. of Lucknow), A. Shukla (IOP, Bhubaneshwar), A. Ray (VECC, Kolkata), Aradhana Shrivastava (BARC, Mumbai), V.K.B. Kota and U. Sarkar (PRL, Ahmedabad).

Appendix F

Neutrino Detectors of the Future: A Comparison

Introduction

This report summarises the relevant information about neutrino detectors being constructed or being planned for the future, including their physics potential and time-scale over which they aim to achieve their physics goals.

The solar and atmospheric neutrino anomalies can be elegantly explained in terms of oscillations among the three active neutrino flavours. Neutrino oscillation hypothesis received further boost from the results of the long baseline experiments KamLAND, with reactor $\bar{\nu}_e$s as source, and K2K, which used accelerator ν_μs as source.

The three neutrino flavours, ν_e, ν_μ and ν_τ, mix to form three mass eigenstates ν_i with masses m_i $(i = 1, 2, 3)$. The mixing matrix, called PMNS matrix, can be parametrised in terms of three mixing angles, $\theta_{12}, \theta_{13}, \theta_{23}$ and a CP violating phase δ as in the case of CKM matrix of the quark sector. Neutrino oscillations depend only on *mass-squared differences* and hence it is not possible to measure the scale of neutrino masses in neutrino oscillation experiments. Tritium beta decay and neutrino-less double beta decay experiments can provide information on the neutrino mass scale. However the mass-squared differences $\delta_{32} = m_3^2 - m_2^2$ and $\delta_{21} = m_2^2 - m_1^2$, along with the mixing angles and the CP violating phase δ, can be measured in long baseline neutrino oscillation experiments.

A physically well motivated form of the PMNS matrix is [49]

$$U = U_{23}(\theta_{23}) U_{\rm ph}(\delta) U_{13}(\theta_{13}) U_{12}(\theta_{12}), \tag{F-1}$$

where

$$U_{23}(\theta_{23}) = \begin{pmatrix} 1 & 0 & 0 \\ 0 & \cos\theta_{23} & \sin\theta_{23} \\ 0 & -\sin\theta_{23} & \cos\theta_{23} \end{pmatrix} \tag{F-2}$$

and

$$U_{\rm ph}(\delta) = \begin{pmatrix} 1 & 0 & 0 \\ 0 & e^{i\delta} & 0 \\ 0 & 0 & e^{-i\delta} \end{pmatrix}. \tag{F-3}$$

The matrices U_{13} and U_{12} can be written in analogy to U_{23}. The mixing matrix U is given explicitly in Appendix B. The results of the CHOOZ experiment, in combination with the analysis of the atmospheric neutrino anomaly, place a stringent bound [52, 199]

$$\sin^2 2\theta_{13} \leq 0.2. \tag{F-4}$$

In the limit of small θ_{13}, it can be shown that

$$\delta_{32} \simeq \Delta_{\rm atm} \quad \text{and} \quad \theta_{23} \simeq \theta_{\rm atm} \tag{F-5}$$

$$\delta_{21} \simeq \Delta_{\rm sol} \quad \text{and} \quad \theta_{12} \simeq \theta_{\rm sol}, \tag{F-6}$$

where $\Delta_{\rm atm}$ and $\theta_{\rm atm}$ are the mass-squared difference and mixing angle needed to resolve the atmospheric neutrino anomaly, *under the assumption that only two flavours are involved in the oscillations.* $\Delta_{\rm sol}$ and $\theta_{\rm sol}$ are also defined in a similar manner.

Presently δ_{21} is measured to great precision by the KamLAND experiment but the accuracy on θ_{12}, from both KamLAND and solar neutrino experiments, is limited [200, 53]. At 3σ, we have,

$$\delta_{21} \sim (7.9 \pm 0.9) \times 10^{-5}\ \text{eV}^2,\ 29^\circ \leq \theta_{12} \leq 39^\circ. \tag{F-7}$$

Further improvement in our knowledge of θ_{12} will require precision solar neutrino experiments.

Analysis of the atmospheric neutrino anomaly gives the bounds (at 3σ), [201]

$$\delta_{32} = (1.4 - 3.3) \times 10^{-3}\ \text{eV}^2,\ 36^\circ \leq \theta_{23} \leq 56^\circ. \tag{F-8}$$

The goals of long baseline experiments are

1. Verifying the oscillation hypothesis directly by observing the energy dependence of the neutrino survival probability,

2. Improving the precision of δ_{32} and θ_{23} and

3. Obtaining, if possible, proof for non-zero values of θ_{13} and δ, otherwise improving the bounds on them.

Sources

Below we give a brief description of the types of neutrino sources being considered.

1. Atmospheric: Atmospheric neutrinos consist of $\nu_\mu, \bar{\nu}_\mu, \nu_e$ and $\bar{\nu}_e$ with comparable fluxes. These neutrinos are produced in the decays of muons, pions and kaons produced in the interactions of cosmic rays with atmospheric nuclei. We expect the total number of muon-type neutrinos to be twice as large as the total number of electron-type neutrinos. The energies of these neutrinos can range from 100 MeV to 100 GeV and beyond, although the flux falls steeply as $E^{-2.7}$ with energy above 1 GeV.

2. Conventional Beams: Conventional beams are essentially beams of ν_μ with small (less than 1%) contamination from other flavours. The ν_e contamination of the beam limits the experiment's ability to observe ν_e appearance and hence to measure θ_{13}. To produce conventional neutrino beams, a beam of high energy protons is directed to a target, consequent positively charged pions are collected and focussed and are allowed to decay in a long decay pipe. After this decay, a reasonably collimated muon neutrino beam is obtained. A muon anti-neutrino beam can be obtained by collecting negatively charged mesons rather than positively charged mesons. Fluxes of neutrino beams are parametrised in terms of number of protons on target (POT) per year. Conventional beams have POT of about 10^{20} per year.

3. *Super-beams*: Super-beams are technology-upgraded versions of conventional beams. Neutrinos in super-beams are generated by using the off-axis technology to produce a narrow band beam, that is, the energy spectrum has a sharp peak. However, the proton fluxes are expected to be higher by a factor of 10 to 50. The source power for super-beams is $\simeq 10^{21}$ POT per year.

4. *Neutrino Factories*: These are based on muon storage rings where it will be possible to capture roughly 10^{20} muons (of either sign) per year. A muon storage ring has a racing track design with long, parallel, straight sections connected at the end by semi-circular sections. Beams of high energy muons ($E \sim 20$ to 50 GeV) circulate in the storage ring and can be made to decay in the straight sections. These decays produce a well collimated and intense neutrino beam. The composition and spectra of intense neutrino beams will be determined by the charge, momentum and polarisation of the stored muons. The beam consists of ν_μ and $\bar{\nu}_e$ if the ring contains μ^-, and it consists of $\bar{\nu}_\mu$ and ν_e if the ring contains μ^+.

Detector types

Below we give a brief description of the types of detectors and their main properties.

1. *Water Cerenkov Detector*: Highly purified water is used as the detecting element. High energy charged particles passing through the water produce Cerenkov light which is detected by Photo Multiplier Tubes (PMTs) surrounding the water. Based on the pattern of Cerenkov light emission, these detectors can identify both electrons/positrons and muons. Energy reconstruction of very high energy neutrinos ($E_\nu \geq 5$ GeV) is difficult because of a large number of particles in the hadron shower produced in the deep inelastic scattering, many of which will be below their Cerenkov threshold. There is no magnetic field with these detectors and hence the charge of a particle cannot be identified. The pure water may be replaced by heavy water or mineral oil as well.

2. *Liquid Argon Detector*: Liquid Argon is used as the detecting medium. The tracks produced by charged particles are identified in the liquid and based on the pattern of tracks the particle is identified. The detector has good calorimetry along with excellent particle identification capability. There is no magnetic field hence it is not possible to distinguish between particles and corresponding anti-particles.

3. *Iron Calorimeter*: Iron Calorimeters consist of iron (steel) modules interspersed with sensitive elements in which charged particles deposit energy. These detectors are cannot be used to detect electron-type neutrinos and hence are capable of observing only are ν_μ and $\bar{\nu}_\mu$. A magnetic field, however, can be added, in which case distinction between ν_μ and $\bar{\nu}_\mu$ interactions is possible.

4. *Emulsion Detector*: In this detector emulsion films (50 μm thick) are employed to observe the trajectories of τ and its decay products. These films are inter-leavened with 1 mm thick lead plates to provide large (1.8 kton) target mass. In addition to the emulsion films, the detector also contains a magnetic spectrometer which measures the charge and the momentum of muons going through it.

Expt.	Detector (mass)	Source	L (Km)	$\langle E_\nu \rangle$ (GeV)	Location
MINOS [39, 154]	Iron Calorimeter (5.4 kton)	Atmospheric Convent'l Beam	15–13000 735	1–100 3, ∼8, ∼11	Soudan, **US**
ICARUS [39, 202]	Liquid Argon TPC (2.35 kton)	Convent'l Beam	732	17	LNGS, **Europe**
OPERA [39, 203]	Emulsion Chamber (1.65 kton)	Convent'l Beam	732	17	LNGS, **Europe**
T2K [204]	Water Cerenkov (50 kton)	Super-beam (Off-axis)	295	0.76	Kamioka, **Japan**
NOνA [205]	Liquid Scintillator (50 kton)	Super-beam (Off-axis)	812	2.22	**US**
D-CHOOZ [206]	Liquid Scintillator (11.3 t)	Reactor	1.05	0.004	**France**
SK-III [207]	Water Cerenkov (50 kton)	Atmospheric Superbeam	15–13000 295	1–100 0.76	**Japan**
UNO [208]	Water Cerenkov (1 Mton)	Atmospheric Super-beam	15–13000 ∼2500	1–100 ∼0.5–7	**US**
Hyper-K [209]	Water Cerenkov (1 Mton)	Atmospheric Super-beam	15–13000 295	1–100 4.0	**Japan**
INO [5]	Iron Calorimeter (50–100 kton)	Atmospheric Super-beam/NF	15–13000 TBD	1–100 TBD	**India**

TBD → To be decided.

Table F.1: Detector type, neutrino source, baseline (L), average energy ($\langle E_\nu \rangle$) and location of the future experiments planned in next 10–15 years.

Physics Potential and Time-scale of future detectors

Expt.	Channel	Physics Potential	Data taking/ Partial result*
MINOS [39, 154]	$\nu_\mu \to \nu_{\mu,e}$	**Atm:** Compare ν_μ and $\bar{\nu}_\mu$ osc. : CPT test **Beam:** $\lvert\delta_{32}\rvert \sim 26\%$, $\sin^2\theta_{23} \sim 78\%$ precision** Improve $\sin^2 2\theta_{13} \sim$ factor of 2 over CHOOZ	Started/2007 2005/2006 2005/2007
ICARUS [39, 202]	$\nu_\mu \to \nu_{e,\mu,\tau}$	**Beam:** τ, e appearance, proton decay $\lvert\delta_{32}\rvert$, $\sin^2\theta_{23}$, $\sin^2 2\theta_{13}$ **Possible Atmospheric ν, Supernova ν**	2005/2009 2005/2009 2005/?
OPERA [39, 203]	$\nu_\mu \to \nu_{e,\mu,\tau}$	**Beam:** τ, e appearance, proton decay $\lvert\delta_{32}\rvert$, $\sin^2\theta_{23}$, $\sin^2 2\theta_{13}$	2006/2010 2006/2010
T2K [204]	$\nu_\mu \to \nu_{e,\mu}$	**Beam:** e appearance $\lvert\delta_{32}\rvert \sim 12\%$, $\sin^2\theta_{23} \sim 46\%$ precision** Improve $\sin^2 2\theta_{13} \sim$ factor of 6 over CHOOZ CP Violation, Proton decay (phase II)	2009/2014 2009/2014 2009/2014 2017/2018
NOνA [205]	$\nu_\mu \to \nu_{e,\mu}$	**Beam:** e appearance Improve $\sin^2 2\theta_{13} \sim$ factor of 6 over CHOOZ Sign δ_{32}, CP Violation $\nu_\mu \to \nu_\mu$ disappearance : CPT test, θ_{23} Search for sterile ν	2011/2012 2011/2012 2011/2017 2011/2012 2011/2012
D-CHOOZ [206]	$\bar{\nu}_e \to \bar{\nu}_e$	**Beam:** $\sin^2 2\theta_{13} < 0.03$, at 90% CL Improve $\sin^2 2\theta_{13} \sim$ factor of 4 over CHOOZ	2007/2010 2007/2010
SK-III [207]	$\nu_\mu \to \nu_{e,\mu}$	**Atm:** $\lvert\delta_{32}\rvert \sim 20\%$, $\sin^2\theta_{23} \sim 40\%$ precision** Improve $\sin^2 2\theta_{13} \sim$ factor of 2.3 over CHOOZ**	2006/2016 2006/2016
UNO [208]	$\nu_\mu \to \nu_{e,\mu,\tau}$	**Atm:** Possible τ appearance, L/E dip **Beam:** Sign δ_{32}, $\sin^2\theta_{13}$ to below 0.005 $\nu_\mu \to \nu_e$ appearance : δ_{21}, θ_{12} **Proton decay, Supernova ν**	2017/2018 2017/2018 2017/2018 2017/?
Hyper-K [209]	$\nu_\mu \to \nu_{e,\mu,\tau}$	**Atm:** Possible τ appearance, L/E dip **Beam:** $\sin^2\theta_{13}$ sensitivity below 10^{-3} Sign δ_{32}, δ_{CP} **Proton decay, Supernova ν**	2017/2018 2017/2018 2017/2018 2017/?
INO [5]	$\nu_\mu \to \nu_\mu$	**Atm:** L/E dip, CPT test $\lvert\delta_{32}\rvert \sim 20\%$, $\sin^2\theta_{23} \sim 60\%$ precision** Sign δ_{32} (100 kton detector) **Beam:** $\lvert\delta_{32}\rvert$, $\sin^2\theta_{23}$, $\sin^2 2\theta_{13}$ precision, δ_{CP}	2010/2013 2010/2015 2010/2017 TBD/+1 Year

$* \to$ Estimated $** \to$ Precision at 3σ (total spread around central value)
TBD $\to$ To be decided.

Table F.2: Physics potential and timescale estimated for the various neutrino experiments planned in next 10–15 years.

Appendix G

Possible Site for INO at Rohtang

Apart from INO at PUSHEP and Rammam, another exciting possibility is the 8,800 meters long tunnel near the Rohtang Pass at Manali. Two important reasons that make this site particularly exciting are that only a cavern/chamber needs to be excavated and that the overburden may be more than any other site that has been surveyed until now.

The foundation stone for the 8800 m-long tunnel at the Rohtang pass was laid by the Prime Minister in June 2002. Apart from building the tunnel which would save 40 km of landslide- and avalanche-prone road, the project involves strengthening and double-laning of the existing road so that it can become an all-weather access to Ladakh. The strategic importance of the road is clear from the Army's plans to move even heavy equipment like artillery guns up this road. All the bridges will be upgraded in a phased manner.

Location and Access

The Rohtang tunnel will bore through the Pir Panjal mountains connecting Kullu-Manali valley (around 2100 m elevation) into Lahaul-Spiti valley. The south portal of the tunnel is located near the Dhundi village. The north portal is located (at 78.3 km mark) on the Manali-Sarchu road.

The south portal is at distance of 20 km from Manali. Access road from Dhundi to the south portal is being expanded, with bridges reinforced to allow free movement of two-lane traffic. Manali is at a distance of 50km from Kullu. There is an airport at Kullu which is connected to Delhi by air. When fully operational, both the south portal and the north portal of the Rohtang tunnel will have helipads. Nearest railhead on broad-gauge is nearly 300km. However, Kullu-Manali is reasonably well connected by road to Shimla, Chandigarh and New Delhi.

Tunnel Details

The south portal is located at an elevation of 3050m and the north portal at an elevation of 3080m. The length of the tunnel is 8802m. The tunnel is 10 meters wide and 10 meters high in a horse shoe shape. The walls will be supported by steel ribs with fibre reinforced concrete. A positive gradient of 1.5 percent is maintained from both sides to allow gravity flow of seepage. Tunnel ventilation is done using semi-transverse system- ventilation from one side only.

Overburden: Fig.G-1 shows the longitudinal cross section of the mountain along the length of the tunnel. The maximum vertical overburden being 1900m at around the 6km

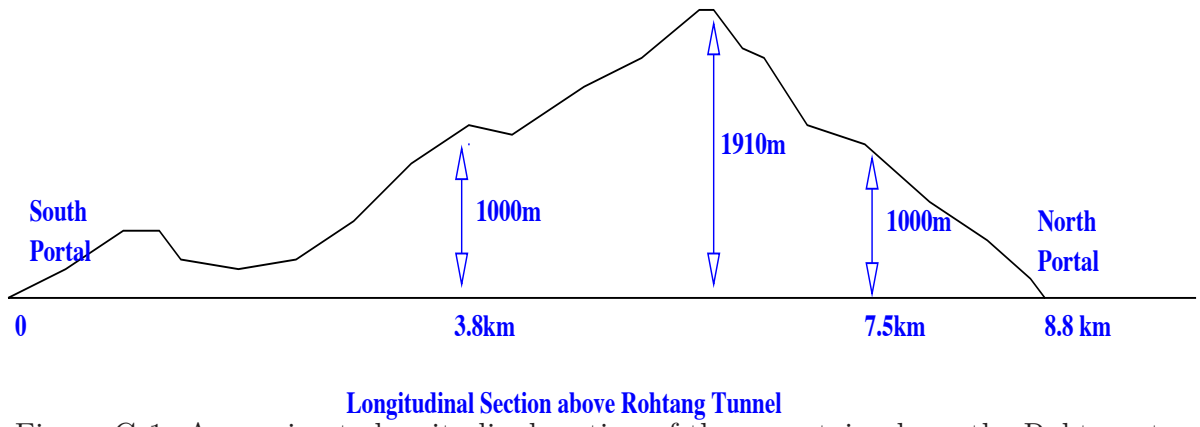

Figure G-1: Approximate longitudinal section of the mountain above the Rohtang tunnel.

from the south portal and 2.8km from the north portal. The vertical overburden is in excess of 1000m from about 3.8km to 6.8km from the south portal.

Rock Type: Uniformly dripping alternate sequence of quartzite, quartzitic schist, quartz-diolite, schist. Density varies from 2.5 to 2.85 with the average being 2.72. The region is in Seismic Zone-4

Cost and Time

The estimated cost of the road tunnel project to be executed by Border Roads Organisation (BRO) is about Rs. 778 crore at 2002 prices. Investment return ratio is about 11 percent. Estimated price escalation is about 7 percent to add to the cost, which is estimated currently at 1700 crore.

The Access road, Manali to Palchan to Solang to south portal, are almost finished. Nearly four bridges need reinforcement. The access road has 13 avalanche sites which need to be managed. There will also be a bypass constructed at Kullu for fast movement towards Manali. The tunnel will take 7-9 years to complete from time zero, which is definitely later than 2005.

INO at Rohtang

As far as INO at Rohtang possibility is concerned, one major civil engineering task will be automatically achieved because the 8800 m long tunnel provides multiple locations where caverns may be excavated as has been done at LNGS in Gran Sasso. The work begins from both ends, probably, by the end of 2005 at the earliest. Since the highest vertical overburden (1900m) is reached in less than 3000m from the north portal, INO cavern excavation will not wait for the completion of the Rohtang tunnel. Further, veering to the right (from north) at the 6000m by a 100m or so increases the vertical overburden to nearly 2000m making it one of the deepest underground laboratories.

Facilities

The Border Roads Organisation (BRO) is likely to create a campus around the beginning of the tunnel near Manali to provide dedicated power supply, ventilation system, water supply and fire services on much larger scale than needed for INO laboratory alone. This fact alone gives a tremendous advantage for INO since many of the maintenance aspects are already built in. Furthermore, the construction of caverns and smaller tunnels may also be undertaken by the same organisations that are involved in the Rohtang tunnel project on a turnkey basis for INO.

While the above factors make this proposal promising there are some issues, minor or major that need further study:

- The project site is situated in Seismic Zone-4 after recent reclassification.
- The time scale of the proposed project is supposed to be between seven to nine years. This is much longer than the estimated time scale at other sites.
- There are 13 avalanche sites on the way to the south portal location from Manali. Heavy snow falls are to be expected in winter. Typically up to 10-20 meters of snow can accumulate.
- Moving heavy machinery and materials is not going to be easy due to weather conditions. However the roads are built to standards which supports transport of very heavy equipment.
- There does not seem to be any industrial infrastructure of the type needed for INO around Manali. The biggest industry is Tourism. There are plenty of opportunities for trekking or simply sight seeing around Manali.

Figure G-2: View of the Rohtang Pass from the highest point at 3980m. The winding approach road from Manali is visible. (Photo courtesy: David Clarke)

Figure G-3: The descent from Rohtang Pass in to Chandra river valley, visible in the background. (Photo courtesy: David Clarke)

Appendix H

Memorandum of Understanding (MoU)

Memorandum of Understanding
FOR NEUTRINO COLLABORATION (NC)

Preamble :

In its X plan proposals relating to basic physics studies, Tata Institute of Fundamental Research in collaboration with Saha Institute of Nuclear Physics,Kolkata (SINP), Variable Energy Cyclotron Centre, Kolkata (VECC), Bhabha Atomic Research Centre, Mumbai (BARC), Institute of Mathematical Sciences, Chennai (IMSc), Harish Chandra Research Institute, Allahabad (HRI), Nuclear Science Centre, New Delhi (NSC) and several Universities had included a programme to take up comprehensive research in the area of neutrino physics. Subsequently the Internal Working Group (IWG) constituted by DAE for examining the plan proposals has agreed to an outlay of Rs. 5 crore proposed by TIFR under their inter-institutional research programmes for this activity (final allocation is yet to be approved). This outlay is meant to be used primarily towards working out the details that will help identify all inputs needed for full realization of the goals of this programme. Copy of the letter from IWG received by the Coordinator of INO programme is enclosed. (See Annexure A.) Recognising that this activity would possibly evolve into a major physics research programme of the DAE for the coming few plan periods, it evidently calls for a multi institutional effort right from its inception. This Memorandum of Understanding (MoU) is designed primarily to provide the necessary framework for forging the required inter-institutional collaboration. The MoU involves Tata Institute of Fundamental Research, Mumbai (TIFR), Saha Institute of Nuclear Physics, Kolkata (SINP), Variable Energy Cyclotron Centre, Kolkata (VECC), Bhabha Atomic Research Centre, Mumbai (BARC), Institute of Mathematical Sciences, Chennai (IMSc), Harish Chandra Research Institute, Allahabad (HRI) and Institute of Physics, Bhubaneswar (IOP). In this document, these institutions will be termed as Nodal Institutes. This MoU spells out the goals as well as the modalities for collaboration.

Background of the collaboration :

Groups of scientists working in the various research organisations and universities have been conducting independent, as well as joint research, on various aspects of Neutrino Physics and related experimental programmes. Such ventures have been very successful in terms of their scientific impact. The expertise of these groups of scientists and the infra-structural facilities available in these institutions are in many ways complementary. Inspired by these facts need has been felt by the community to have a national facility for future experiments

in neutrino physics. Accordingly this MoU is made for the specific purpose of exploring the **feasibility of creating an India-based Neutrino Observatory (henceforth called INO)**.

Goals of the collaboration :

The activities of the collaboration will include R&D efforts towards detector design and construction, survey for a suitable site location, detector simulation studies, and human resources development for the INO. The near-term goal will be to prepare a detailed project report (DPR) that will include discussion of all the above activities, and examine in depth the feasibility of setting up such an India-based Neutrino Observatory and explore international participation. In terms of human resources development, the goal will be to train manpower in this area as well as foster international collaboration. Travel between Academic Institutions, including Universities in India, to create interest amongst young research workers, and other scientific staff in INO activities will be a key component of the programme. This will also be augmented by holding regular group meetings at suitable locations, as well as meetings with International participation. There will be visits to institutions and laboratories abroad for soliciting their participation and also to get detector know how as and when necessary.

Methodology :

1. National Neutrino Collaboration Group (NNCG) is formed with the scientific members from both the Nodal Institutions as well as of members of other interested institutions. (See Annexure B.)

2. The academic members belonging to additional research organisations and the universities may also be later included in NNCG. the functioning and activities of NNCG will be coordinated by a Programme Management Committee (PMC) selected from the members of the NNCG. A Scientific Steering Committee (SSC) and an Advisory Council (AC) are also being constituted.

3. The current list of members of the PMC, SSC and AC are given in the attached Annexure C. PMC, SSC would meet once every quarter and AC once every six months.

4. New members can be inducted in to NNCG after approval by PMC.

5. Pre- and post-doctoral candidates can be recruited to work at any one of the nodal institutes to work exclusively for NC. Such recruitment must have prior approval of the PMC and these personnel should work for NC till the preparation of DPR on a yearly renewal basis. Remuneration for such appointees will be paid as per existing norms.

6. Research findings arising out of the collaborative projects covered by this MoU may be published (presented) in national and international journals (seminars/symposia/workshops) jointly by the researchers directly involved in the project as decided by the PMC.

Management of Funds :

1. TIFR will be the coordinating Institute as far as management of the NNCG funds is concerned during this feasibility study period. It will receive, monitor and distribute the funds made available to the NNCG by the funding agencies among various nodal institutes, as decided by PMC . For this purpose TIFR may open a separate bank A/c.

2. All authorised expenses borne by NNCG members in INO-related activity will be debited from this fund.

3. The PMC will have the sole authority to decide on and coordinate expenditure related to any INO activity during the feasibility study period. The PMC members are authorised to ratify any financial transactions between TIFR and the NNCG members.

4. Local travel expenses may be authorised by the local PMC member, but all other expenses have to be approved by the PMC, in advance. These include purchase of equipments for labs, international travel, fellowships for the pre- and post-doctoral recruits etc.

5. The nodal institute should initially arrange for the payment of fellowship to the pre- and post-doctoral recruits, and this will be subsequently reimbursed from the funds of NNCG available at TIFR on a regular basis.

6. For normal travel related expenses, the members of NNCG belonging to the Nodal Institutions may apply to their home Institution for an advance for authorised INO-related expenditure, which will be subsequently reimbursed from the NNCG funds available at TIFR.

7. For travel related expenses of the scientists of other institutions following procedures will be adopted. (i) For the visit to any Nodal Institution, expenses will be initially borne by that Nodal Institution and this will subsequently be reimbursed from the NNCG funds available at TIFR. (ii) For visits to places other than Nodal Institutions, expenses will be directly reimbursed by TIFR from the NNCG funds available at TIFR.

8. Purchase of all capital equipments and contracts (for survey, consultancy etc.) after PMCs approval will be processed by TIFR in accordance with TIFR purchase/approval of contract procedure irrespective of the ultimate place of delivery of the equipment or contract implementation. Inventory for the capital equipments has to be maintained separately by each nodal institute and will be considered as assets of respective institutions.

9. For the purchase of small consumables, funds may be transferred to the concerned nodal institute after PMC approval.

Institutional responsibilities :

1. Each Nodal Institute will provide the necessary infrastructure and other facilities to the members associated with this project so that the feasibility report can be prepared in the shortest period of time.

2. In pursuing collaborative activities, participating scientists of all the Nodal Institutes will agree to respect and abide by the rules and regulations of their respective institutes.

Scope and tenure of the MoU :

1. Any article of the MoU may be modified or changed only by a written agreement jointly by the signatories. The modifications will be effective from the date on which they are modified unless otherwise agreed to.

2. The tenure of this present MoU will be till the completion and submission of the detailed Project Report (DPR), at the end of the feasibility study. The scope and tenure of the MoU may then be extended, if deemed necessary by the participating institutes.

Signed:[1]

DIRECTOR
Tata Institute of Fundamental Research, Mumbai
Date :

DIRECTOR
Saha Institute of Nuclear Physics, Kolkata
Date :

DIRECTOR
Bhabha Atomic Research Centre, Mumbai
Date:

DIRECTOR
Variable Energy Cyclotron Centre, Kolkata
Date:

DIRECTOR
Harish-Chandra Research Institute, Allahabad
Date:

DIRECTOR
Institute of Mathematical Sciences, Chennai
Date:

DIRECTOR
Institute of Physics,
Bhubaneswar
Date:

[1]The MoU was signed by the directors of all the nodal institutions and countersigned by the Chairman, Atomic Energy Commission and Secretary, DAE.

Annexure A: Copy of the letter from IWG, DAE to Coordinator of INO Programme

Annexure B

National Neutrino Collaboration Group

I. Nodal Institutes

TIFR
B.S. Acharya, Sudeshna Banerjee, P.N. Bhat, S.R. Dugad, P. Ghosh, K.S.Gothe, S.K. Gupta, S.D. Kalmani, N. Krishnan, Naba K. Mandal, B.K.Nagesh, P.Nagaraj, Biswajit Paul, A.K.Ray, B. Satyanarayana, S.Upadhya, Piyush Verma

SINP
Pratap Bhattacharya, Sudeb Bhattacharya, Sukalyan Chattopadhyay, Ambar Ghoshal, Asimananda Goswami, Kamales Kar, Debasish Majumdar, Palash B. Pal, Satyajit Saha, Manoj Saran, Sandip Sarkar, Swapan Sen

VECC
Subhasish Chattopadhyay, M.R.Dutta Mazumdar, P. Ghosh, G.S.N. Murthy, Tapan Nayak, Y.P. Viyogi

BARC
V.M. Datar

IMSc
D. Indumathi, M.V.N. Murthy

IOP
S.C. Phatak, D.P. Mohapatra

HRI
Anindya Datta, Raj Gandhi, Srubabati Goswami, S. Rakshit

II. Other Institutions

NSC, New Delhi
Amit Roy

Calcutta University, Kolkata
Amitava Raychaudhuri

Panjab Univ., Chandigarh
M.M. Gupta, J.B. Singh

H.P. University, Shimla
S.D. Sharma

P.R.L., Ahmedabad
A.S. Joshipura, S.D. Rindani

North Bengal Univ.
A. Bhadra, B. Ghosh, A. Mukherjee, S.K. Sarkar

IIT, Mumbai
S. Umasankar

Annexure C

Members of the Programme Management Committee

Director	TIFR, Mumbai,	Chairman
Naba K. Mondal,	TIFR, Mumbai	Coordinator
P.N. Bhat,	TIFR, Mumbai	
V.M. Datar,	BARC, Mumbai	
Raj Gandhi,	HRI, Allahabad	
Kamales Kar,	SINP, Kolkata	
M.V.N. Murthy,	IMSc., Chennai	
S.C.Phatak,	IOP, Bhubaneswar	
A. Raychaudhuri,	Physics Dept., Calcutta Univ., Kolkata	
Y.P. Viyogi,	VECC, Kolkata	

Scientific Steering Committee

Prof. R. Cowsik	Indian Institute of Astrophysics, Bangalore
Prof. H.S. Mani	S.N. Bose Centre for Basic Sciences, Kolkata
Prof. V.S. Narasimham	Tata Institute of Fundamental Research, Mumbai
Prof. G. Rajasekaran	The Institute of Mathematical Sciences, Chennai
Dr. Amit Roy	Nuclear Science Centre, New Delhi
Prof. Bikash Sinha	Saha Institute of Nuclear Physics and Variable Energy Cyclotron Centre, Kolkata

Advisory Council for Neutrino Collaboration

Director, TIFR
Director, BARC

Director, VECC
Director, SINP
Director, IMSc
Director, HRI
Director, IOP
Nominee of Chairman, AEC
Coordinator of INO PMC

Bibliography

[1] C.V. Achar *et al.*, Phys. Lett., **18**, 196 (1965); *ibid.* **19** 78 (1965); F. Reines *et al.*, Phys. Rev. Lett. **15**, 429 (1965).

[2] M.R.K. Krishnaswamy *et al.*, Phys. Lett. **B 106**, 339 (1981); M.R.K. Krishnaswamy *et al.*, Pramana **19**, 525 (1982).

[3] M.V.N. Murthy and U. A. Yajnik, for the INO Working group, Pramana, J. Phys. **55**, 347 (2000).

[4] INO Collaboration Internal Report, INO-2002-01, submitted to the Department of Atomic Energy, 2002.

[5] See http://www.imsc.res.in/∼ino. Talks, papers and reports related to INO may be found in this site.

[6] Y. Fukuda *et al.*, (Super-Kamiokande Collaboration), Phys. Rev. Lett. **81** 1562 (1998): hep-ex/9807003.

[7] Y. Fukuda *et al.*, (Super-Kamiokande Collaboration), Phys. Rev. Lett. **82** 2644 (1999): hep-ex/9812014.

[8] S. Fukuda *et al.*, (Super-Kamiokande Collaboration), Phys. Rev. Lett. **85** 3999 (2000): hep-ex/0009001.

[9] Y. Fukuda *et al.*, (Super-Kamiokande collaboration), Phys Rev. Lett. **82**, 2430 (1999); **86** 5651 (2001).

[10] Q. R. Ahmad *et al.*, (SNO collaboration), *ibid.* **87**, 071301 (2001).

[11] B. Aharmim *et al.*, (SNO Collaboration): hep-ex/0407029.

[12] M. B. Smy *et al.*, (Super-Kamiokande Collaboration), Phys. Rev. **D 69**, 011104(2004): hep-ex/0309011.

[13] S. N. Ahmed *et al.*, [SNO Collaboration], Phys. Rev. Lett. **92**, 181301 (2004): nucl-ex/0309004.

[14] J. Yoo *et al.*, (Super-Kamiokande Collaboration), Phys. Rev. **D 68**, 092002(2003): hep-ex/0307070.

[15] F. Reines and C.L. Cowan, Jr., Phys. Rev. **92**, 830 (1953).

[16] Figure taken from the talk presented by P. Bhattacharjee at the Neutrino-2001 meeting, The Institute of Mathematical Sciences, Chennai, February 2001.

[17] The list of references on Standard Model and Neutrino oscillations is huge. Here we give references to books and reviews where all the essential details needed for this report are available:
J.N. Bahcall, *Neutrino Astrophysics* (Cambridge Univ.Press, 1989);
G. Rajasekaran. *Phenomenology of neutrino oscillations*, *Pramana*, **55**, 19 (2000);
R. N. Mohapatra and Palash Pal, *Massive neutrinos in Physics and Astrophysics* (World Scientific, Singapore, 2004);
N.G. Cooper, Ed., *Celebrating the Neutrino*, Published in "Los Alamos Science", No. 25 (1997).
D. Indumathi, M.V.N. Murthy and G. Rajasekaran, Eds., *Perspectives in Neutrino Physics*, Proceedings of Indian National Science Academy **76** (2004).

[18] B. T. Cleveland *et al.*, Astrophys. J. **496**, 505 (1998); Nucl. Phys. B (Proc. Suppl.) **38**, 47 (1995).

[19] W. Hampel *et al.*, (Gallex collaboration), Phys. Lett. **B447**, 127 (1999).

[20] J.N. Abdurashitov *et al.*, (SAGE collaboration), Phys. Rev. **C60**, 055801 (1999).

[21] M. Altmann *et al.*, (GNO collaboration), Phys. Lett. **B490**, 16 (2000): hep-ex/0006034.

[22] W.W.M. Allison *et al.*, (Soudan-2 Collaboration), Phys. Lett. **B449** 137 (1999): hep-ex/9901024.

[23] M. Ambrosio *et al.*, (MACRO Collaboration), Phys. Lett. **B478**, 5(2000).

[24] M. Ambrosio *et al.*, (MACRO Collaboration), Phys. Lett. **B566**, 35 (2003): hep-ex/0304037.

[25] M. Sanchez *et al.*, (Soudan 2 Collaboration), Phys. Rev. **D68**, 113004 (2003): hep-ex/0307069.

[26] K. Eguchi *et al.*, [KamLAND Collaboration], Phys. Rev. Lett. **90**, 021802 (2003): hep-ex/0212021.

[27] M. H. Ahn *et al.*, [K2K Collaboration], Phys. Rev. Lett. **90**, 041801 (2003): hep-ex/0212007.

[28] D.A. Petyt, for the MINOS-NuMI Collaboration, Joint Experimental/Theoretical Physics seminar at Fermi Lab, 30 March 2006. A pdf file of the talk may be found at http://www-numi.fnal.gov/talks/results06.html.

[29] S. Goswami, talk at Neutrino 2004, see S. Goswami, A. Bandyopadhyay and S. Choubey, hep-ph/0409224.

[30] J.N. Bahcall, M.C. Gonzalez-Garcia, C. Peña-Garay, JHEP 0302, 009 (2003), hep-ph/0212147; M.C. Gonzalez-Garcia, preprint hep-phh/0211054, talk given at the 10th international conference on supersymmetry and unification of fundamental interactions, SUSY02, DESY, Hamburg, June 2002.

[31] G. L. Fogli, E. Lisi, A. Marrone and A. Palazzo, hep-ph/0506083.

[32] The KATRIN Collab., C. Weinheimer, review talk at Neutrino 2002.

[33] Neutrino mass limits have been reviewed recently by
Carlo Giunti, hep-ph/0308206, NuFact 03, 5th International Workshop on Neutrino Factories & Superbeams, 2003; Christian Weinheimer, hep-ex/0306057, 10th Int. Workshop on Neutrino Telescopes, Venice/Italy, March 2003; Jean-Luc Vuilleumier, hep-ex/0306010, XXXVIII Rencontres de Moriond, Electroweak interactions and Unified Theories, 2003.

[34] C.L. Bennett *et al.*, Astrophys. J. **583** (2003) 1.

[35] Ariel Goobar, Steen Hannestad, Edvard Mortsell and Huitzu Tu astro-ph/0602155.

[36] K.S. Hirata, *et al.*, (Kamiokande-II Collaboration), Phys. Rev. **D38** 448 (1988).

[37] R. Cisneros, Astro. Sp. Sci. **10**, 87 (1971); M. Voloshin, M. Vysotskii, L.B. Okun, JETP **64**, 446 (1986), Sov. J. Nucl. Phys. **44**, 440 (1986); for a recent review see, Yifang Wang, hep-ex/0411028, talk given at 32nd Intl. Conf. on High Energy Physics, 2004, Beijing, P.R. China.

[38] C. Athanassopoulos, *et al.* (LSND Collaboration), Phys. Rev. Lett. **81**, 1774 (1998); Phys. Rev. **C58**, 2489 (1998).

[39] P. Huber, M. Lindner, M. Rolinec, T. Schwetz and W. Winter, hep-ph/0412133; talk given by T.S. at the NOW2004 workshop, Conca Specchiulla (Otranto, Italy), 11–17 Sept. 2004; A. Rubbia, hep-ph/0412230.

[40] Y. Ashie *et al.* (Super-Kamiokande Collaboration), hep-ex/0404034.

[41] G. Bhattacharyya, H.Pas, L. Song and T.J. Weiler, Phys. Lett. **B564**, 175 (2003): hep-ph/0302191.

[42] N. Y. Agafonova *et al.*, *MONOLITH: A massive magnetized iron detector for neutrino oscillation studies,* LNGS-P26-2000; http://castore.mi.infn.it/∼monolith/ .

[43] For a comprehensive list of ongoing, future experiments as well as theory of neutrino oscillations, solar neutrinos and atmospheric neutrinos, see The Neutrino Oscillation Industry page at http://www.hep.anl.gov/ndk/hypertext/nuindustry.html and follow the links; another useful site for comprehensive information on the status of neutrino physics is The Ultimate Neutrino page at http://cupp.oulu.fi/neutrino/.

[44] J. N. Abdurashitov *et al.*, [SAGE Collaboration], J. Exp. Theor. Phys. **95**, 181 (2002) [Zh. Eksp. Teor. Fiz. **122**, 211 (2002)]: astro-ph/0204245.

[45] S. Fukuda *et al.*, [Super-Kamiokande Collaboration], Phys. Lett. B **539**, 179 (2002): hep-ex/0205075.

[46] Q. R. Ahmad *et al.*, [SNO Collaboration], Phys. Rev. Lett. **89**, 011301 (2002): nucl-ex/0204008.

[47] C. Saji, talk given at NOON04, http://www-sk.icrr.u-tokyo.ac.jp/noon2004/ .

[48] Z. Maki, M. Nakazawa, S. Sakata, Prog. Theor. Phys. **28**, 870 (1962).

[49] T. K. Kuo and J. Pantaleone, Rev. Mod. Phys. **61** 937 (1989).

[50] L. Wolfenstein, Phys. Rev. D **17**, 2369 (1978); S. P. Mikheev and A. Y. Smirnov, Sov. J. Nucl. Phys. **42**, 913 (1985) [Yad. Fiz. **42**, 1441 (1985)].

[51] M. Maltoni, T. Schwetz, M.A. Tortola, J.W.F. Valle New J.Phys. **6**, 122 (2004); hep-ph/0405172.

[52] CHOOZ Collaboration: M. Appolonio *et al.*, Phys. Lett. **420B**, 397 (1998), Phys. Lett. **466B**, 415 (1999).

[53] T. Schwetz, Acta Phys. Polon. **B 36**, 3203 (2005), Talk given at the XXIX International Conference of Theoretical Physics, September 2005, Ustron, Poland: hep-ph/0510331.

[54] S. Goswami, Phys. Rev. D **55**, 2931 (1997); M. Cirelli, G. Marandella, A. Strumia and F. Vissani, Nucl. Phys. B **708**, 215(2005).

[55] V. Agrawal, T. K. Gaisser, P. Lipari and T. Stanev, Phys. Rev. D **53**, 1314 (1996): hep-ph/9509423.

[56] H. L. Lai *et al.*, Phys. Rev. D **55**, 1280 (1997): hep-ph/9606399.

[57] P. Picchi and F. Pietropaolo, ICGF RAP. INT. 344/1997, Torino 1997 (CERN preprint SCAN-9710037).

[58] T. Tabarelli de Fatis, Eur.Phys.J. C24, 43 (2002).

[59] Sergio Palomares-Ruiz , S.T. Petcov, arXiv: hep-ph/0406096.

[60] For details see, D. Indumathi and M.V.N. Murthy, Phys. Rev. **D71**, 013001,(2005): hep-ph/0407336.

[61] S. Choubey and P. Roy, Phys. Rev. **D73**, 013006 (2005).

[62] For details see, D. Indumathi, M.V.N. Murthy, G. Rajasekaran and Nita Sinha, hep-ph/0603264

[63] R. Gandhi, P. Ghoshal, S. Goswami, P. Mehta and S. Uma Sankar, Phys. Rev. Lett. **94**, 051801 (2005): hep-ph/0411252

[64] R. Gandhi, P. Mehta and S. Uma Sankar, *Matter effects in atmospheric μ^-/μ^+ in Magnetized Iron Calorimeters*, A note prepared for solar and atmospheric working group of American Physical Society, HRI Preprint, HRI-P-04-10-001.

[65] M. C. Bañuls, G. Barenboim and J. Bernabéu, Phys. Lett. B **513**, 391 (2001): hep-ph/0102184.

[66] A. Datta, R. Gandhi, P. Mehta and S. Uma Sankar, Phys. Lett. B **597**, 356 (2004): hep-ph/0312027.

[67] V. D. Barger *et al.*, Phys. Rev. Lett. **85**, 5055 (2000): hep-ph/0005197.

[68] T.D.Lee and C.N.Yang, Phys rev **98** , 1501 (1955).

[69] L.B.Okun, Sov J Nucl Phys , **10** 206 (1969); For a review see A.D.Dolgov , Phys Rept **320**, 1 (1999).

[70] E.G.Adelberger, B.R.Heckel and A.E.Nelson, hep-ph /0307284.

[71] A.S.Joshipura and S. Mohanty,Phys.Lett.B584, 103 (2004): hep-ph/0310210; A.S. Joshipura and S. Mohanty, *Constraining long-range leptonic forces using iron calorimeter detectors*, PRL Preprint, October 2004.

[72] J.A. Grifols and E. Masso , Phys. Lett. **B 579**, 123(2004).

[73] R. Foot, Mod. Phys. Lett. **A 6**, 527 (1991); X.-G. He, G.C. Joshi , H. Lew and R.R. Volkas, Phys. Rev. **D 44**, 2118 (1991); R. Foot *et al.*, Phys. Rev. **D 50**, 4571 (1994).

[74] Report of the APS Neutrino study group, R. N. Mohapatra *et al.*, www.physics.umd.edu/ep/mohapatra/rabinu.html.

[75] G.Rajasekaran, Neutrino Factories and Superbeams (5th International Workshop on Neutrino Factories and Superbeams, NuFact03), AIP Conference Proceedings 721, Ed: Adam Para, p. 243 (2004): hep-ph/0402246; See http://www.imsc.res.in/∼ino.

[76] R. Saakian, Nucl. Phys. Proc. Suppl. **111**, 169 (2002).

[77] G. Battistoni, A. Ferrari, T. Montaruli, P.R. Sala, Astropart. Phys. **19**, 269 (2003), Erratum *ibid.* **19**, 291 (2003).

[78] Paolo Lipari, Maurizio Lusignoli, Francesca Sartogo, Phys. Rev. Lett. **74**, 4384 (1995).

[79] C. Albright *et al.*, hep-ex/0008064.

[80] S. Geer, Phys. Rev. **D 57** 6989 (1998), hep-ph/9712290, erratum *ibid.* **D 59** 039903 (1999).

[81] R. Gandhi, P. Ghoshal, S. Goswami, P. Mehta and S. Uma Sankar, Phys. Rev. Lett. **94**, 051801 (2005): hep-ph/0408361.

[82] E Kearns, Talk at Neutrino 2004.

[83] M. Diwan *et al.*, hep-ex/0211001.

[84] Matter effects for atmospheric neutrinos are also discussed e.g. in E. K. Akhmedov *et al.*, Nucl. Phys. B **542**, 3 (1999); J. Bernabeu *et al.*, Phys. Lett. B **531**, 90 (2002).

[85] V. S Berezinsky, S. V Bulanov, V. A. Dogiel, V.L. Ginzburg and V.S. Ptuskin, *Astrophysics of Cosmic Rays*, (North Holland, Amsterdam) 1990.

[86] T.K. Gaisser, *Cosmic Rays and Particle Physics*, (Cambridge University Press, Cambridge) 1990.

[87] M.S. Longair, *High Energy Astrophysics*, (Cambridge University Press, Cambridge) 1992.

[88] T. Stanev, *High Energy Cosmic Rays*, (Springer-Praxis, Berlin) 2003.

[89] Joerg R. Hoerandel, Invited talk, presented at the "Workshop on Physics of the End of the Galactic Cosmic Ray Spectrum", Aspen, USA, April 25 - 29, 2005, astro-ph/0508014.

[90] M. Nagano and A.A. Watson, Rev. Mod. Phys. **72**, 689 (2000).

[91] HiRes-MIA Collaboration, T. Abu-Zayed *et al.*, astro-ph/0208243.

[92] AGASA Collaboration, M. Takeda *et al.*, Astropart.Phys. **19**, 447 (2003).

[93] P. Bhattacharjee and G. Sigl, Phys. Reports **327**, 109 (2000); Astropart. Phys. **16**, 373, (2000).

[94] D. De Marco and T. Stanev, Phys.Rev. **D72** 081301, (2005): astro-ph/0506318.

[95] M. Bertaina, for the EAS-TOP and MACRO Collaborations , *28th ICRC, Tsukuba 2003, Cosmic Rays*, 115 (2003).

[96] T. Antoni *et al.*, KASCADE Collaboration Astropart. Phys. **16**, 373, (2000).

[97] O.A. Gress *et al.*, TUNKA Collaboration *Proceedings of the 25th ICRC***4**, 129, (1997).

[98] J. R. Horandel *et al.*, KASCADE Collaboration, *Proceedings of the 26th ICRC***1**, 337, (1999).

[99] M. Aglietta *et al.*, EAS-TOP Collaboration Astropart. Phys. **10**, 1, (1999).

[100] S.I. Nikolsky, Nucl. Phys. Proc. Suppl. **B 75A**, 217, (1999).

[101] A. A. Petrukhin, *Proceedings of the XI Rencontres de Blois, "Frontiers of Matter"* Blois, France, (1999).

[102] D. Kazanas and A. Nicolaidis, astro-ph/0103147.

[103] D. Kazanas and A. Nicolaidis, Gen.Rel.Grav. **35**, 1117, (2003): hep-ph/0109247.

[104] For a review and references, see J. Horandel, astro-ph/0508014.

[105] B. Peters, Nuovo Cim. Suppl. **14**, 436, (1959).

[106] I.S. Alekseev and G. T. Zatsepin *Proceedings of the ICRC***1**, 326, (1960).

[107] R. P. Kokoulin and A. A. Petrukhin, Sov. J. Part. Nucl **21**(3), 332 (1990).

[108] R. P. Kokoulin and A. A. Petrukhin, Nucl. Instrum. Methods Phys. Res. A **263**, 468 (1988).

[109] D. Muller *et al.*, TRACER Collaboration, to appear in *Proceedings of the 29th ICRC* Pune, (2005).

[110] G. Navarra, *et al.*, Nucl. Instrum. Methods Phys. Res. A **518**, 207 (2004).

[111] H. Falcke *et al.*, Nature **435**, 313, (2005).

[112] V. Berezinsky, astro-ph/0505220.

[113] G. Sigl, hep-ph/0109202.

[114] R. Gandhi, Nucl. Phys. Proc. Suppl. **91**, 453, (2000): hep-ph/0011176.

[115] R. Gandhi, C.Quigg, M.H. Reno, I.Sarcevic, Astropart. Phys. **5**, 81, (1996): hep-ph/9512364.

[116] R. Gandhi, C.Quigg, M.H. Reno, I.Sarcevic, Phys.Rev. **D58**, 093009, (1998): hep-ph/9807264.

[117] T. Gaisser, F. Halzen and T. Stanev, Phys. Rept. **258**, 173, (1995).

[118] A. Silvestri for the AMANDA Collaboration, Int. Jour. of Mod. Phys **A20**, 3096 (2005).

[119] T. DeYoung for the ICECUBE Collaboration, Int. Jour. of Mod. Phys **A20**, 3160 (2005).

[120] M. Circella for the NEMO Collaboration, ICRC, Pune, 2005.

[121] L. V. Volkova, Sov. Jour. Nucl. Phys. **31** 784, (1980).

[122] T.K. Gaisser *et al.*, Phys. Rev. **D38**, 85 (1988); G. Barr*et al.*, Phys. Rev. **D39**, 3532 (1989).

[123] P. Lipari, Astropart. Phys. **1** 195 (1993).

[124] M. Thunman, G.Ingelman, P. Gondolo, Astropart.Phys. **5** 309 (1995).

[125] M. Aglietta *et. al.*, LVD Collaboration, Phys. Rev. **D60** 112001 (1999).

[126] M. Nagano *et. al.*, Journ. of Physics G: Nucl. Phys. **12** 69, (1986).

[127] E. Zas, F. Halzen and R. Vazquez, Astropart. Phys. **1** 297 (1993).

[128] O Ryazhskaya, L. Volkova and O. Saavedra, Nucl. Phys. Proc. Suppl. **B 110**, 531, (2002).

[129] L. Pasquali, M. H. Reno and I. Sarcevic, Phys. Rev. **D59**, 034020, (1999).

[130] E. Bugaev, V. Naumov, S. Sinegovsky and E. Zaslavskaya, Nuovo Cim. **C12**, 41, (1989).

[131] G. Gelmini, P. Gondolo and G. Varieschi, Phys. Rev. **D61**, 036005, (2000); *ibid.* Phys. Rev. **D61**, 056011, (2000).

[132] A. Martin, M. Ryskin and A. Stasto, Acta Phys.Polon. **B34**, 3273, (2003): hep-ph/0302140.

[133] S. R. Kel'ner and Yu. D. Kotov, Sov. J. Nucl. Phys. **7** 237, (1968).

[134] A. A. Petrukhin and V.V. Shestakov, Can J. Phys. **46**, s337(1968).

[135] L. B. Bezrukov and E. V. Bugaev, Sov. J. Nucl. Phys. **33**, 635 (1981); E.V. Bugaev and Yu. V. Shlepin, Phys.Rev. **D67**, 034027, (2003): hep-ph/0203096.

[136] M.R. Krishnaswamy *et al.*, Phys. Lett. B **57**, 105 (1975); Pramana, **5**, 59 (1975).

[137] H. Faissner *et al.*, Phys. Lett. B**60**, 401(1976).

[138] A.C. Benvenuti *et al.,* Phys. Rev. Lett. **32**, 125(1974); *ibid.*, 1454 (1974); Phys. Rev. Lett. **35**, 1486 (1975).

[139] A. de Rujula *et al.*, Phys. Rev. Lett. **35**, 628 (1975).

[140] G. Rajasekaran and K.V.L. Sarma, Pramana **5**, 78 (1975).

[141] J.C. Pati and A. Salam, Preprint ICTP/75/73, (1975).

[142] G.V. Fedotovich *et al.*, Proc. Int. Conf. on Instrumentation for Colliding Beam Physics, Stanford, 1982.

[143] R. Santonico *et al.*, Nucl. Inst. and Meth. **A263**, 20(1988); See also, R. Santonico Nucl. Inst. and Meth. **A456**, 1 (2000).

[144] G. Anelli *et al.*, Nucl. Inst. and Meth. **A300**, 572 (1991).

[145] N.K. Mondal, Invited talk at the 6th ACFA workshop on *Physics and detector at Linear Collider*, Mumbai, December 2003.

[146] M. Abbrescia *et al.*, (CMS Collaboration), Nucl. Inst. and Meth. **456**, 103 (2000); See also, Muon Technical Design Report, CERN/LHCC Report 97–32, 15 December, 1997.

[147] G. Aielli *et al.*, (ATLAS Collaboration), Nucl. Inst. and Meth. **456**, 77(2000); See also, Muon Spectrometer Technical Design Report, CERN/LHCC 97–22, 5 June, 1997.

[148] P. Colrain *et al.*, (LHCb Collaboration), Nucl. Inst. and Meth. **A456**, 62 (2000); See also, MUon System Technical Design Report, CERN/LHCC 2001-010, 28 May, 2001.

[149] R. Arnaldi *et al.*, (ALICE Collaboration), Nucl. Inst. and Meth. **A456**, 73 (2000); See also, Muon Spectrometer Technical Design Report, CERN/LHCC 97–22, 13 August, 1999.

[150] M. Ambrosio *et al.*, (MONOLITH collaboration), Nucl. Inst. and Meth. **A456**, 67 (2000).

[151] M. Yamaga *et al.*, (BELLE collaboration), Nucl. Inst. and Meth. **A456**, 109 (2000).

[152] POISSON/SUPERFISH Reference Manual, Los Alamos Code Group MS H829.

[153] MagNet6.0 Code, Infolytica Corporation, USA.

[154] M. Thomson (MINOS Collaboration), Talk at *XXIst International Conference on Neutrino Physics and Astrophysics (Neutrino-2004)*, Paris, June 14-19, 2004, see http://neutrino2004.in2p3.fr/ ;
P. Shanahan, Eur. Phys. J. C **33**, s834 (2004).

[155] The NUANCE Neutrino Generator, D. Casper, Nucl. Phys. Proc. Suppl. **112** 161 (2002) (http://www.ps.uci.edu/∼nuint/nuance/default.htm).

[156] M. Honda, T. Kajita, K. Kasahara and S. Midorikawa, Phys.Rev. **D70**, 043008 (2004): astro-ph/0404457.

[157] GEANT - Detector Description and Simulation Tool, CERN Program Library W5013 (http://wwwasd.web.cern.ch/wwwasd/geant/).

[158] C.A. Ayre *et al.*, J. Phys **G 1**, 584 (1975);
B.C. Rastin, J. Phys **G 10**, 1609 (1984);
O.C. Allkofer, K. Carstensen and W.D.Dau, Phys. Lett. **B 36**, 425 (1971);
J. Jokisch *et al.*, Phys. Rev. **D 19**, 1368 (1979).

[159] The Particle Data Group, S. Eidelman *et al.*, Phys. Lett. **B 592**, 1 (2004), section on Cosmic Rays revised Mar 2002 by T.K. Gaisser and T. Stanev, http://pdg.lbl.gov/

[160] L.M. Krauss, S.L. Glashow and D.N. Schramm, Nature **310**, 191 (1984).

[161] R.S. Raghavan *et al.*, Phys. Rev. Lett. **80**, 635 (1998).

[162] H. Nunokawa *et al.*, hep-ph/0308175; F. Mantovani *et al.*, hep-ph/0309013.

[163] S. Mohanty, hep-ph/0302060.

[164] F. Mantovani *et al.*, Phys. Rev. **D 69**, 013001 (2004); S. Mohanty, hep-ph/0502241.

[165] R.S. Raghavan, hep-ex/0208038.

[166] M. Maurette, Ann. Rev. Nucl. Sci. **26**, 319 (1976).

[167] A. De Rujula, S. Glashow, R. Wilson and G. Charpak, Phys. Rep. **99**, 341 (1983).

[168] C E Aalseth *et al.*, Mod Phys. Lett **A 17**, 1475 (2002): hep-ex/0202018.

[169] H V Klapdor-Kleingrothaus, hep-ph/0205228.

[170] B.V. Sreekantan and S. Naranan, Proc. Ind. Acad. Sci. **43**, 116 (1956).

[171] S. Miyake, V.S. Narasimham and P.V. Ramanamurthy, Nuovo Cimento **32**, 1505 (1964); Nuovo Cimento **32**, 1524 (1964).

[172] M.G.K. Menon *et al.*, Proc. Roy. Soc. **A301**, 137 (1967); M.R. Krishnaswamy *et al.*, Proc. Roy. Soc. **A323**, 489 (1971).

[173] M.R. Krishnaswamy *et al.*, Phys. Lett. **B 27**, 535 (1968); Acta. Phys. Hungarica (Suppl) **4**, 21 (1969), Pramana **5**, 5 (1975).

[174] P. N. Bhat and P.V. Ramanamurthy, J. of Phys. **4**, 453 (1978).

[175] The Kolar KGF group, M.R. Krishnaswamy, M.G.K. Menon, N.K. Mondal, V.S. Narasimham, B.V. Sreekantan, Y. Hayashi, N. Ito, S. Kawakami, S. Miyake, Nuovo Cimento **C 9** (1986) 167.

[176] V.M. Datar, C.V.K. Baba, S.K. Bhattacherjee, C.R. Bhuinya, A. Roy, Nature **318** 547, (1985).

[177] G. Rajasekaran. *Phenomenology of neutrino oscillations*, Pramana **55**, 19 (2000).

[178] B. Pontecorvo, JETP **6**, 429 (1958).

[179] B. Kayser, *Phys. Rev.* **D 24**, 110 (1981); C.Giunti, C. W. Kim, W. Lam, *ibid.* **D 44**, 3635 (1991).

[180] P. Zucchelli, Phys. Lett. **B 532,** 166 (2002).

[181] M. Mezzetto, J. Phys. **G 29,** 1771 (2003).

[182] J. Bouchez, M. Lindroos, M. Mezzetto, AIP Conf. Proc. **721**, 37 (2004): hep-ex/0310059.

[183] J. Burguet-Castell, *et al.,* Nucl. Phys. **B 695,** 217 (2004): hep-ph/0312068.

[184] B. Pontecorvo, JETP **6,** 429 (1958); **7**, 172 (1958); Z. Maki, M. Nakagawa, S. Sakata, Prog. Theor. Phys. **28**, 870 (1962).

[185] M. Lindroos, "Accelerator based neutrino beams", Talk at Moriond meeting, March 2003.

[186] B. Autin *et al.,* J. Phys. **G 29,** 1785 (2003): physics/0306106.

[187] F. Terranova, A. Marotta, P. Migliozzi, M. Spinetti, Eur. Phys. J. **C 38,** 69 (2004): hep-ph/0405081.

[188] C.H. Llewellyn Smith, Phys. Rep. **3**, 261 (1972).

[189] For parton distribution functions, see, for example, M. Gluck, E. Reya, A. Vogt, Z. Phys. **C 67,** 433 (1995).

[190] G. L. Fogli, G. Nardulli, "Results about a new model of weak one pion production: NC case" (Talk);

D. Rein, L. M. Sehgal, Annals of Physics **133**, 79 (1981).

[191] A. Bandyopadhyay *et al.*, Phys. Lett. **B 608**, 115 (2005): hep-ph/0406328.

[192] M. Maltoni, T. Schwetz, M.A. Tortola, J.W.F. Valle, New J. Phys. **6**, 122 (2004).

[193] V.D. Barger, S. Pakvasa, K. Whisnant, R.J.N. Phillips, Phys. Rev. **D 22**, 2718 (1980).

[194] Report of the working group of the APS multidivisional neutrino study. arXiv:hep-ph/0412300, Dec. 2004.

[195] C. Arnobaldi *et al.*, Nucl. Instrum. and Meth. A **518**, 775 (2004).

[196] H.V. Klapdor-Kleingrothaus *et al.*, Nucl. Instrum. and Meth. **A 511**, 341 (2003).

[197] H.V. Klapdor-Kleingrothaus *et al.*, Phys. Lett. **B 586**, 198 (2004).

[198] C. Arnobaldi *et al.*, Phys. Rev. Lett. **95**, 142501 (2005).

[199] M. Narayan, G. Rajasekaran and S. Uma Sankar, Phys. Rev. **D 58**, 031301 (1998).

[200] J. N. Bahcall, M. C. Gonzalez-Garcia and C. Pena-Garay, hep-ph/0406294.

[201] Y. Ashie *et al.*, [Super-Kamiokande Collaboration], Phys. Rev. **D 71**, 112005 (2005): hep-ex/0501064.

[202] A. Bueno, [ICARUS Collaboration] Talk at *XXIst International Conference on Neutrino Physics and Astrophysics (Neutrino-2004)*, Paris, June 14-19, 2004, see http://neutrino2004.in2p3.fr/;
J. Lagoda, see http://nanp.dubna.ru/2003/ .

[203] D. Autiero, (OPERA Collaboration), Talk at *XXIst International Conference on Neutrino Physics and Astrophysics (Neutrino-2004)*, Paris, June 14-19, 2004, see http://neutrino2004.in2p3.fr/;
M. Dracos, Talk at *The 4th International Conference on non-accelerator new physics (NANP 2003)*, see http://nanp.dubna.ru/2003/ .

[204] Y. Hayato, (T2K Collaboration) Talk at *XXIst International Conference on Neutrino Physics and Astrophysics (Neutrino-2004)*, Paris, June 14-19, 2004, see http://neutrino2004.in2p3.fr/ ;
Y. Itow *et al.*, hep-ex/0106019;
see http://neutrino.kek.jp/jhfnu/ .

[205] NOvA: Proposal to Build an Off-Axis Detector to Study muon-netrino $\rightarrow$ electron-neutrino Oscillations in the NuMI Beamline, FERMILAB-PROPOSAL-0929, see http://library.fnal.gov/archive/test-proposal/0000/fermilab-proposal-0929. shtml/ .
D. Ayres *et al.*, *Letter of intent to build an off-axis detector to study $\nu_\mu \rightarrow \nu_e$ oscillations with the NuMI neutrino beam*, hep-ex/0210005, see http://www-off-axis.fnal.gov/ ;
A. Weber, Eur. Phys. J C **33**,843(2004); M. Messier, Talk at *XXIst International Conference on Neutrino Physics and Astrophysics (Neutrino-2004)*, Paris, June 14-19, 2004, see http://neutrino2004.in2p3.fr/ .

[206] L. Oberauer, Talk at *XXIst International Conference on Neutrino Physics and Astrophysics (Neutrino-2004)*, Paris, June 14-19, 2004, see http://neutrino2004.in2p3.fr/ ;
T. Lasserre, Talk at *The 5th workshop on Neutrino Oscillations and their Origin*, see http://www-sk.icrr.u-tokyo.ac.jp/noon2004/ ;
K. Anderson *et al.*, *White paper report on using nuclear reactors to search for a value of theta(13)*,hep-ex/0402041.

[207] H. Gallagher, Talk at *XXIst International Conference on Neutrino Physics and Astrophysics (Neutrino-2004)*, Paris, June 14-19, 2004, see http://neutrino2004.in2p3.fr/ ;
T. Kajita, Talk at *The 5th workshop on Neutrino Oscillations and their Origin (NOON-2004)*, see http://www-sk.icrr.u-tokyo.ac.jp/noon2004/ ;
H. Back *et al.*, hep-ph/0412016.

[208] *Expression of Interest for the Study of Nucleon Decay and Neutrino Physics Using a Large Underground Water Cherenkov Detector*, see
http://ale.physics.sunysb.edu/uno/publications.shtml/ ;
Physics potential and feasibility of UNO (The UNO whitepaper), SBHEP01-3 (June 2001), edited by D. Casper, C. K. Jung, C. McGrew, C. Yanagisawa, see http://ale.physics.sunysb.edu/uno/publications.shtml/ ;
C. K. Jung, hep-ex/0005046;
AIP Conf. Proc. **533** (2000), edited by M. V. Diwan and C. K. Jung.

[209] K. Nakamura, Talk at *Conference on Neutrinos and Implications for Physics Beyond the Standard Model*, C. N. Yang Institute for theoretical physics, SUNY, Stony Brook, Oct 11-13, 2002, see http://insti.physics.sunysb.edu/itp/conf/neutrino/talks/nakamura.pdf .

[210] R. Gandhi, P. Mehta and S. Uma Sankar, *Matter effects in atmospheric μ^-/μ^+ events*, A note prepared for solar and atmospheric working group of American Physical Society, HRI-P-04-10-001;
R. Gandhi, P. Ghoshal, S. Goswami, P. Mehta and S. Uma Sankar, hep-ph/0411252.